AN ABSTRACT OF THE THESIS OF

EDGAR L ANDREAS for the degree of DOCTOR OF PHILOSOPHY

in OCEANOGRAPHY presented on June 13, 1977

Title: OBSERVATIONS OF VELOCITY AND TEMPERATURE AND ESTIMATES OF MOMENTUM AND HEAT FLUXES IN THE INTERNAL BOUNDARY LAYER OVER ARCTIC LEADS

Abstract approved: Redacted for privacy
Dr. Clayton A. Paulson

The primary purpose of the AIDJEX Lead Experiment (ALEX) of early 1974 was to measure the turbulent component of the heat flux from Arctic leads in winter. This thesis describes that experiment, summarizes the data taken on the downwind side of the leads, and discusses the determination of the sensible and latent heat and momentum fluxes over Arctic leads.

Three methods are used to evaluate the sensible heat flux. The basic estimate relies on an energy conservation approach which requires upwind and downwind temperature profiles and the downwind velocity profile. The second method uses the empirically-determined flux-gradient relationships, which are approximately valid very near the surface of the lead. Thirdly, measurements of the correlation between vertical velocity and temperature fluctuations give the sensible heat flux directly. In addition, several

low quality humidity profiles allow estimates of the latent heat flux, again on the basis of energy conservation. Both the sensible and latent heat fluxes correlate with bulk parameters and, hence, can be estimated with only a few bulk measurements.

Though the primary emphasis of ALEX was on the heat flux determination, the raw data alone -- the velocity and temperature profiles -- are of considerable interest. Seldom have internal thermal boundary layers of geophysical scale been so extensively studied. Seventy-six pairs of velocity and temperature profiles from within the boundary layer and more than 30 u and w spectra and uw cospectra tell a great deal about thermal boundary layer processes. The velocity profile, in particular, within the layer is very complex. It is modified by the tremendous vertical heat flux and affected near the surface by the roughness transition between relatively smooth ice and the rougher water of the lead. A comparison of upwind and downwind temperature profiles yields the internal thermal boundary layer height, δ, the height at which the downwind temperature profile rejoins the upwind profile. That height is primarily a function of the stability parameter z_0/L, where z_0 is the surface roughness and L is the Monin-Obukhov length, but also depends on the upwind stability and, of course, the fetch across the lead.

Spectra and cospectra from over the lead and the consequent integral statistics are unique for basically two reasons. First, the spectral data was obtained very near the surface; therefore, Reynolds numbers were small. Secondly, the flows were fetch-limited. This horizontal inhomogeneity apparently affects the uw cospectra most; they contain more spectral energy at higher frequencies than do cospectra characterizing horizontally homogeneous conditions.

Observations of Velocity and Temperature and Estimates of Momentum and Heat Fluxes in the Internal Boundary Layer Over Arctic Leads

by

Edgar L Andreas

A THESIS

submitted to

Oregon State University

in partial fulfillment of
the requirements for the
degree of

Doctor of Philosophy

Completed June 13, 1977

Commencement June 1978

APPROVED:

Redacted for privacy

Associate Professor of Oceanography
in charge of major

Redacted for privacy

Dean of School of Oceanography

Redacted for privacy

Dean of Graduate School

Date thesis is presented June 13, 1977

Typed by Deanna L. Cramer for Edgar L Andreas

ACKNOWLEDGEMENTS

I would like to express sincere thanks to the following, who contributed substantively and essentially to the completion of this thesis:

Dr. Clayton Paulson, my major professor, whose counsel was invaluable;

Drs. Gunnar Bodvarsson, John Allen, Harry Bryden, Thomas McClennan, Kilho Park, and Gerald Davis, who served either full or partial terms on my advisory committee;

Dr. Richard Williams--office mate, question-answerer, and sounding board--without whose expertise ALEX could not have succeeded;

Dr. Jack Shreffler, whose thorough numerical study of the heat flux from leads and understanding of boundary transfer processes (shared while we backpacked in the North Cascades) were of inestimable value to this thesis;

Ron Lindsay, who not only provided the upwind data but also was a sympathetic fellow-sufferer as we sorted out similar calibration and analysis problems;

Andreas Heiberg and David Bell of the AIDJEX Office, who were the Lone Ranger and Tonto of ALEX--always arriving in the nick of time to get the good guys out of a tight spot;

Leon Childers, who turned a metal box into the R.V. Big Blue, our instrument hut;

Asa Robinson, without whose assistance our gear would have never gotten out of Corvallis;

Personnel of the Naval Arctic Research Laboratory, who flew us, muscled our gear, helped construct the artificial leads, gave advice on ice conditions, and did whatever else was necessary to make ALEX go;

Charlie Johnson, who could handle a helicopter so delicately and so precisely that Nadia Comaneci seemed like an auto mechanic in comparison;

Dr. Richard Johnson and Mike Hooning, who freely gave computing help;

Ron Hill, who did his usual class act on the graphics;

David Reinert, who turned my nonprofessional drawings into 8 x 10 glossies which looked Ron Hill perfect;

The Forsyths, whose home was an eye in the hurricane of my thesis research;

My mother, who understood and somehow managed to explain to the relatives what her son was still doing in school;

The National Science Foundation, which supported this research through Grant GV-37145A#1 to Oregon State University and contract C625 with the University of Washington;

And Diane, who held my hand through much of this.

TO MY MOTHER,

Frances M. Andreas

If I caused the wind to change
with one wave of my hand . . .

Gordon Lightfoot
"If I Could"

TABLE OF CONTENTS

Table of Contents -- continued

LIST OF FIGURES

List of Figures -- continued

Appendix Figures

List of Figures -- continued

LIST OF TABLES

Appendix Tables

OBSERVATIONS OF VELOCITY AND TEMPERATURE AND ESTIMATES OF MOMENTUM AND HEAT FLUXES IN THE INTERNAL BOUNDARY LAYER OVER ARCTIC LEADS

1. INTRODUCTION

Honor the High North ever and ever . . .
Robert W. Service
"Men of the High North"

1.1. THE ARCTIC HEAT BUDGET

The Earth is a heat engine, a thermodynamic system, converting heat energy from the sun into the mechanical energy of atmospheric and oceanic circulations. The goal of meteorology and oceanography is to understand the dynamics of the air and water realms and the interaction of the two. Therefore, since solar heat is the sole source of energy driving the global circulation, heat budget studies are one avenue to this understanding. How much heat arrives from the sun? How much is returned to space and where? What portion is reflected at density interfaces? Which surfaces absorb how much? What is the rate of transfer from here to there?

The Arctic region is a huge heat sink in the planetary thermodynamic system. Because the sun's incoming energy is concentrated around the equator, the poles receive much less energy than do lower latitudes. Hence, the resulting temperature gradient between low and high

latitudes forces the oceans and atmosphere to answer the polar call for warmth. Warm currents and warm air masses transport heat into the Arctic while the region exports 'cold' in the form of cold air masses, cold currents, and ice.

Because the Arctic is such a sink for the planet's heat, its heat budget is of considerable consequence. And the yearly variability of that budget is similarly important: do variations in the Arctic heat budget have any relation -- whether as cause or consequence -- to climatic anomalies? What is the state of the Arctic Ocean during continental glaciation? How would the heat budget and particularly the pack ice cover respond to a prolonged heating or cooling of the atmosphere?

Some have hypothesized that the Arctic Ocean has two quasi-steady states -- an ice-covered and an ice-free state -- which are intimately connected with the climate over the entire planet (Ewing and Donn, 1956, 1958; Fletcher, 1965; Donn and Ewing, 1966). When the Arctic is ice-free, it provides a northern moisture source and so fosters continental glaciation; when ice-covered there is no moisture source and, consequently, an interglacial period. But others refute this theory claiming the Arctic Ocean has never been ice-free and so is not a controlling factor in continental glaciation (Clark, 1971).

Uncertainty in several terms of the Arctic heat budget allows such antithetical views. Considering that even year to year Arctic climatic anomalies are proving "difficult to unravel" (Oort, 1974), anomalies with periods of 10,000 years are yet well beyond the limits of our understanding. We must start with the basics first -- define all the pieces of the Arctic heat budget puzzle. Observations in the Arctic are a necessity. Too often terms in the heat budget are estimated using bulk formula which have rarely been tested against ground truth in the Arctic. This thesis will, thus, discuss an in situ investigation of one term in the Arctic heat budget -- the turbulent flux of heat from Arctic leads in winter.

Through the winter the Arctic Ocean is almost totally covered by a rind of pack ice about three meters thick. But due to the stress imposed by wind and water the ice occasionally cracks and separates. This chink in the pack ice which at first exposes open water but may, as time passes and freezing occurs, contain ice in various stages of formation, including a complete cover of new ice up to several centimeters thickness, we shall refer to as a lead.

The origin of the term 'lead' to mean a crack in the pack ice is obscure but may have come from the days of the wooden-hulled sealing and whaling ships. Nansen (1897) gives us a clue: throughout his book, 'channel' appears where we infer 'lead'. That is, a lead provides an avenue

for ships: sealers can take their fragile vessels only where the channels lead.

Seemingly no study has yet been made to determine the distribution of physical dimensions of leads: most published information on size is simply of a descriptive nature. Zakhavov (1966) mentions leads which "stretch unbroken" for several hundred kilometers between the shore ice and the floating ice in the Laptev Sea. Auferheide and Pitzl (1970) encountered leads two miles wide and six to seven miles long on their snowmobile ride to the North Pole in 1968. When Nansen and Johansen left the Fram in early 1895 and tried to reach the North Pole by ski and dog sled, they were thwarted, in part, by continually having to negotiate 'channels' from ten to fifty meters wide and perhaps a kilometer in length (Nansen, 1897).

Most agree that leads have limited areal coverage. Untersteiner (1964), Badgley (1966), and Coachman (1966) each estimate that in winter there is one percent or less open water in the Arctic Ocean; Wittman and Schule (1966) say two percent is a realistic figure.

How can such small features in the pack ice be of any significance in the Arctic heat budget? During the winter the surface ocean water is at near freezing, -1.7°C, while the lower atmosphere may be -20°C to -40°C; however, the ubiquitous pack ice is a very good insulator and so generally keeps the two thermally separated. But leads disrupt

the integrity of the ice. Air and water are allowed intimate contact, and the large temperature difference between the two drives a tremendous outpouring of heat, sensible, latent, and radiative, from the ocean to the atmosphere. The magnitude of this exchange has been estimated to be two orders of magnitude greater than the heat flux through mature ice (Badgley, 1966). Consequently, even if leads cover only one percent of the ocean area, they still account for roughly one half of the turbulent heat exchange between ocean and atmosphere during the Arctic winter.

Badgley (1966) provides two tables which give us a more quantitative picture of the part leads play in the surface heat budget of the Arctic Ocean. Table 1.1 is his estimate of the surface heat budget for mature ice; Table 1.2 is the heat budget for a lead surrounded by pack ice. The notation in the tables is:

α	the albedo of the surface
S	incident solar radiation (direct and diffuse)
$S(1-\alpha)$	solar radiation absorbed
O	outgoing surface infrared radiation
I	incoming infrared absorbed at the surface
O-I	net infrared
R	= O-I-$S(1-\alpha)$, the surface radiation balance
H	sensible heat flux to air
H_L	latent heat flux to air
B	= $R+H+H_L$, the surface energy balance

Table 1.1. The estimated average heat flux during each month for mature ice at 80°N (after Badgley, 1966). In R, H, H_L, and B, the fluxes are upward if positive.

	JAN	FEB	MAR	APR	MAY	JUN	JUL	AUG	SEP	OCT	NOV	DEC	YEAR
α(%)	-	-	83	81	82	78	78 to 54	56 to 78	84	-	-	-	-
							mw/cm^2						
S	-	-	1.26	6.46	10.74	11.55	8.90	5.02	1.22	-	-	-	-
S(1-α)	-	-	.21	1.23	1.93	2.54	3.02	1.66	.20	-	-	-	.90
0	6.88	6.64	6.64	7.12	8.92	11.91	12.24	11.78	11.08	9.78	8.38	7.11	9.04
I	6.08	5.71	5.52	5.76	8.01	10.98	11.14	11.39	10.41	9.11	7.18	5.99	8.11
0-I	.80	.93	1.12	1.36	.91	.93	1.10	.39	.67	.67	1.20	1.12	.93
R	.80	.93	.91	.13	-1.02	-1.61	-1.92	-1.27	.47	.67	1.20	1.12	.03
H	-.43	-.35	-.37	0	.35	.37	0	.11	.19	-.06	-.16	-.24	-.05
H_L	0	0	0	0	.27	.35	.19	.02	-.14	-.16	-.11	-.02	.03
B	.37	.58	.54	.13	-.40	-.89	-1.73	-1.14	.52	.45	.93	.86	.02

Table 1.2. The estimated average heat flux during each month for a lead at 80°N surrounded by pack ice (after Badgley, 1966). In R and B, the fluxes are upward if positive.

	JAN	FEB	MAR	APR	MAY	JUN	JUL	AUG	SEP	OCT	NOV	DEC	YEAR
α(%)	-	-	10	10	10	10	10	10	10	-	-	-	-
						mw/cm^2							
S	-	-	1.26	6.46	10.74	11.55	8.90	5.02	1.22	-	-	-	-
S(1-α)	-	-	1.13	5.81	9.67	10.40	8.01	4.52	1.10	-	-	-	3.4
0	11.78	11.78	11.78	11.78	11.78	11.91	12.24	11.78	11.78	11.78	11.78	11.78	11.8
I	6.08	5.71	5.52	5.76	8.01	10.98	11.14	11.39	10.41	9.11	7.18	5.99	8.1
0-I	5.70	6.07	6.26	6.02	3.77	.93	1.10	.39	1.37	2.67	4.60	5.79	3.7
R	5.70	6.07	5.13	.21	-5.90	-9.47	-6.91	-4.13	.27	2.67	4.60	5.79	.3
H	22.5	25.2	25.2	22.4	12.6	.4	0	.1	2.8	8.4	15.4	22.5	13.1
H_L	2.4	2.7	2.7	2.4	1.3	0	0	0	.3	.9	1.6	2.4	1.4
B	30.6	34.0	33.0	25.0	8.0	-9.1	-6.9	-4.0	3.4	12.0	21.6	30.7	14.8

In the tables, R, H, H_L, and B are upward if positive.

On comparing the R, H, H_L, and B components for both mature ice and leads in winter, we see how the occurrence of leads greatly increases the heat loss by the ocean. The B term in winter is more than fifty times larger for leads than for the pack ice; and most of this increase is contributed by the sensible heat flux, H. Doronin (1966) estimates H and R only and these are consistent with Badgley's values. Vowinckel and Taylor (1965) likewise predict similar magnitudes; they claim their estimate of the sensible heat flux from the surface in the central Arctic would increase by 40% per year if, instead of the total ice cover they assumed, there was one percent open water.

Badgley (1966) based his estimates of H and H_L in Table 1.2 on actual velocity, temperature, and humidity profiles recorded over a lead near Barrow, Alaska in 1962. Miyake (1965) tried similar measurements in 1960, constructing an artificial lead in the shore-fast ice near Barrow. These are apparently the only attempts at an experimental investigation of the turbulent heat flux from leads. And these results are limited. Each experiment lasted only a couple of days at a single site; hence, few environmental and physical parameters were sampled. Several wind tunnel studies have attempted to measure the heat flux from warm water to cooler air (Mangarella, et al., 1971, 1973; Coantic and Favre, 1974). But these could not

reproduce the large temperature difference and the very cold and dry air of the Arctic. Clearly, a more thorough investigation was desirable since we would ultimately like to predict the heat flux by measuring only the width of a lead and such bulk environmental parameters as the wind velocity, air temperature, and water temperature.

The Arctic Ice Dynamics Joint Experiment (AIDJEX) sponsored by the National Science Foundation (NSF) provided an excellent opportunity for such research; consequently, the AIDJEX Lead Experiment (ALEX) was organized for early 1974 (Paulson and Smith, 1974). The primary goal of our participation in ALEX was to establish a method for estimating the turbulent heat flux from Arctic leads by measuring a few relevant, bulk parameters. Therefore, during the six weeks of ALEX we made heat flux measurements over real and artificial leads of various widths and under a host of environmental conditions. This thesis discusses those heat flux measurements.

1.2. THE INTERNAL BOUNDARY LAYER

There is another intriguing area to our research which must flavor this thesis. That is ALEX as a turbulence experiment on a geophysical scale. As will become evident in Chapter 2, what we are doing during ALEX is studying how an air flow -- originally in equilibrium with a surface -- is modified by a change in surface conditions. In

our case, the flow is initially in equilibrium with the upwind ice. When it impinges on the lead -- which has a much warmer surface and probably a different surface roughness -- its velocity and temperature profiles and, consequently, the momentum and heat fluxes are altered. The region which is disturbed by the new surface is called an 'internal' boundary layer (IBL) -- 'internal' because it is imbedded in the planetary boundary layer.

Research into such turbulence problems began only fairly recently because the thing is so difficult. Elliott's (1958a, 1958b) pioneering work and much of the subsequent experimental (e.g., Bradley, 1968; Plate, 1971) and numerical (e.g., Peterson, 1969; Taylor, 1969; Shir, 1972) research have concentrated on flows encountering a change in surface roughness. The boundary layer is, thus, an internal 'momentum' boundary layer.

Taylor (1970) has tried to model an internal 'thermal' boundary layer, which results when a flow feels a change in surface temperature but no change in surface roughness. Miyake (1965) has made an analytic attempt at understanding the internal thermal boundary layer. And Shreffler (1975), as part of the AIDJEX program, has constructed a numerical model specifically of flow over an Arctic lead but had only one set of Badgley's (1966) velocity and temperature profiles with which to test his results. In addition, the thermal boundary layer has been investigated in wind

tunnels (Mangarella, et al., 1973; Coantic and Favre, 1974). But ALEX is one of the few times thermal boundary layers of geophysical size have been observed (see Figure 1.1). This is a rare opportunity to compare theory and laboratory results with the real world.

It should be apparent from this discussion that there are two regions of importance in the flow. To understand the effects of the change in surface conditions, one must look not only at the flow within the boundary layer but also at the undisturbed, upwind regime. This thesis focuses on what is happening in the boundary layer. The thesis by Lindsay (1976) chronicles the upwind flow during ALEX and should be considered a companion volume to this one.

1.3. SIDELIGHTS

Leads are sites of intense processes. The large temperature difference between water and air and the resultant heat flux drives most of these. Therefore, although the principle motivation for our heat flux measurements was to facilitate improved estimates of the Arctic heat budget, our results are of consequence in several other areas of study which will not be treated directly in this thesis.

Because of the rapid heat loss in winter, leads are areas of prolific ice formation. Three things can happen to ice: it is formed, melted in the Arctic, or transported

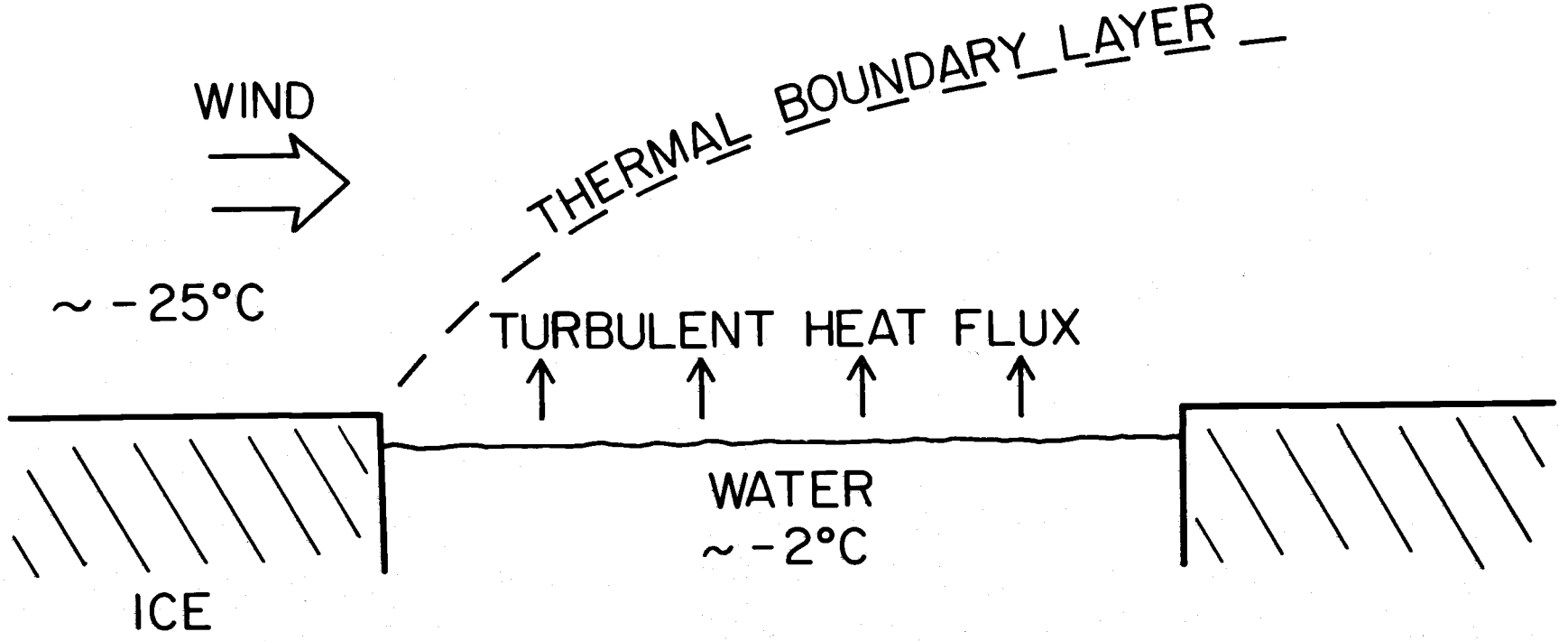

Figure 1.1. The thermal boundary layer over an Arctic lead.

south out of the ocean. The ice budget is, thus, a sub-budget of the total Arctic heat budget. The heat flux from leads is, therefore, critical in this budget, too.

Leads also have the potential for generating small scale thermohaline circulation (Smith, 1973). When the pack ice cracks and exposes warm ocean water to the dry and very cold atmosphere, the combined effects of ice formation and evaporation may increase the surface salinity by as much as 2.5 °/₀₀ (Zakharov, 1966). Because in seawater at near freezing, salinity changes determine density changes, this surface water becomes more dense than the underlying water and so will sink as a plume until it reaches water of equal density (Smith, 1974) -- probably in the halocline between 50 and 100 meters (Coachman and Barnes, 1962). Here it spreads out as a layer. This sinking water will likely be replaced by the vertical and horizontal advection of water under the ice. But because in the Arctic Ocean the water temperature generally increases with depth from the surface down to the Atlantic water between 200 and 900 meters (Worthington, 1953), this advection could carry more heat to the surface (Doronin, 1963). To investigate this thermohaline circulation in the vicinity of leads, a group headed by J. D. Smith of the Department of Oceanography at the University of Washington also participated in ALEX.

Such thermohaline circulation has several important implications. For example, mixing surface water into lower layers allows for the aeration of these layers -- a consequence which may have significant impact on the biological activity in the Arctic. In fact, Zakharov (1966) states that convection reaching 200 to 300 meters has been observed. Off the Eurasian coast where the continental shelf is very broad and shallow, such convection may at times reach the ocean floor. Secondly, the cooling of the surface water in leads coupled with its downward transport in plumes may account for the supercooled water which is often observed in Arctic Ocean temperature profiles (Coachman, 1966; Katsaros, 1973).

2. THE AIDJEX LEAD EXPERIMENT

> There always comes a time when one must choose between contemplation and action. This is called becoming a man.
>
> Albert Camus
> The Myth of Sisyphus

The scale of the Arctic Ice Dynamics Joint Experiment made our lead research possible. Including ALEX in the AIDJEX program gave us the opportunity to take advantage of logistic and technical support gathered for the AIDJEX assault. Consequently, four different research programs were carried out as part of ALEX. The Air-Sea Interaction Research Group from the School of Oceanography at Oregon State University and a similar group from the Department of Atmospheric Sciences of the University of Washington (UW) made atmospheric observations over leads. J. D. Smith led a group from the Department of Oceanography of the University of Washington which made oceanic observations (Smith, 1974). Bjorn Holmgren of the Geophysical Institute of the University of Alaska measured radiative fluxes (Holmgren and Weller, 1974). And John Kelley of the Institute of Marine Science of the University of Alaska investigated the CO_2 exchange in leads (Kelley, 1974).

In late February of 1974 the ALEX participants assembled at the Naval Arctic Research Laboratory (NARL)

near Barrow, Alaska, and the experiment, thus, began. Heiberg's (1974) log is a good day to day account of the activities of all groups in the ALEX program. So, henceforth, we will concentrate on the atmospheric observations.

2.1. SITES

ALEX of necessity had three phases instead of the two originally planned. We were to begin by first looking at flows over artificial leads built on Elson Lagoon (see Figure 2.1) then move onto the pack ice in the second phase to sample real leads. However, the pack was most uncooperative, presenting few real leads in the area accessible to us; hence, we returned finally to Elson Lagoon and built a larger artificial lead.

These artificial leads were constructed by pumping sea water into long, polyethylene tubes and laying the tubes out in a semicircle on the ice. They froze quickly and we, thus, had a container which when filled with sea water was a 'lead' 20 to 30 centimeters deep. The lagoon itself was our sea water source. We pumped the water up through a hole in the ice, injected it into the pond at one corner, and let it drain back into the lagoon through a hole in the opposite corner. In this way a pond was held at constant temperature with only minimal freezing around the edges. The ponds were semicircular so that with our sensors at the center of the straight side, we could

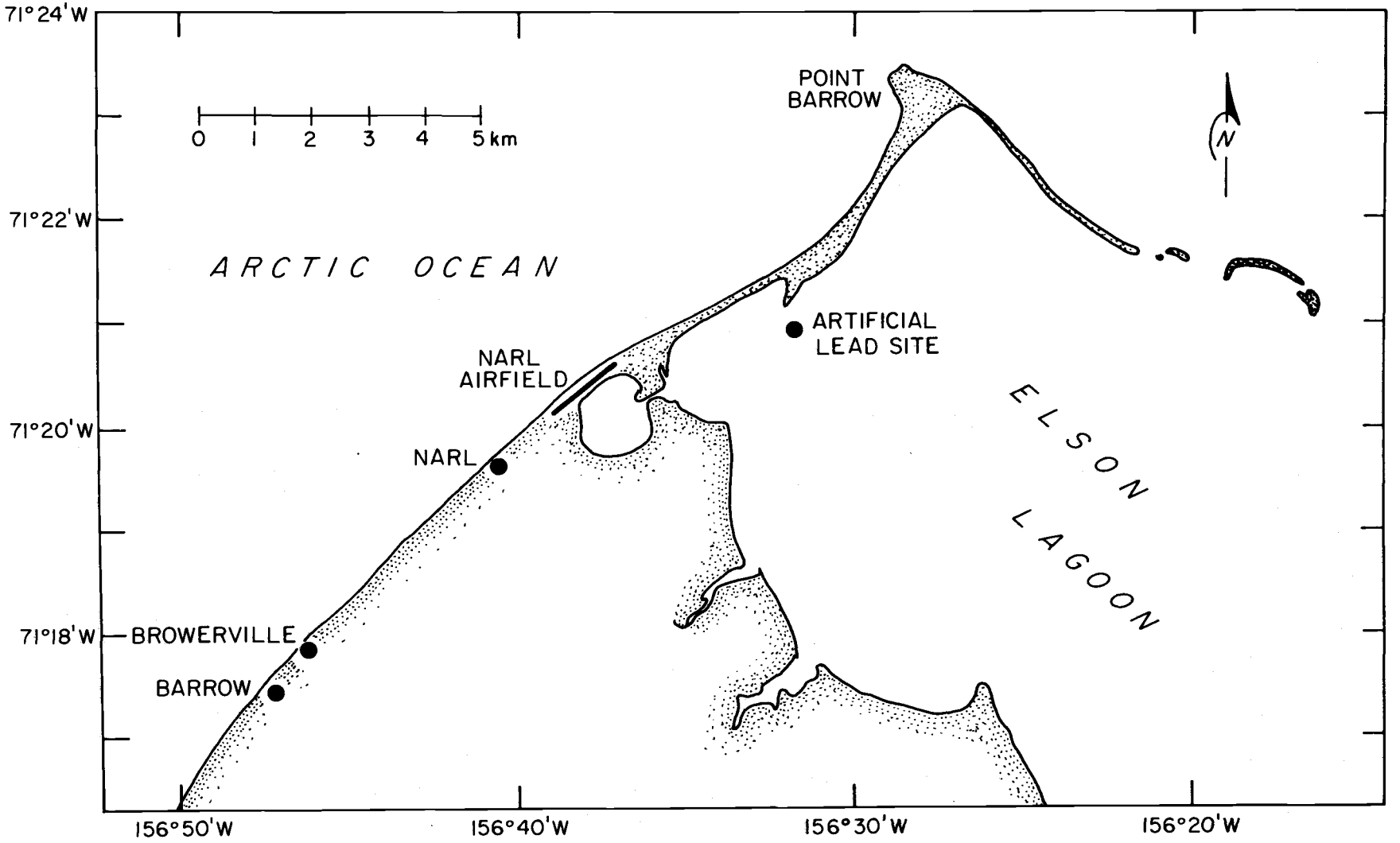

Figure 2.1. Point Barrow, Alaska, and vicinity. The ALEX artificial lead experiment was conducted on Elson Lagoon.

track the wind through almost 180° without much change in water fetch. Ultimately we had to build three such ponds. The first two were each of ten meter radius but facing different directions to follow a fickle wind. The third pond, which became necessary in the absence of suitable real leads, had a radius of 20 meters.

Sampling over these artificial leads let us debug our instrumentation, better define our experimental procedure, control the all-important geometry of the air flow, and proceed at a more relaxed pace; because when we got to a real lead we would have little time for confusion and hardly any control over the wind. As soon as leads open, ice begins forming in them and within 24 hours the thickness of new ice may be several centimeters.

When we finished our first series of artificial lead experiments we regrouped at NARL and began looking for real leads. Heiberg (1974) details the search and deployment procedure. Before we would commit ourselves to deployment, a lead had to meet strict requirements. It had to be fairly narrow -- 100 meters or less -- so the internal boundary layer would not be too high on the downwind side. The wind had to be nearly perpendicular to its long dimension for reasons which will be obvious later. The lead had to be through mature ice to insure safe sites for the camps on either side. Smooth ice nearby was necessary on both sides so small planes could land. The upwind side

had to be free of hummocks and pressure ridges, which would void our assumptions of equilibrium flow upwind. And the lead had to be within a 30 to 40 mile radius of NARL so search and deployment could be accomplished in one day (about ten hours of daylight).

The first satisfactory lead we found was a good one. We camped on it for two days and got nine hours of useful data on the downwind side of the lead before a wind shift during the night of the first day stopped us. However, as we turned our sensors with the wind, we eventually found ourselves upwind of the lead with the UW group downwind. So we recorded an additional six hours in this configuration.

When we set down on our second real lead, it was about a quarter of a mile across; but we were desperate for a site as the pack ice was persistently uncooperative. By the time we were operational (two hours), the lead had closed to a hundred meters. Two hours later after one 90 minute data run, open water vanished and in its place a rumbling pressure ridge began advancing on our camp. We evacuated. The pack ice remained tight for a solid week. And we returned to Elson Lagoon for the large artificial lead experiment.

2.2. THE INSTRUMENT HUT

As I have explained in Chapter 1, to properly investigate atmospheric processes over leads it is essential to sample both the undisturbed upwind flow and the flow over the lead. Hence, twin instrumentation packages were necessary -- the one upwind usually manned by the University of Washington group; the downwind, by the Oregon State contingent.

The primary component of each of these setups was a helicopter-transportable, army surplus instrument hut, which provided shelter and quarters for two to three people during the experiments on both Elson Lagoon and on the pack ice and contained the electronics for obtaining, conditioning, and recording our turbulence observations. Each hut was accoutered with a 60 cycle, five kilowatt generator for powering the requisite electronics; for heating, a propane stove, which could maintain a 40°C temperature difference between the hut floor and the ceiling seven feet above; and bunks. In addition, each hut was mounted on two large, wooden skids to prevent its freezing onto the ice and to facilitate sliding if ice movements threatened it.

2.3. THE TWO TOWERS

Two towers, which during transport were mounted to the outside of the hut, held our sensor arrays during

periods of observation. One tower we call the 'profile tower'; the other is the 'flux tower'. The profile tower was equipped to make velocity, temperature, and humidity profiles over the lead. The flux tower had transducers for making direct measurements of momentum and heat fluxes using the eddy correlation technique. Tower sensors were connected to the hut electronics with 100 meter, teflon-coated cables.

Both towers were of modular design and built of aluminum tubing. The principle feature of each was a four meter arm which could rotate in the vertical and so lift our sensors from within centimeters of the surface to a height of about four meters. A small electric motor mounted on each tower powered this up and down motion. The arm also swiveled in a horizontal plane and therefore could be manually oriented into the wind. Figure 2.2 is a drawing of an ALEX instrument tower.

2.4. PROFILE TOWER TRANSDUCERS

The profile tower generated profiles by continually cycling one set of sensors up and down through the boundary layer, stopping at each of five predetermined, logarithmically-spaced heights for usually a minute. By using one set of sensors thusly, we avoided some complications. First, and most obvious, is the fact that this scheme did not require the large battery of transducers which is

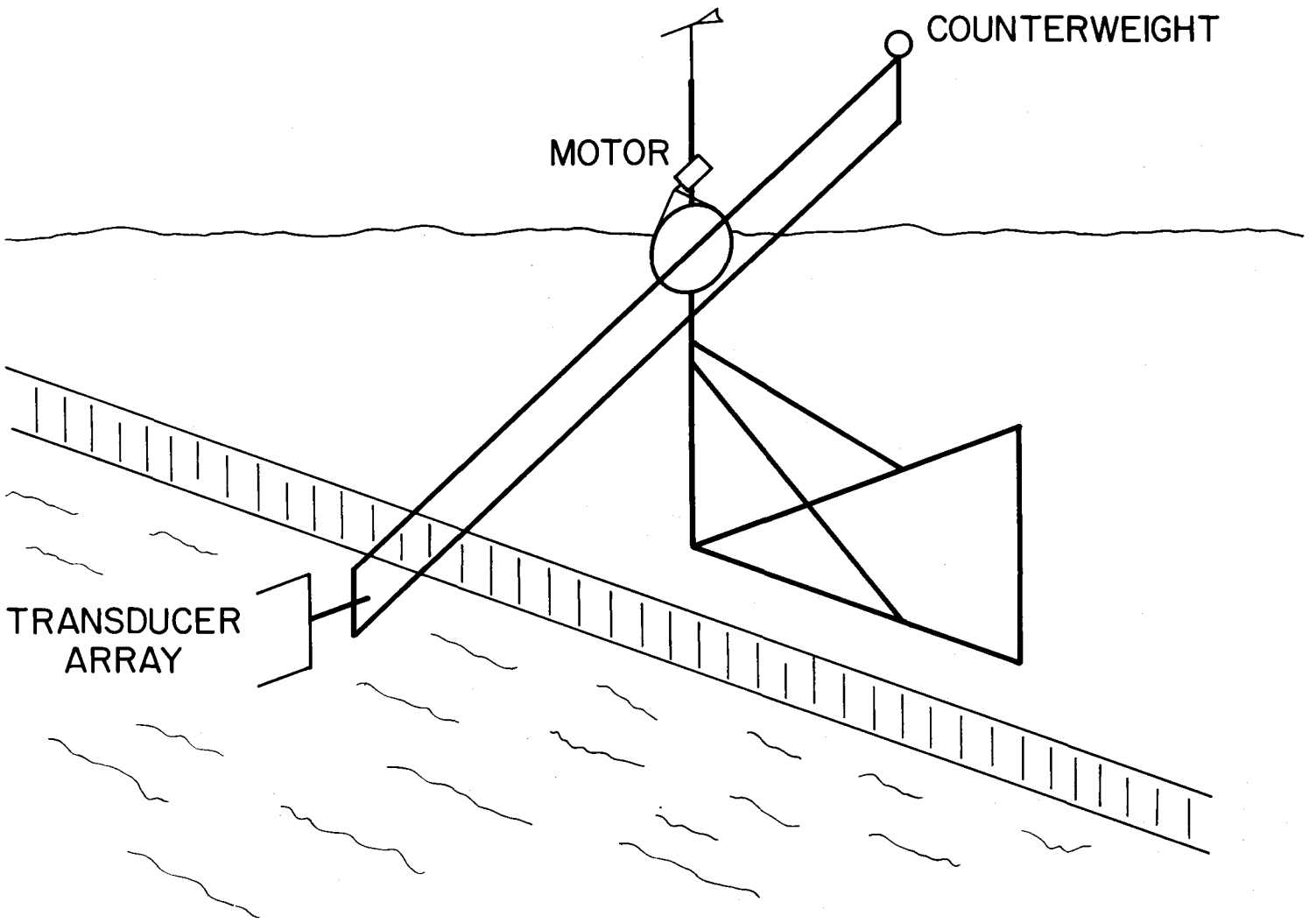

Figure 2.2. An ALEX instrument tower.

typical in most profiling work. Secondly, and in the long run more significant, was our eliminating the inter-calibration problems inherent in using more than one sensor to measure the same quantity. Admittedly, with only one sensor per observable, there is always a question of confidence in the result. We were not, however, without a means to judge the validity of our profile measurements: sensors on the nearby flux tower were also measuring the same average quantities but at fixed heights. Thus, the profiling method we chose allowed us to make very precise determinations of the shape of the velocity and temperature profiles in the internal boundary layer. For our work, that shape -- the relative magnitudes of the observables between different heights -- is as interesting as the absolute values of the observables.

The velocity transducer on the profile tower was a Thermo-Systems Inc. (TSI) 1210-20 hot-film probe: its sensing element is a vertically-oriented, cylindrical hot-film with diameter 0.051 mm and aspect ratio 20 (Figure 2.3).

All our temperature transducers were 0.5 mil Chromel-Constantan thermocouples welded between wire supports at the end of a small diameter rod 15 cm long. The profiling thermocouple was mounted next to the hot-film and referenced to a 0°C thermocouple reference stimulator, which with the thermocouple amplifiers was incorporated into the

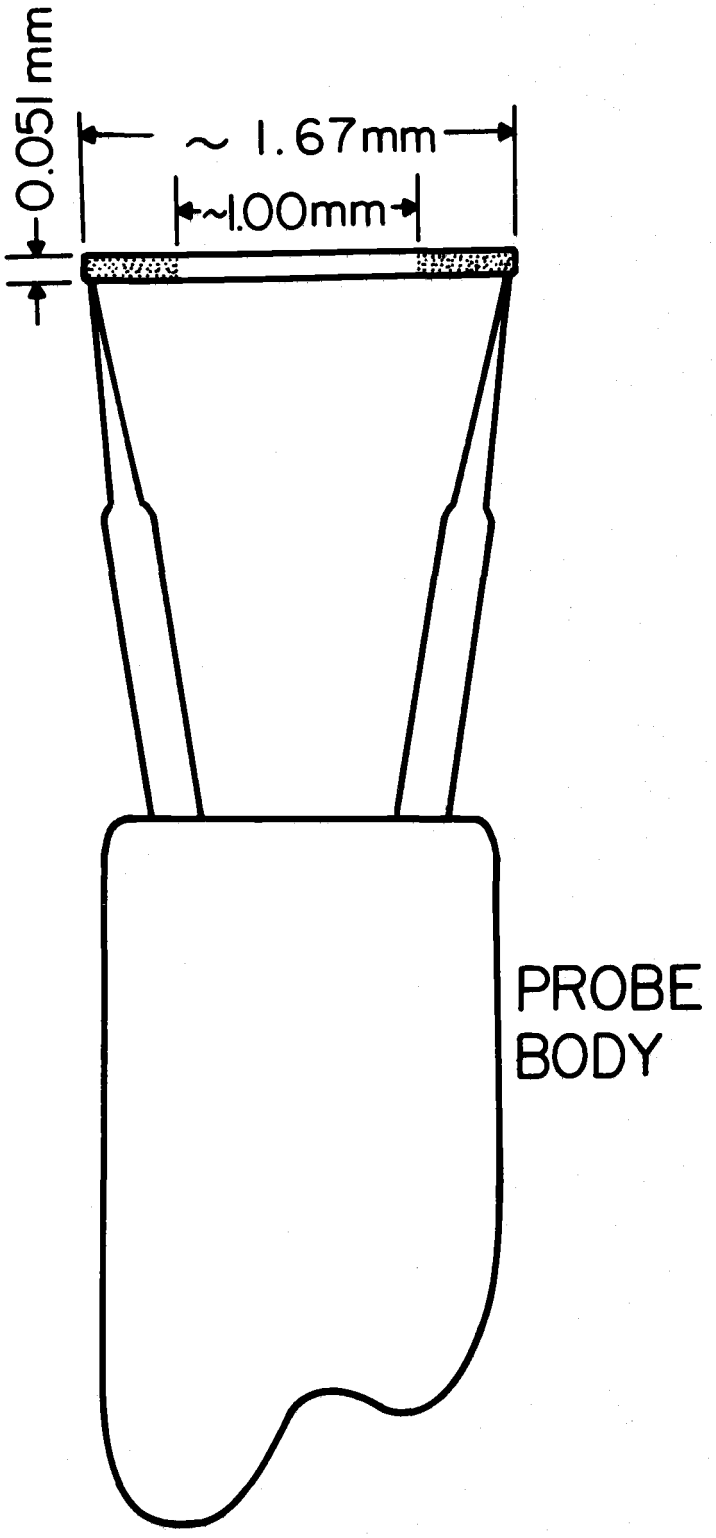

Figure 2.3. A single-sensor TSI hot-film probe. The stippled area is gold plated and so defines a 1 mm sensing length.

sensor arrays. Two other thermocouples, one mounted at the lower array position with the hot-film and the aforementioned thermocouple and a second mounted 50 cm above, were referenced to each other. We thus hoped to increase the density of our profile temperature observations and get estimates of temperature differences over 50 cm. But that differencing pair was just another source of joy for the Arctic gremlins: it never did give reasonable absolute temperature differences though its variance agreed with that measured by the lower thermocouple. Only by doing an ad hoc calibration of the differencing pair for each run using the lower thermocouple as the standard could we extend our temperature profile upward an additional 50 cm.

Midway between the lower temperature and velocity transducers and the upper differencing thermocouple we mounted a carbon hygristor as a humidity sensor. The resistance of the hygristor element is sensitive to moisture; hence, when the hygristor is placed in an oscillating circuit, the frequency of oscillation is related to the humidity. Unfortunately, the humidity circuit was inoperative for the first three-quarters of ALEX and the humidity values from the final quarter are suspicious; therefore, we have little faith in our moisture observations.

A Thornwaite three-cup anemometer sat stationary atop the profile tower and so gave us an additional point

for velocity profiles and provided a fixed-height velocity reference for making sampling corrections to the velocity profiles. The cup anemometer seems to have been somewhat affected by the cold -- it inhibited the frequency response of the cups. Average velocities generally were consistent with hot-film velocities, but the trace from the cups on our strip chart recorder was often uneventful. The Arctic cold had made the cups a low-pass velocity filter.

The arm on the profile tower cycled through five levels starting near the top of the boundary layer and working downward until it reached the lowest height -- usually 10 to 20 centimeters. It would then return to the upper level and begin again. A potentiometer on the gear of the motor which moved the arm was a monitor for the heights of these levels. Inside the hut, electronics designed by the University of Washington group allowed infinite control of the tower heights and sampling interval. Each height at which the tower arm would stop was set on one of five potentiometers mounted together on a panel. A sixth potentiometer set the sampling interval. The panel electronics associated a continuous voltage with the tower potentiometer and from that we knew the arm height. In addition, the tower control panel assigned a discrete voltage signal to each level and thereby told us which potentiometer had positioned the arm. Hence, if necessary, we could also determine the arm height from this incremental

voltage knowing the potentiometer settings. Generally, this system was very reliable in returning the sensing array to the same heights as it made continuing passes through the boundary layer.

Figure 2.4 is a typical strip chart record of the more interesting profile tower signals (the x-film velocities are flux tower signals), and so demonstrates the essence of our profiling routines. Notice the sampling interval for this run is about 90 seconds. The temperature traces appear one-sided because the ambient upwind temperature is a lower bound while the presence of the much warmer lead initiates positive excursions from this bounding value. The fetch across the lead in this example is 8.1 m. Hence, since the variability of the temperature trace suggests that at 1.40 m or maybe even 0.93 m the lead is having little influence on the profile, the thermal boundary layer height here is roughly one-tenth of the fetch.

2.5. FLUX TOWER TRANSDUCERS

The velocity transducers on the flux tower were TSI 1241-20 crossed sensor hot-film probes. These have the same sensing elements as our single-sensor hot-film probe, but each contains two such sensors mounted at right angles (Figure 2.5). We placed one crossed sensor probe at the lower position of the transducer array and the second at the upper array position, 50 cm above. The crossed sensor

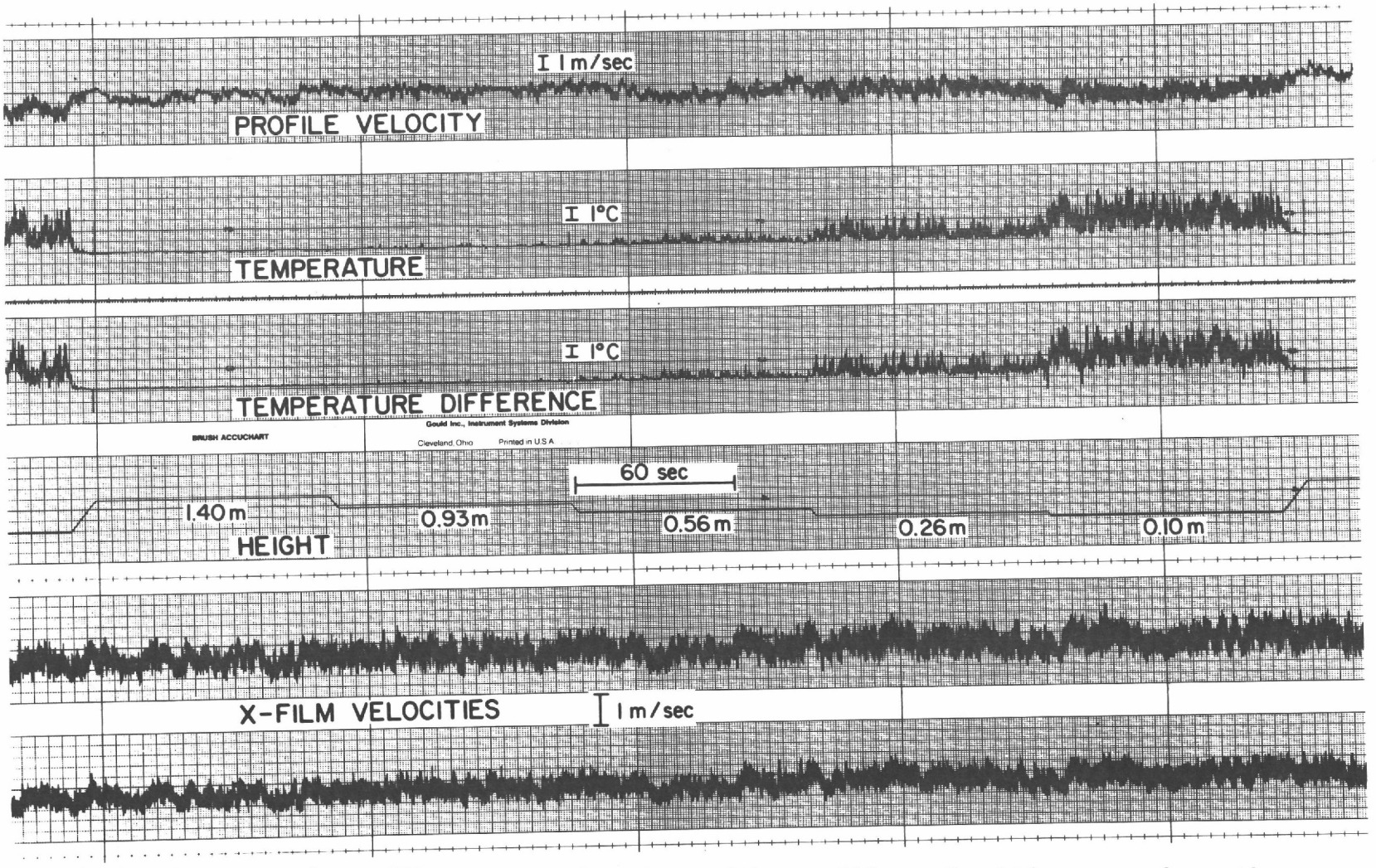

Figure 2.4. Traces of profile tower signals. (The x-film velocities are from the flux tower.) The fetch is 8.1 meters.

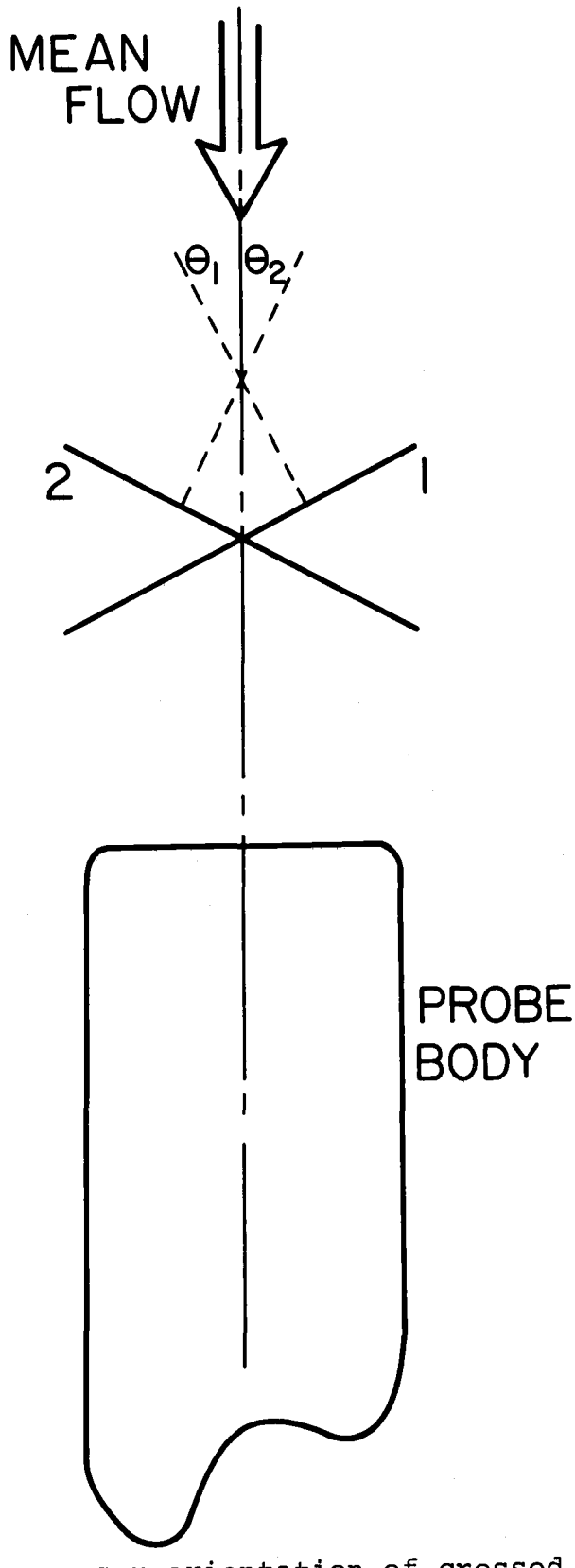

Figure 2.5. The sensor orientation of crossed hot-film probes. Ideally θ_1 and θ_2 are 45°.

pairs were oriented in a vertical plane parallel to the mean wind. We thus could measure longitudinal and vertical velocities at two heights.

Temperature transducers were like those on the profile tower, 0.5 mil Chromel-Constantan thermocouples. We placed the absolute temperature thermocouple and one of the differencing thermocouples at the upper array position next to the crossed hot-film probe there. The second thermocouple of the differencing pair was mounted with the lower crossed hot-film. With these temperature and vertical velocity measurements, we hoped to make a direct determination of the heat flux. However, again the differencing thermocouples did strange things: the temperature difference they yielded was never accurate though the signal variance was consistent with that from both the absolute thermocouple and the profiling array.

Both profile and flux tower thermocouples suffered from another problem which we had anticipated. They frosted over incredibly fast. By watching the strip chart record of any of the temperature signals we could see the frequency response decrease with time as rime formed around the sensor. All our sensors were right above the lead and the combination of evaporation and very cold temperatures doomed the thermocouples. The hot-films, of course, were in the same position but operated at temperatures in excess of 200°C and so could not frost over. In preparation for

ALEX we had recognized the potential for such riming and, therefore, designed the thermocouple electronics with a heating circuit for thawing the rime on the sensors when necessary. But that circuit itself was not too reliable; consequently, about every half hour someone had to take an electric heat gun out to the towers and defrost the thermocouples.

Perhaps here might be a good place to explain why we took such small, fragile velocity and temperature sensors into such a harsh environment. Two considerations are of prime importance. First, we required sensors small enough to accurately measure all scales that contribute to the desired variances and covariances. These smallest scales are of order one-tenth of the height of the measurement -- i.e., 1 cm or less. Secondly, the sensors had to have a frequency response high enough to follow these small scale, rapid motions. The spectra and cospectra presented by Kaimal, Wyngaard, Izumi, and Coté (1972) suggest that to accurately determine the variances and covariances, our sensors had to respond to frequences of at least

$$f = 5 \frac{U}{z} \quad , \qquad 2.1$$

where z is the measurement height and U is the average longitudinal velocity there. In our application this frequency is about

$$f \approx 5\left(\frac{100 \text{ cm/sec}}{10 \text{ cm}}\right) = 50 \text{ Hz}. \qquad 2.2$$

We expect the limit of the thermocouples is 50 Hz; but the hot-film sensors are capable of much higher frequency response.

At the top of the flux tower we mounted a Thornthwaite wind vane. Because the crossed hot-films define a vertical plane, it was especially important that we always had them head-on into the wind; thus, mounting the wind vane nearby for referencing was prudent. But despite our foresight we could not always keep pace with the changing wind. The nearness of the wind vane was then again important because if deflections from the mean wind direction are small (less than 10°), the crossed hot-film velocities can be corrected using the angle of deflection (Andreas, 1977a). Sometimes the wind vane had the same problem as the cups -- the cold limited its frequency response. Hence, it usually underestimated the variance in wind direction but seemed to adequately sample the mean direction.

The array arm on the flux tower was motorized like that on the profile tower but did not cycle up and down. Rather we left it at a fixed height for the entire run, usually with the lower sensors within 20 cm of the surface.

Figure 2.6 shows a strip chart record of flux tower signals.

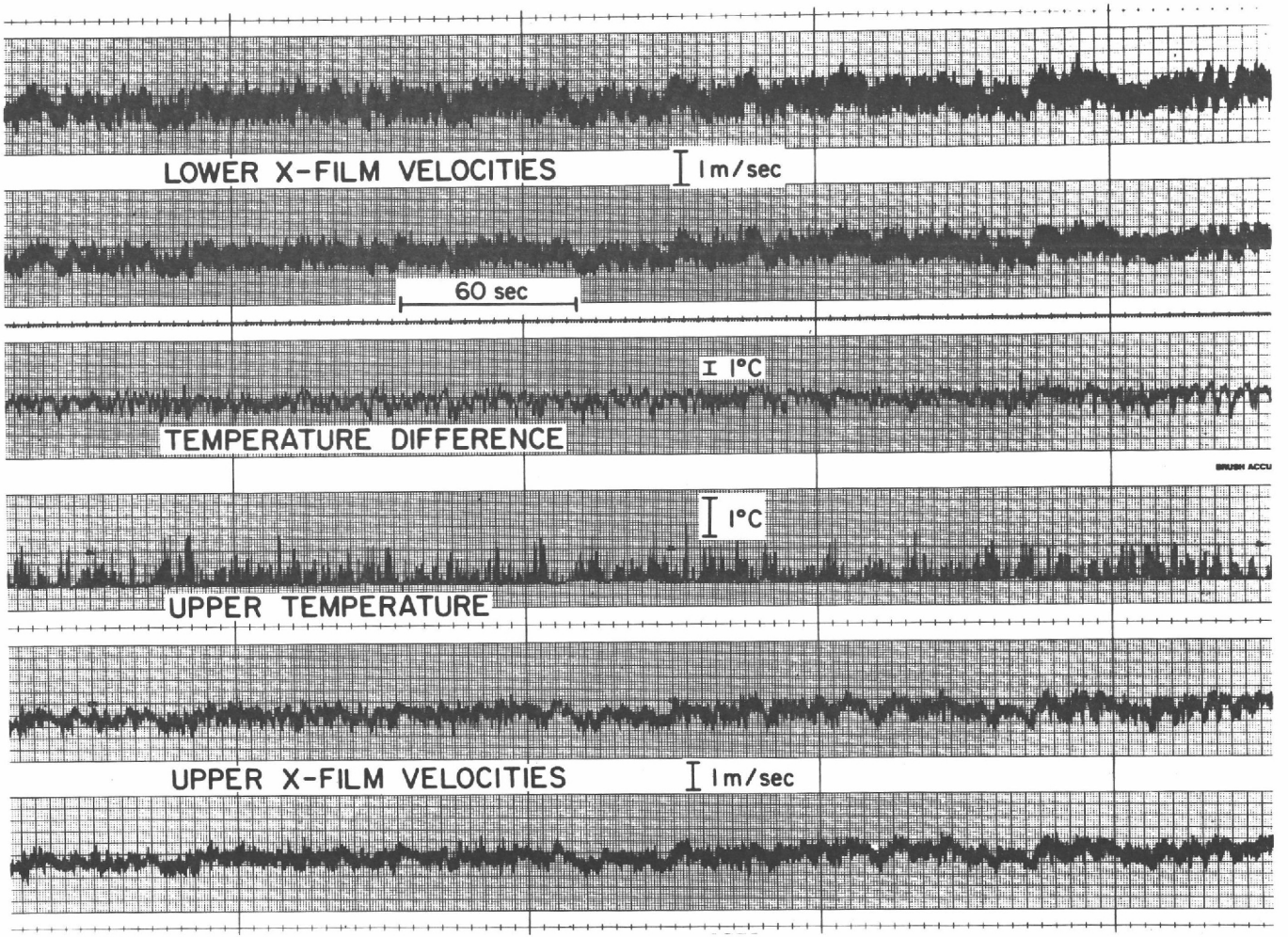

Figure 2.6. A typical strip chart recording of flux tower signals. The lower sensors are 12 cm above the water, the upper ones, 62 cm. The fetch is 8.1 meters.

2.6. DATA ACQUISITION

The instrument hut contained in a large, shock-mounted rack all the electronics for powering, monitoring, conditioning, and recording the signals from the two towers.

Crossed sensor hot-films were used in conjunction with TSI electronics (power supply, 1051-2; anemometer-linearizer, 1054A; 5:1 bridge, 1056). A Disa anemometer (main unit, 55M01; standard bridge, 55MIO; linearizer, 55D10) operated the straight hot-film. Both these are linearizing units: the signal from the anemometer bridge is linearized so that the transducer voltage is a nearly linear function of the wind speed. The velocity signal from the profiling hot-film was used not only for velocity information but was also electronically differentiated. Hence, on appealing to Taylor's hypothesis and assuming isotropy, we had a means for estimating dissipation.

A control box built specifically for ALEX by the University of Washington group, as mentioned above, housed the electronics for all the temperature and humidity transducers as well as those for changing and monitoring the profile arm heights.

The cup anemometer and wind vane had their own individual power supplies.

Generally, before being recorded the signals were passed through gain-offset devices (G/O's) which had been built by the OSU Technical Planning and Development Group.

These gain-offsets removed the mean of the signal and amplified its fluctuations to take advantage of the full dynamic range of our recording equipment. In our log we noted the individual gain and offset settings for each G/O and, therefore, after calibration could reproduce the original signal from the recorded signal.

Our recording unit was a Hewlett-Packard 3960 four-channel, analog tape recorder, which we operated at 3 3/4 inches/sec. Three channels were used in the FM mode. On these we recorded the two lower hot-film signals from the flux tower and the differentiated profiling hot-film signal. We sent all the remaining signals to voltage-controlled oscillators (VCO's), each operating in a different frequency band. These VCO outputs were mixed and recorded as one all-encompassing signal on the fourth tape recorder channel, which was set up in a direct record mode. When it came to digitizing, we reformed the individual components of this multiplexed signal by passing it through a bank of Sonex discriminators.

These discriminators were mounted in the hut rack so we could monitor any signal as it was being recorded. There were two methods of visual monitoring. We could use a small Tektronics oscilloscope or a six channel strip-chart recorder (Gould Brush). In fact, the strip-chart recorder ran continuously, monitoring the more important

signals, and was invaluable in setting up the gain-offset devices before we began a recording run.

Figure 2.7 is a flow chart of our signal processing and recording scheme during ALEX.

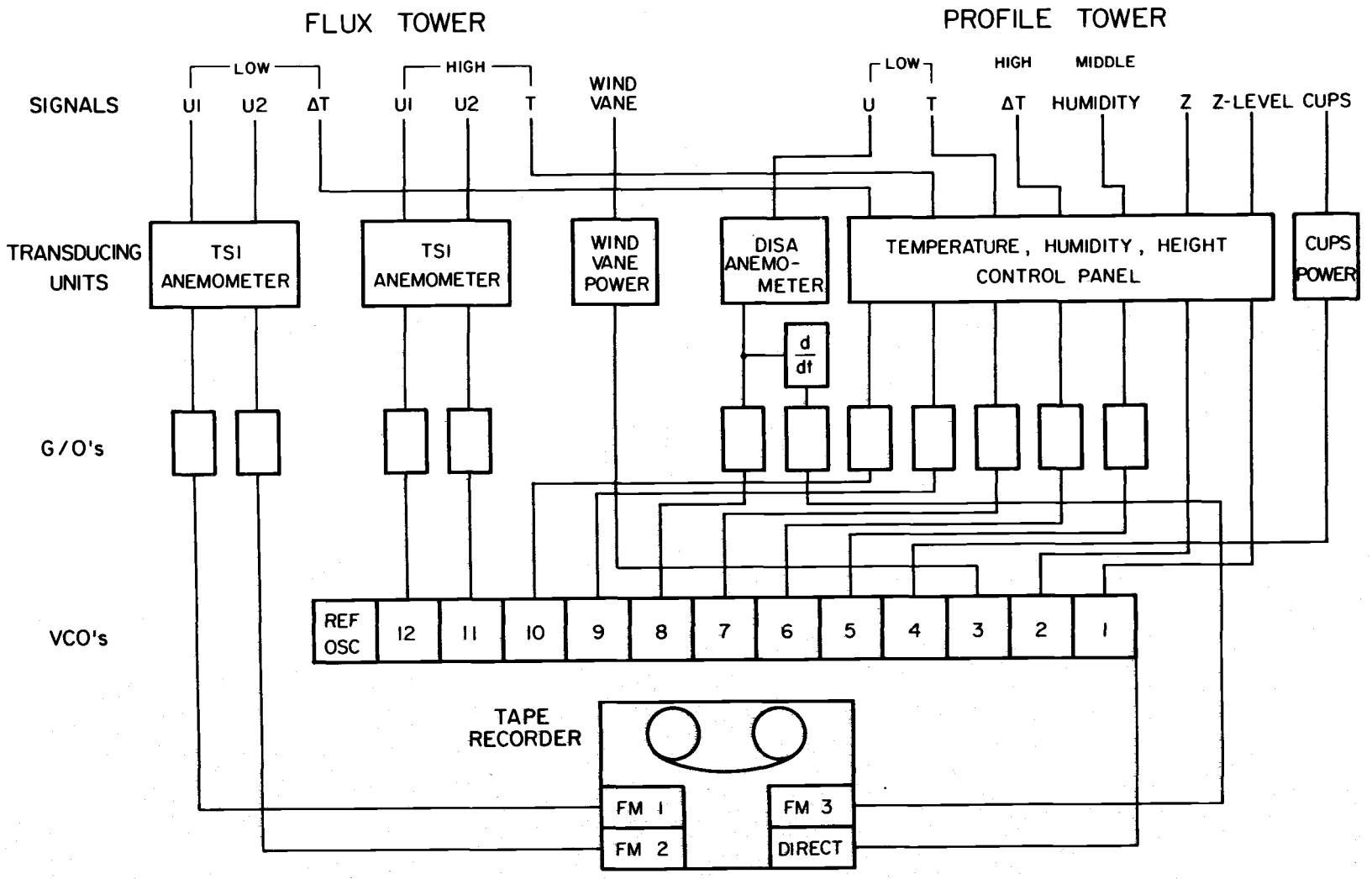

Figure 2.7. A flow chart of signal processing and recording during ALEX.

3. CALIBRATION, DIGITIZATION, AND DATA CONDITIONING

> To judge the direction of the wind it is enough to look at a single blade of grass.
>
> Daisetz T. Suzuki
> Zen and Japanese Culture

3.1 HOT-FILM CALIBRATION

Most of our efforts for the several months immediately following ALEX were directed toward devising a method for converting the hot-film signals we recorded back into velocities. We tried to calibrate the hot-films before ALEX and during the experiment as need dictated. And we made a thorough calibration at the conclusion of ALEX of all sensors which remained intact. But this calibration was unsatisfactory: we did not have the means to produce air flows for calibration purposes as cold as those observed during the experiment. Hence, it was essential for us to develop a basic understanding of the response of the hot-films in cold temperatures before we could proceed with our analysis.

Andreas (1977a, 1977b) explains the hot-film calibration routine we ultimately defined. In summary, the Nusselt number, N, a nondimensional rate of heat transfer from the hot-film sensor, is an exponential function of the Reynolds number, R:

$$N = A + BR^n, \qquad 3.1.1$$

where A, B and n are dimensionless constants unique for each sensor. The Nusselt number and Reynolds number are

$$N = \frac{E_B^2 R_s}{\pi R_t^2 (T_s - T_e) L\kappa} \qquad 3.1.2$$

and

$$R = \frac{Ud}{\nu} . \qquad 3.1.3$$

Figure 3.1, which is a schematic diagram of our anemometer bridges, may clarify the notation. In 3.1.2 and 3.1.3,

E_B	the bridge voltage
R_s	the sensor resistance during operation
R_t	$= R_s + R_3 + R_c + R_{int} + R_{ps}$ (R_c, R_{int}, and R_{ps} are cable resistance, internal probe resistance, and probe support resistance, respectively).
T_e	the environmental temperature
T_s	the sensor temperature during operation
L	the sensor length
κ	the thermal conductivity
U	the wind speed
d	the sensor diameter
ν	the kinematic viscosity

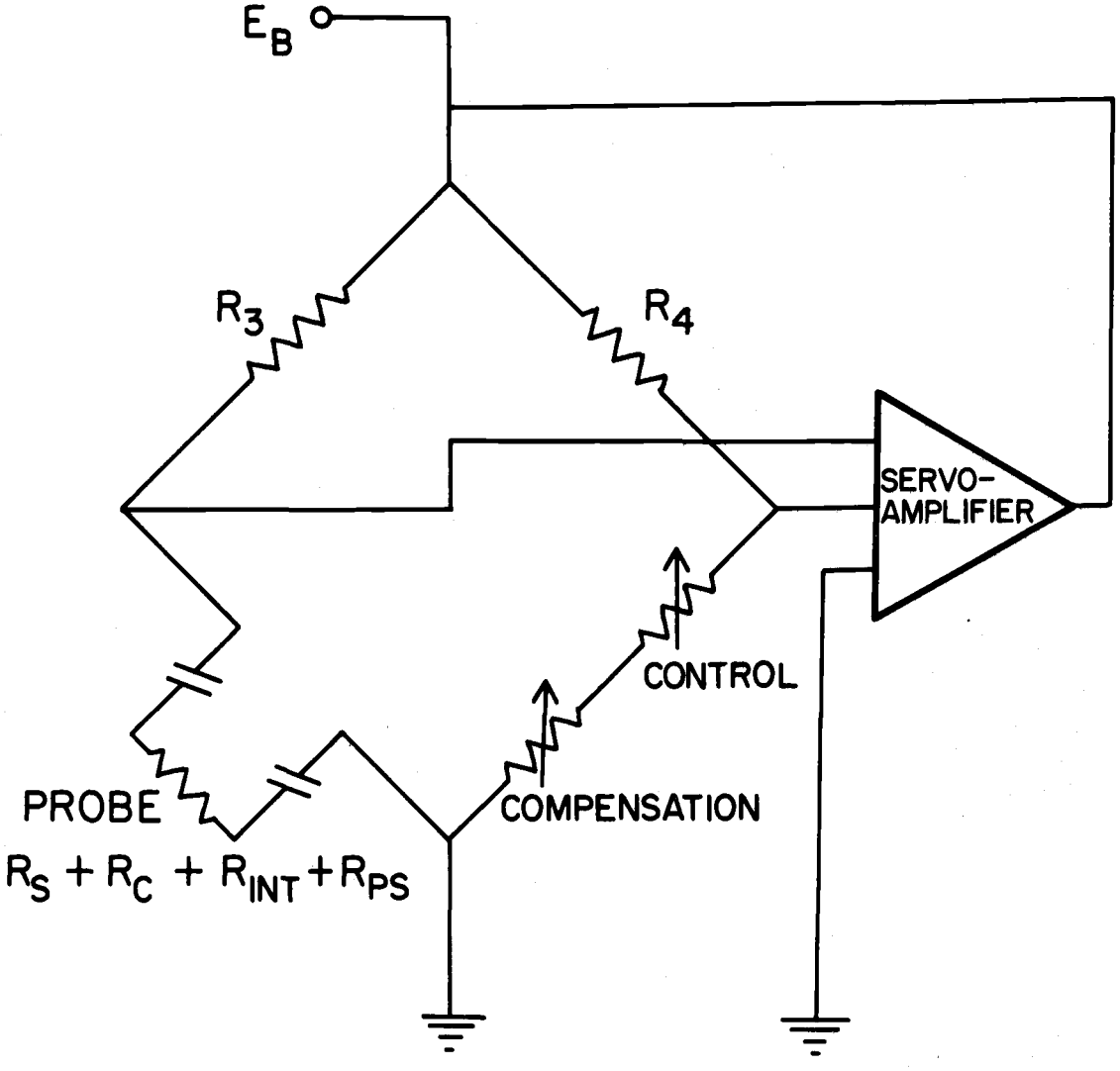

Figure 3.1. A typical anemometer bridge.

Both κ and ν are temperature-dependent parameters which we evaluate at $\frac{1}{2}(T_e + T_s)$.

At the end of ALEX we calibrated the anemometer linearizers and modeled each linearizer setup with an equation of the form

$$E_B^2 = P + QE_L^m \quad . \qquad 3.1.4$$

E_L is the linearizer output voltage and P, Q, and m are constants associated with each setup. Letting

$$N = HE_B^2 \qquad 3.1.5$$

and

$$R = JU, \qquad 3.1.6$$

we combine 3.1.1 and 3.1.4 to form

$$U = J^{-1}B^{-1/n}[HP - A + HQE_L^m]^{1/n} \qquad 3.1.7$$

-- a relation between wind speed and the linearizer voltage we recorded. Because n and m are nearly the same and HP - A is small, U is almost linearly dependent on E_L.

Equation 3.1.7 is, however, an oversimplification for the crossed hot-films because, unlike the straight hot-films, they were not operated perpendicular to the mean wind. In other words, for crossed sensors, U is really a smaller, effective velocity, U_{eff}, rather than the actual wind speed. That wind speed can be gotten from U_{eff} (i.e.,

from equation 3.1.7) by understanding how nonperpendicular wind incidence affects the hot-film response. We investigated that too and found we could relate U to U_{eff} knowing two angles; one, the angle the sensor normal makes with the probe axis (the θ's in Figure 2.4); and two, the wind vane angle, which measures how far the mean wind wanders from the vertical plane defined by the crossed sensors.

3.2 CUP ANEMOMETER CALIBRATION

Before leaving Corvallis for the Arctic we calibrated several sets of cup anemometers in a wind tunnel on the OSU campus. This calibration yielded a linear relation between anemometer output voltage and wind speed. But on returning to OSU and beginning our analysis we saw that cup velocities were systematically higher than hot-film velocities. The cups were calibrated at 18°C but used in the Arctic at -20°C to -35°C. Hence, we hypothesized that the concomitant increase in air density enhanced momentum transfer, causing the cups to rotate faster in the Arctic than they did at the same air speed in warmer temperatures. Therefore, we had to apply a density (temperature) correction to our calibration.

Ramachandran (1968) presents a theory of the cup anemometer in which the air density plays an essential role. Applying his work to our particular cup assembly, we derived a velocity correction based on absolute temperature,

$$U_2 = U_1 \left[1 - \frac{\left(1 + \frac{0.235}{U_1}\right)\left(1 - \frac{T_2}{T_1}\right)}{2 + 0.588\ U_1}\right] . \qquad 3.2.1$$

Here U_1 is the velocity we would predict after a calibration at temperature T_1, and U_2 is the true velocity when T_2 is the ambient temperature. Equation 3.2.1 likewise corrects standard deviations of cup velocities. The constants depend on cup size and response characteristics and, consequently, are appropriate only for our particular anemometer. This correction amounts to about a 4% decrease when U_1 is 3 m/sec and about 6% if U_1 is 1 m/sec. When we applied it to our cup speeds, results agreed much better with the hot-films but at times were still somewhat high.

3.3 THERMOCOUPLE CALIBRATION

The thermocouple calibration was a real nightmare. At NARL we calibrated the thermocouples in the ethanol bath of a Neslab Circulator (RTE-4). But back at OSU when we began the data analysis, we found the average thermocouple temperatures were seldom within 5°C of mercury thermometer observations we made at the same time and location. The thermocouples were for some unknown reason not adhering to their own calibration. Hence, we began an odyssey in search of temperature truth.

Nobody's temperatures agreed with anybody else's. The profile temperatures did not agree with the flux tower temperatures, and neither agreed with our thermometer readings. And when we tried to compare OSU and UW temperatures, despair was rampant. Ultimately, we simply had to believe our thermometer and base a corrected thermocouple calibration on the thermometer readings taken during the experiment. This solution at least provided internal consistency and improved the agreement between OSU and UW thermocouples. In the end, the absolute temperature is probably accurate to within no better than a degree. But the shape of the temperature profile itself is just as important: because we used a single thermocouple to generate profiles, the relative temperature difference between levels is good to 0.05°C.

The signal variances of the absolute thermocouples on the profile and flux towers were consistent with each other and with the variances of the differencing thermocouples. Worry over the absolute temperature difference associated with the differencing pair on the flux tower was unnecessary. We would use them only for correlation estimates of the heat flux; so their correctly predicting temperature fluctuations was all we asked.

3.4. MISCELLANEOUS CALIBRATION

As explained in Chapter 2, we had two methods for determining the height of the profiling arm. A calibration performed at NARL shortly after our arrival gave us linear calibration equations relating the arm height either to the settings of the potentiometers on the height control panel or to the voltage across the potentiometer on the tower itself. In contrast, someone had to measure the height of the flux tower arm for each run.

The calibration of VCO's and gain-offsets was checked periodically during lulls in ALEX. We made a thorough calibration of gain-offsets and rechecked the VCO's at the conclusion of the experiment before shipping the equipment home from NARL. Table 3.1 lists the center frequencies of our VCO's and their high and low frequency bandedges. Clearly, the associated discriminators must have the same frequencies. The VCO output (a frequency) is linearly related to the input voltage.

The wind vane was calibrated at OSU before we left for the Arctic. Since it is merely a voltage divider, we could easily check its calibration during the course of the experiment.

3.5. DIGITIZATION

Our raw data from ALEX consisted primarily of 28 magnetic tapes, each the record of a 90 minute experimental

Table 3.1. Center and bandedge frequencies of the VCO's and Sonex discriminators.

Channel	Low Bandedge (Hz)	Center Frequency (Hz)	High Bandedge (Hz)
1	370.0	400.0	430.0
2	518.0	560.0	602.0
3	675.2	730.0	784.8
4	888.0	960.0	1032.0
5	1202.5	1300.0	1397.5
6	1572.5	1700.0	1827.5
7	2127.5	2300.0	2472.5
8	2775.0	3000.0	3225.0
9	3607.5	3900.0	4192.5
10	4995.0	5400.0	5805.0
11	6798.8	7350.0	7901.2
12	9712.5	10,500.0	11,287.5
Reference Oscillator	13,412.5	14,500.0	15,587.5

run. We digitized these data tapes in the School of Oceanography on a PDP 11/05, storing the results on 2400 foot magnetic tapes. The PDP has a twelve bit word, a six bit byte, and writes 800 bytes/inch on the magnetic tape. Consequently, since we broke our data down into records of 1024 samples, the digital tape used 3.31 inches to store one record of one signal, including an inter-record gap.

Our data fell into two logical groups, 'profile' signals and 'flux' signals. The profile signals were those from which we would generate velocity, temperature, and humidity profiles and so averaging would be our primary analysis operation. From the flux signals we hoped to get the heat and momentum fluxes directly: our method would be spectral analysis. Therefore, the flux signals required a higher digitization rate than the profile signals. During the digitization we constructed 'profile' files using a digitization rate of 40 samples/sec and 'flux' files with a rate of 250 samples/sec.

Because of the interruptions necessitated by our having to thaw out the thermocouples, we rarely had more than 20 or 25 minutes of continuous, good data on an analog tape. Therefore, in general, both flux and profile files consisted of 15 to 25 minutes of real-time data. Because of the different digitization rates, we could store about 15 profile files on a digital tape but only four or five flux files. We finished the digitization with four profile

tapes containing 59 files and 17 flux tapes of 63 files.

The analog to digital hardware on the PDP 11 converts an analog input signal between plus and minus ten volts into an integer between -2048 and 2047. The output range of the Sonex discriminators which were used to demodulate the multiplexed signals is between plus and minus twelve volts. And the FM tape recorder channels have a -2.5 volt to 2.5 volt output range. Hence, to make full use of the dynamic range of the A to D converter during the digitization we amplified some signals and attenuated others. All were low pass filtered. Both this amplitude conditioning and the filtering were accomplished with electronic filters having a -3 db point at the Nyquist frequency and a 40 db/decade rolloff above that.

In Table 3.2 we list the particulars of our digitization process. Sections A1, A11, and A12 of Appendix A make a few more points relevant to digitization.

3.6. MORE ON DATA CONDITIONING

We have already described the conditioning that preliminary results indicated was necessary for cup speeds and thermocouple temperatures. Our data preparation also involved correcting the profiling hot-film velocities for sampling errors.

In using one velocity sensor to establish wind profiles we could be misled by a gusty wind. For example, if

Table 3.2. The 'profile' and 'flux' groupings, digitization rates, and filter characteristics.

Signal	Digitization Rate (Hz)	Filter Cut-off (Hz)	Filter Gain
PROFILE:			
Velocity	40	20	0.75
Temperature	40	20	0.75
Temperature Difference	40	20	0.75
Humidity	40	20	0.75
Height	40	20	0.75
Cups	40	20	0.75
Wind Vane	40	20	0.75
FLUX:			
Lower U1	250	125	4
Lower U2	250	125	4
Temperature Difference	250	125	0.75
Upper U1	250	125	0.75
Upper U2	250	125	0.75
Temperature	250	125	0.75

after recording at one profile level for a minute, we moved our velocity transducer to a lower level and the wind decreased for that minute, we would see an artificially steep gradient between the two levels. Paulson (1967) suggests a method for reducing the error introduced by such fluctuations using a fixed-level transducer to provide information for an entire experimental run. Our cup anemometer was such a fixed transducer. The correction formula we applied to the profile velocities was

$$U_i = U_{mi} - \frac{\sigma_i}{\sigma_c} (U_c - U_{ci}) \quad . \qquad 3.6.1$$

Here U_{mi} and σ_i are the measured roving probe velocity and sample standard deviation at level i, respectively; U_c and σ_c are the cup velocity and sample standard deviation for the entire run; and U_i is the corrected velocity at level i when U_{ci} is the average cup velocity while the profiling probe is at level i.

Results from the wind vane also got some scrutiny. I have discussed how the wind vane angle was a key to the validity of crossed sensor velocities. For small angles, these velocities should be reliable; but for deflections larger than 10° they are doubtful. Therefore, when we found a wind vane angle larger than 10°, we eliminated the corresponding flux file from subsequent analysis. Thirteen of the 63 flux files met this fate.

Lastly, all profile temperature data was converted to potential temperature by adding the adiabatic correction. That is,

$$T_{pot} = T_{obs} + \frac{gz}{c_p} \quad , \qquad 3.6.2$$

where z is the height; g is the acceleration of gravity, 982.7 cm/sec; and c_p is the specific heat of air, 1.006 joules $gm^{-1}{}^{\circ}C^{-1}$. This correction never amounted to more than 0.03°C.

4. THE INTEGRAL METHOD OF HEAT FLUX ESTIMATION

> The March wind is fretful, fretting the languid waves into murmurs.
>
> Rabindranath Tagore
> Fruit-Gathering

4.1 MATHEMATICAL FOUNDATION

Our primary estimates of the heat flux from leads during ALEX come from the 'integral' method. This is simply an energy conservation approach. Upwind and downwind temperature and velocity profiles are measured and the increase in heat energy in the air downwind over that upwind is calculated. That increase must be supplied by the lead and so establishes its heat flux.

Assume we have a linear lead with the mean wind velocity perpendicular to its long dimension. The air flow over the lead is thus two-dimensional. Suppose further that the flow upwind is in equilibrium with the upwind ice (horizontal homogeneity) and that both upwind and downwind flows are in steady state. We let the positive x-axis be in the direction of the mean wind: z is positive upward. Define δ -- a function of x -- and F as the thermal boundary layer height and fetch, respectively.

We can summarize upwind and downwind flows.

Upwind:

$$\partial_t \to 0$$

$$\partial_x,\ \partial_y \to 0$$

$$V, W = 0 \qquad 4.1.1$$

$$\overline{wt_i} \text{ is constant with height}$$

Here the t, x, and y subscripts indicate partial derivatives with respect to time and x and z coordinates. Capitals are time-averaged variables. Lower case u, w, and t will be fluctuations from the average longitudinal and vertical velocity and temperature, respectively.

Downwind:

$$\partial_t \to 0$$

$$\partial_y \to 0$$

$$V = 0 \qquad 4.1.2$$

$$T(\delta) = T_i(\delta)$$

$$\overline{wt}\,|_\delta = \overline{wt_i}$$

$T(z)$ and $T_i(z)$ are, respectively, the downwind and upwind temperatures.

Over the lead but within the thermal boundary layer the equations for continuity and temperature diffusion are, thus,

$$\partial_x U + \partial_z W = 0 \ , \qquad 4.1.3$$

$$U\partial_x T + W\partial_z T = \partial_x(-\overline{ut} + D\partial_x T) + \partial_z(-\overline{wt} + D\partial_z T) , \qquad 4.1.4$$

where D is the thermal diffusivity. We do not want to work with all these remaining terms, so consider a scale analysis to establish which are the most important. Clearly, x and z scales should be F and δ, respectively. If U and W are the horizontal and vertical velocity scales, equation 4.1.3 predicts

$$W \sim U \frac{\delta}{F} \ . \qquad 4.1.5$$

We are not yet sure just how to scale $\overline{wt}$ and $\overline{ut}$, though we have the intuition that over the lead $\overline{wt}$ will be larger than $\overline{ut}$. The temperature scale should be some fraction of the water-ice temperature difference:

$$T \sim c[T_w - T_i(0)] = \Delta T \ . \qquad 4.1.6$$

Now summarize 4.1.4 in terms of these scales,

$$\frac{U\Delta T}{F} + \left(\frac{U\delta}{F}\right)\frac{\Delta T}{\delta} \sim \frac{1}{F}\left(\overline{ut} + \frac{D\Delta T}{F}\right) + \frac{1}{\delta}\left(wt + \frac{D\Delta T}{\delta}\right) \ , \qquad 4.1.7$$

or

$$1 + 1 \sim \frac{\overline{ut}}{U\Delta T} + R_x^{-1}P^{-1} + \frac{F}{\delta}\frac{\overline{wt}}{U\Delta T} + R_x^{-1}P^{-1}\left(\frac{F}{\delta}\right)^2 \ . \qquad 4.1.8$$

Here R_x is the length (fetch) Reynolds number and P is the Prandtl number. For typical conditions we encountered

during the experiment,

$$R_x = \frac{UF}{\nu} \sim \frac{(100 \text{ cm/sec})(1000 \text{ cm})}{0.13 \text{ cm}^2/\text{sec}} \sim 10^6 , \qquad 4.1.9$$

$$P = \frac{\nu}{D} = \frac{0.13}{0.18} \sim 0.7 . \qquad 4.1.10$$

We have already demonstrated in Chapter 2 that δ is of order one-tenth of F. Therefore, the second and fourth terms on the right side of 4.1.8 are negligible compared to the terms on the left side.

From Badgley's (1966) and Shreffler's (1975) estimates, we expect $\overline{wt}$ to be roughly 20 cm $\text{sec}^{-1}\cdot\text{C}^{-1}$. Hence,

$$\frac{\overline{wt}}{U\Delta T} \sim \frac{20}{(100)(5)} = 0.04 . \qquad 4.1.11$$

Since this term is also multiplied by F/δ, it is of the same order as the terms on the left side of 4.1.8 and must be retained. But $\overline{ut}/U\Delta T$ in 4.1.8 is 10 to 100 times smaller than one and so we feel justified in neglecting it. Equation 4.1.4 thus reduces for our problem to

$$U\partial_x T + W\partial_z T = -\partial_z \overline{wt} . \qquad 4.1.12$$

Because the upwind temperature, $T_i(z)$, is not a function of x, we can write 4.1.12 as

$$U\partial_x(T - T_i) + W\partial_z(T - T_i) + W\partial_z T_i = -\partial_z \overline{wt} , \qquad 4.1.13$$

or

$$\partial_x[U(T-T_i)] - (T-T_i)\partial_x U + \partial_z[W(T-T_i)] - (T-T_i)\partial_z W$$

$$+ W\partial_z T_i = -\partial_z \overline{wt} \ . \qquad 4.1.14$$

Notice that the second and fourth term here add to zero by virtue of 4.1.3; so

$$\partial_x[U(T-T_i)] + \partial_z[W(T-T_i)] + W\partial_z T_i = -\partial_z \overline{wt} \ . \qquad 4.1.15$$

The first two terms in 4.1.15 are of order

$$\frac{U\Delta T}{F} \sim \frac{(100)(5)}{1000} = 0.5. \qquad 4.1.16$$

The term on the right is about the same size,

$$\frac{\overline{wt}}{\delta} \sim \frac{20}{100} = 0.2. \qquad 4.1.17$$

$W\partial_z T_i$ is an order of magnitude smaller than these: Lindsay (1976) shows that upwind temperature slopes were usually no more than 0.2 °C/m. Therefore,

$$W\partial_z T_i \sim \frac{U\delta}{F}\,\partial_z T_i \sim \frac{(100)(100)}{1000}\left(\frac{0.2}{100}\right) = 0.02. \qquad 4.1.18$$

Consequently, we may write 4.1.15 as

$$\partial_x[U(T-T_i)] + \partial_z[W(T-T_i)] = -\partial_z \overline{wt} \ . \qquad 4.1.19$$

Let us integrate 4.1.19 over z from z = 0 to the top of the thermal boundary layer, $z = \delta$.

$$\int_0^{\delta} \partial_x[U(T-T_i)]dz + \int_0^{\delta} \partial_z[W(T-T_i)]dz = -\int_0^{\delta} \partial_z \overline{wt}\, dz \,. \quad 4.1.20$$

Again scale analysis suggests we can write the partial derivatives in 4.1.20 as total differentials. And using Leibnitz's rule we rearrange the first term. The result is

$$\partial_x \int_0^{\delta} U(T-T_i)dz - [U(T-T_i)\,|_{\delta}\,\partial_x\delta + \int_0^{\delta} d[W(T-T_i)]$$

$$= -\int_0^{\delta} d\overline{wt} \,. \quad 4.1.21$$

The boundary layer height, δ, is defined as the height where the temperature flux, $\overline{wt}$, returns to its (constant) upwind value and where the temperature profile over the lead merges back into the upwind temperature profile. Thus, the second term on the left in 4.1.21 is zero. The differentials integrate quickly and we get

$$\partial_x \int_0^{\delta} U(T-T_i)dz + [W(T-T_i)\Big|_0^{\delta} = -\overline{wt}\Big|_0^{\delta} . \quad 4.1.22$$

Again $T-T_i$ at $z = \delta$ is zero and W at $z = 0$ must also be zero: the second term on the left above has consequently integrated to zero. We are left with

$$\partial_x \int_0^{\delta} U(T-T_i)dz = \overline{wt}_0 - \overline{wt}_i \,. \quad 4.1.23$$

Lastly, integrate 4.1.23 over x from the upwind edge of the lead to a fetch F,

$$\int_0^F dx\left[\partial_x \int_0^\delta U(T-T_i)\,dz\right] = \int_0^F (\overline{wt}_0 - \overline{wt}_i)\,dx \ . \qquad 4.1.24$$

In the lefthand term, the z integration removes the z dependence of the bracketed quantity; hence, the x integrand is a total differential,

$$\int_0^F d\left[\int_0^\delta U(T-T_i)\,dz\right] = \int_0^F (\overline{wt}_0 - \overline{wt}_i)\,dx \ . \qquad 4.1.25$$

This integrates immediately to

$$\int_0^{\delta(F)} U(F,z)\,[T(F,z) - T_i(z)]\,dz = \int_0^F (\overline{wt}_0 - \overline{wt}_i)\,dx. \qquad 4.1.26$$

If we multiply both sides by $\rho\ c_p$ evaluated at the surface temperature of the lead, we arrive at the equation which is the foundation of the integral method for heat flux estimation;

$$\rho\ c_p \int_0^{\delta(F)} U(F,z)\,[T(F,z)-T_i(z)]\,dz = \int_0^F (H_0 - H_i)\,dx \ , \qquad 4.1.27$$

where

$$H \equiv \rho\ c_p \overline{wt} \ . \qquad 4.1.28$$

Notice we are not quite rigorous in saying $H_i = \rho\ c_p \overline{wt}_i$ is the upwind heat flux since $\rho\ c_p$ is evaluated at the water temperature rather than the upwind temperature. However, this simplification makes negligible difference because $\overline{wt}_i$

is small compared to $\overline{wt}_o$ and the difference between $\rho\ c_p$ upwind and downwind is only a few percent.

The righthand side of 4.1.27 is the principle goal of this research -- it is the sensible heat transferred to the atmosphere from the lead. We have related it to the vertically-integrated product of downwind velocity and the difference between downwind and upwind temperatures -- hence, the name 'integral method'. Appendix E contains an alternative derivation of 4.1.27 based on the energy and mass budgets.

H_i does not depend on x and Shreffler (1975) has demonstrated that H_o depends only slightly on x. Therefore, from 4.1.27 we can approximate the average surface heat flux (per unit area) by

$$\frac{1}{F}\ \rho\ c_p \int_o^{\delta} U(T-T_i)dz \approx H_o - H_i\ . \qquad 4.1.29$$

Equations 4.1.27 and 4.1.29 should now make our experimental procedure clear. By measuring velocity and temperature profiles through the internal thermal boundary layer and knowing the upwind temperature profile, it is possible to determine the heat energy a lead loses to the atmosphere. These profile measurements must extend through the top of the boundary layer since the IBL height, δ, is a limit of integration.

While the profile sensors were cycling up and down through the boundary layer, sensors on our flux tower were measuring velocity and temperature fluctuations at two

fixed heights for a direct determination of the sensible heat fluxes at those heights. Therefore, let us reconsider 4.1.19 with the thought of comparing the integral heat flux estimates with the direct measurement of $\rho c_p \overline{wt}$ at height z'.

Integrate 4.1.19 from z = 0 to z = z',

$$\int_o^{z'} \partial_x[U(T-T_i)]dz + \int_o^{z'} \partial_z[W(T-T_i)]dz = -\int_o^{z'} (\partial_z \overline{wt})dz. \quad 4.1.30$$

Again the second and third terms are perfect differentials and we apply Leibnitz' rule to the first term,

$$\partial_x \int_o^{z'} U(T-T_i)dz - [U(T-T_i)\Big|_{z'} \partial_x z' + \int_o^{z'} d[W(T-T_i)]$$

$$= -\int_o^{z'} d\overline{wt} \; . \quad 4.1.31$$

z' is independent of x so the second term on the left here is zero. Hence,

$$\partial_x \int_o^{z'} U(T-T_i)dz + [W(T-T_i)\Big|_{z'} = -(\overline{wt}\Big|_{z'} - \overline{wt}_o). \quad 4.1.32$$

As before, integrate over x from 0 to F,

$$\int_o^F d[\int_o^{z'} U(T-T_i)dz] + \int_o^F [W(T-T_i)\Big|_{z'} dx = -\int_o^F (\overline{wt}\Big|_{z'} - \overline{wt}_o)dx. \quad 4.1.33$$

This yields

$$\int_{o}^{z'} U(F,z)\,[T(F,z) - T_i(z)]\,dz + \int_{o}^{F} [W(T-T_i)\Big|_{z'}\,dx$$

$$= -\int_{o}^{F} (\overline{wt}\Big|_{z'} - \overline{wt}_o)\,dx \ . \qquad 4.1.34$$

We can evaluate the first term in 4.1.34 from our profile measurements. The integral method gives us $\overline{wt}_o$. And $\overline{wt}\Big|_{z'}$ is what our flux sensors are seeing. The second term on the left of 4.1.34 is beyond our capabilities however; but we can say something of its behavior. $T-T_i$ is always positive -- that's essential in our definition of the thermal boundary layer. Now what does $W(x,z)$ do?

The roughness parameter of sea ice, z_o, is usually found to be in the range 0.01 cm to 0.02 cm (Untersteiner and Badgley, 1965; Ling and Untersteiner, 1974). Linday's (1976) upwind values are also generally of this size. Our estimates of z_o over leads, on the other hand, are for the most part larger than 0.02 cm. In fact, a run by run comparison of downwind and upwind z_o's shows that the downwind z_o is almost always larger than z_o upwind (see Appendix C for the tabulated values). We will say more about our z_o values in Chapter 5; but here we simply want to point out that the flow is feeling a change in surface roughness. Consequently, the thermal boundary layer is mixed with an internal momentum boundary layer.

Because the flow undergoes a transition from a smooth to a (relatively) rough surface, the horizontal velocity

near the surface would decrease if there were no surface temperature change (e.g., Bradley, 1968). On the other hand, if there were no roughness change, just the surface temperature step, the flow would accelerate (Taylor, 1970; Shreffler, 1975). Superimposing the two effects complicates matters. But it appears that if the temperature step is large enough and the roughness transition small enough, the accelerative profile will ultimately develop at some height above the surface.

Here, since the vertical velocity upwind is zero, W must go negative to assure continuity (see quation 4.1.3); it will, however, remain small in magnitude because of the relative thinness of the IBL. Above the boundary layer, the longitudinal velocity profile will rejoin the upwind profile and W will return to zero. In summary, W essentially remains negative -- or at least non-positive -- throughout the layer. It seems reasonable to conclude that $W \leq 0$ in the thermal boundary layer.

With this insight equation 4.1.34 becomes

$$\int_0^{z'} U(T-T_i)dz \geq -\int_0^F (\overline{wt}\Big|_{z'} - \overline{wt}_0)dx \ , \qquad 4.1.35$$

or

$$\overline{wt}\Big|_{z'} \geq \overline{wt}_0 - \frac{1}{F}\int_0^{z'} U(T-T_i)dz \ . \qquad 4.1.36$$

This expression finally relates our direct flux measurements to the integral results and sets a lower bound for comparisons.

4.2. THE BOUNDARY LAYER PROFILES

In Figures 4.1 to 4.4 we have plotted, in groups of similar fetch, 76 velocity and temperature profiles made during ALEX. Averaging time for these profiles is generally 15 to 25 minutes. We have omitted plotting cup anemometer data since it seemed to give the velocity profiles an unreal curvature. Figure 4.4 contains profiles taken over a real lead: the others are from artificial leads. In Appendix B we tabulate our profile measurements.

During ALEX the water temperature was always measured to be between -2.0°C and -2.4°C; therefore, the air temperature exerts primary control over the slope of the temperature profile. The reader may remark that these water temperatures are unusually cold. They indeed are. But most of the ALEX runs were on Elson Lagoon, which is a shallow, isolated body. Kelley (1974) reports that the salinity of the water he sampled in the lagoon during ALEX always exceeded 42‰. The temperatures measured are compatible with this salinity. The -2.1°C surface temperatures are associated with the natural lead we observed. Considering that the accuracy of all our surface temperature measurements is ±0.2°C, this is not a surprisingly low

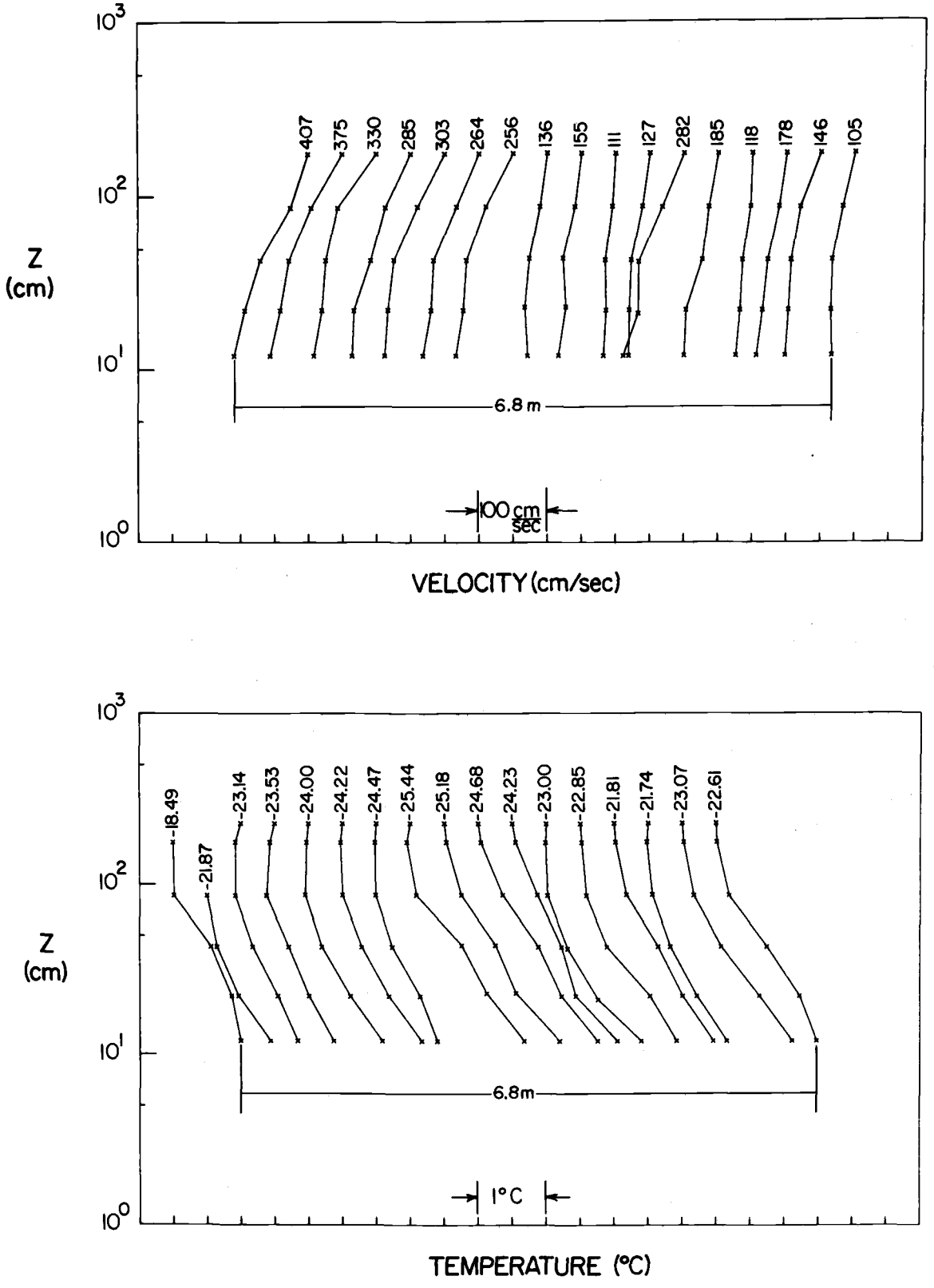

Figure 4.1. Artificial lead. March 12 and 13, 1974. The numbers above the profiles are the velocity and temperature at the highest level. The numbers underneath give the fetch.

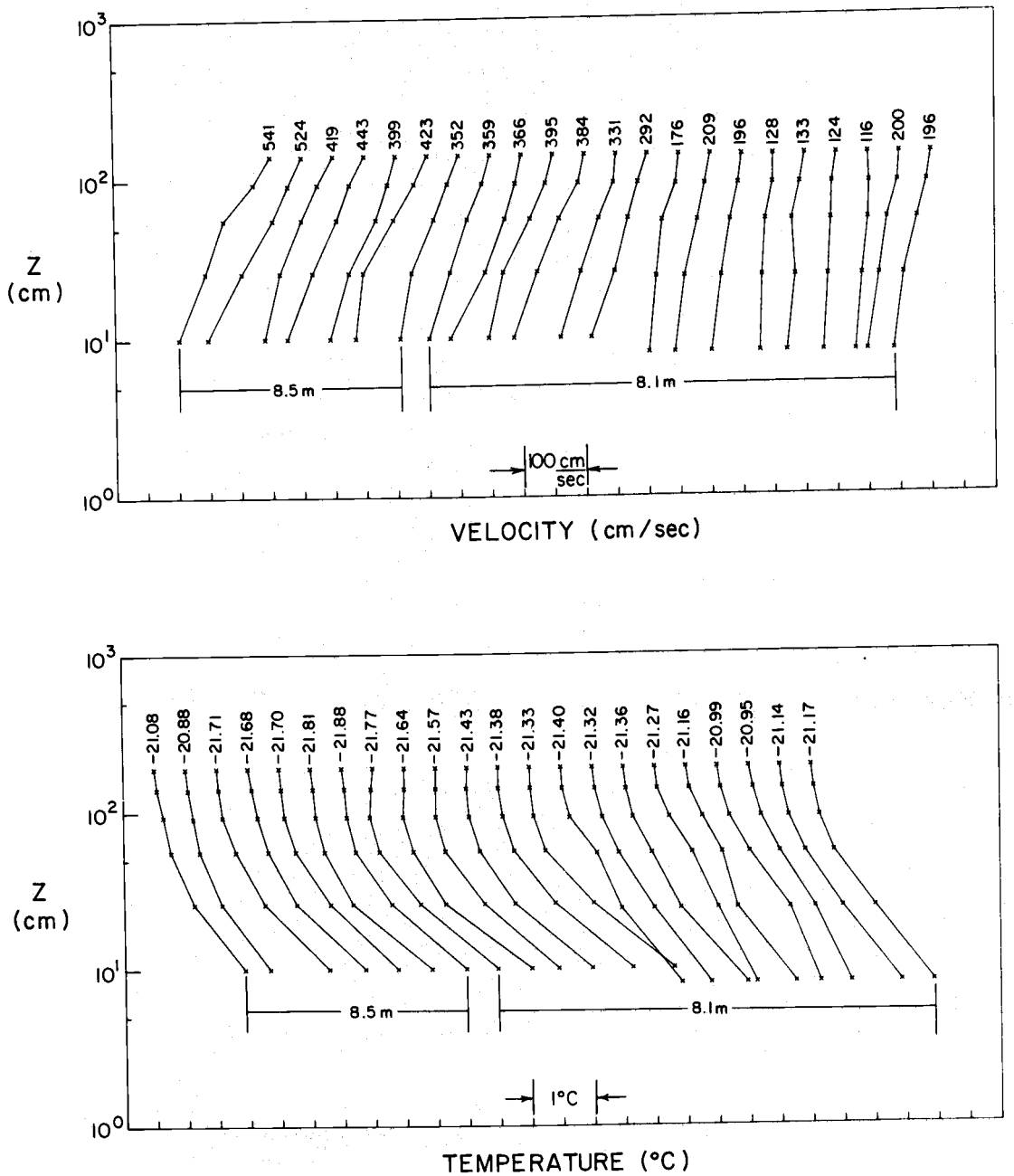

Figure 4.2. Artificial lead. March 11 and 12, 1974.

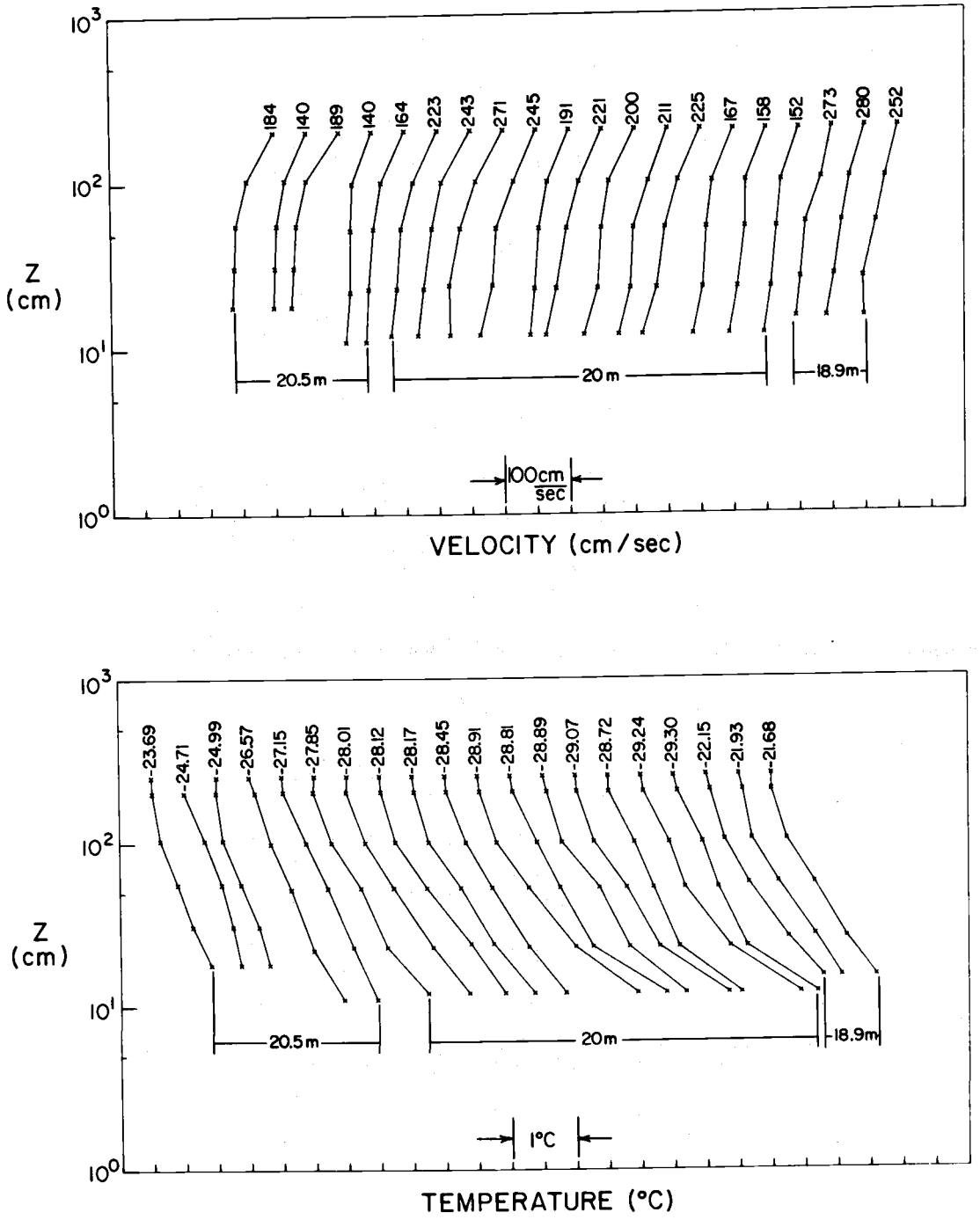

Figure 4.3. Artificial lead. April 2 and 3, 1974.

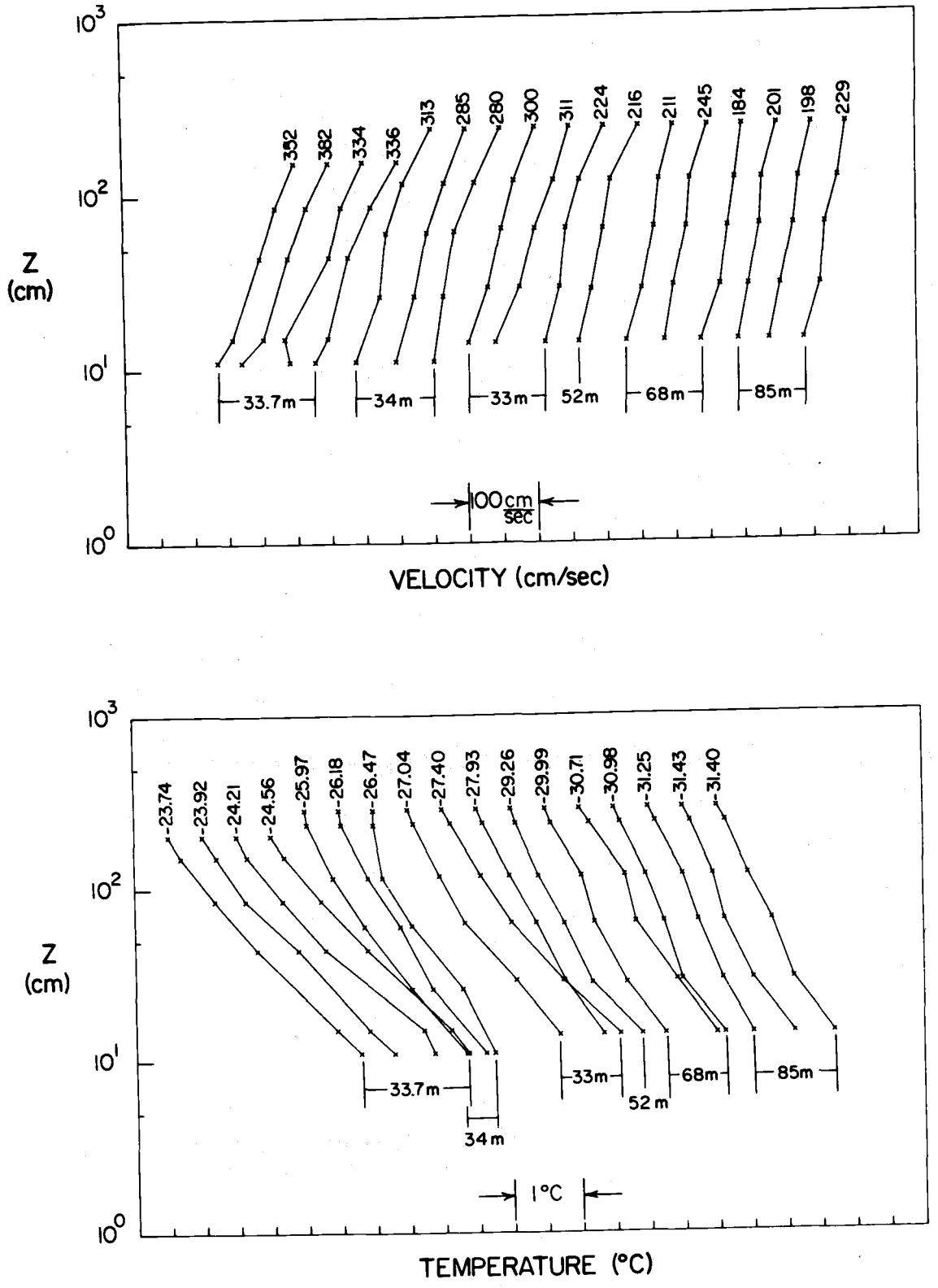

Figure 4.4. Real lead. March 19 and 20, 1974.

temperature either when we recall the salt flux at the surface of leads due to the evaporation and ice formation.

The wind speeds are generally low and the velocity profiles occasionally erratic. However, in the mid-region of the profiles, especially at the longer fetches, the increased turbulent mixing driven by the heat flux is apparently accelerating the flow from its upwind profile. But often the lowest profile point turns to slower speeds. This may be an indication that increased surface roughness is, indeed, slowing the flow in the vicinity of the surface, partially offsetting the tendency for the heat flux to accelerate it.

Lindsay's (1976) upwind observations give us the ambient stability. Upwind conditions are unstable for the profiles in Figure 4.2 and mostly stable for the remaining profiles pictured. If our profile observations are reaching the top of the boundary layer, we should be able to read these stabilities at the top of the temperature profiles. But at the longest fetches particularly, the upwind stability is not showing up in the temperature profiles. That is, we have not found the top of the boundary layer; for these profiles the integral method of heat flux estimation is inapplicable.

From studying these profiles it is apparent that the thermal boundary layer height, δ, depends not only on fetch but also on wind speed. At lower wind speeds the

boundary layer is higher or not apparent. When we try to analyze the IBL height in Chapter 6, this effect will manifest as a dependence of δ on local stability.

4.3. A DEMONSTRATION OF THE INTEGRAL METHOD

Chapter 5 contains a figure summarizing the heat fluxes we calculate using the integral method and Appendix C tabulates these results. Here we would like to take four representative profile sets -- two with unstable upwind conditions and two with stable conditions -- and demonstrate the use of the integral method. Figure 4.5 shows the profiles we will consider. Do not be misled into thinking that the upwind and downwind temperature profiles agreed from the start as well as they do in Figure 4.5. In Chapter 3 we discussed thermocouple calibration problems but also emphasized the importance of the profile shapes. To join the temperature profiles in Figure 4.5, we have matched upwind and downwind profile shapes above the boundary layer, taking the downwind temperature as the reference temperature. The goodness in fit at the top of the profiles confirms the validity of this method.

The z integration in equation 4.1.27 is from zero to the top of the boundary layer. Since operationally we perform the integration by connecting velocity and temperature points with logarithmic arcs, $z = 0$ becomes z_0. Conditions at z_0 are $U = 0$ and $T = T_w$ (the water temperature).

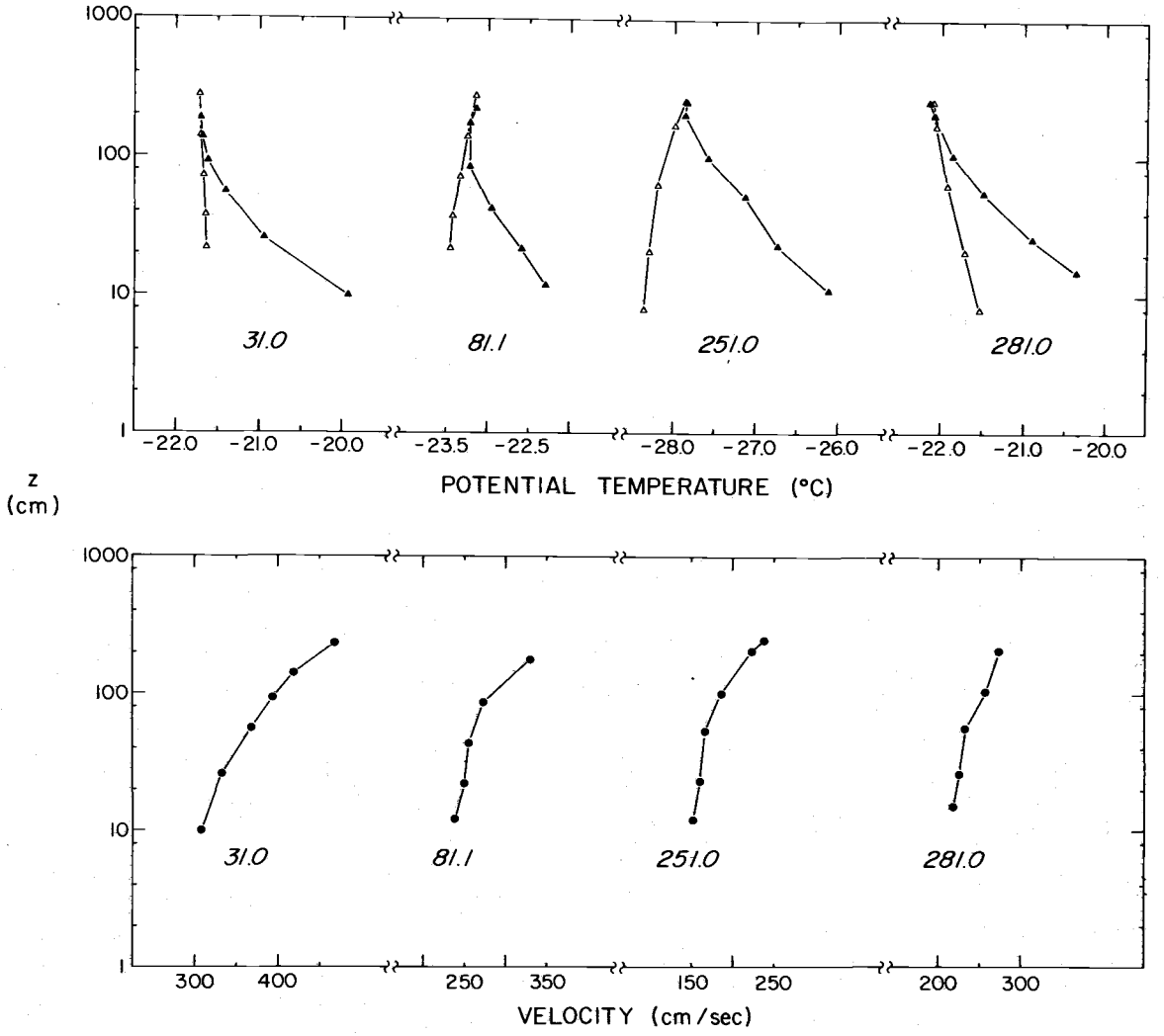

Figure 4.5. Four profile sets with which the integral method will be demonstrated. Open triangles are upwind temperatures; darkened triangles are downwind.

For purposes of the integration, we related z_0 to the friction velocity, u_*, through

$$z_0 = \frac{2\nu}{u_*} \quad , \qquad 4.3.1$$

where ν is the kinematic viscosity. This gave roughness lengths of about 0.02 cm. We will show in the next chapter that 4.3.1 is really not the proper form for z_0 though it gives values of the correct order. Fortunately, z_0 does not have much effect on the integration: z_0 may range over three orders of magnitude while the profile integral changes by less than 10%.

For the specific heat, c_p, which 4.1.27 requires, we consult National Bureau of Standards Circular 564 (Hilsenrath, et al., 1955). Its value at the water temperatures we encountered is 1.006 joules $gm^{-1}{}^{\circ}C^{-1}$. The air density, ρ, at the surface of the lead is

$$\rho = 1.2929 \times 10^{-3} gm/cm^3 \left(\frac{273.16}{T_w}\right)\left(\frac{p}{760}\right) \quad , \qquad 4.3.2$$

where p is the atmospheric pressure in millimeters of mercury.

Table 4.1 is a tabulation of the results of the integral method applied to the four data sets of Figure 4.5. We have separated the integration into segments to show how different height regions contribute to the total. The 'Total Flux' refers to equation 4.1.27. The 'Average

Table 4.1. Integral heat flux estimates from the four profile sets in Figure 4.5. The arrow shows the 50% point of the integration.

RUN	31.0	81.1	251.0	281.0
Fetch (m)	8.5	6.8	20.0	18.9
Upwind	unstable	stable	stable	unstable
δ (cm)	164	165	248	213
Height (cm)	Integral Contribution (w/cm)			
0-5	8.63	7.34	6.06	6.06
5-10	4.86	4.05	3.78	4.00
10-20	→5.41	→3.72	4.13	→4.18
20-40	5.76	4.62	→5.86	4.73
40-80	4.93	4.00	8.20	4.68
80-150	1.78	1.72	7.15	2.73
150+	0.10	0.11	2.56	0.74
Total Flux (w/cm)	31.5	25.6	37.7	27.1
Average Flux (mw/cm^2)	37.0	37.6	18.9	14.4

Flux' is the fetch-averaged quantity, equation 4.1.29.

It is important here to recognize how close to the surface things happen in this transfer process. The arrow in each 'Integral Contribution' column of Figure 4.5 marks the 50% point of the integration. In other words, the portions of the profiles above and below the arrow contribute equal amounts to the integration in 4.1.27. This means then -- because of 4.1.36 -- that the average vertical heat flux is reduced to one-half its surface value in the height region denoted by the arrow. Compare these heights with the boundary layer height, δ. They are typically $\frac{1}{10}\,\delta$. Most of the escaping heat is not rising very far before it is carried away from the lead.

4.4. COMPARISON WITH THE DIRECT MEASUREMENTS

Here would be the perfect place to present our direct measurements of $\rho\, c_p \overline{wt}$, call on equation 4.1.36, and so compare profile and direct estimates of the sensible heat flux. Our original attempt at that comparison was an abject failure: the direct estimates were 10% to 50% what they should have been on the basis of 4.1.36. On plotting temperature spectra and the cospectra of wt we saw what was wrong. These spectra seldom contained much energy beyond the peak frequency since riming of the thermocouples limited their frequency response. Thus, the direct determination badly underestimated the value of $\overline{wt}$.

In an attempt to mathematically correct for the attenuation of the high frequency temperature signals, we appealed to the spectral and cospectral shapes reported by Panofsky and Mares (1968) and Kaimal, Wyngaard, Izumi, and Coté (1972). These suggest that the cospectra of uw and wt have coincident peaks and that in the inertial subrange

$$\frac{Co_{wt}}{Co_{uw}} \approx 2.9 \frac{\overline{wt}}{\overline{uw}} , \qquad 4.4.1$$

where Co is the cospectra. Since our uw cospectra seem very good and because we generally reach the peak of the wt cospectrum, 4.4.1 gives us a method for correcting our direct estimates of $\overline{wt}$. Basically, we assume that at the frequency of the peak

$$\overline{wt} = \overline{uw} \frac{Co_{wt}}{Co_{uw}} . \qquad 4.4.2$$

In the inertial subrange Co_{wt} is estimated from 4.4.1 using the value of $\overline{wt}$ from 4.4.2. An interpolation establishes Co_{wt} between the peak and the presumed start of the inertial subrange. Finally, we integrate Co_{wt} and get a revised estimate of $\overline{wt}$.

Admittedly there's a lot of handwaving going on here. But the original wt cospectra were so deficient in spectral energy at the higher frequencies (Figure 4.6) that we gave up hope of a confident comparison between direct and profile heat flux estimates. Hence, any reasonable method of

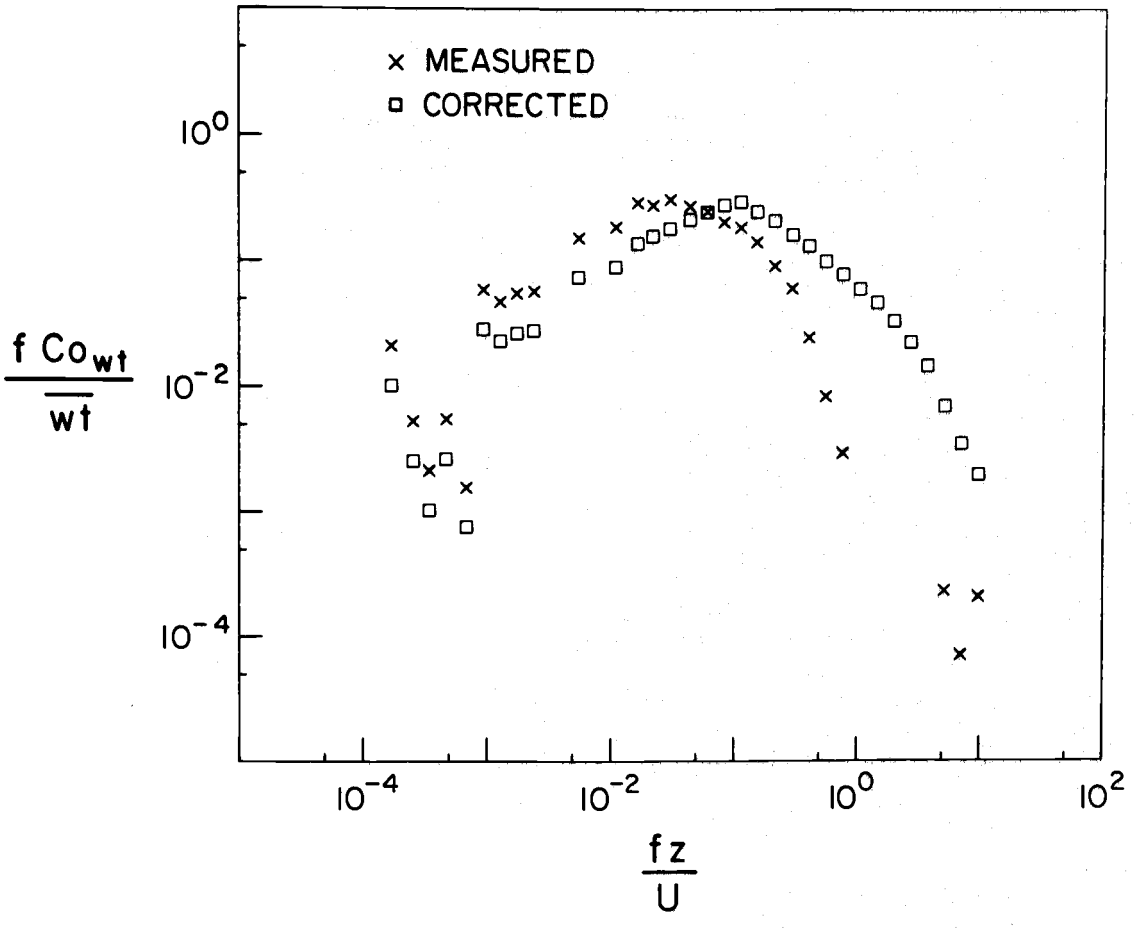

Figure 4.6. A measured and corrected wt cospectrum 11 cm above the surface. The fetch is 7.2 m. Measured value of $\rho\, c_p\, \overline{wt}$ is 5.0 mw/cm^2; corrected value is 11.9 mw/cm^2; integral estimate (equation 4.1.36) is 12.0 mw/cm^2.

putting the spectral energy back is justifiable. We will be satisfied with ballpark harmony. And this correction method gave us that. In fact, the corrected estimates of $\rho\, c_p \overline{wt}$ agreed with the profile estimates in the sense of equation 4.1.36 about as well as we could hope (for that comparison, see Appendix D). We are, consequently, reassured that the integral method is yielding proper values of the sensible heat flux from Arctic leads.

4.5. LATENT HEAT FLUX

As explained earlier, the original plan for ALEX included provisions for determining the latent heat flux from leads in addition to the sensible heat flux. Electronics problems pretty much thwarted these plans. However, we did salvage five humidity profiles of questionable quality (Figure 4.7) -- questionable because we have no other humidity observations with which to compare them. We compute the latent heat fluxes associated with these profiles here.

The integral method is again our approach. For our purposes, humidity behaves just like temperature: we can, thus, immediately reinterpret 4.1.27 and 4.1.29 in terms of the latent heat flux. These become, respectively,

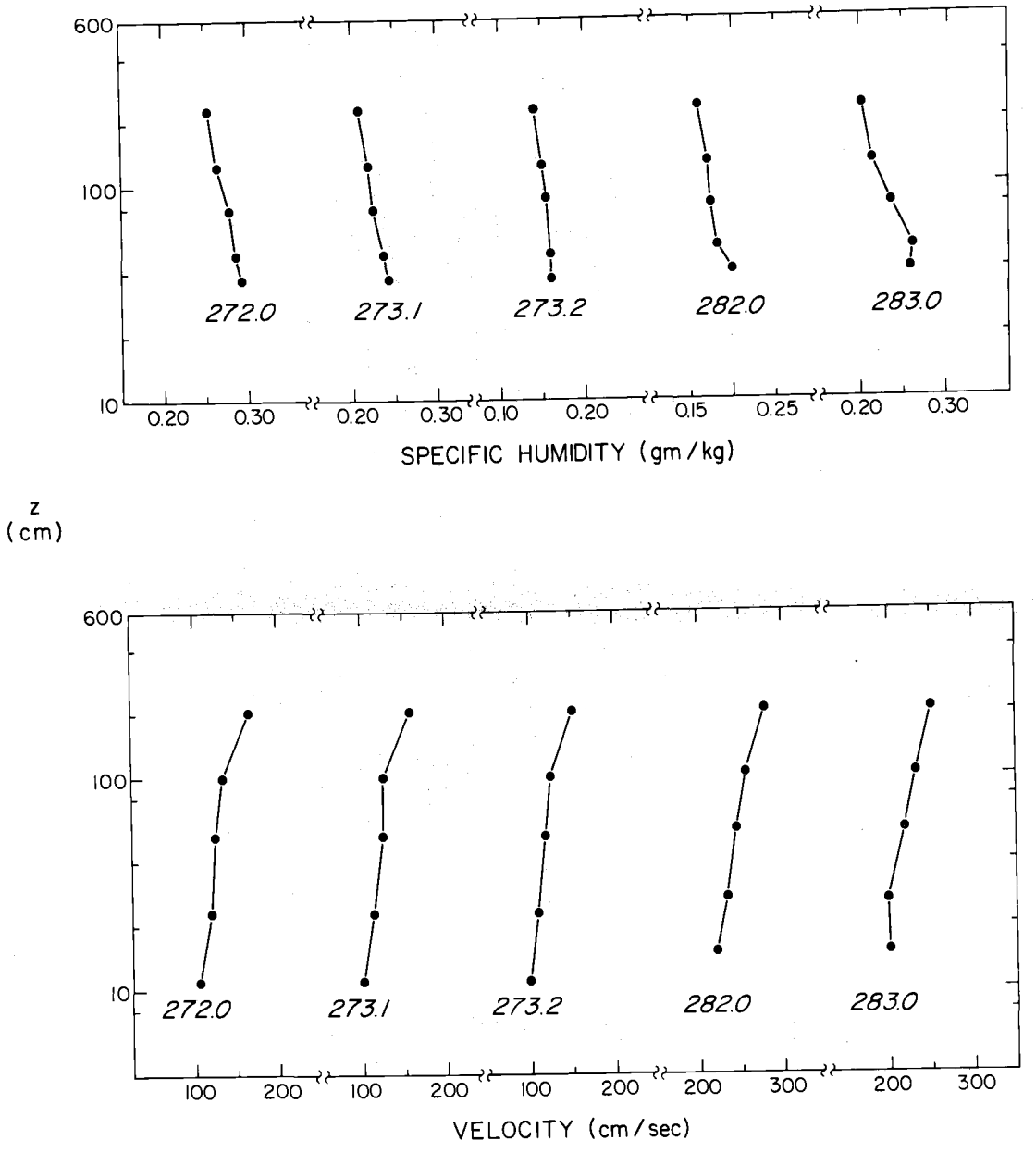

Figure 4.7. Humidity and velocity profiles. Artificial lead. April 3, 1974.

$$\rho L_v \int_o^{\delta_q} U(F,z)\,[Q(F,z)-Q_i(z)]\,dz = \int_o^F (H_{L_O} - H_{L_i})\,dx \qquad 4.5.1$$

and

$$\frac{1}{F}\,\rho L_v \int_o^{\delta_q} U(F,z)\,[Q(F,z)-Q_i(z)]\,dz \approx H_{L_O} - H_{L_i} \,. \qquad 4.5.2$$

Here L_v is the latent heat of vaporization; δ_q, the height of the moisture boundary layer; Q, the average specific humidity; H_{L_O}, the surface latent heat flux; and H_{L_i}, the upwind latent heat flux. Clearly,

$$H_L \equiv \rho L_v \overline{wq} \,, \qquad 4.5.3$$

where q is the fluctuating specific humidity.

We have not measured upwind humidity profiles and, hence, will assume the upwind profile is constant with height and has the value it has at the top of the boundary layer. This assumption implies that H_{L_i} is zero. These necessities are not detrimental to our estimates because the severe Arctic cold and the absence of upwind moisture sources ensure that the upwind specific humidity will be an order of magnitude smaller than the specific humidity at the surface of the lead. Therefore, any upwind humidity structure will have no significant effect on the profile integration.

Our hygristor sensed relative humidity. To convert these observations into the specific humidity which 4.5.2 requires is an involved algebraic process. It's clearer if

we work backwards. The specific humidity, Q (units of gm/gm), is related to the vapor pressure, e, thusly (Kraus, 1971),

$$Q = \frac{\frac{m_w}{m_a}\frac{e}{p}}{1 - \frac{m_a - m_w}{m_a}\frac{e}{p}} , \qquad 4.5.4$$

where m_w and m_a are the molecular weights of water and air, respectively, and p is the atmospheric pressure. The vapor pressure, e, comes from the relative humidity, r, through

$$e = r\, e_{sat} , \qquad 4.5.5$$

where e_{sat} is the saturation vapor pressure. This saturation vapor pressure depends on the air temperature and is tabulated in the Smithsonian Meteorological Tables (List, 1971).

We assume the air is saturated with vapor at the surface of the lead and so assign a specific humidity at z_0 dictated by the water temperature. However, Roll (1965) points out that the saturation vapor pressure of air over salt water, e_{sw}, is less than the saturation vapor pressure over distilled water, e_{dw}. He gives

$$e_{sw} = e_{dw}(1 - 0.000537\ S) , \qquad 4.5.6$$

in which S is the salinity in parts per thousand. Therefore, to assign a surface humidity, we require an estimate of the salinity. Assuming the water in the lead is at its freezing temperature, T_{fp}, and that the salinity has defined that freezing point, we find the surface salinity from the measured water temperature with (Neumann and Pierson, 1966)

$$T_{fp} = -0.003 - 0.0527\ S - 0.00004\ S^2\ . \qquad 4.5.7$$

Finally, we choose a latent heat of vaporization consistent with the surface temperature using (Kraus, 1971)

$$L_v = 2500.3 - 2.344\ T\ , \qquad 4.5.8$$

where L_v is in joules/gm when T is in °C.

When all these conversions have been made, we apply 4.5.2 to calculate the latent heat flux. Table 4.2 compares the latent heat fluxes for our five runs with the corresponding sensible heat fluxes. The numbers seem to be of the proper size: the latent heat flux accounts for 1/6 to 1/3 of the total turbulent heat flux from the leads we observed. Shreffler (1975) suggests a value of 1/4 is typical. Badgley (1966) finds the latent heat flux to be more like 1/10 of the total turbulent flux (see Table 1.2).

Table 4.2. A comparison of sensible and latent heat fluxes. All these leads are artificial.

Run	Fetch (m)	T_{ice} (C°)	Average Flux (mw/cm^2)	
			Sensible	Latent
272.0	20.0	-29.2	15.42	3.25
273.1	20.0	-29.7	15.32	3.13
273.2	20.0	-29.8	15.49	2.84
282.0	18.9	-21.0	13.04	7.06
283.0	18.9	-20.8	13.17	7.08

5. THE FLUX-GRADIENT METHOD OF FLUX ESTIMATION

But lo, a stir is in the air!
The wave -- there is a movement there!
Edgar Allan Poe
"The City in the Sea"

Because our direct measurements of the heat flux proved unreliable, we sought an alternative method of estimating heat and momentum fluxes for the purposes of checking the quality of the integral method. The empirical flux-gradient equations (Businger, et al., 1971; Dyer, 1974) relate velocity and temperature profile gradients in a constant flux layer to corresponding momentum and heat fluxes. This restriction to a constant flux layer presents difficulties, because, obviously, the region above a lead is not a constant flux layer. But perhaps far enough downwind from the leading edge of the lead or very near the surface, the flow will be in approximate equilibrium with the new surface (Bradley, 1968; Rao, et al., 1974). We proceed on this assumption and try to keep it valid by using only the lowest two profile points and the surface conditions. That is, we apply the flux-gradient technique to three-point profiles in which none of the points is ever more than 31 cm above the surface. And these profiles are always at least 6.8 m from the front edge of the lead.

5.1. THE FLUX-GRADIENT EQUATIONS AND TECHNIQUE

There are two sets of flux-gradient relations: one for unstable conditions, another for stable conditions. Since the flow is always unstable over the lead we need not bother discussing equations for a stable regime.

The essence of the flux-gradient approach is in the definition of nondimensional velocity and temperature gradients, ϕ_m and ϕ_h, respectively,

$$\phi_m = \frac{kz}{u_*} \partial_z U \ , \qquad 5.1.1$$

$$\phi_h = \frac{z}{t_*} \partial_z T \ , \qquad 5.1.2$$

where

k = 0.4, von Kármán's constant

u_* = $(\frac{\tau}{\rho})^{\frac{1}{2}}$, the friction velocity

τ the surface stress

t_* = $-\frac{\overline{wt}}{ku_*}$

$\overline{wt}$ the surface temperature flux

For unstable conditions, ϕ_m and ϕ_h are (Paulson, 1970; Dyer, 1974)

$$\phi_m = (1 - 16 \frac{z}{L})^{-\frac{1}{4}} \ , \qquad 5.1.3$$

$$\phi_h = (1 - 16 \frac{z}{L})^{-\frac{1}{2}} \ , \qquad 5.1.4$$

where z is the height and L is the Monin-Obukhov length,

$$L = -\frac{\bar{T}}{g}\frac{u_*^3}{k\overline{wt}} = \frac{\bar{T}}{g}\frac{u_*^2}{k^2 t_*} \quad . \qquad 5.1.5$$

Here $\bar{T}$ is a temperature representative of the layer and g is the acceleration of gravity.

Paulson (1970) has demonstrated how 5.1.1 and 5.1.2 may be integrated since ϕ_m and ϕ_h are known. The integrations yield

$$U(z) = \frac{u_*}{k}\left[\ln\frac{z}{z_0} - \psi_m\right] \qquad 5.1.6$$

$$T(z) = T_w + t_*\left[\ln\frac{z}{z_H} - \psi_h\right] \quad , \qquad 5.1.7$$

with

$$\psi_m = 2\ln\left[\frac{1+x}{2}\right] + \ln\left[\frac{1+x^2}{2}\right] - 2\arctan x + \frac{\pi}{2} \qquad 5.1.8$$

$$\psi_h = 2\ln\left[\frac{1+x^2}{2}\right] \quad , \qquad 5.1.9$$

and

$$x = \left(1 - 16\frac{z}{L}\right)^{\frac{1}{4}} \quad . \qquad 5.1.10$$

In 5.1.7, z_H is the roughness length for temperature, which is not necessarily equal to z_0 (Garratt and Hicks, 1975).

Having equations 5.1.6 to 5.1.10, the flux-gradient technique for estimating the momentum and heat fluxes, u_*^2 and ku_*t_*, respectively, is an iterative procedure:

1. Take $\frac{z}{L} = 0$. Fit the velocity data, U(z) and ln z, and the temperature data, T(z) and ln z, with least

squares lines. From 5.1.6 and 5.1.7 get zeroth order estimates of u_* and t_*.

2. Use u_* and t_* to calculate L. Find $\frac{z}{L}$ for each height and subsequently $\psi_m(\frac{z}{L})$ and $\psi_h(\frac{z}{L})$.

3. According to 5.1.6 and 5.1.7, U and T are linear functions of ln z - ψ_m and ln z - ψ_h, respectively. So fit the data in this form with least squares lines.

4. This least squares linear regression yields new values of u_* and t_*.

5. Use u_* and t_* in 5.1.6 and 5.1.7 to predict U(z) and T(z) and check how these predictions differ from the data by calculating the sums of squared deviations for both data sets.

6. If these two sums are still larger than some desired limits but smaller than for the previous iteration, return to Step 2 and iterate again.

7a. If the sums of squared deviations have become acceptably small, the current u_* and t_* will predict the fluxes.

7b. If the sums have begun increasing, the u_* and t_* from the previous iteration best reflect the fluxes.

5.2. The z_0 CONTENTION

Since our plan for using the flux-gradient technique is to fit only two profile points and assign z_0 (where U=0) and z_H (where $T=T_w$), this choice of z_0 and z_H is critical.

The simplest model would be to make z_0 and z_H constant and, henceforth, forget about them. But there is compelling evidence that over water z_0, at least, depends on the wind speed (e.g., Kitaigorodskii and Volkov, 1965; Smith and Banke, 1975).

There are basically two parameterizations for the dependence of z_0 on wind speed. The first is for an 'aerodynamically smooth' flow (e.g., Tennekes and Lumley, 1972; Csanady, 1974),

$$z_0 = e^{-2} \frac{\nu}{u_*} . \qquad 5.2.1$$

The second applies at higher wind speeds where the flow will be 'aerodynamically rough'. This is the Charnock relation (Charnock 1955, 1958; Wu, 1969),

$$z_0 = C \frac{u_*^2}{g} , \qquad 5.2.2$$

where C is a supposed universal constant. The aerodynamic character of the flow is usually determined by its roughness Reynolds number,

$$R_* = \frac{u_* z_0}{\nu} . \qquad 5.2.3$$

There are three aerodynamic regions (Businger, 1973):

$$\begin{aligned} &\text{smooth:} && R_* \leq 0.13 \\ &\text{transition:} && 2.5 > R_* > 0.13 \\ &\text{rough:} && R_* \geq 2.5 \end{aligned} \qquad 5.2.4$$

Relations 5.2.1 and 5.2.2 are distinctly different. For the smooth case the roughness length decreases with increasing wind speed: for Charnock's relation it increases. Hence, a close examination of our data should make the choice between 5.2.1 and 5.2.2 easy.

In Figure 5.1 we show the correlation between our flux tower measurements of $(-\overline{uw})^{\frac{1}{2}}$ and velocity -- that flux tower average velocity logarithmically extrapolated to 50 cm. These measurements were always made within 42 cm of the surface and usually within 20 cm. (See Appendix D for a tabulation of the data.) The line in the figure is

$$(-\overline{uw})^{\frac{1}{2}} = 0.0643\ U_{0.5} - 0.77\ , \qquad 5.2.5$$

which gives $(-\overline{uw})^{\frac{1}{2}}$ in cm/sec for $U_{0.5}$ in cm/sec.

Some might be concerned about the accuracy of a logarithmic extrapolation in such an unstable layer. Bradley's (1972) work implies that so near the surface it will be valid even under pronounced instability. Nevertheless, we desire further assurance since much of what we do later is based on 5.2.5. From our profile data we can interpolate between velocity measurements above and below 50 cm and so make a very confident estimate of $U_{0.5}$. When $(-\overline{uw})^{\frac{1}{2}}$ is plotted against this profile velocity, $U_{0.5_p}$, the resultant correlation is

$$(-\overline{uw})^{\frac{1}{2}} = 0.0707\ U_{0.5_p} - 1.59\ . \qquad 5.2.6$$

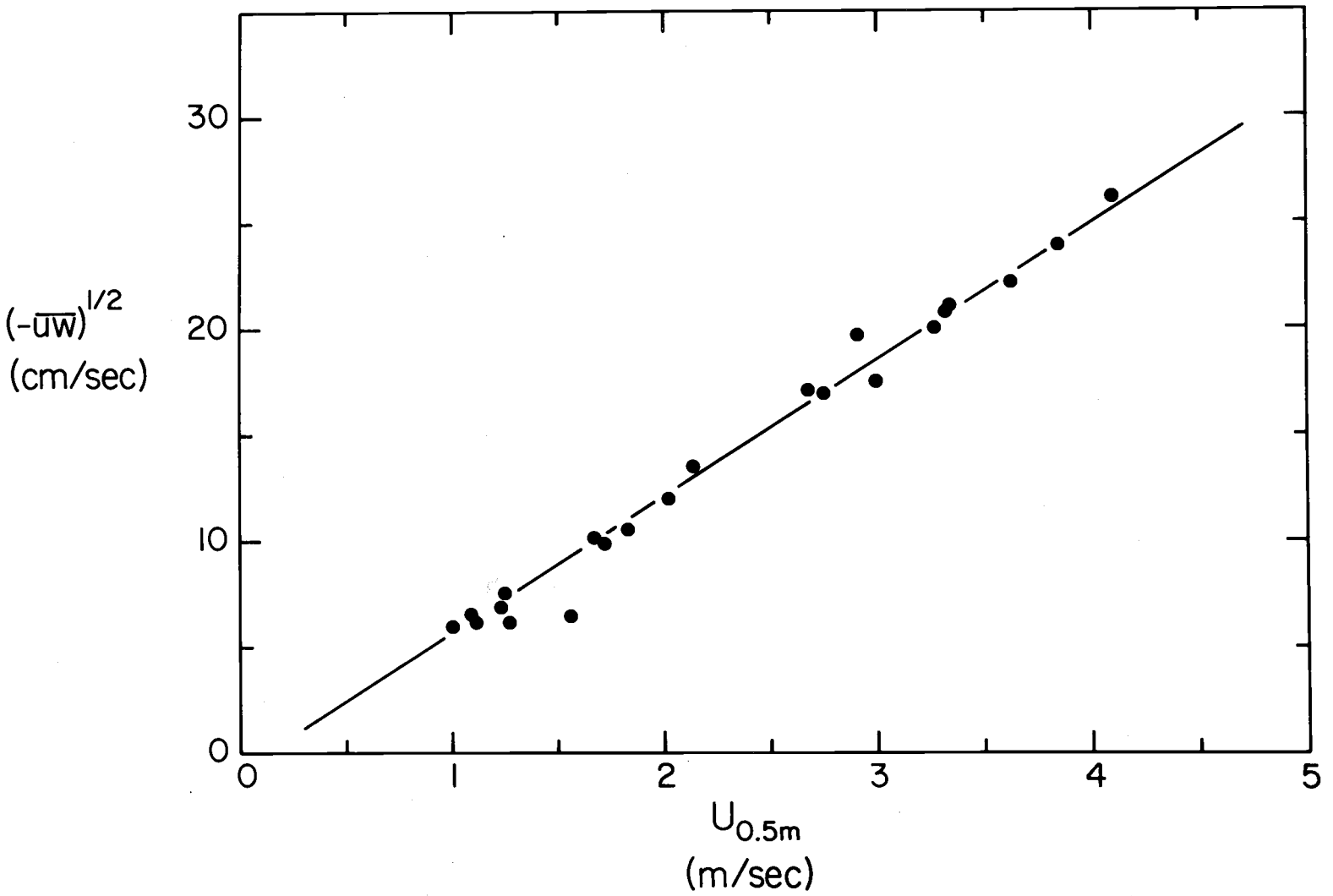

Figure 5.1. Flux tower measurements of $\overline{uw}$ and velocity. $U_{0.5}$ is the velocity extrapolated to 50 cm. The line is equation 5.2.5.

There was more scatter in this plot than in Figure 5.1, but the results of the two agree: the multiplicative constants in 5.2.5 and 5.2.6 are close and the additive constants are definitely negative. In other words, the extrapolation which led to 5.2.5 seems to introduce no significant error despite the instability of the layer. We prefer 5.2.5 to 5.2.6 because of the good correlation in Figure 5.1 and the fact that the profile data was not always simultaneous with the flux data.

From Taylor's (1970) and Shreffler's (1975) numerical experiments we infer that in boundary layers developing over heated surfaces, $-\overline{uw}$ should be constant to within five percent for heights of at least 20 cm. Therefore, we identify $(-\overline{uw})^{\frac{1}{2}}$ with u_* and interpret 5.2.5 as a drag relation. By assuming a logarithmic profile to 10 meters, we compute a drag coefficient referenced to this height and compare it with other reported coefficients. A mid-range value of 250 cm/sec for $U_{0.5}$ converts 5.2.5 to

$$C_{10} = \left(\frac{u_*}{U_{10}}\right)^2 = 1.76 \times 10^{-3} \quad , \qquad 5.2.7$$

which is roughly 30% higher than most observations of an open water drag coefficient (cf. Miyake, et al., 1970a; Sheppard, et al., 1972; Smith and Banke, 1975). This disparity is a very good indication of the intense mixing in the IBL initiated by the vertical heat flux. The multiplicative constant in 5.2.5 is, however, in

remarkable agreement with a result quoted by Hicks (1976) for grassland,

$$u_* = 0.0632\ U_{0.5} + 2.22\ . \qquad 5.2.8$$

Consider what the result 5.2.5 implies concerning z_0. If -- as according to Bradley (1972) -- near the surface the logarithmic velocity law,

$$U = \frac{u_*}{k} \ln \frac{z}{z_0}\ , \qquad 5.2.9$$

is always approximately true, we have from 5.2.5

$$k\ U_{0.5} = (a\ U_{0.5} + b)\ \ln \frac{50}{z_0}\ . \qquad 5.2.10$$

So

$$z_0(\text{cm}) = 50\ e^{\frac{-k}{a+b/U_{0.5}}}\ . \qquad 5.2.11$$

Since b is non-zero, z_0 must be a function of wind speed. We can find out more by differentiating z_0 with respect to $U_{0.5}$,

$$d_{U_{0.5}} z_0 = 50\ e^{\frac{-k}{a+b/U_{0.5}}}\ \left[\frac{-bk}{(a\ U_{0.5}+b)^2}\right]\ . \qquad 5.2.12$$

Because b is negative, the quantity in brackets is always positive in the wind speed range for which 5.2.5 is valid. Thus, our observations indicate that z_0 increases with increasing wind speed (increasing u_*). The balance swings toward Charnock's relation.

The obvious thing to do now is search the literature for an acceptable value of the constant C in 5.2.2. Table 5.1 summarizes some of the Charnock constants we find. Seemingly our search has failed to uncover a universally accepted value for C; the tabulated constants range over an order of magnitude. Kitaigorodskii and Volkov (1965), in fact, present a forceful exposition of how nonuniversal the Charnock constant apparently is.

But let us experiment with two values. American investigators are fairly closely grouped about C = 0.012. On the other hand, the Russians prefer C = 0.035 (Monin, 1970). The z_0 values that each of these constants predict in the u_* range of our observations are very small -- 0.01 cm is an upper limit with 0.002 cm a lower bound. But we expect z_0 to be around 0.02 cm since that is a typical value for flows over water.

On calculating roughness Reynolds numbers using z_0 = 0.02 cm we discover the problem. R_* is always smaller than five and most often has values characteristic of flows in the transition region between aerodynamically smooth and rough. Phillips (1969) casts doubts on the validity of the Charnock relation in transitional flows and we recall that most investigators have verified it only at high wind speeds. In other words, our data seem to fall in the unexplored area where neither the smooth flow parameterization nor the Charnock relation correctly models z_0. Hence,

Table 5.1. Some reported values of Charnock's constant.

Source	C	Comments
Charnock (1955)	0.0067	Small reservoir and laboratory channel.
Charnock (1958)	0.0123	
Kitaigorodskii and Volkov (1965)	0.035	Over 1000 observations from several data sets ranging from laboratory to open ocean.
Hidy and Plate (1966)	0.011	Laboratory results. $u_* > 20$ cm/sec.
Wu (1968)	0.0112	Laboratory study. Confirm at high wind speeds.
Wu (1969)	0.0156	Compilation of laboratory and oceanic observations.
Laykhtman and Snopkov	0.074	Quoted by Kitaigorodskii (1969).
Hicks (1972)	0.016	Bass Strait (off Australia) and Lake Michigan.
Hsu (1974)	$\frac{2\pi H}{gT^2}$	Dominant wave height and period.
Smith and Banke (1975)	0.0144	Seaward of a sandspit.

with these two baselines and our data as a map, let us survey this area.

The integral method has given us an estimate of ku_*t_*, and our eddy correlation measurements yield $-\overline{uw} \approx u_*^2$. Hence, is it possible to select reasonable values for z_0 and z_H which when plugged into the flux-gradient equations result in momentum and heat flux estimates compatible with these? We first tried a range of constant z_0's and z_H's. But no constant value for the two gave consistent estimates over the entire velocity range of our data. Therefore, we at last settled on the scheme

$$z_0 = 0.00014\ U_{0.5} - 0.005\ ,$$
$$z_H = 0.03\ \text{cm}, \qquad 5.2.13$$

where z_0 is in centimeters for $U_{0.5}$ in cm/sec.

In the next section we will show graphically how well these formulations of the roughness lengths worked in the flux-gradient technique. But here we still have a few things to report concerning our trek in the transition region.

Some might take exception with our choice of $z_H = 0.03$ cm. It has been suggested that z_H is inversely proportional to u_* (Garratt and Hicks, 1973; Hicks, 1975),

$$z_H = k\,\frac{D}{u_*}\ , \qquad 5.2.14$$

where, as before, k is von Kármán's constant and D is the thermal diffusivity. But there is nothing in our data which implies this is a better model of temperature roughness length than the one we have chosen. So we stay with simplicity.

The relation between z_0 and $U_{0.5}$ in 5.2.13 is admittedly not very aesthetic. Let us use 5.2.5, identifying $(-\overline{uw})^{\frac{1}{2}}$ with u_*, to rewrite it:

$$z_0 = 2.18 \times 10^{-3} u_* - 3.32 \times 10^{-3} . \qquad 5.2.15$$

This is a little better: z_0 is a linear function of u_*. However, we discover that in the u_* region for which 5.2.13 was originally confirmed, 5.2.15 is well-represented by

$$z_0 = 0.4 \left(\frac{\nu}{g^2}\right)^{1/3} u_* . \qquad 5.2.16$$

This is a new parameterization for z_0 which we suggest is valid for flows in or slightly beyond the transition region where neither 5.2.1 nor 5.2.2 applies.

Figure 5.2 summarizes the various relations between z_0 and u_* we have been discussing and offers heuristic support for 5.2.16. For aerodynamically smooth flow, z_0 is proportional to ν/u_*: for fully rough flows it is proportional to u_*^2/g. Thus, intuitively it seems there should be a region between the two regimes in which z_0 is constant or where it depends linearly on u_*. The fact that $(\nu/g^2)^{1/3}$

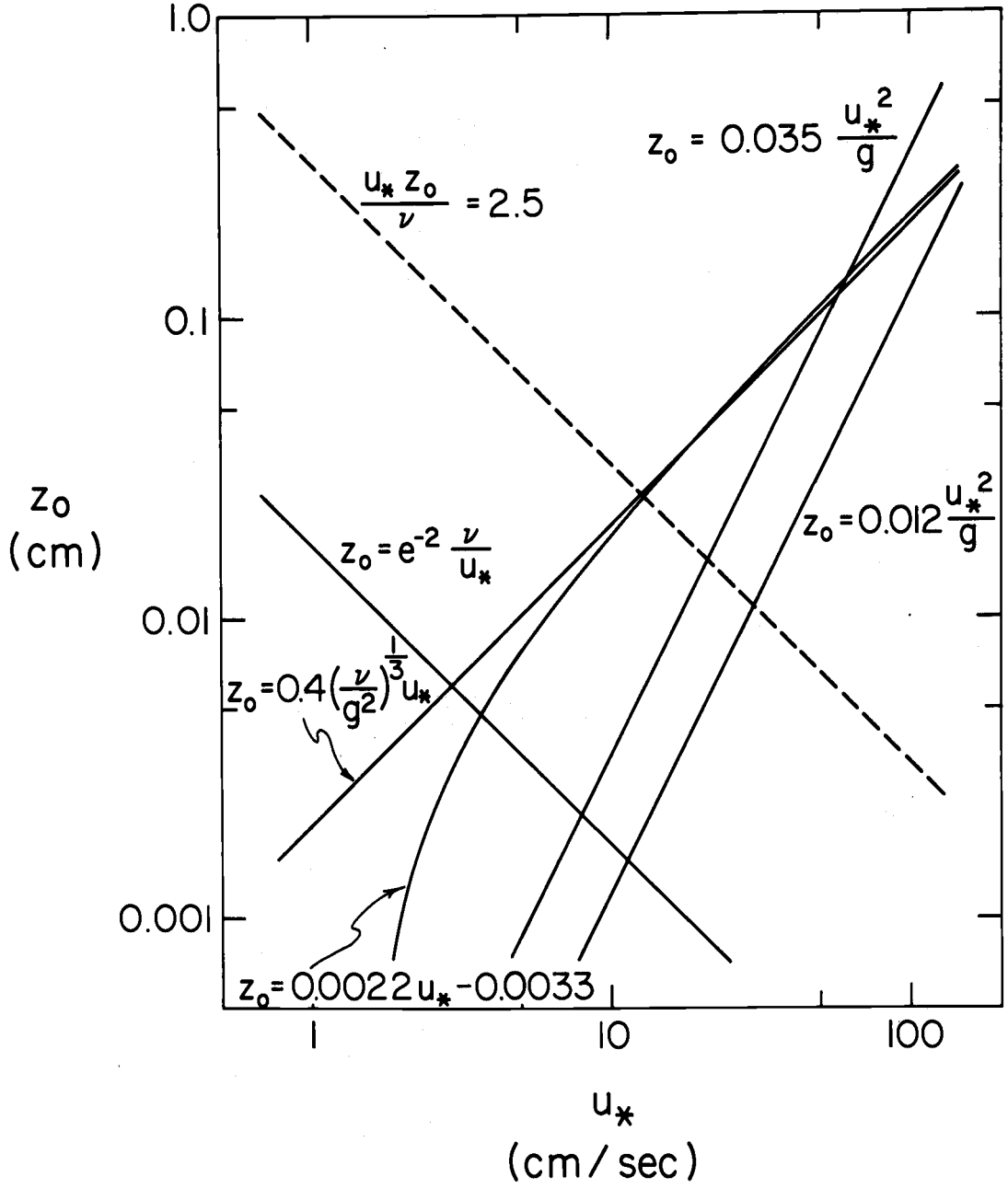

Figure 5.2. Various suggestions of the u_* dependence of z_0. $z_0 = e^{-2}\ \nu/u_*$ is also the boundary between smooth and transition regions. The dashed line separates transition and rough regions.

can give the linear dependence correct dimensions and the proper order of magnitude supports this contention.

The smooth flow parameterization implies that the surface presents no inherent roughness elements to the flow and, therefore, the molecular viscosity must dictate a length scale. On the other hand, Charnock's formulation is interpreted to mean that gravity waves determine the roughness length (Phillips, 1969). Wu (1968) suggests there might also then be a wind speed region in which capillary waves act as the roughness elements. For such flows the surface tension, σ, would be important in parameterizing z_0. Because air flows we observed were always fetch-limited, capillary waves, indeed, might be defining z_0. Therefore, we rewrite 5.2.16 in a form which contains σ as a parameter,

$$z_0 = 0.12 \left(\frac{\sigma}{\rho_w g^3}\right)^{\frac{1}{4}} u_* \quad . \qquad 5.2.17$$

Here ρ_w is the water density.

We conclude this section by emphasizing that relations 5.2.13, 5.2.16, and 5.2.17 are as yet strictly empirical results, though the parameters in 5.2.16 and 5.2.17 are physically suggestive. The parameter groupings have been examined under no other conditions than the ones described in this thesis; they may not prove universal when tested at other temperatures.

5.3. FLUX-GRADIENT RESULTS

A comparison of our flux-gradient estimates of heat and momentum fluxes with our other measurements makes the tedium of the last section satisfying.

In Figure 5.3 we have plotted the flux-gradient estimates of surface heat flux against the integral estimates of the same quantity. The results lie fairly uniformly about the 1:1 line. There does seem to be a systematic discrepancy at longer fetches; but the integral method is as likely at fault as the flux-gradient method. For the longer fetches upwind conditions were almost always stable. Matching a stable upwind temperature profile with the downwind profile was much trickier than matching an unstable one. And the fact that at longer fetches the thermal boundary layer is higher adds further uncertainty to the integral results. Therefore, we have no justification for attributing the scatter in Figure 5.3 solely to the flux-gradient technique. Rather, we are pleased how Figure 5.3 indicates that, on the average, flux-gradient and integral estimates would predict the same flux.

Figure 5.4 compares the flux-gradient estimate of u_* with our direct measurement of $(-\overline{uw})^{\frac{1}{2}}$. The two generally agree to within six percent though there is a systematic difference at higher u_*. We have never intended to imply that over a lead $(-\overline{uw})^{\frac{1}{2}}$ measured at a height of 20 cm should equal u_*. We do expect it to be within a few percent

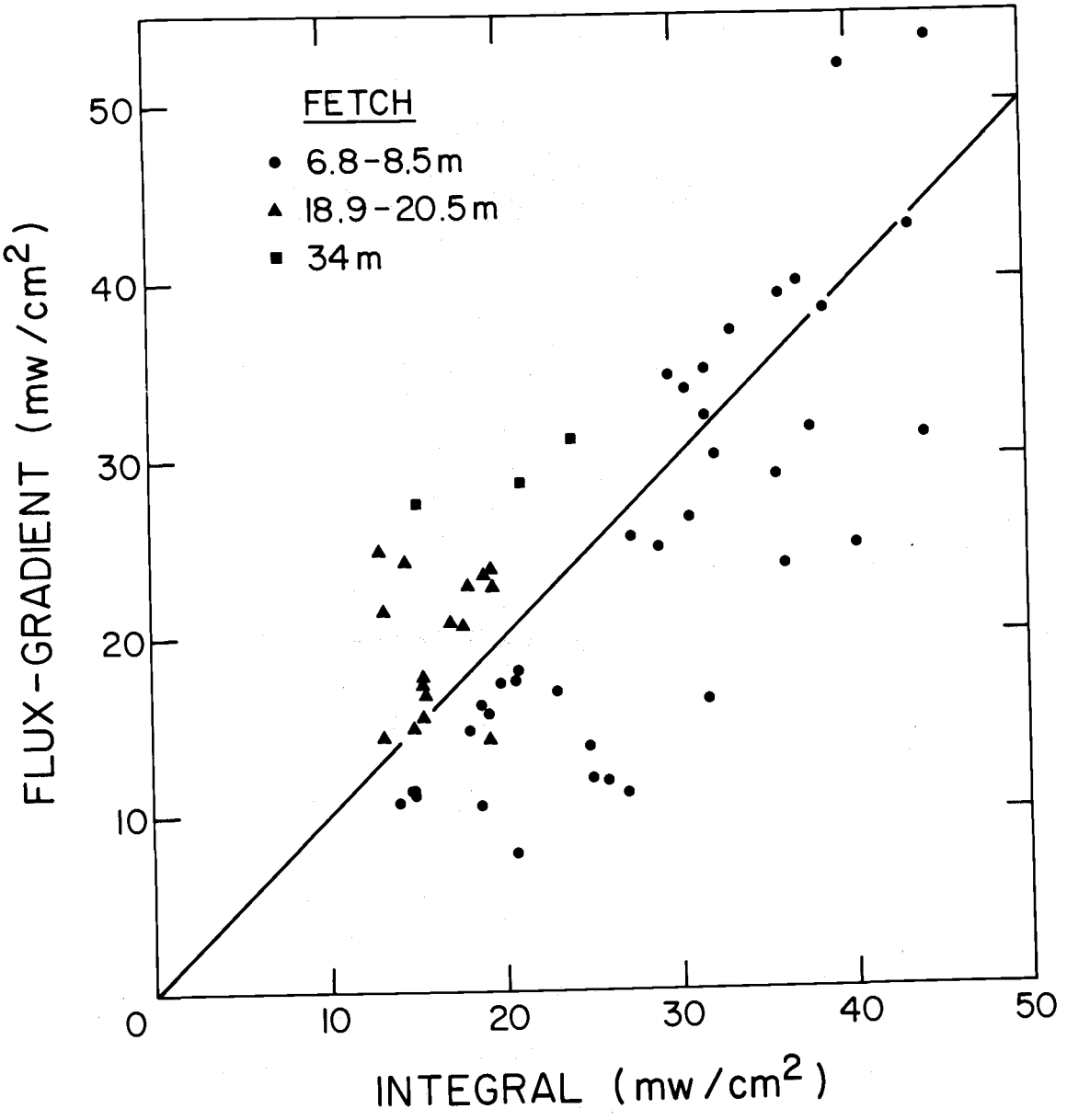

Figure 5.3. Heat flux comparison.

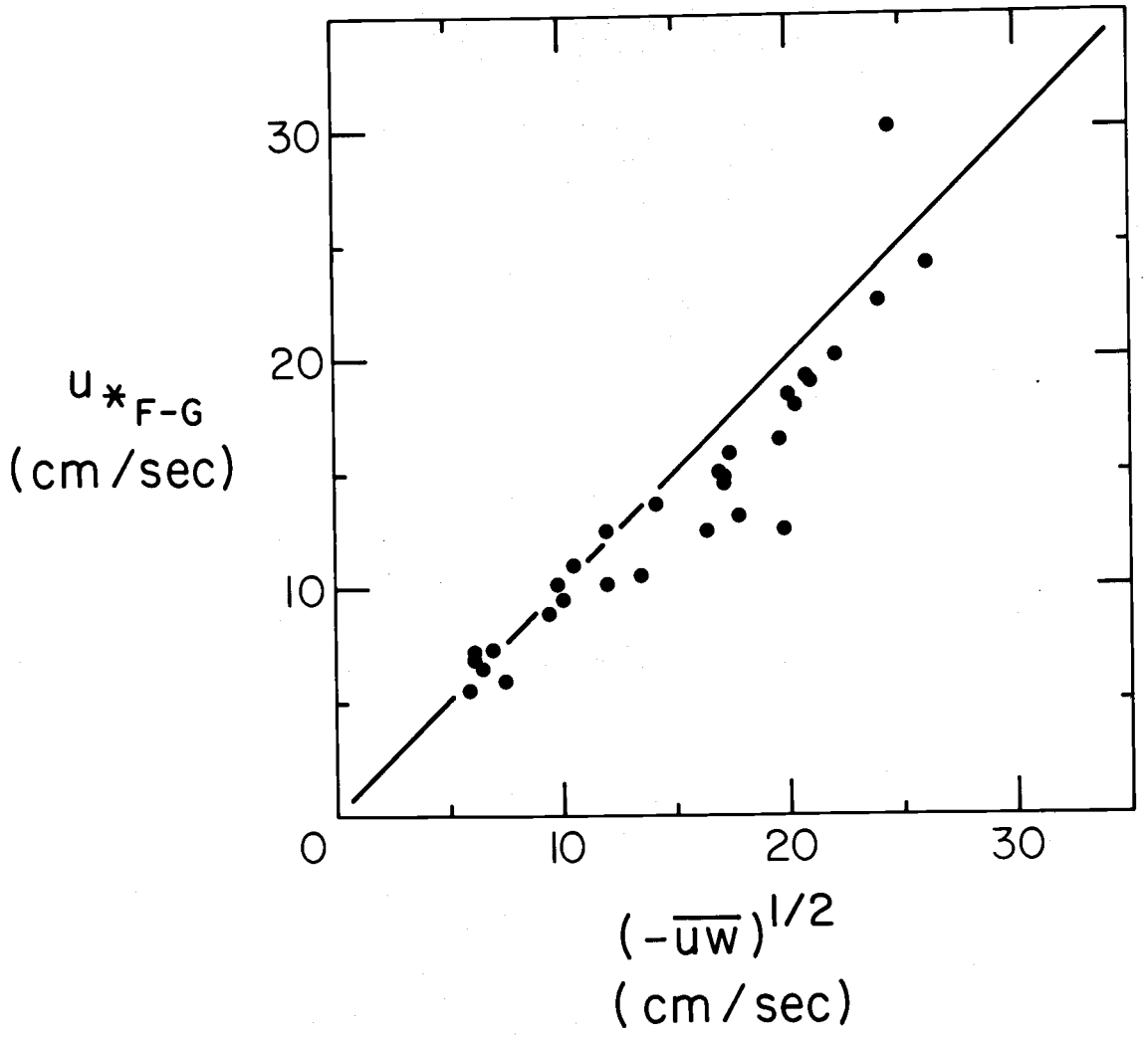

Figure 5.4. Flux-gradient estimate of u_* versus direct measurement of $\overline{uw}$.

though, since $-\overline{uw}$ was measured so near the surface. But our observations are not detailed enough to judge the effects of different fetches and wind speeds. Therefore, it's not clear where responsibility for the systematic differences in Figure 5.4 lies. $(-\overline{uw})^{\frac{1}{2}}$ might not necessarily be u_*; and u_{*F-G} might not be u_* either, because the appropriateness of the flux-gradient technique likely has a fetch dependence or, equivalently, a velocity dependence.

The Monin-Obukhov lengths, L, which are incidental in the flux-gradient estimation procedure, offer good insight into the very unstable character of the flow over the lead. The L's associated with our velocity and temperature profile pairs range from a minuscule -9.5 cm to a maximum value of -468 cm -- which is still small by normal standards. The combination of large water-air temperature differences and the light winds which prevailed during most of ALEX account for such small lengths.

Of course, an interpretation of the Monin-Obukhov length for our problem is not straightforward. The significance and worth of L in surface layer meteorology is a consequence of its being invariant with height through constant flux layers. However, the internal boundary layer is not a constant flux layer -- L may be a strong function of height. In other words, what we call L as yet has only the mathematical form of a Monin-Obukhov length and not the attendant physical interpretation; it remains

to be established whether this L has a meaning for processes other than those occurring near the surface.

In summary, the flux-gradient technique we have outlined in this chapter offers valuable support for our other estimates of heat and momentum fluxes from Arctic leads. Although the flux-gradient equations have proven validity only in horizontally homogeneous conditions where the fluxes are constant with height, we have used them here in an internal boundary layer with surprising success. Our precaution of selecting only the lowest two profile heights and assigning surface conditions to give three-point profiles apparently minimizes the effects of the non-equilibrium character of the flow.

6. PREDICTIVE SCHEMES

> We can be absolutely certain only about things we do not understand.
>
> Eric Hoffer
> The True Believer

6.1. A SIMPLE, ILLUSTRATIVE MODEL

To introduce a few of the nondimensional parameters which will be used in this chapter for characterizing the heat flux from leads, let us consider a very rudimentary model of the growth of the thermal boundary layer. We make no pretense that this model is a realistic picture of nature. Rather its recommendations are that it contains an essence of the physics, is mathematically trivial, yet yields the very parameters which we will later use to predict heat flux.

Consider a volume of Arctic air of height h, length L, and width Δy moving along the surface of the ice with velocity U in the x direction. The temperature of the ice and the air is T_i. At x=0 this mass encounters a lead of infinite extent in y and with surface heat flux H (per unit area) and water temperature T_w. Because the air parcel is heated as it flows over the warm lead, it expands upward and in the x direction: the flow is two-dimensional, so its width does not change. Assume the air continues moving with velocity U. Let's look at the situation just as the back end of the volume reaches the front edge of the lead.

Suppose the air mass now has a height δ, the height of the thermal boundary layer, and a length F. Figure 6.1 shows the details of the model.

The first law of thermodynamics requires that the change in internal energy of the air parcel, ΔE, be equal to the heat added, Q, minus the work the parcel does in expanding, ΔW,

$$\Delta E = Q - \Delta W \ . \qquad 6.1.1$$

By definition

$$\Delta E = M \, c_p \, \Delta T \ , \qquad 6.1.2$$

where M is the mass of the volume and ΔT is its temperature change. Notice

$$M = \rho V \ , \qquad 6.1.3$$

if V is the volume.

Because the work of expansion is done at constant pressure, p,

$$\Delta W = p \, \Delta V \ , \qquad 6.1.4$$

where ΔV is the volume change. But from the ideal gas law

$$\frac{V_1}{V_2} = \frac{T_1}{T_2} \qquad 6.1.5$$

-- the initial and final volumes and temperature. Hence,

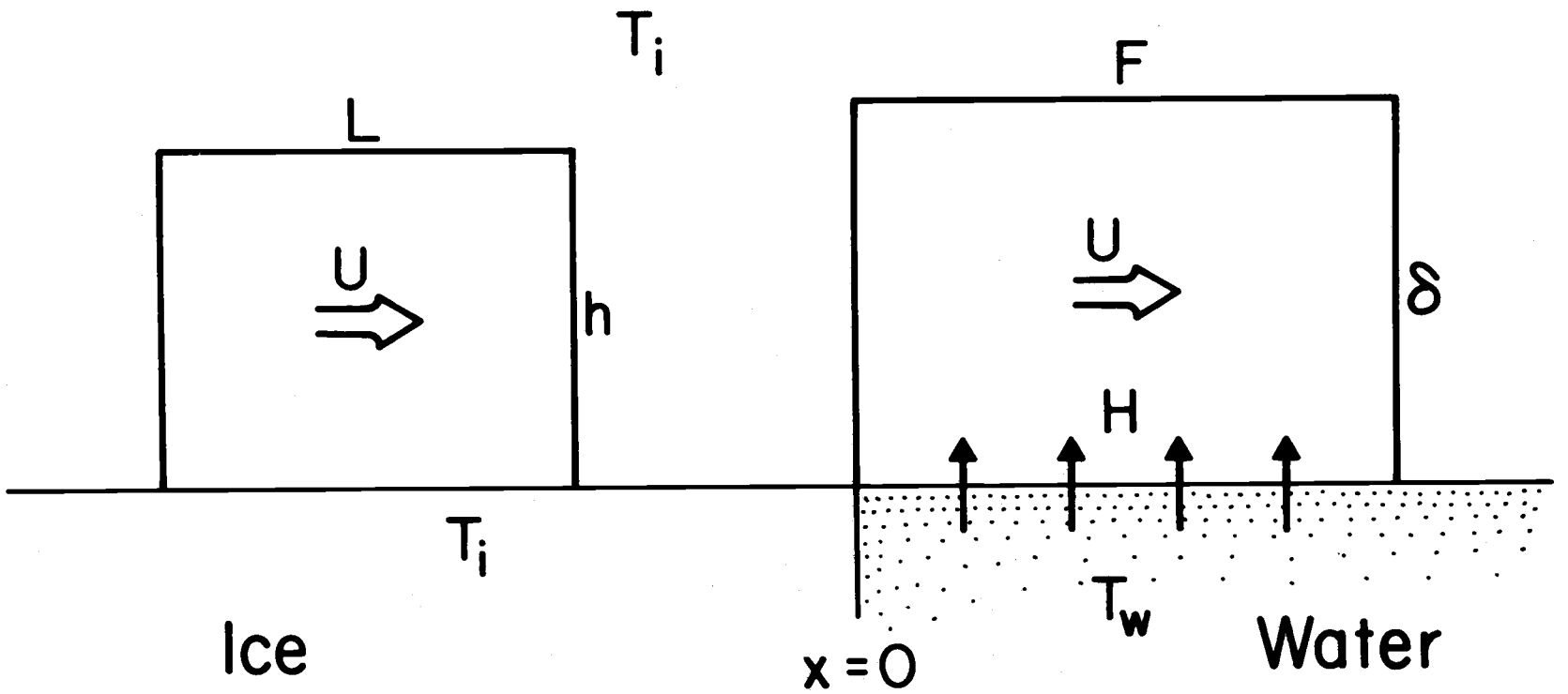

Figure 6.1. A simple model of boundary layer growth.

$$\Delta V = V_2 - V_1 = V_2\left(\frac{T_2 - T_1}{T_2}\right) \quad . \qquad 6.1.6$$

In our model T_1 is T_i. Let's say

$$T_2 = \tfrac{1}{2}(T_w + T_i). \qquad 6.1.7$$

Thus, from 6.1.2 and 6.1.3

$$\Delta E = \tfrac{1}{2}\,\rho\, c_p (T_w - T_i)\,\delta\, F\, \Delta y \quad . \qquad 6.1.8$$

And from 6.1.6

$$\Delta V = \frac{T_w - T_i}{T_w + T_i}\,\delta\, F\, \Delta y \quad . \qquad 6.1.9$$

One form of the equation of state for an ideal gas is (Lumley and Panofsky, 1964)

$$p = \rho \frac{G}{m} T \quad , \qquad 6.1.10$$

where G is the universal gas constant and m is the molecular weight of the gas. However, we prefer to write (Halliday and Resnick, 1966, page 586)

$$\frac{G}{m} \approx \frac{2}{5} c_p \quad ; \qquad 6.1.11$$

so for our model

$$p = \frac{1}{5}\,\rho\, c_p (T_w + T_i) \quad . \qquad 6.1.12$$

Finally, we evaluate Q, which is simply the total heat added to the air volume as it moves over the lead. The time required for the mass to flow out entirely over the lead is

$$t' = \frac{F}{U} . \qquad 6.1.13$$

Therefore,

$$Q = \int_0^{t'} H\ \Delta y\ x\ dt$$

$$= \Delta y\ H \int_0^{t'} Ut\ dt$$

$$= \tfrac{1}{2}\ \Delta y\ H\ U\ t'^2$$

$$Q = \tfrac{1}{2}\ \Delta y\ H\ \frac{F^2}{U} . \qquad 6.1.14$$

Now we can bring everything together as 6.1.1 requires. From 6.1.8, 6.1.9, 6.1.12 and 6.1.14 we get

$$\tfrac{1}{2}\ \rho\ c_p(T_w-T_i)\ \delta\ F\ \Delta y = \tfrac{1}{2}\ H\ \frac{F^2}{U}\ \Delta y - \frac{1}{5}\ \rho\ c_p(T_w-T_i)\ \delta\ F\ \Delta y , \qquad 6.1.15$$

or

$$\frac{7}{5}\ \rho\ c_p(T_w - T_i)\ \delta = \frac{HF}{U} . \qquad 6.1.16$$

Rearranging 6.1.16, we derive our first nondimensional parameter of heat transfer, the Stanton number,

$$St \equiv \frac{H}{\rho\ c_p(T_w-T_i)\ U} = \frac{7}{5}\ \frac{\delta}{F} . \qquad 6.1.17$$

The term on the right side is also of some interest -- it contains the ratio of IBL height to fetch. Using the identity

$$\frac{\kappa}{\rho\, c_p} = D \ , \qquad 6.1.18$$

where κ is the thermal conductivity and D is again the thermal diffusivity, 6.1.17 becomes

$$N \equiv \frac{HF}{\kappa(T_w - T_i)} = \frac{7}{5}\left(\frac{\delta}{F}\right) R_x\, P \ . \qquad 6.1.19$$

The Nusselt number, N, is a second important dimensionless parameter of heat transfer. Equation 6.1.19 relates it to the length (fetch) Reynolds number,

$$R_x = \frac{UF}{\nu} \ , \qquad 6.1.20$$

and the Prandtl number,

$$P = \frac{\nu}{D} \ . \qquad 6.1.21$$

Notice that using 6.1.17 in 6.1.19 gives us a last relation -- which is true by definition, not just for this problem:

$$N = St\, R_x\, P \ . \qquad 6.1.22$$

Hopefully, after this brief introduction to the dimensionless groups which are most often used in heat transfer studies, the next sections will go more easily.

Though we do not expect our simple model to have any predictive value, the suggestion how to proceed is there.

6.2. SENSIBLE HEAT FLUX: INTEGRAL RESULTS

Because the integral method of heat flux estimation is the more basic approach, whenever we write 'heat flux' in this section, it will be an estimate made by that method. The flux-gradient technique would probably yield estimates easier to fit with bulk models because of the smoothing inherent in the process. But that technique is still not totally proven in our application; so we'll concentrate our analysis on the more physically founded estimates of the integral method.

The bulk parameters used in defining the Nusselt, Stanton, and length Reynolds numbers of the last section will now have to be carefully assigned values. After a lot of experimentation we choose to write

$$R_x = \frac{U_{0.5}\, x}{\nu} \qquad 6.2.1$$

$$N = \frac{H\, x}{\kappa(T_w - T_{0.5})} \qquad 6.2.2$$

$$St = \frac{H}{\rho\, c_p\, U_{0.5}(T_w - T_{0.5})} \qquad 6.2.3$$

In these, x is the fetch, T_w is the surface water temperature, and $U_{0.5}$ and $T_{0.5}$ are the velocity and temperature, respectively, 50 cm above the lead at the fetch x. H is

the average surface heat flux (equation 4.1.29); so Hx is the total heat flux (equation 4.1.27). The remaining quantities, ν, κ, ρ, and c_p, are all temperature dependent: we evaluate them at T_w.

The only debatable parameter choices here are $U_{0.5}$ and $T_{0.5}$. We have discussed earlier the complex shape of the velocity profile over the lead. Within the boundary layer that profile is a function of the surface roughness transition, the heat flux, and the fetch, and above the boundary layer is prescribed by the upwind stability. Consequently, the specification of a reference height is critical. There is no externally imposed 10 meter (bridge of the ship) reference -- which would be of questionable value anyway, likely being above the IBL and, thus, necessitating an accounting for upwind stability. Therefore, we are free to select a velocity reference height within the boundary layer where the complicating effects on the profile will be minimal. In Chapter 5 we demonstrated that 50 cm was such a height.

Why not then also measure the temperature at that height? One might argue that the ambient air temperature would be a better choice. But this isn't a wind tunnel -- upwind stabilities are variable, so the upwind temperature is a function of height. Clearly, then the only logical upwind reference temperature is $T_i(0)$, the temperature of the ice. And, in fact, this is not a bad choice in place

of $T_{0.5}$. However, with $T_i(0)$ instead of $T_{0.5}$, the results we will discuss would have been more scattered because of the variety in upwind stability and the uncertainty of our $T_i(0)$ measurements.

Figure 6.2 presents our first relation between the sensible heat flux from leads and bulk quantities. The line is

$$N = 0.18\ R_x^{0.71} \quad . \qquad 6.2.4$$

This is in good agreement with wind tunnel results reported by Coantic and Favre (1974) for latent heat fluxes,

$$N_L = 0.08\ R_x^{0.75} \quad . \qquad 6.2.5$$

Because of the different ways in which the bulk parameters were selected, we would not expect the multiplicative constants in 6.2.4 and 6.2.5 to agree; the exponents on R_x, however, are in happy accord.

Kays (1966, page 239) presents a theoretical result with which we might also compare 6.2.4. He looks at a flow encountering a constant-temperature, flat plate and predicts

$$St\ P^{0.4} = 0.0295\ R_x^{-0.2} \quad . \qquad 6.2.6$$

Using 6.1.22, we rewrite 6.2.4 as

$$St\ P\ R_x = 0.18\ R^{0.71} \quad , \qquad 6.2.7$$

or

$$St = 0.18\ P^{-1}\ R_x^{-0.29} \quad . \qquad 6.2.8$$

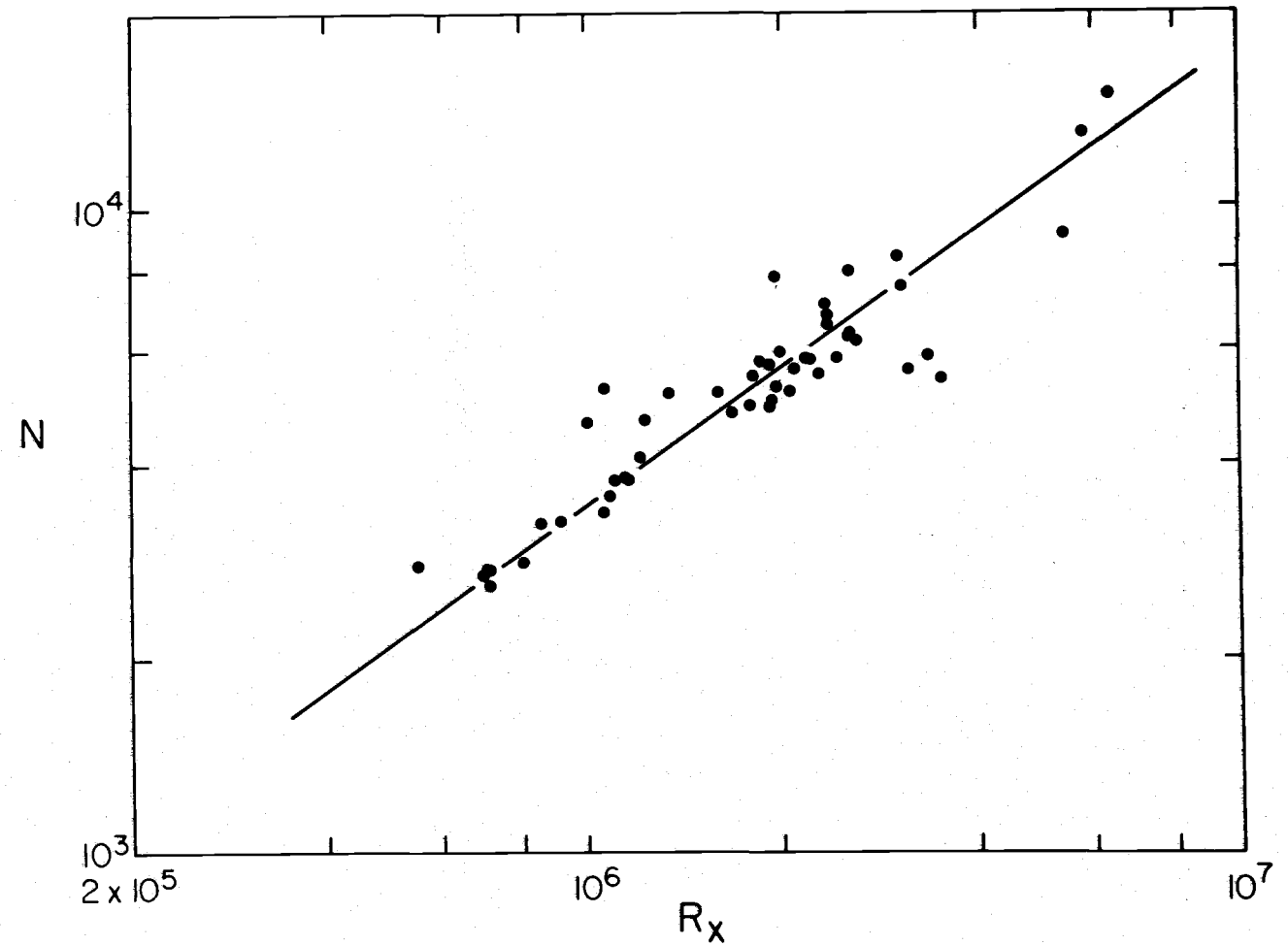

Figure 6.2. The Nusselt number correlated with fetch Reynolds number. The line is equation 6.2.4.

With a value for the Prandtl number of 0.714, this becomes

$$St = 0.204\ R_x^{-0.29} , \qquad 6.2.9$$

while the theoretical result, equation 6.2.6, is

$$St = 0.0338\ R_x^{-0.2} . \qquad 6.2.10$$

This isn't superb agreement and is a first indication of the difficulty we will have in this section correlating the Stanton number with the length Reynolds number.

Since log-log plots tend to make even scattered data look good, Figure 6.3 shows a linear plot of N versus R. Again the result is useful as the data gather around the line

$$N = 2.24 \times 10^{-3}\ R_x + 1120 . \qquad 6.2.11$$

Compare 6.2.11 with Schlichting's (1968, page 662) theoretical prediction for transfer from a heated, flat plate,

$$N = C_\infty\ R_x . \qquad 6.2.12$$

To get 6.2.12 he set the Prandtl number equal to one and based the drag coefficient, C_∞, on the free stream velocity. Our Prandtl number, 0.71, is near enough to one to justify continuing the comparison. In equation 5.2.7 we showed that the empirical drag relation, 5.2.5, corresponds

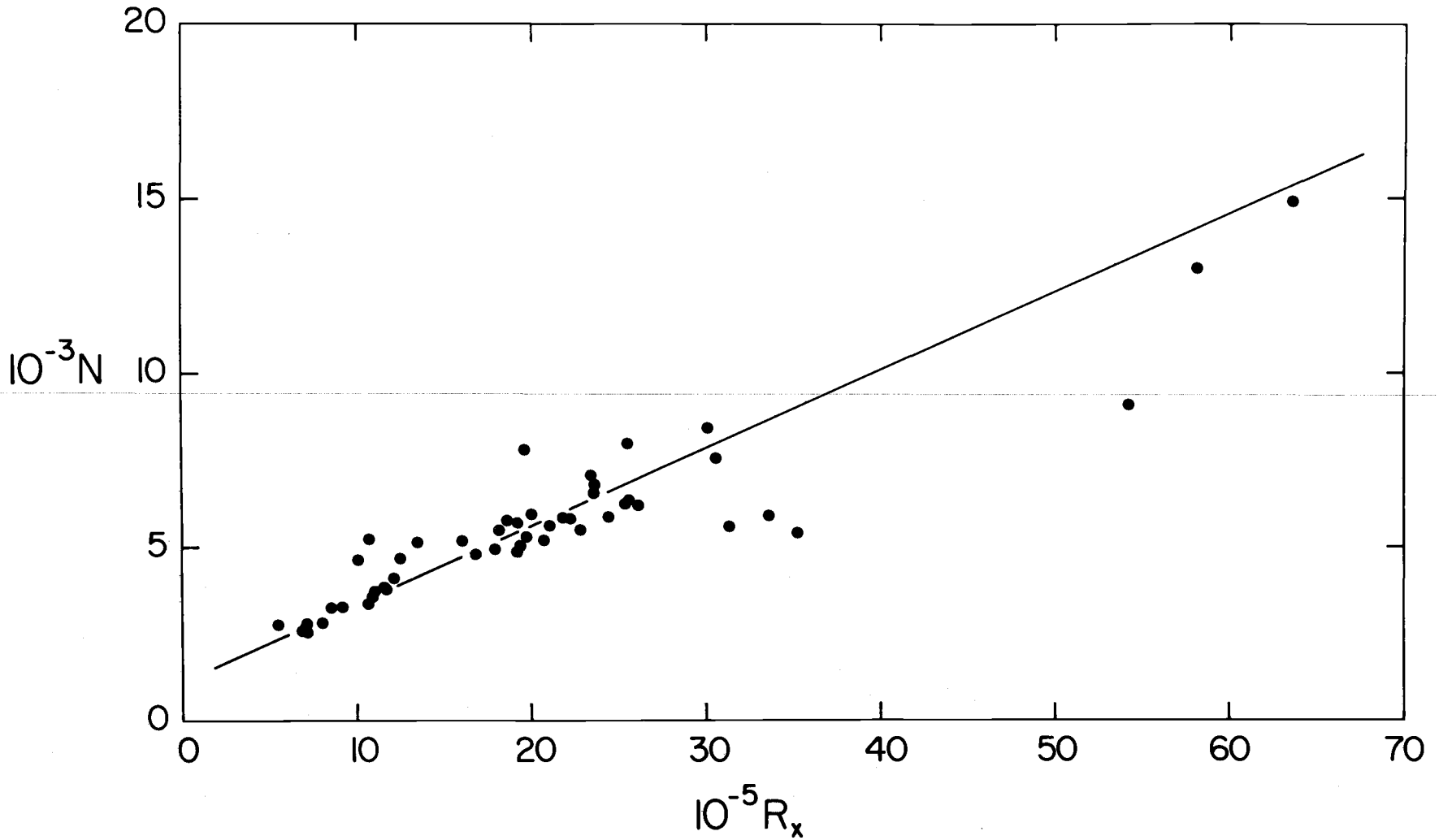

Figure 6.3. The Nusselt number and the length Reynolds number linearly correlated. The line is equation 6.2.11.

to a 10 meter drag coefficient of 1.76×10^{-3}. If we use this as the free stream drag coefficient, Schlichting's result applied to our problem predicts

$$N = 1.76 \times 10^{-3} R_x \quad . \qquad 6.2.13$$

Considering the approximations involved and the fact that the C_{10} calculated in 5.2.7 does not reflect the non-zero intercept of 5.2.5 (which is likely associated with the additive constant in 6.2.11), this theoretical result is remarkably close to our observational relation, 6.2.11. That linear equation between N and R is apparently a good one.

In an effort to provide a little something for everyone, we lastly show a plot of the Stanton number versus R_x in Figure 6.4. As hinted before, the correlation is not exceptional. The line we have drawn through the data is

$$St = 0.56 R_x^{-0.35} \quad . \qquad 6.2.14$$

Again check this against the Kays (1966) relation of equation 6.2.10. Mangarella, Chambers, Street, and Hsu (1971, 1972, 1973) are also fond of the Stanton number. Though they relate it to a Reynolds number defined differently than R_x, we infer from their work that the Stanton number is proportional to (roughly) $R_x^{-0.25}$ (Mangarella, et al., 1973). This is closer to Kay's theoretical prediction (equation 6.2.10) than to our result, 6.2.14.

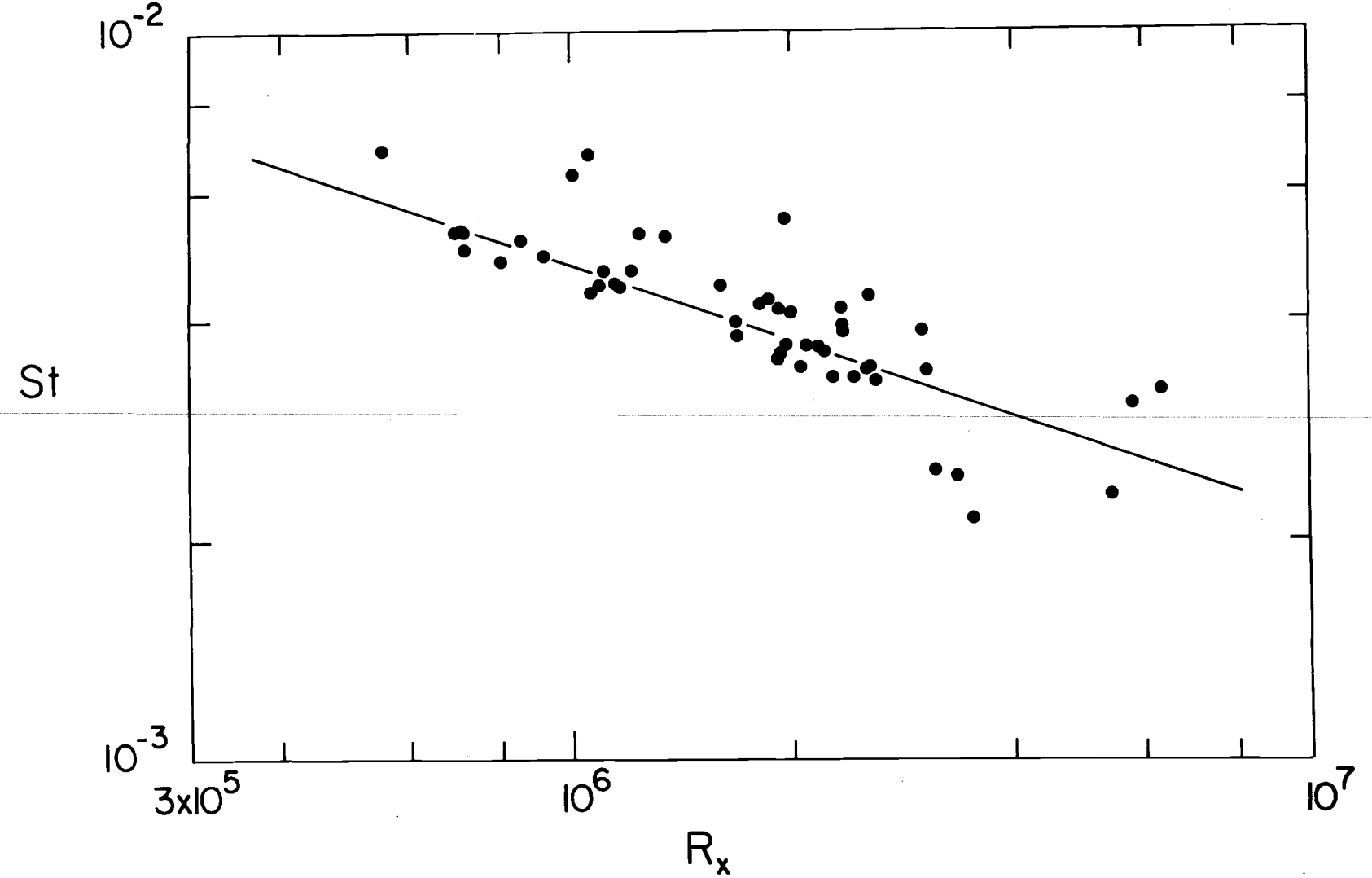

Figure 6.4. The Stanton number correlated with fetch Reynolds number. The line is equation 6.2.14.

However, let us also compare this $R_x^{-0.25}$ dependence with the Stanton number relation we deduced from our Nusselt number correlation (equation 6.2.9). The Reynolds number term here, $R_x^{-0.29}$, agrees well with the suggested $R_x^{-0.25}$ dependence of Mangarella, Chambers, Street, and Hsu. And the Coantic-Favre result (equation 6.2.5) also implies St is proportional to $R_x^{-0.25}$ (using 6.1.22 to convert N to St). The experimental evidence, thus, suggests that the exponent of R_x in the theoretical result 6.2.10 is too large; instead a correlation of St with $R_x^{-0.25}$ seems more realistic.

Despite the apparent popularity of the Stanton number, our data correlate best when the heat flux is non-dimensionalized in the form of a Nusselt number. This is likely a consequence of how the wind speed enters the non-dimensionalization. The Stanton number contains $U_{0.5}$ while the Nusselt number does not. Thus, because the $U_{0.5}$ and $T_w-T_{0.5}$ values have the largest relative uncertainty of the bulk quantities, St will be more scattered than N.

Hopefully, the equations we have presented in this section make the procedure for predicting sensible heat fluxes from leads obvious. Equations 6.2.4, 6.2.11, and 6.2.14 relate the surface heat flux to certain bulk parameters. Hence, measuring the bulk parameters is sufficient to allow a prediction of the sensible heat flux.

6.3. SENSIBLE HEAT FLUX: FLUX-GRADIENT RESULTS

Since we have made flux-gradient estimates of the heat flux, it's interesting to also devise a procedure for predicting the flux on the basis of these. Remember, the flux-gradient surface heat flux is

$$H = -\rho c_p k u_* t_* . \qquad 6.3.1$$

Equation 5.2.5 already relates u_* to a bulk variable.

In Figure 6.5 we likewise estimate t_* from bulk quantities. The line is

$$t_* = 0.195(T_{0.5} - T_w) + 0.475 . \qquad 6.3.2$$

Recalling our flux-gradient method, the correlation in Figure 6.5 is not that surprising. Because z_H was constant at 0.03 cm, equation 5.1.7 says

$$T_w - T_{0.5} = -t_*[\ln(\frac{50}{0.03}) - \psi_h(\frac{50}{L})] . \qquad 6.3.3$$

Hence, though stability effects introduce a modicum of scatter, t_* should be a nearly linear function of $T_w - T_{0.5}$.

The quick result of this section is that on the basis of 5.2.5 and 6.3.2 it is again possible to predict the sensible heat flux from bulk measurements.

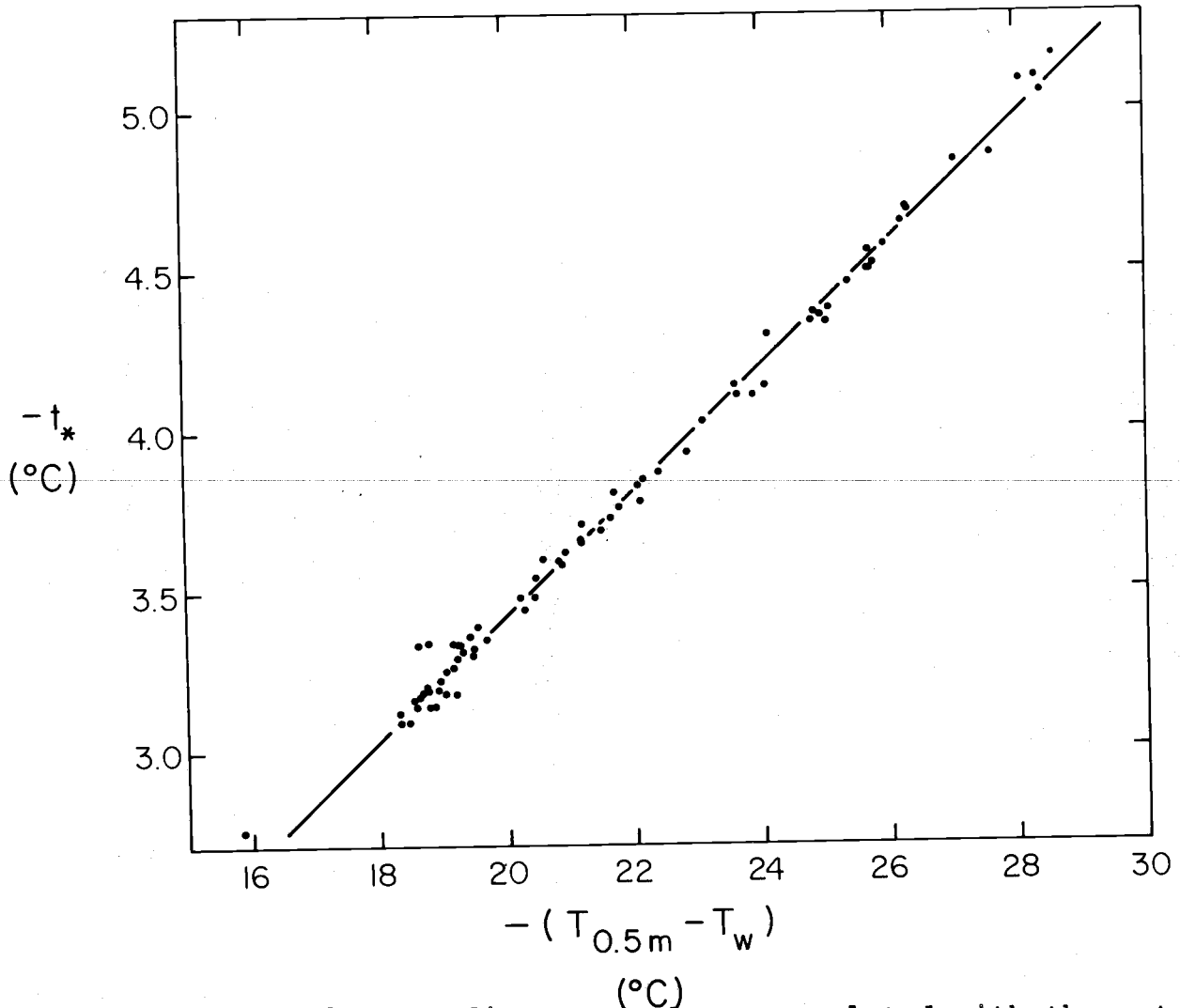

Figure 6.5. t_* from the flux-gradient procedure correlated with the water-air temperature difference. The line is equation 6.3.2.

6.4. LATENT HEAT FLUX

We do not have enough quality data to formulate an empirical relation for latent heat flux as we have for sensible heat flux. But consider. The diffusion equations of temperature and humidity are the same; so there is a similarity between the turbulent transfer mechanisms for heat and moisture (Brutsaert, 1975). Over water, the spectra of temperature and humidity are alike (Phelps and Pond, 1971). In laboratory experiments over water when waves are not breaking and, consequently, generating vapor mechanically, Stanton numbers for latent and sensible heat fluxes are nearly the same (Mangarella, et al., 1973). And lastly, the Coantic-Favre result (equation 6.2.5) for latent heat is much like our relation for sensible heat (equation 6.2.4). The implications are that if we know how to estimate the sensible heat flux, H, we also know how to estimate the latent heat flux, H_L.

From 6.2.4 we simply say

$$N_L = 0.18\ R_x^{0.71}\ , \qquad 6.4.1$$

where N_L is the Nusselt number associated with the latent heat flux: that is,

$$N_L = \frac{H_L\ x}{\rho\ L_v D_w (Q_w - Q_{0.5})}\ . \qquad 6.4.2$$

In this, D_w is the molecular diffusivity of water vapor

at the surface temperature, Q_w is the specific humidity at the water surface, and $Q_{0.5}$ is the humidity at 50 cm. From 6.1.18, 6.2.2, and 6.4.2 we write

$$\frac{H_L\ x}{\rho\ L_v D_w (Q_w - Q_{0.5})} = \frac{H\ x}{\rho\ c_p D (T_w - T_{0.5})} \quad , \qquad 6.4.3$$

or

$$H_L = H\ \frac{L_v D_w (Q_w - Q_{0.5})}{c_p D (T_w - T_{0.5})} \quad . \qquad 6.4.4$$

There is nothing terrifically profound in this result. We have simply given the Bowen ratio,

$$B = \frac{c_p D (T_w - T_{0.5})}{L_v D_w (Q_w - Q_{0.5})} \quad , \qquad 6.4.5$$

a mathematical form. Had we chosen to equate Stanton numbers instead of Nusselt numbers, B would have been essentially the ratio derived by Roll (1965, page 253) for more restrictive conditions.

Table 6.1 compares the values of H_L predicted on the basis of 6.4.4 with our integral estimates of it. Despite the low quality of our humidity profiles, the agreement is encouraging. Notice that the Bowen ratio over leads is an order of magnitude larger than usual values for the open ocean.

Because the specific humidity is closely tied to the temperature and because in the Arctic $Q_{0.5}$ is typically

Table 6.1. Prediction of the latent heat flux from the sensible heat flux using equation 6.4.4.

RUN	H (mw/cm^2)	H_L (mw/cm^2)		B
		Predicted	Measured	
272.0	15.42	4.98	3.25	3.10
273.1	15.32	4.92	3.13	3.12
273.2	15.49	5.10	2.84	3.04
282.0	13.04	5.93	7.06	2.20
283.0	13.17	5.95	7.08	2.22

10% of Q_w, we can use 6.4.4 to estimate H_L for all the profiling runs although there are humidity values for only five of them. We simply assume the relative humidity at 50 cm is 100%. Q_w is usually about 3.10 gm/kg; but at -25°C and 100% relative humidity, $Q_{0.5}$ is 0.50 gm/kg; at 50% relative humidity it is 0.25 gm/kg. Therefore, any error introduced by this assumption of saturation at 50 cm should be under 10%. The results of these latent heat flux calculations are tabulated in Appendix C.

6.5. MOMENTUM FLUX

Equation 5.2.5 is essentially our method for estimating the surface momentum flux (stress). Because it requires $U_{0.5}$ be measured 50 cm from the surface, it should approximate u_* to within five percent despite the complications the large surface heat flux introduces (cf. Bradley, 1972).

Our flux tower was equipped to make direct measurements of $\overline{uw}$ at two levels separated by 50 cm so we could see how the stress profile changed with height. Spectral analysis was used to deduce $\overline{uw}$ from the lower measurements -- the Nyquist frequency was 125 Hz. All upper level flux tower values are the results of straightforward correlation calculations: for example,

$$\overline{uw} = \frac{1}{N} \sum_{j=1}^{N} (U_j - U)(W_j - W) \quad . \qquad 6.5.1$$

Here, clearly, U and W are the average longitudinal and vertical velocities and U_j and W_j are the individual observations. The sampling rate for the data which went into these calculations was 5 Hz. Hence, the upper $\overline{uw}$ value is not as statistically certain as the lower one: nevertheless, a comparison of the $\overline{uw}$ values at the two heights makes an unambiguous statement about the shape of the stress profile.

We have 32 pairs of lower and upper $\overline{uw}$ measurements. Nineteen of these are made over leads of short fetch -- 7.2 to 8.5 meters. Thirteen pairs are from leads with longer fetches -- five from a thirty-four meter lead and the remaining eight in the 19.0 to 19.8 meter range. Over the 34 m lead the lower $\overline{uw}$ measurement was made at 50 cm. For virtually all the remaining runs it was within 20 cm of the surface. In 15 of the 19 $\overline{uw}$ pairs at short fetch, the lower $-\overline{uw}$ value is greater than the upper $-\overline{uw}$ value. On the other hand, for <u>all</u> 13 of the $\overline{uw}$ pairs at longer fetch, the upper $-\overline{uw}$ is larger than the lower one. Table 6.2 summarizes what we have just written.

This kind of stress profile behavior is just what Taylor's (1970) and Shreffler's (1975) numerical models have predicted. Figure 6.6, taken from Shreffler's (1975) thesis, shows the stress profiles his model generated on

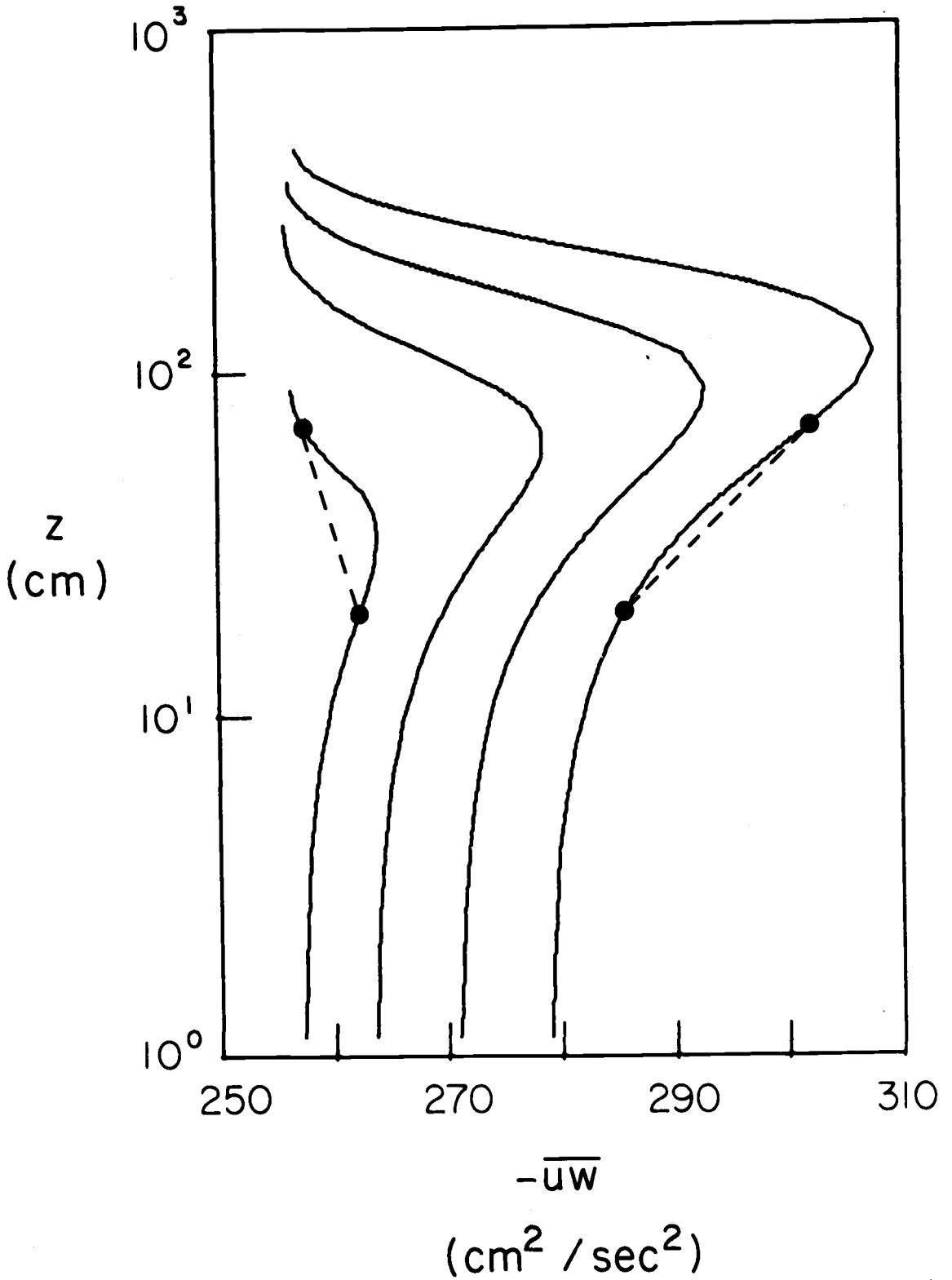

Figure 6.6. Stress profiles predicted by Shreffler (1975) from Badgley's (1966) lead data. The fetches are, from left to right, 5, 10, 15 and 20 m. The dashed lines interpret our observations.

Table 6.2. Comparison of lower and upper $-\overline{uw}$ measurements.

Fetch (m)	7.2 - 8.5	19.0 - 34
Pairs	19	13
Lower > Upper	15	0
Lower < Upper	4	13

the basis of Badgley's (1966) Arctic lead velocity and temperature data. On it we have tried to suggest our observed $\overline{uw}$ relationships at short and long fetches.

Because Shreffler's prediction is for only one unique set of environmental conditions, we cannot make an extensive quantitative comparison of our observations with his model. However, for a couple of our runs the surface heat flux and surface stress were near those he modeled. A comparison of these few sets with the profiles in Figure 6.6 suggests Shreffler's model underestimates the $\overline{uw}_{hi}/\overline{uw}_{lo}$ ratio at longer fetches. For example, at a fetch of 20 m, if $-\overline{uw}_{lo}$ is measured at 20 cm and $-\overline{uw}_{hi}$ at 70 cm, the model yields

$$\frac{\overline{uw}_{hi}}{\overline{uw}_{lo}} = 1.06 \ . \qquad 6.5.2$$

In contrast, our observations would suggest the ratio is more like 1.4, a value closer to what Taylor (1970) predicts.

The question must eventually arise, "Why does the stress profile have the shape it does?" Look at the U momentum equation,

$$U\,\partial_x U + W\,\partial_z U = \partial_z\,(-\overline{uw})\ . \qquad 6.5.3$$

This dictates how the stress profile depends on the velocities. And we have a good qualitative idea of the velocity profiles over the lead.

In Chapter 4 we explained that if the flow felt only a smooth to rough surface transition, it would decelerate. Both Shreffler (1975) and Taylor (1970) show the flow accelerating near the surface when it encounters an increase in surface temperature but no roughness change. Thus, close to the surface the superposition of the two effects makes things confusing. Higher up, the flow will indeed accelerate as the positive heat flux fosters mechanical mixing which ultimately increases the average horizontal velocity. Here W must be negative to preserve continuity. Near the top of the boundary layer U returns to its upwind value, so $\partial_x U$ becomes vanishingly small; W remains negative but small.

Understanding this, we examine 6.5.3. Near the surface the first term on the left dominates; so $-\overline{uw}$ will increase with height if the heat flux influences the flow

more than the roughness transition or will decrease with height if the opposite is true. Slightly higher, the first term is definitely positive: $-\overline{uw}$ must increase with height. Throughout the layer the second term on the left is non-positive but small because of its W dependence; the first term, thus, continues to force a $-\overline{uw}$ increase with height. Finally, near the top of the layer, $\partial_x U$, becomes so small that the second term on the left (which is negative) becomes dominant: $-\overline{uw}$, therefore, decreases to its upwind value. The stress profile is thus buxom.

6.6. THERMAL BOUNDARY LAYER HEIGHT

A discussion of the thermal boundary layer height, δ, necessitates an unequivocal definition of it. Thermal and momentum boundary layers are regions of disturbed temperature and velocity profiles. But fundamentally, it is the altered heat and momentum fluxes within the layers that support the profiles -- they are really the truer representatives of the boundary layer. Ideally then, the thermal or momentum boundary layer height should be defined as the point where the heat or momentum flux within the layer returns to its upwind value. But clearly, a determination of δ on this basis is prohibitive except for well-instrumented, unhurried operations. Therefore, most still traditionally rely on the more available temperature or velocity profiles for getting δ.

We have adopted the standard procedure for defining δ. It is the height at which

$$0.0005 \geq \frac{T(\delta) - T_i(\delta)}{T_w - T_i(0)} \quad . \qquad 6.6.1$$

Here $T(\delta)$ is the IBL temperature at δ; $T_i(\delta)$, the upwind temperature at δ; and T_w and $T_i(0)$, the water and ice temperature, respectively. Because in the Arctic $T_w - T_i(0)$ was always roughly 20°C, equation 6.6.1 is approximately

$$0.01 \geq T(\delta) - T_i(\delta) \quad , \qquad 6.6.2$$

which is consistent with the limits we ascribe to our thermocouples.

As an alternative to this profile method and to the aforementioned flux method, C. A. Paulson (personal communication) has suggested the possibility of defining the thermal boundary layer height on the basis of signal variance. Rather than the well defined, steady-state, easily knowable line we have been portraying it as, the top of the thermal boundary layer is a billowing, oscillating thing which summits to definition only in the statistical sense. That is, a fixed height may sometimes be within the layer and at other times outside. There is, in other words, an intermittency in temperature observations near the top of the layer. See, for example, the temperature traces in Figure 2.4. By examining temperature records

with regard to this intermittency it seems possible to derive a boundary layer height with more statistical significance than the δ based on 6.6.1. Though the analysis this method would entail is beyond our scope, the idea is good and may be of use to others.

Elliott's (1958) paper, which was the herald of American internal boundary layer research, contains equations for predicting the heights of both internal momentum and thermal boundary layers. Apparently, only Miyake (1965) has offered alternatives to these. But he finds neither the relation he suggests nor Elliott's equation consistently predicts the thermal boundary heights he observed -- though the essentials of Elliott's momentum height prediction have been verified elsewhere (e.g., Bradley, 1968; Panofsky and Petersen, 1972). Therefore, we attempt to deduce from our data an expression for calculating the thermal boundary layer height.

Because Elliott's (1958) thermal boundary height relation is so attractively simple, we consider it a starting point. He writes

$$\frac{\delta}{z_0} = 0.35\left(\frac{x}{z_0}\right)^{0.8} , \qquad 6.6.3$$

where x is the fetch over the warmer (or colder) surface. But we realize on contemplating our temperature profiles that this is too simple. There must be a wind speed

dependence stronger than that contained in z_0; higher speeds stretch the layer downwind rather than letting it grow upward. Conversely, a large surface heat flux promotes vertical growth. These two considerations imply that the IBL height may be proportional to a local stability parameter.

Miyake (1965) first suggested the use of $-z_0/L$ for characterizing stability effects on boundary layer growth. On embracing this parameterization, we discover it has more influence on δ than the fetch does. The relation which best describes our thermal boundary height measurements is

$$\frac{\delta}{z_0} = \beta\left(-\frac{z_0}{L}\right)^{0.8}\left(\frac{x}{z_0}\right)^{0.4} . \qquad 6.6.4$$

Here L is the Monin-Obukhov length which derives from our flux-gradient estimations of Chapter 5.

Intuitively, we feel that upwind stability should also have an effect on the boundary layer height. Stable upwind conditions would suppress thermal boundary layer growth while upwind instability would enhance it. Figure 6.7 supports this conjecture while demonstrating the strong $-z_0/L$ dependence of δ. Therefore, β in 6.6.4 is a constant reflecting the dependence of boundary height on upwind stability. Table 6.3 summarizes our calculated values of β and contains the evidence to let us reject with greater than 95% confidence the hypothesis that

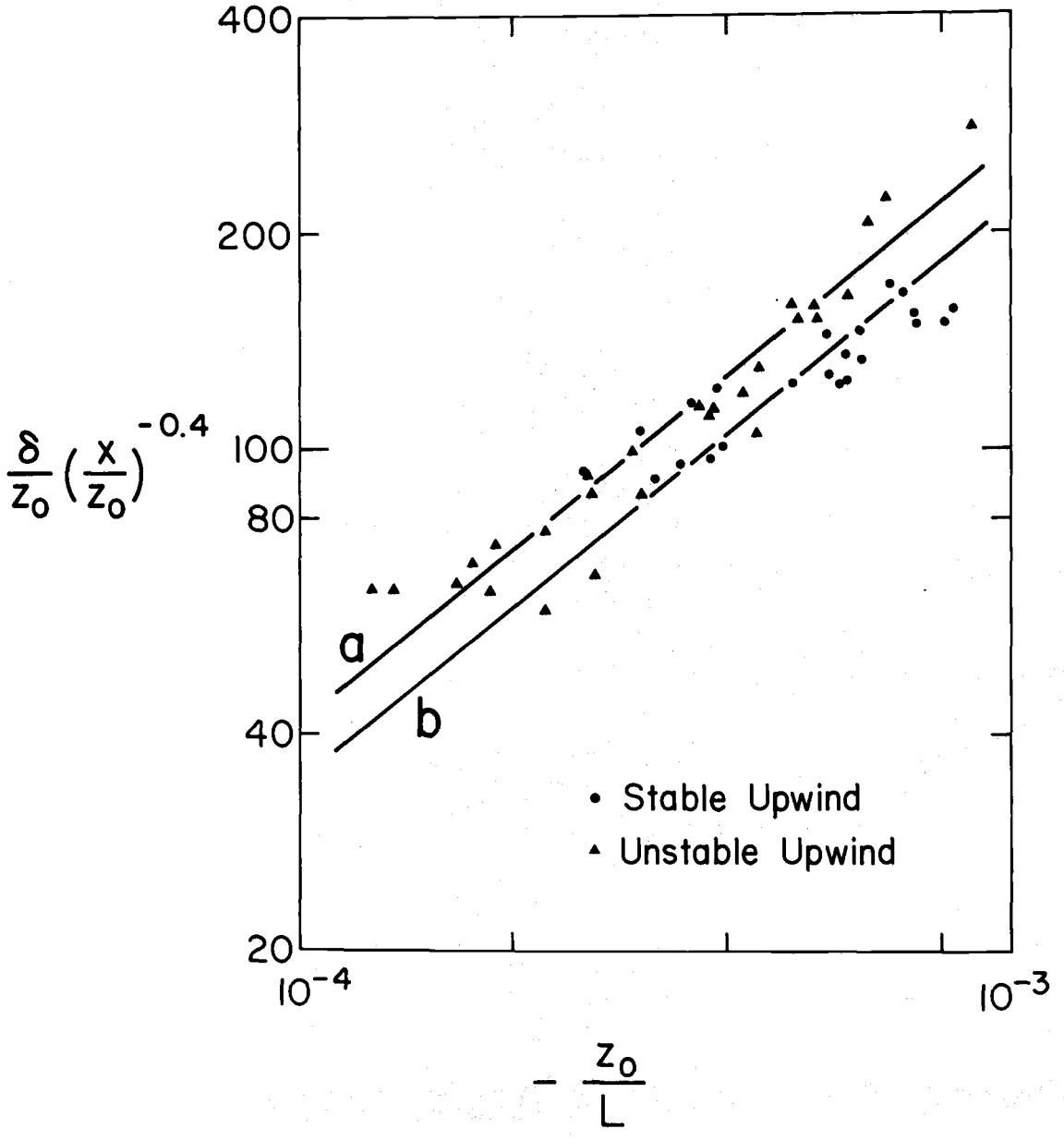

Figure 6.7. Dependence of boundary layer heights on $-z_0/L$ and upwind stability. The lines are equation 6.6.4 with $\beta = 6.6 \times 10^4$ for a and $\beta = 5.5 \times 10^4$ for b.

Table 6.3. Values of β in equation 6.6.4.

Upwind	Unstable	Stable
Observations	27	22
β	6.6×10^4	5.5×10^4
Standard Deviation:		
of Sample	0.9×10^4	0.7×10^4
of Mean	0.2×10^4	0.2×10^4

upwind stability has no effect on boundary layer growth (e.g., Brunk, 1965, page 258).

Figure 6.8 presents all our thermal boundary height observations and compares these individually to the model they collectively suggest (i.e., equation 6.6.4). The scatter is an indication of the difficulty inherent in determining δ. Nonetheless, this set is valuable, being the largest collection of geophysical observations of thermal boundary height we know of.

Equation 6.6.4 needs further confirmation before being accepted as a trustworthy prognostic tool. Since our data were primarily for low wind speeds ($u_* < 30$ cm/sec) and fetches of 20 m and less, we would like to see other results in stronger winds and for longer fetches. If 6.6.4 withstands these tests, consider its implications. Because L contains the surface heat flux, 6.6.4 would offer another method for heat flux estimation on the basis of bulk measurements.

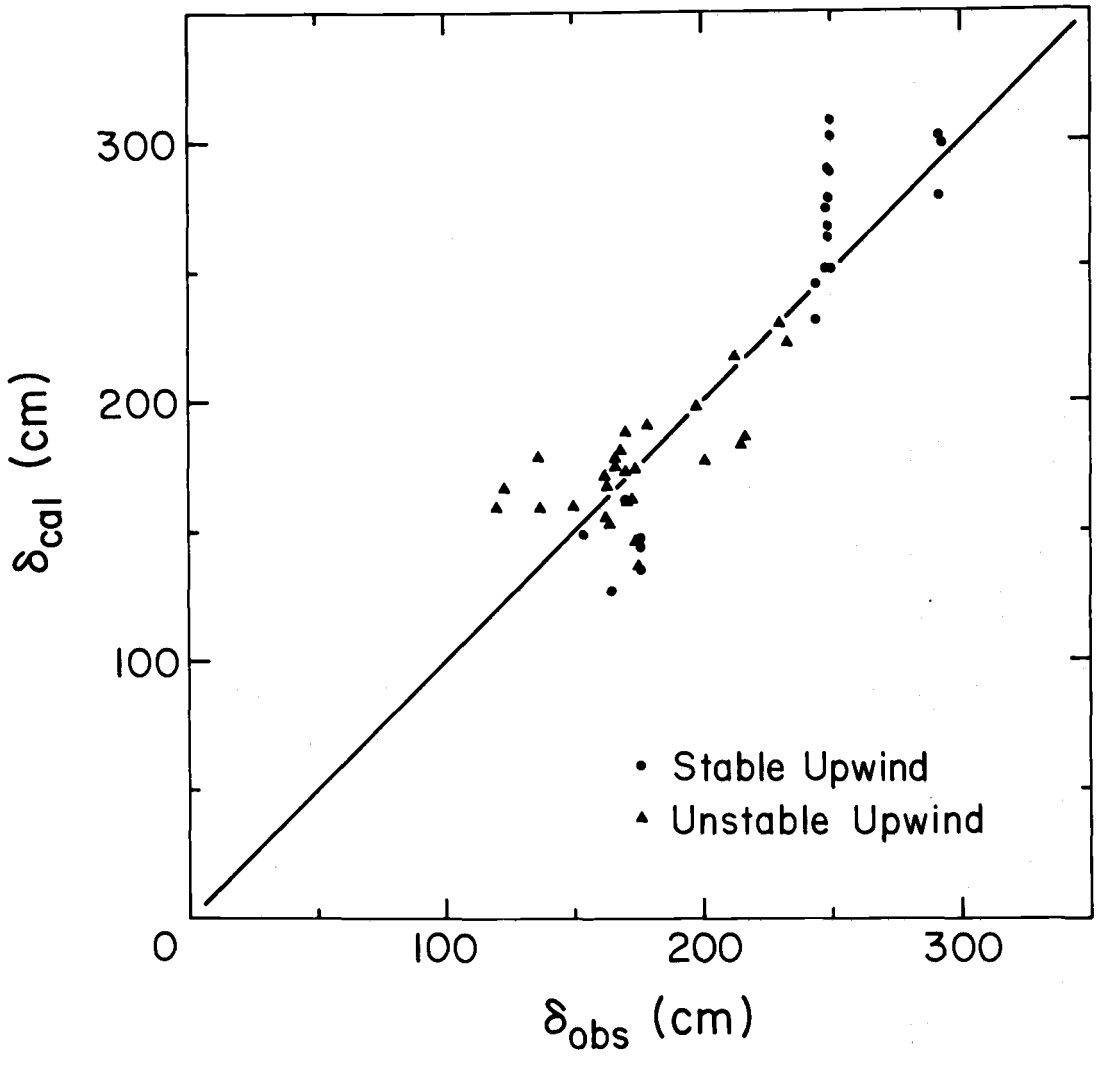

Figure 6.8. Observed thermal boundary heights compared to the predictions of equation 6.6.4.

7. SPECTRAL CHARACTERISTICS AND INTEGRAL STATISTICS

> And science is . . . nothing but the determination to establish differences.
>
> Hermann Hesse
> Narcissus and Goldmund

When we refer to 'spectra' or 'cospectra' in this chapter we will mean spectral or cospectral density estimates. Appendix A thoroughly details the procedure for reducing time series to spectral density estimates; therefore, we will add only a few words of supplementary information.

ALEX was designed to measure spectra of longitudinal and vertical velocity and temperature fluctuations, Φ_u, Φ_w, Φ_t, respectively, as well as cospectra and quadrature spectra of uw and wt, Co_{uw}, Qd_{uw}, Co_{wt}, Qd_{wt}. But as explained, because of the limited response of the thermocouples, the temperature-related spectra are doubtful. Hence, they are omitted from this discussion: we concentrate on Φ_u, Φ_w, and Co_{uw}. The 'integral statistics' of the turbulence properties we will describe are gotten by integrating the spectrum or cospectrum -- thus, the name.

7.1. FUNDAMENTALS

Both digital profile and flux tapes contained record lengths of 1024 data points. Before performing the

spectral analysis on the flux files, we grouped four such records into a block of length 4096. In other words, the N which appears throughout Appendix A is, for this analysis, 4096. The number of blocks, B, per file was variable but generally exceeded 55. Hence, the shortest spectral files contained time series which usually ran at least

$$\frac{(55)(4096)}{(250)(60)} = 15.0 \text{ minutes} . \qquad 7.1.1$$

The longest useable time series we collected over leads were 29.8 minutes -- average length was about 22 minutes. In addition, we made several runs over ice. Here, because the riming problem was less severe, some of these files were 35 minutes long.

To allay worries that only 15 minutes of turbulence data may be insufficient to yield useful spectra and spectral statistics, we investigated the effects of averaging time on the statistics. Figure 7.1 summarizes our results. In it, though the mean velocity is varying throughout, the statistics reach fairly steady values at about 17 minutes. $\overline{u^2}^{\frac{1}{2}}$ is the least steady of the statistics, as we would expect; yet it changes by less than two percent after seventeen minutes. Consequently, we feel our time series are long enough to have meaningful spectra and statistics.

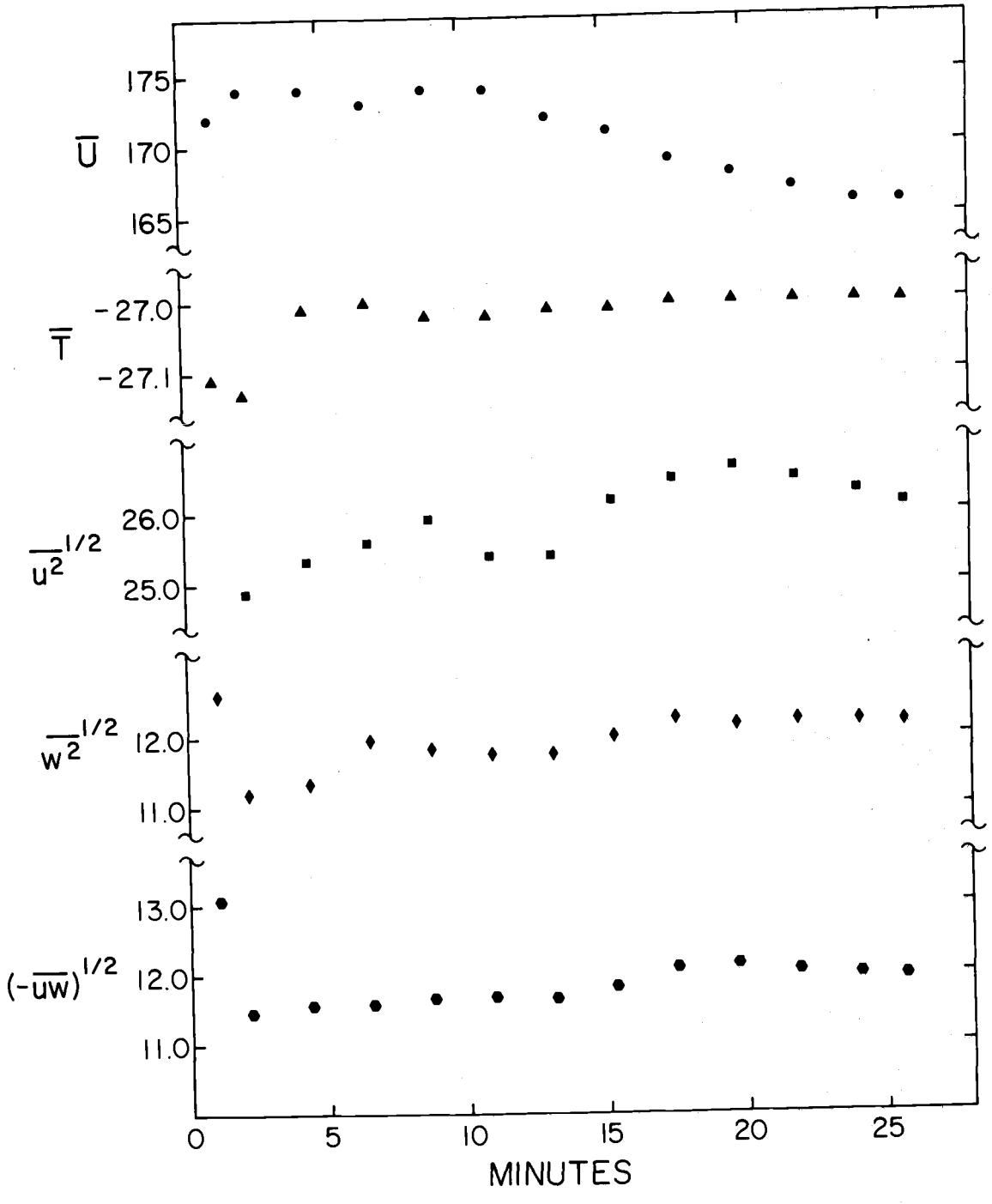

Figure 7.1. Effect of averaging time on integral statistics.

7.2. SPECTRA OVER ICE

The University of Washington group, which was usually positioned upwind of the leads, was equipped as our downwind group was and, therefore, had the capability to determine upwind spectra. However, because that analysis has not been done, we cannot compare simultaneous upwind and downwind spectra. But while encamped at the real lead site, we found ourselves for a time on its upwind side due to the caprice of the wind. The nearest upwind pressure ridge was about 1 km away and there was no open water for at least several kilometers upwind. So we continued recording over this smooth, snow-covered ice fetch. In the absence of any upwind spectra from the University of Washington group, for the purpose of checking our spectral technique, and as a transitional step for getting into the more complicated downwind spectra, we here present the spectra of these runs.

To facilitate comparison of our spectra with those reported elsewhere, in this chapter we plot only normalized spectra and cospectra against the nondimensional frequency,

$$\hat{f} = \frac{fz}{U} \ . \qquad 7.2.1$$

Here f is the frequency (Hz) associated with the spectral estimate, z is the height of observation, and U is the average velocity at z. The goal of such normalization is

to collapse diverse spectra into a presumably universal shape. Customarily, $u_*^2 = -\overline{uw}$ is used to normalize velocity spectra and cospectra (e.g., Busch and Panofsky, 1968; Kaimal, et al., 1972). But our spectra are more consistent when $\overline{w^2}$ normalizes $f\Phi_u$ and $f\Phi_w$ and $\overline{uw}$ normalizes fCo_{uw} (cf. Miyake, et al., 1970b; Pond et al., 1971). In Figure 7.2 all our spectra over ice are so normalized and do collapse neatly into similar shapes at the higher frequencies.

A comparison of the low frequency end of the vertical velocity spectra with the uw cospectra shows why $\overline{w^2}$ is a better normalization for Φ_u and Φ_w than $\overline{uw}$ is. The cospectra contain significant energy in this range. And because there are few degrees of freedom in spectral estimates at such low frequencies, the estimates are highly variable. This combination of relatively large though poorly known cospectral estimates at low frequency makes $\overline{uw}$ a less statistically certain quantity than $\overline{w^2}$.

A review of nondimensional spectra and cospectra collected in the atmospheric surface layer under homogeneous conditions (e.g., Busch and Panofsky, 1968; Miyake, et al., 1970b; Kaimal, et al., 1972) confirms the accuracy of the results in Figure 7.2. Our spectra and cospectra have peaks of the proper magnitude and in the usually reported frequency range. The high frequency behavior of Φ_u and Φ_w apparently follows Kolmogorov's -2/3 law (in these coordinates) for the inertial subrange. And the cospectra

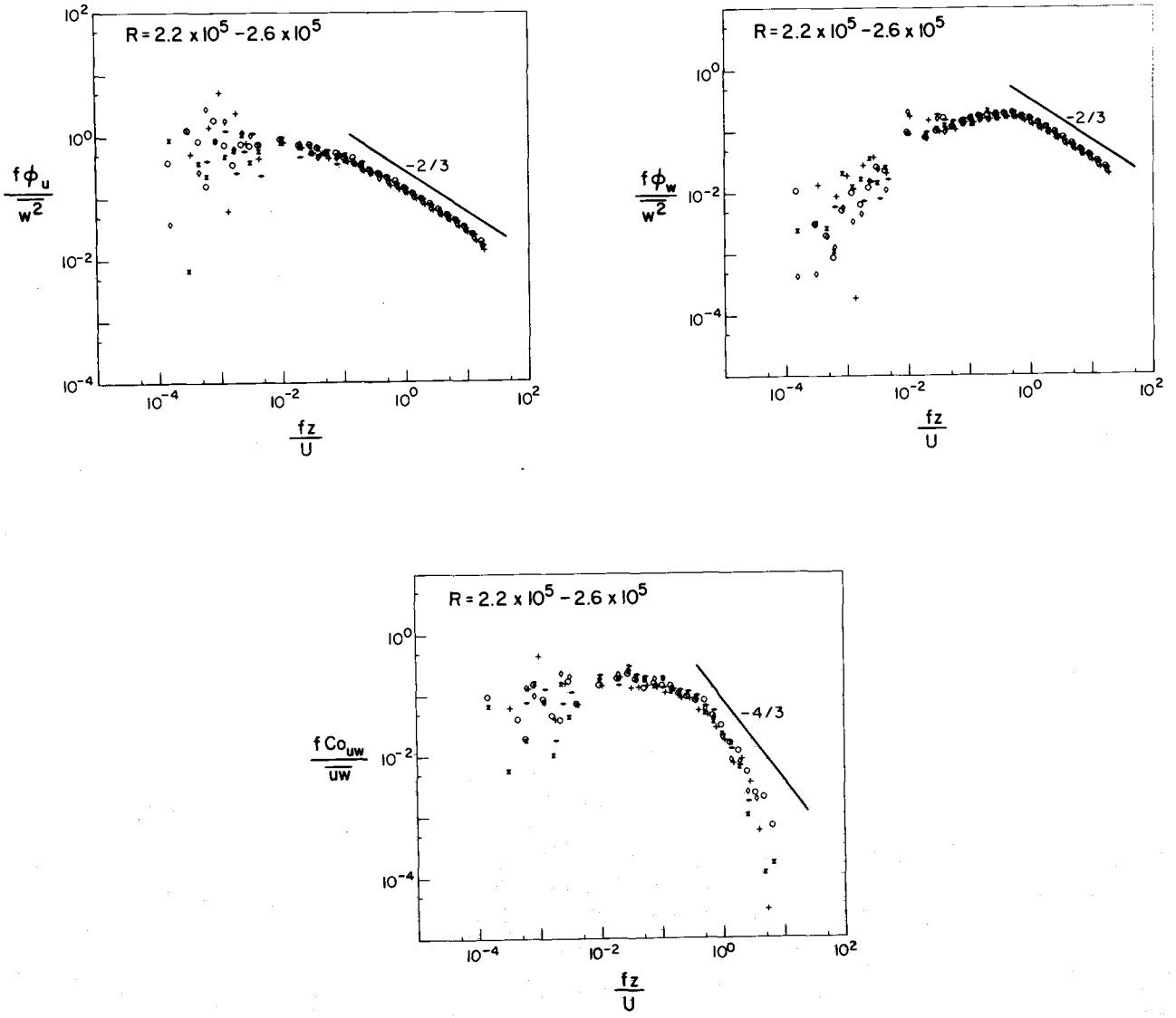

Figure 7.2. Spectra collected over Arctic ice. R gives the Reynolds number range.

suggest a -4/3 dependence at higher frequencies though are not in total accord here. This postulated -4/3 dependence of Co_{uw} in the inertial subrange (e.g., Wyngaard and Cote, 1972) has not received the overwhelming experimental confirmation that the -2/3 dependence for individual velocity spectra has. Other subrange behavior has been observed (Panofsky and Mares, 1968; Miyake, et al., 1970b).

Pointing out the Reynolds number range, which is given in the upper left of each spectral plot, leads into a short digression. The Kolmogorov (1941) inertial subrange hypotheses are valid only in the limit of large Reynolds numbers. Tennekes and Lumley (1972, page 266) infer an inertial subrange exists only for R of order 10^5 or greater. Our over-ice spectra, for which z is 65 cm, have an R this large. For tower-mounted instrumentation, which is a usual source of spectra appearing in the literature, z may be 50 m and more; therefore, R would be roughly 10^7 and the inertial subrange, consequently, extensive.

But whether R is large enough to support an inertial subrange or not, its magnitude still affects the shape of the spectrum. The dissipation range of the spectrum shows the energy in the highest frequency (or smallest scale) motions of the flow. These highest frequencies correspond to the inverse of the Kolmogorov microscale for time,

$$f_k = \left(\frac{\varepsilon}{\nu}\right)^{\frac{1}{2}} . \qquad 7.2.2$$

Since the dissipation rate is approximately

$$\varepsilon \approx \frac{u_*^3}{kz}, \qquad 7.2.3$$

we find

$$\frac{f_k z}{U} \approx k^{-\frac{1}{2}} \left(\frac{u_*}{U}\right)^{3/2} \left(\frac{Uz}{\nu}\right)^{\frac{1}{2}} \qquad 7.2.4$$

$$\approx k^{-\frac{1}{2}} \left(\frac{u_*}{U}\right)^{3/2} R^{\frac{1}{2}} . \qquad 7.2.5$$

That is, because u_*/U is only a weak function of velocity and height near the surface, the nondimensional frequency of the spectral dissipation range increases with Reynolds number. The spectrum is contracted or spread out depending on the magnitude of R.

The purpose of this discussion was twofold. First, we wanted to review the often forgotten condition that R must be large before an inertial subrange can develop. Secondly, to prepare for the next section, which presents spectra characterized by smaller Reynolds numbers, we have shown how the magnitude of R affects the spectrum.

7.3 SPECTRA OVER LEADS

With the last section as background and the spectra therein for comparison, Figures 7.3, 7.4, and 7.5 show nondimensional spectra and cospectra made over leads with fetches from 7.2 m to 34 m. The spectra are grouped

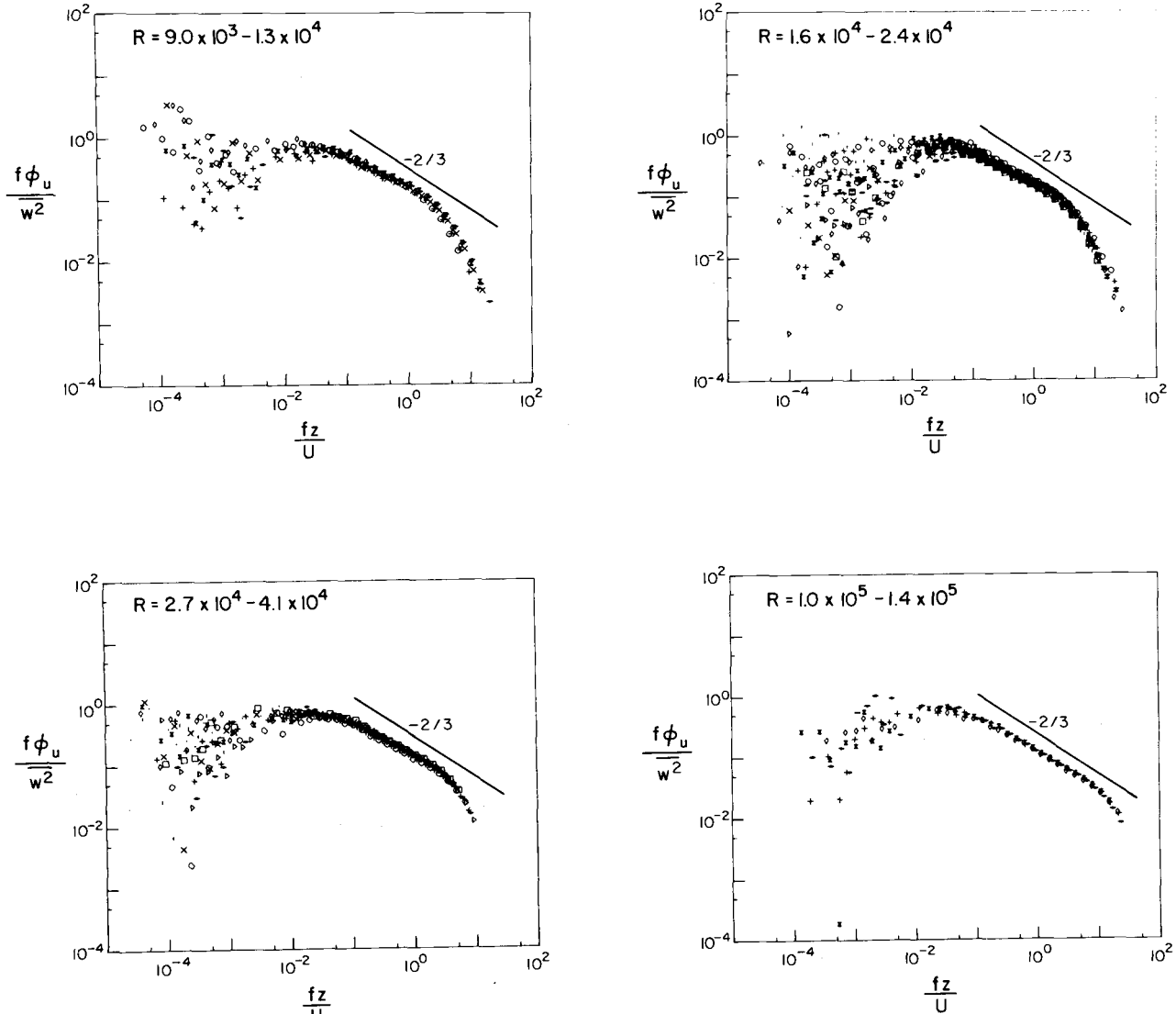

Figure 7.3. Spectra of longitudinal velocity fluctuations over leads. R gives the Reynolds number range.

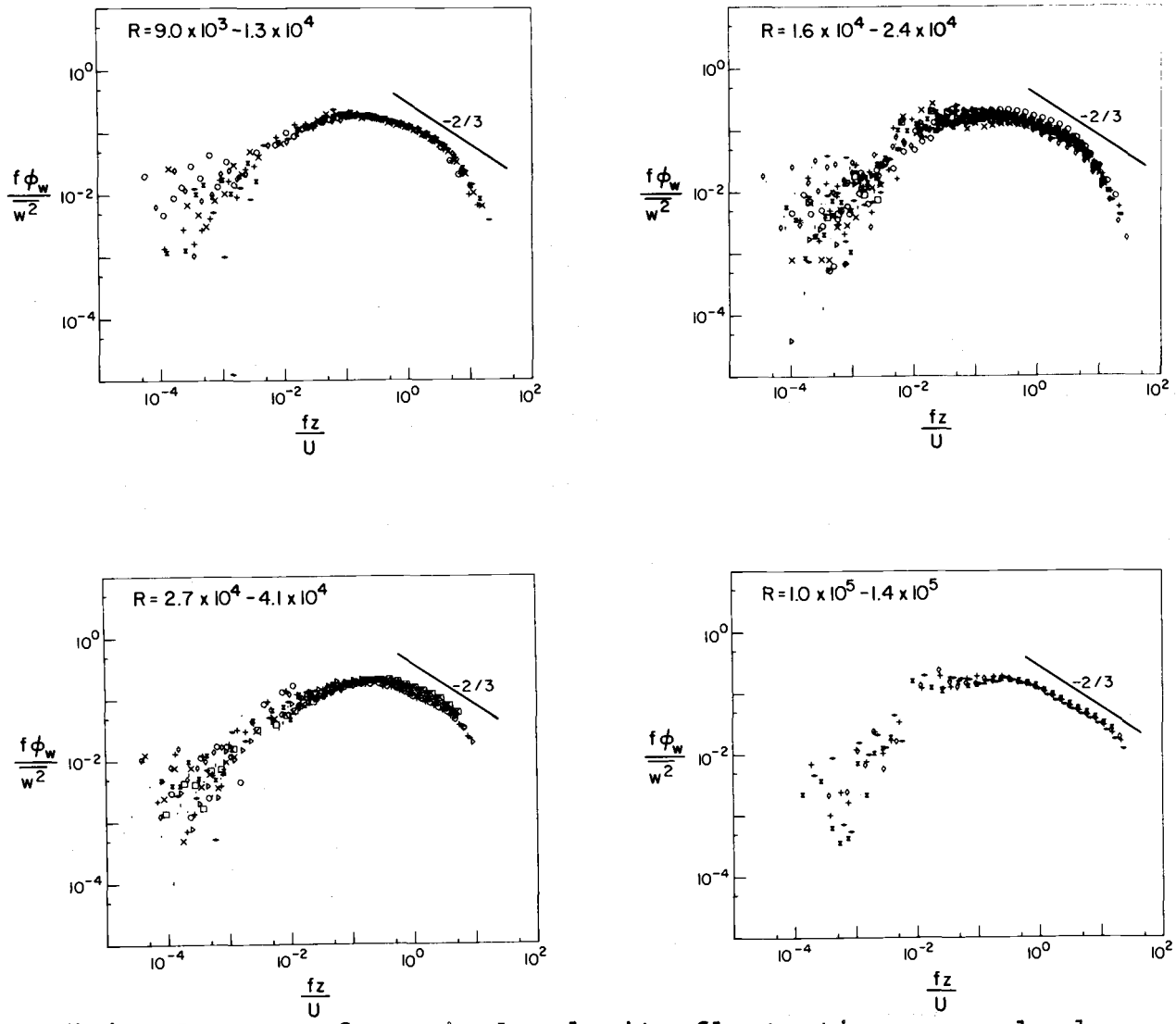

Figure 7.4. Spectra of vertical velocity fluctuations over leads.

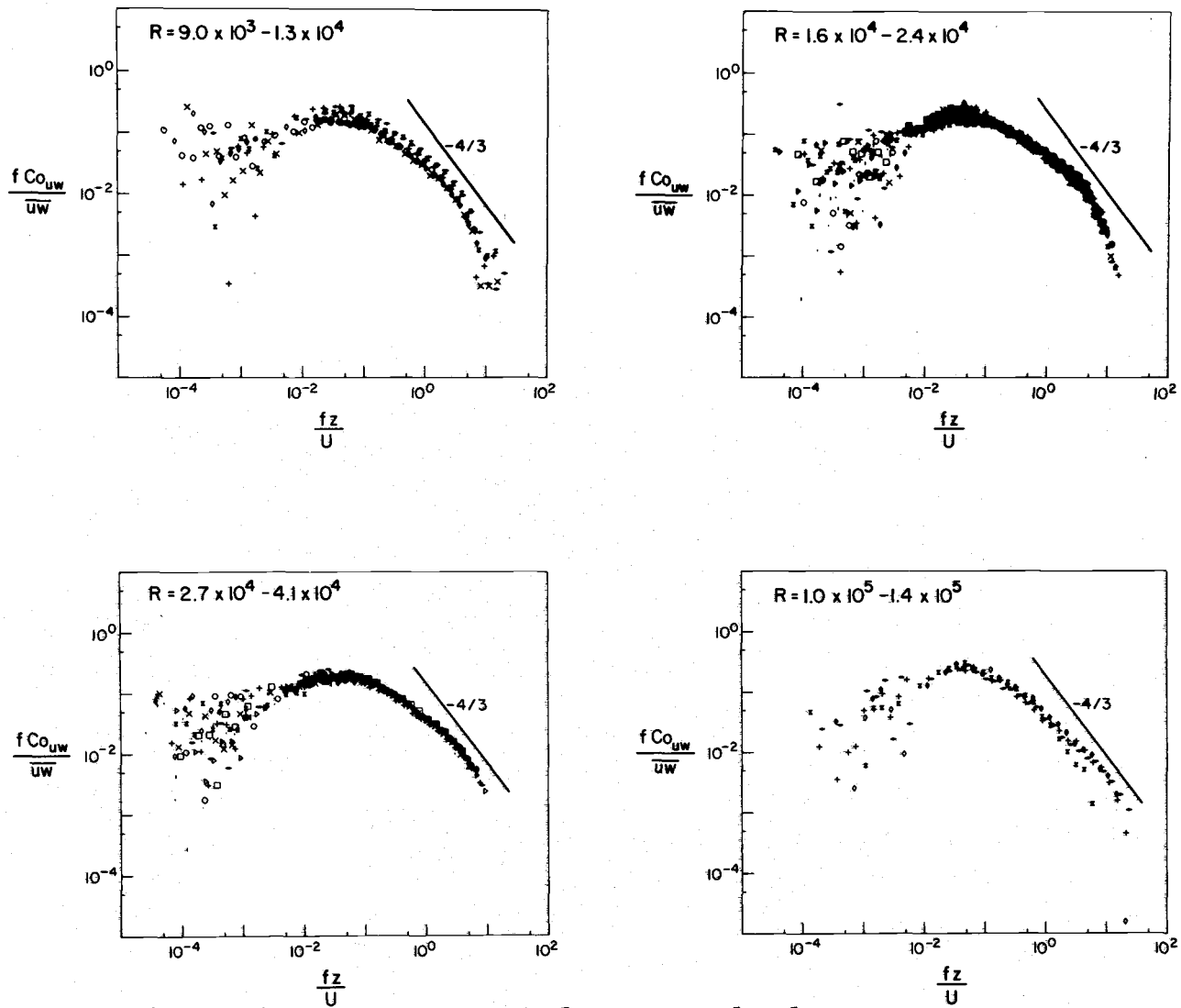

Figure 7.5. Cospectra of uw over leads.

according to Reynolds number and largely without regard to fetch. The highest Reynolds number plot in each figure does, however, happen to contain only spectra made over the 34 m lead since our sensors were higher above the water here.

In each plot the line shows the inertial subrange behavior we found in the spectra over ice. However, the spectra of this section seldom have that frequency dependence -- the Reynolds number is not large enough. The longitudinal velocity spectra come closest: as R increases, an inertial subrange begins stretching out to approach the -2/3 slope. But even for the highest Reynolds number range, it's doubtful that Φ_w and Co_{uw} have inertial subranges.

A second motivation for the Reynolds number grouping is the very high frequency behavior of the spectra. At the lowest Reynolds numbers there is a recognizable dissipation region. With increasing R this moves to higher frequencies as 7.2.4 shows it must. Finally, for the largest R range there is only the merest trace of a change in spectral slope hinting at the presence of a dissipation region.

The low frequency end of the spectra also appears to be a function of Reynolds number. We are looking especially at Φ_u and Co_{uw}: energy levels tend to fall as R increases. But consider the horizontal length scales

represented by this frequency region. Because the non-dimensional frequencies are less than 0.01, characteristic eddy size is 10 m or more. Therefore, the low frequency energy is likely not associated with the lead but instead reflects larger scale atmospheric processes. Realizing this, we can refer for guidance to published spectral shapes for horizontally homogeneous conditions (Kaimal, et al., 1972). At the low frequency end, the spectra and cospectra depend on z/L. There is more energy at large -z/L and much less at large z/L. Of coincidence, our smallest Reynolds number range corresponds primarily with unstable upwind conditions while the largest R range occurred during stable ambient conditions. Apparently, the low frequency dependence on R is accidental.

The frequencies of the spectral and cospectral peaks do not change with Reynolds number nor do the heights of the peaks. Both peak frequencies and magnitudes coincide with those of the ice-fetch spectra.

After interpreting the somewhat unique shape of these spectra as primarily a Reynolds number dependence, we look for effects attributable to the nearby lead. For example, we might expect a feature near the nondimensional frequency corresponding to the fetch of the lead. This is roughly

$$\hat{f}_x \approx \frac{z}{x} \qquad 7.3.1$$

-- about 0.01 for our observations. But clearly, nothing is evident here. In a qualitative search of the spectra, there appears to be no hint of the presence of the lead. We need the quantitative results of the next section to point out where the inhomogeneity is manifested.

7.4. INTEGRAL STATISTICS

As we've shown, the measurement of $\overline{w^2}$ is more certain and thus easier than the measurement of $-\overline{uw}$. But because $-\overline{uw}$ is the more desirable quantity, trying to relate $\overline{w^2}$ and $-\overline{uw}$ is a valuable endeavor. Presumably the ratio $\overline{w^2}^{\frac{1}{2}}/u_*$ is a universal function of z/L. However, that function has been slow in emerging. For example, in neutral conditions reported values of $\overline{w^2}^{\frac{1}{2}}/u_*$ generally range from 0.9 (Monin, 1970) to 1.4 (McBean, 1971). And the ratio seems to be different over land and water (Busch, 1973).

In unstable conditions there is a firm theoretical basis in Monin-Obukhov similarity for the behavior of $\overline{w^2}^{\frac{1}{2}}/u_*$ (e.g., Businger, 1973). As -z/L increases beyond about 0.5 (Businger, 1973; Wyngaard, 1973) -- that is, in an atmosphere approaching free convection -- $\overline{w^2}^{\frac{1}{2}}/u_*$ is predicted to be proportional to $(-z/L)^{1/3}$. However, again the proportionality constant is in question. Because in the Arctic we measured $\overline{w^2}$ and $\overline{uw}$ for the stability parameter -z/L spanning almost three decades, we offer our results here for comparison. The data is also listed in Appendix D.

Figure 7.6 is a plot of $(\overline{w^2}/-\overline{uw})^{\frac{1}{2}}$ versus z/L. L is the Monin-Obukhov length from our flux-gradient results; $-\overline{uw}$ is the stress measurement from the lower flux sensors, which for all but eight of the points in Figure 7.6 were within 23 cm of the surface; and the $\overline{w^2}$ come from both lower and upper flux sensors.

Although both $\overline{uw}$ and L are presumably functions of height, the data in Figure 7.6 show no systematic difference between upper and lower levels. There are two regions in the figure. For -z/L less than 0.4, the $(\overline{w^2}/-\overline{uw})^{\frac{1}{2}}$ ratio is constant with a value of 0.99 ± 0.05 (95% confidence). Above -z/L = 0.4, the points turn upward and approach the $(-z/L)^{1/3}$ dependence. The general shape of this plot is in excellent agreement with similar ones given by Businger (1973) and Wyngaard (1973), particularly with regard to the break toward the +1/3 dependence.

The ratio, however, is lower than for most other findings. We muse on possible reasons. Initial suspicion falls on our use of $(-\overline{uw})^{\frac{1}{2}}$ measured somewhere above the surface rather than u_*. In fact, we have shown in Chapter 6 how $-\overline{uw}$ increases with height in the presence of an upward heat flux. Could $(-\overline{uw})^{\frac{1}{2}}$ at 20 cm exceed u_* by 40 percent -- the factor necessary to bring our results into agreement with previous estimates? Probably not. Taylor's (1970) and Shreffler's (1975) numerical experiments and Bradley's (1972) field work all show that the stress profile should

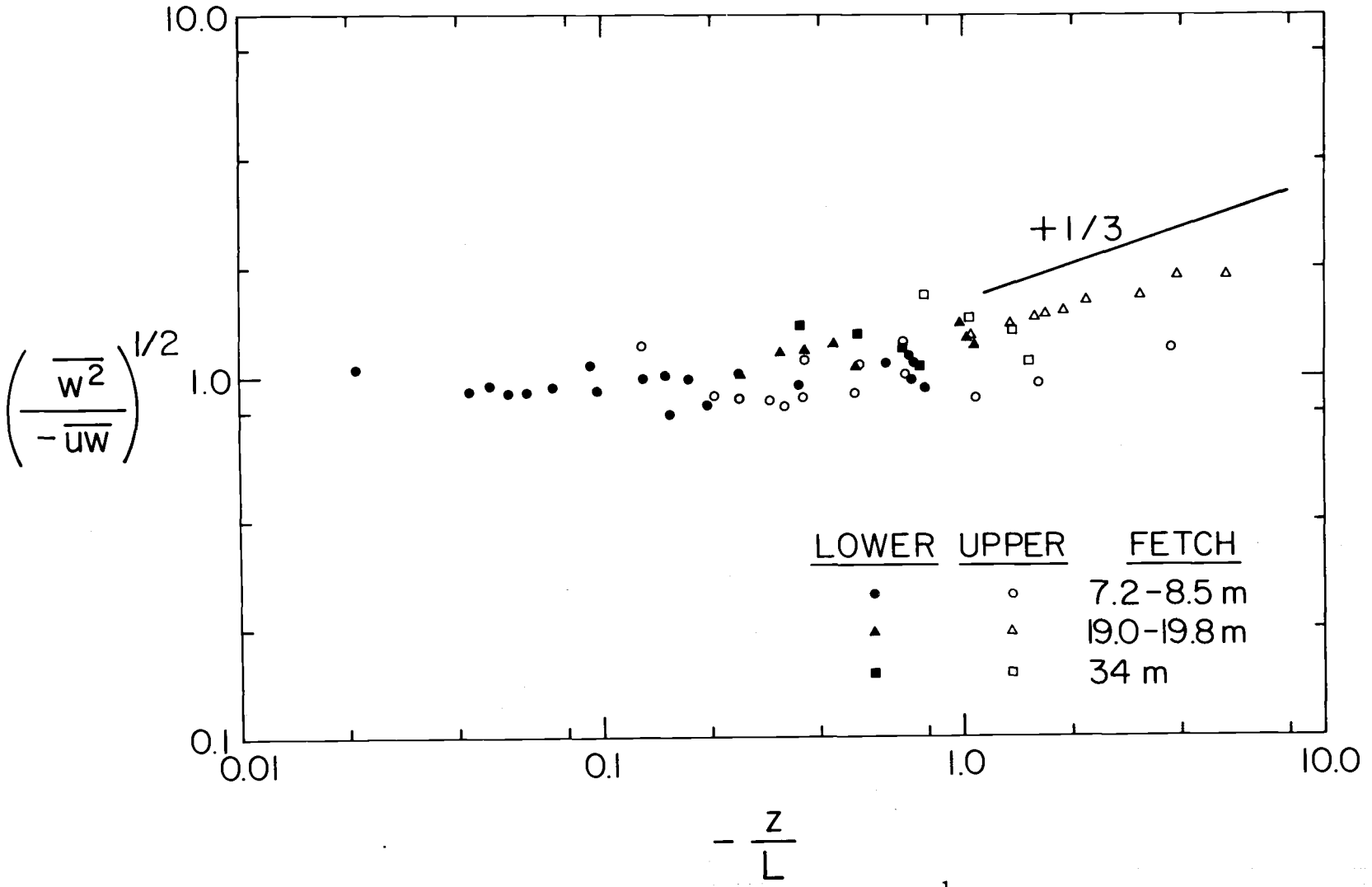

Figure 7.6. The dependence of $(\overline{w^2}/-\overline{uw})^{\frac{1}{2}}$ on z/L.

be virtually constant to heights greater than 20 cm.

Secondly, consider L: we have already expressed our doubts concerning its meaning in the IBL, which is not a constant flux layer. If anything, a systematic error in L would affect the horizontal position of the data, not its level. Yet we find the horizontal positioning in good agreement with other results: the change in slope toward the +1/3 dependence occurs in our plot at just the z/L value where it does in others. This result and our finding in Chapter 6 that z_0/L is a prime determinant of boundary layer height are indirect evidence of the worth of L despite its dubious origin. Within 20 to 50 centimeters of the surface it may not be as variable with height as we at first thought it would.

The finger finally points at $\overline{w^2}$. About one-third of the values plotted in Figure 7.6 are from measurements made within 20 cm of the surface; and practically all the measurements are within 70 cm of the surface. So near the surface vertical velocity fluctuations should be reduced compared to fluctuations higher up. Therefore, the smallness of our $(\overline{w^2}/-\overline{uw})^{\frac{1}{2}}$ ratio may be a boundary effect. Lumley and Panofsky (1964) summarize measurements of the ratio in pipe flow and within a boundary layer which support this explanation. For these two flows, in which the boundary is important by definition, $(\overline{w^2})^{\frac{1}{2}}/u_*$ is 1.05.

The cospectra of uw also contain evidence as to why $(\overline{w^2}/-\overline{uw})^{\frac{1}{2}}$ is smaller than the values usually reported. Compare these cospectra with the uw cospectra for horizontal homogeneity in Figure 7.2. The former contain much more energy at high frequency than do the latter, which fall rapidly above fz/U = 1. This too implies that the $(\overline{w^2}/-\overline{uw})^{\frac{1}{2}}$ ratio would be smaller over leads than for horizontally homogeneous conditions.

Since $\overline{w^2}/-\overline{uw}$ is linked with z/L, again a method for making an indirect estimate of sensible heat flux arises. If $\overline{w^2}$ and $-\overline{uw}$ can be measured and the functional dependence of their ratio on z/L is known, L and, consequently, $\overline{wt}$ can be established.

The $(\overline{u^2}/-\overline{uw})^{\frac{1}{2}}$ ratio is also an interesting statistic; but there is considerable uncertainty over its value and, indeed, doubt whether it should take universal form. This is simply because Φ_u contains energy due to large scale atmospheric motions while the variables used in Monin-Obukhov scaling reflect only local conditions (McBean, 1971).

In Figure 7.7 we plot our measurements of $\overline{u^2}$ at the lower flux tower level. The line drawn in by eye is

$$\left(\frac{\overline{u^2}}{-\overline{uw}}\right)^{\frac{1}{2}} = 2.15 \; . \qquad 7.4.1$$

This concurs with the simple sum of the individual ratios, 2.19 ± 0.06 (95% confidence). Neither stability nor

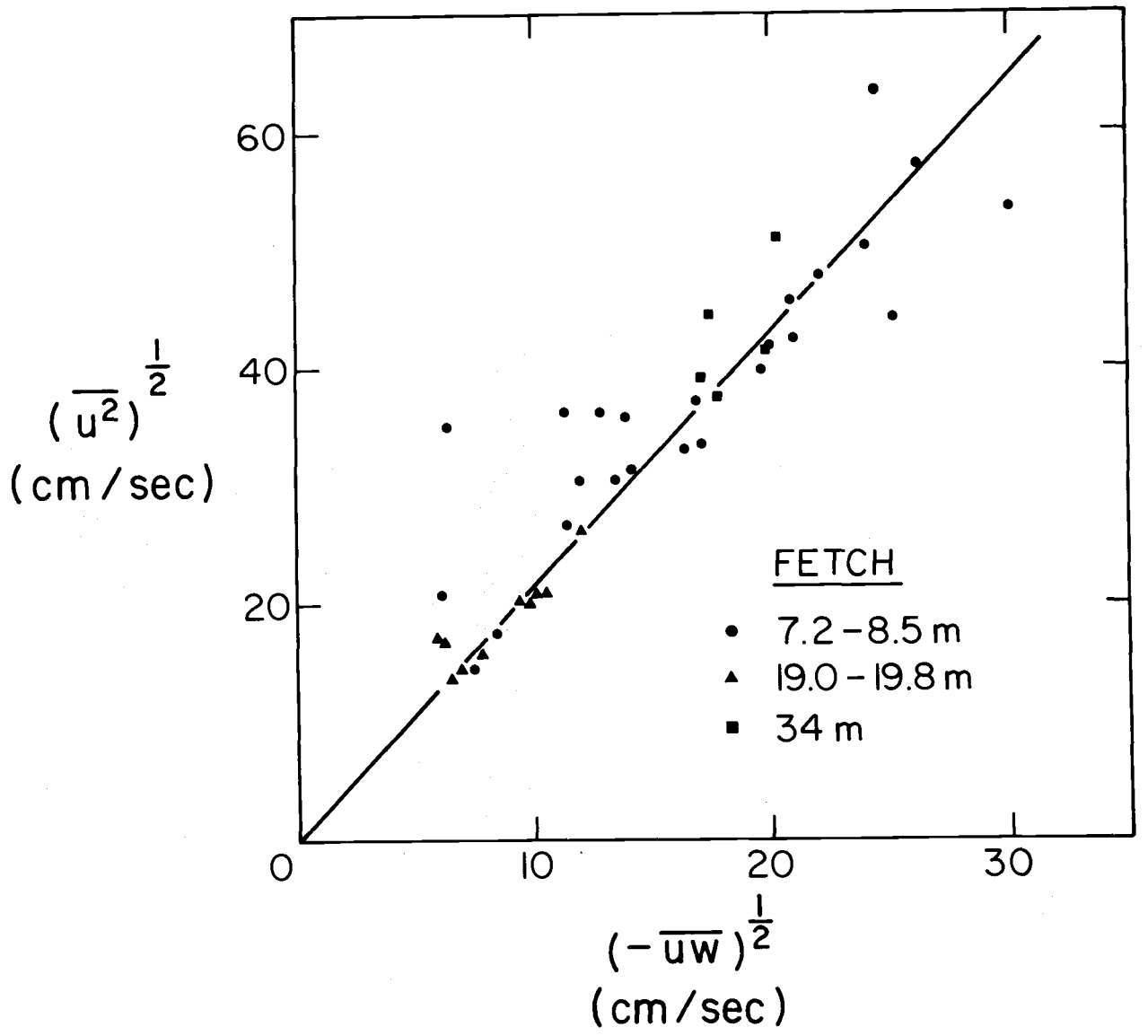

Figure 7.7. $\overline{u^2}$ correlated with $(-\overline{uw})^{\frac{1}{2}}$. The line is equation 7.4.1.

fetch influence this ratio: in the z/L range (-1.6, -0.02) and for fetches from 7.2 m to 34 m, it shows no definable trends with either.

As with $(\overline{w^2}/-\overline{uw})^{\frac{1}{2}}$, our $(\overline{u^2}/-\overline{uw})^{\frac{1}{2}}$ ratio is smaller than values usually reported. Typical values in the literature for measurements over the ocean in unstable conditions are in the range 2.6 to 2.8 (Miyake, et al., 1970b; Pond, et al., 1971). We again infer that the smallness of our ratio is due to the effects of the horizontal inhomogeneity on $-\overline{uw}$ as evidenced in the uw cospectra.

8. SUMMARY

> Only the ideas that we actually live are of any value.
>
> Hermann Hesse
> Demian

The heat transferred through leads is a substantial part of the total energy the Arctic Ocean loses to the atmosphere during the winter. This thesis recounts the AIDJEX Lead Experiment whose main purpose was to measure the turbulent component of that heat flux.

The sensible heat flux from leads was determined in three different ways. The primary estimate derived from an integral or energy conservation approach. The second relied on published findings relating fluxes to temperature and velocity profiles--the flux-gradient technique. Thirdly, a direct measurement yielded the Reynolds flux, $\overline{wt}$, after necessary corrections. Each of these methods gave a heat flux estimate consistent with the others. A typical value of sensible heat flux at the surface of Arctic leads in winter is 25 mw/cm^2. In addition, we made five measurements of latent heat flux and found it to account for 1/6 to 1/3 of the total turbulent heat flux from leads.

From the integral estimates of sensible heat flux we devised several methods for predicting the surface flux by measuring a few bulk parameters. On recognizing the similarity between the turbulent transfer of heat and moisture,

these were extended to include a latent heat flux prediction. For both sensible and latent heat fluxes the principal prediction equation is

$$N = 0.18\ R_x^{0.71}\ , \qquad 8.1$$

where N is the Nusselt number appropriate for either sensible or latent heat transfer. From direct measurements of the Reynolds stress, we correlated surface stress with a bulk parameter,

$$u_* \approx (-\overline{uw})^{\frac{1}{2}} = 0.0643\ U_{0.5} - 0.77\ . \qquad 8.2$$

Equations 8.1 and 8.2 now provide a means for making estimates of heat and momentum fluxes over leads on the basis of a few routine measurements.

We made the assumption that the flux-gradient relationships are valid near the surface of the lead. They then yielded surface heat and momentum fluxes; the Monin-Obukhov length, L, which we henceforth used as a stability parameter; and, indirectly, z_0, which is critical in the IBL height relation. The value of all these results, in part, justifies the original assumption. Seldom have the equations been used so near the surface or for such seemingly inhomogeneous conditions as in our work. But we have demonstrated that, with due caution, the flux-gradient relationships can have a domain of applicability even in flows which are largely inhomogeneous.

The profiles and these flux-gradient results suggest a new, linear relationship between z_0 and u_* over water, particularly in the transition region between aerodynamically smooth and rough flow. It is

$$z_0 = 0.4 \left(\frac{\nu}{g^2}\right)^{1/3} u_* \quad . \tag{8.3}$$

From our many observations of thermal boundary layer height, δ, we have developed an equation to predict that height,

$$\frac{\delta}{z_0} = \beta \left(-\frac{z_0}{L}\right)^{0.8} \left(\frac{x}{L}\right)^{0.4} \quad , \tag{8.4}$$

where x is the fetch and β is a constant which depends on upwind stability. This expression does need further confirmation for longer fetches and stronger winds. In fact, it might be good to reevaluate the whole concept of boundary layer height. Which is the more useful definition of that height; the point where the flux returns to its upwind value, or the point where the profile returns to its upwind value? Are these necessarily different heights? Maybe an alternative criterion which recognizes the oscillating nature of the top of the boundary layer is better than either. An investigation of these options would be an interesting turbulence problem.

The more than 70 pairs of velocity and temperature profiles we collected are supplemented by simultaneous

measurements of $\overline{uw}$ at two levels. Together these give a picture of the internal thermal boundary layer. The velocity profile within the IBL is accelerated in its mid-region through a coupling with the large vertical heat flux. Near the surface the profile is accelerated less--or maybe even decelerated--by the roughness change. And above the IBL, upwind and downwind velocities merge. Therefore, the stress profile has an emphatic bulge somewhat below the top of the IBL.

We presented more than thirty sets of spectra, Φ_u, Φ_w, and Co_{uw}, made over leads and plotted in normalized form. On comparing these with reported spectra for horizontally homogeneous conditions and also with the spectra from our observations over ice, it seems that Co_{uw} contains most of the effects of the horizontal inhomogeneity. Its energy content above the peak frequency is much greater than that observed in cospectra characterizing more homogeneous conditions. The spectral velocity statistics are consequently lower. $(\overline{w^2}/-\overline{uw})^{\frac{1}{2}}$ has a value of 0.99 for z/L in the interval (-0.4, 0.0) and is likely affected by the nearness of the measurements to the surface. $(\overline{u^2}/-\overline{uw})^{\frac{1}{2}}$ is 2.15 and depends on neither fetch nor stability.

Spectra of temperature and cospectra of wt are still required over leads since our thermocouples failed at the higher frequencies. The gap in our understanding of flow over leads due to the absence of these spectra is hard to

evaluate. The wt cospectra would be very interesting because the velocity profile within the IBL is strongly influenced by the intense mixing, which is, in turn, driven by the vertical heat flux. And the measurement of $\overline{t^2}$ and $\overline{wt}$ at different levels would have let us make a more confident determination of thermal boundary layer heights.

Humidity measurements of high enough quality to permit a calculation of the Reynolds flux are seldom routine anywhere. Succeeding with them in the Arctic would require exceptional skill and the determination of Charlie Finley. Nevertheless, to properly measure the latent heat flux over a lead and so verify our inferred relation, equation 6.4.1, they will likely be necessary because the applicability of the integral method is doubtful. Temperatures are so cold that vapor escaping from the lead may immediately condense and freeze on the nearest salt particle. Profile humidity values would then always be systematically lower with profile temperatures higher reflecting the latent heat lost by the vapor. It's an ambiguous system to describe with only bulk averages.

In closing, we want to emphasize for any contemplating a polar experiment how difficult it is doing research in the Arctic environment. The cold affects more than just the dexterity of your hands and the color of your nose. Coupled with the extreme dryness of the air, it causes often subtle and always bothersome problems. We

anticipated the riming of our thermocouples but not that it would be too severe for even the built-in heating circuitry to combat. When we strung our cables from the instrument hut to the towers, the cold lowered their resistance so much that our hot-film anemometers had to be modified. The cup anemometer turned faster in the Arctic than it did at the same wind speed in warmer Oregon. A portion of the thermocouple electronics was mounted with the sensors on the two towers. The effects of the cold on the characteristics of this circuitry was likely responsible for the inconsistency in thermocouple calibration.

So firstly, take infinite pains in the calibration of transducers. Calibrate in conditions as nearly Arctic as possible. Also plan for in situ calibration, preferably using references with well-established temperature response. Secondly, be prepared for a wide range of modifications to the instrumentation and the experimental design. It's impossible to guess everything in the Arctic bag of surprises.

BIBLIOGRAPHY

ANDREAS, E. L. 1977a. Analysis of hot-film velocity data. (to be published).

_____. 1977b. The calibration of short, cylindrical hot-film velocity sensors. (to be published).

AUFERHEIDE, A. C., and PITZL, G. 1970. Observations on ice regions of the Arctic Ocean. Arctic 23: 133-136.

BADGLEY, F. I. 1966. Heat budget of the surface of the Arctic Ocean. In Proceedings of the Symposium on the Arctic Heat Budget and Atmospheric Circulation, ed., J. O. Fletcher. Rand Corporation (RM-5233-NSF): 267-277.

BRADLEY, E. F. 1968. A micrometeorological study of velocity profiles and surface drag in the region modified by a change in surface roughness. Q. J. R. Meteorol. Soc. 94: 361-379.

_____. 1972. The influence of thermal stability on a drag coefficient measured close to the ground. Agric. Meteorol. 9: 183-190.

BRUNK, H. D. 1965. An Introduction to Mathematical Statistics, 2nd ed. Blaisdell Publishing Co., 429p.

BRUTSAERT, W. 1975. A theory of local evaporation (or heat transfer) from rough and smooth surfaces at ground level. Water Resour. Res. 11: 543-550.

BUSCH, N. E. 1973. On the mechanics of atmospheric turbulence. In Workshop on Micrometeorology, ed., D. A. Haugen. American Meteorological Society: 1-65.

BUSCH, N. E., and PANOFSKY, H. A. 1968. Recent spectra of atmospheric turbulence. Q. J. R. Meteorol. Soc. 94: 132-148.

BUSINGER, J. A. 1973. Turbulent transfer in the atmospheric surface layer. In Workshop on Micrometeorology, ed., D. A. Haugen. American Meteorological Society: 67-100.

BUSINGER, J. A., WYNGAARD, J. C., IZUMI, Y., and BRADLEY, E. F. 1971. Flux-profile relationships in the atmospheric surface layer. J. Atmos. Sci. 28: 181-189.

CHARNOCK, H. 1955. Wind stress on a water surface. Q. J. R. Meteorol. Soc. 81: 639.

_____. 1958. A note on empirical wind-wave formulae. Q. J. R. Meteorol. Soc. 84: 443-447.

CLARK, D. L. 1971. Arctic Ocean ice cover and its late Cenozoic history. Geol. Soc. Am. Bull. 82: 3313-3323.

COACHMAN, L. K. 1966. Production of supercooled water during sea ice formation. In Proceedings of the Symposium on the Arctic Heat Budget and Atmospheric Circulation, ed., J. O. Fletcher. Rand Corporation (RM-5233-NSF): 497-529.

COACHMAN, L. K., and BARNES, C. A. 1962. Surface water in the Eurasian Basin of the Arctic Ocean. Arctic 15: 251-277.

COANTIC, M., AND FAVRE, A. 1974. Activities in, and preliminary results of, air-sea interaction research at I. M. S. T. Adv. Geophys. 18A: 391-405.

CSANADY, G. T. 1974. The 'roughness' of the sea surface in light winds. J. Geophys. Res. 79: 2747-2751.

DONN, W. L., and EWING, M. 1966. A theory of ice ages III. Science 152: 1706-1712.

DORONIN, YU. P. 1963. On the heat balance of the central Arctic. In Soviet Data on the Arctic Heat Budget and Its Climatic Influence, ed., J. O. Fletcher, B. Keller, and S. M. Olenicoff. Rand Corporation (RM-5003-PR): 193-205.

_____. 1966. Characteristics of the heat exchange. In Proceedings of the Symposium on the Arctic Heat Budget and Atmospheric Circulation, ed., J. O. Fletcher. Rand Corporation (RM-5233-NSF): 247-266.

DYER, A. J. 1974. A review of flux-profile relationships. Boundary-Layer Meteorol. 7: 363-372.

ELLIOTT, W. P. 1958a. The growth of the internal boundary layer in the lower atmosphere. Ph.D. Thesis, A. & M. College of Texas, Department of Oceanography and Meteorology, 55p.

_____. 1958b. The growth of the atmospheric internal boundary layer. Trans., Am. Geophys. Union 39: 1048-1054.

EWING, M., and DONN, W. L. 1956. A theory of ice ages. Science 123: 1061-1066.

_____. 1958. A theory of ice ages II. Science 127: 1159-1162.

FLETCHER, J. O. 1965. The Heat Budget of the Arctic and Its Relation to Climate. Rand Corporation (R-444-PR), 179p.

GARRATT, J. R., and HICKS, B. B. 1973. Momentum, heat and water vapour transfer to and from natural and artificial surfaces. Q. J. R. Meteorol. Soc. 99: 680-687.

HEIBERG, A. 1974. AIDJEX Lead Experiment, spring 1974, field operations report. AIDJEX Bull. 26: 23-31.

HICKS, B. B. 1972. Some evaluations of drag and bulk transfer coefficients over water bodies of different sizes. Boundary-Layer Meteorol. 3: 201-213.

_____. 1975. A procedure for the formulation of bulk transfer coefficients over water. Boundary-Layer Meteorol. 8: 515-524.

_____. 1976. Wind profile relationships from 'Wangara' experiment. Q. J. R. Meteorol. Soc. 102: 535-551.

HIDY, G. M., and PLATE, E. J. 1966. Wind action on water standing in a laboratory channel. J. Fluid Mech. 26: 651-687.

HILSENRATH, J., BECKETT, C. W., BENEDICT, W. S., FANO, L., HOGE, H. J., MASI, J. F., NUTTALL, R. L., TOULOUKIAN, Y. S., and WOOLLEY, H. W. 1955. Tables of Thermal Properties of Gases: National Bureau of Standards Circular 564. U.S. Government Printing Office, 488p.

HOLMGREN, B., and WELLER, G. 1974. Local radiation fluxes over open and freezing leads in the polar pack ice. AIDJEX BULL. 27: 149-166.

HSU, S. A. 1974. A dynamic roughness equation and its application to wind stress determination at the air-sea interface. J. Phys. Oceanogr. 4: 116-120.

KAIMAL, J. C., WYNGAARD, J. C., IZUMI, Y., and COTÉ, O. R. 1972. Spectral characteristics of surface-layer turbulence. Q. J. R. Meteorol. Soc. 98: 563-589.

KATSAROS, K. B. 1973. Supercooling at the surface of an Arctic lead. J. Phys. Oceanogr. 3: 482-486.

KAYS, W. M. 1966. Convective Heat and Mass Transfer. McGraw-Hill, 387p.

KELLEY, J. J. 1974. Effect of open leads on the exchange of CO_2 between the atmosphere and surface sea water. AIDJEX Bull. 27: 121-124.

KITAIGORODSKII, S. A. 1969. Small-scale atmosphere-ocean interactions. Izv., Acad. Sci., USSR, Atmos. Oceanic Phys. 5: 641-649.

KITAIGORODSKII, S. A., and VOLKOV, YU. A. 1965. On the roughness parameter of the sea surface and the calculation of momentum flux in the near-water layer of the atmosphere. Izv., Acad. Sci., USSR, Atmos. Oceanic Phys. 1: 566-574.

KOLMOGOROV, A. 1941. The local structure of turbulence in incompressible viscous fluid for very large Reynolds' numbers. C. R. Dokl. Acad. Sci. URSS 30: 301-305.

KRAUS, E. B. 1971. Atmosphere-Ocean Interaction. Clarendon Press, 275p.

LINDSAY, R. W. 1976. Wind and temperature profiles taken during the Arctic leads experiment. Master's Thesis, University of Washington, Department of Atmospheric Sciences, 89p.

LING, C.-H., and UNTERSTEINER, N. 1974. On the calculation of the roughness parameter of sea ice. J. Geophys. Res. 79: 4112-4114.

LIST, R. J. 1971. Smithsonian Meteorological Tables, 6th ed. Smithsonian Institution Press, 527p.

LUMLEY, J. L., and PANOFSKY, H. A. 1964. The Structure of Atmospheric Turbulence. Interscience, 239p.

MANGARELLA, P. A., CHAMBERS, A. J., STREET, R. L., and HSU, E. Y. 1971. Energy and mass transfer through an air-water interface. Tech. Rept. No. 134, Stanford University, Department of Civil Engineering, 175p.

_____. 1972. Laboratory and field interfacial energy and mass flux and prediction equations. J. Geophys. Res. 77: 5870-5875.

MANGARELLA, P. A., CHAMBERS, A. J., STREET, R. L., and HSU, E. Y. 1973. Laboratory studies of evaporation and energy transfer through a wavy air-water interface. J. Phys. Oceanogr. 3: 93-101.

McBEAN, G. A. 1971. The variations of the statistics of wind, temperature and humidity fluctuations with stability. Boundary-Layer Meteorol. 1: 438-457.

MIYAKE, M. 1965. Transformation of the atmospheric boundary layer over inhomogeneous surfaces. Scientific Rept., University of Washington, Department of Atmospheric Sciences, 63p.

MIYAKE, M., DONELAN, M., McBEAN, G., PAULSON, C., BADGLEY, F., and LEAVITT, E. 1970a. Comparison of turbulent fluxes over water determined by profile and eddy correlation techniques. Q. J. R. Meteorol. Soc. 96: 132-137.

MIYAKE, M., STEWART, R. W., and BURLING, R. W. 1970b. Spectra and cospectra of turbulence over water. Q. J. R. Meteorol. Soc. 96: 138-143.

MONIN, A. S. 1970. The atmospheric boundary layer. Annu. Rev. Fluid Mech. 2: 225-250.

NANSEN, F. 1897. Farthest North, vol. II. Harper and Brothers Publishers, 714p.

NEUMANN, G., and PIERSON, W. J., JR. 1966. Principles of Physical Oceanography. Prentice-Hall, Inc., 545p.

OORT, A. H. 1974. Year-to-year variations in the energy balance of the Arctic atmosphere. J. Geophys. Res. 79: 1253-1260.

PANOFSKY, H. A., and MARES, E. 1968. Recent measurements of cospectra for heat-flux and stress. Q. J. R. Meteorol. Soc. 94: 581-585.

PANOFSKY, H. A., and PETERSEN, E. L. 1972. Wind profiles and change of terrain roughness at Risø. Q. J. R. Meteorol. Soc. 98: 845-854.

PAULSON, C. A. 1967. Profiles of wind speed, temperature and humidity over the sea. Ph.D. Thesis, University of Washington, Department of Atmospheric Sciences, 128p.

_____. 1970. The mathematical representation of wind speed and temperature profiles in the unstable atmosphere. J. Appl. Meteorol. 9: 857-861.

PAULSON, C. A., and SMITH, J. D. 1974. The AIDJEX Lead Experiment. AIDJEX Bull. 23: 1-8.

PETERSON, E. W. 1969. Modification of mean flow and turbulent energy by a change in surface roughness under conditions of neutral stability. Q. J. R. Meteorol. Soc. 95: 561-575.

PHELPS, G. T., and POND, S. 1971. Spectra of the temperature and humidity fluctuations and of the fluxes of moisture and sensible heat in the marine boundary layer. J. Atmos. Sci. 28: 918-928.

PHILLIPS, O. M. 1969. The Dynamics of the Upper Ocean. Cambridge University Press, 261p.

PLATE, E. J. 1971. Aerodynamic Characteristics of Atmospheric Boundary Layers. U. S. Atomic Energy Commission, 190p.

POND, S., PHELPS, G. T., PAQUIN, J. E., McBEAN, G., and STEWART, R. W. 1971. Measurements of the turbulent fluxes of momentum, moisture, and sensible heat over the ocean. J. Atmos. Sci. 28: 901-917.

RAMACHANDRAN, S. 1968. A new theory for cup anemometers. Indian J. Meteorol. Geophys. 19: 281-284.

RAO, K. S., WYNGAARD, J. C., and COTÉ, O. R. 1974. The structure of the two-dimensional internal boundary layer over a sudden change of surface roughness. J. Atmos. Sci. 31: 738-746.

ROLL, H. U. 1965. Physics of the Marine Atmosphere. Academic Press, 426p.

SCHLICHTING, H. 1968. Boundary-Layer Theory, 6th ed. trans., J. Kestin. McGraw-Hill, 748p.

SHEPPARD, P. A., TRIBBLE, D. T., and GARRATT, J. R. 1972. Studies of turbulence in the surface layer over water (Lough Neagh). Part I. Instrumentation, programme, profiles. Q. J. R. Meteorol. Soc. 98: 627-641.

SHIR, C. C. 1972. A numerical computation of air flow over a sudden change of surface roughness. J. Atmos. Sci. 29: 304-310.

SHREFFLER, J. H. 1975. A numerical model of heat transfer to the atmosphere from an Arctic lead. Ph.D. Thesis, Oregon State University, School of Oceanography, 135p.

SMITH, J. D. 1973. Lead driven convection in the Arctic Ocean. (abstract only) Trans., Am. Geophys. Union 54: 1108-1109.

_____. 1974. Oceanographic investigations during the AIDJEX Lead Experiment. AIDJEX Bull. 27: 125-133.

SMITH, S. D., and BANKE, E. G. 1975. Variation of the sea surface drag coefficient with wind speed. Q. J. R. Meteorol. Soc. 101: 665-673.

TAYLOR, P. A. 1969. On wind and shear stress profiles above a change in surface roughness. Q. J. R. Meteorol. Soc. 95: 77-91.

_____. 1970. A model of airflow above changes in surface heat flux, temperature and roughness for neutral and unstable conditions. Boundary-Layer Meteorol. 1: 18-39.

TENNEKES, H., and LUMLEY, J. L. 1972. A First Course in Turbulence. MIT Press, 300p.

VOWINCKEL, E., and TAYLOR, B. 1965. Energy balance of the Arctic; IV. Evaporation and sensible heat flux over the Arctic Ocean. Arch. Meteorol. Geophys. Bioklimatol., Ser. B 14: 36-52.

UNTERSTEINER, N. 1964. Calculation of temperature regime and heat budget of sea ice in the central Arctic. J. Geophys. Res. 69: 4755-4766.

UNTERSTEINER, N., and BADGLEY, F. I. 1965. The roughness parameter of sea ice. J. Geophys. Res. 70: 4573-4577.

WITTMANN, W. I., and SCHULE, J. J., JR. 1966. Comments on the mass budget of Arctic pack ice. In Proceedings of the Symposium on the Arctic Heat Budget and Atmospheric Circulation, ed., J. O. Fletcher. Rand Corporation (RM-5233-NSF): 215-246.

WORTHINGTON, L. V. 1953. Oceanographic results of project Skijump I and Skijump II in the polar sea, 1951-1952. Trans., Am. Geophys. Union 34: 543-551.

WU, J. 1968. Laboratory studies of wind-wave interactions. J. Fluid Mech. 34: 91-111.

_____. 1969. Wind stress and surface roughness at air-sea interface. J. Geophys. Res. 74: 444-455.

WYNGAARD, J. C. 1973. On surface layer turbulence. In Workshop on Micrometeorology, ed., D. A. Haugen. American Meteorological Society: 101-149.

WYNGAARD, J. C., and COTÉ, O. R. 1972. Cospectral similarity in the atmospheric surface layer. Q. J. R. Meteorol. Soc. 98: 590-603.

ZAKHAROV, V. F. 1966. The role of flaw leads off the edge of fast ice in the hydrological and ice regime of the Laptev Sea. Oceanology 6: 815-821.

APPENDICES

APPENDIX A

SPECTRAL ANALYSIS IN THE ATMOSPHERIC SURFACE LAYER

> Perilous to us all are the devices of an art deeper than we possess ourselves.
>
> J. R. R. Tolkien
> The Two Towers

A1. INTRODUCTION

The numerous books on time series analysis (Jenkins and Watts, 1968; Bendat and Piersol, 1972; Otnes and Enochson, 1972; Kanasewich, 1975) are often both too general and too specific -- too general because they emphasize the mathematical formalism rather than the practical result, and too specific because when they do get practical their solutions are not usually applicable to your problem. Hence, after studying these texts, each must write his own cookbook of time series analysis. The Air-Sea Interaction Group at Oregon State University has evolved a spectral analysis procedure for time series from the turbulent atmospheric surface layer -- this is the first edition of our cookbook.

The energy in surface layer turbulence is spread over a wide frequency range: thus, the spectral window smoothing techniques which might be applied, for example, in the reduction of oceanic wave or velocity series are not really appropriate -- there are no spectral peaks to isolate. Rather in our turbulence research the overall shape of the

spectrum and the total area under it (which, in general, is not preserved by smoothing with most spectral windows) are the two features of interest. Clearly, the analysis of turbulence data has a different focus than that concerned with more periodic processes.

Our problem is this: we record one or more simultaneous time series of surface layer turbulence (e.g., velocity, velocity time derivative, temperature, temperature derivative) as voltages in analog form on magnetic recording tape. This analog tape is subsequently digitized at a sampling rate of $1/\Delta$, where Δ may range from one second to 1/6000 second, with the digital results stored as integers on a computer-compatible digital tape. The information on this digital tape is broken down into 'files', 'blocks', and 'records'. A record is the smallest piece of information which can be passed between tape and computer: for example, one record could contain several hundred digital values and require five inches of magnetic tape for storage. Usually, however, this record length, L, is a power of two such as 1024, 2048, or 4096. During the analysis of the time series one or more records may constitute a block of length N, where N is again a power of two. The file will, thus, contain B blocks, each with N values, where BN is typically of order one million for turbulence time series.

A2. THE FOURIER TRANSFORM

Given a time series $\{x_k\}$ of length N, the Fourier transform pair is defined as

$$X_n = \sum_{k=0}^{N-1} x_k \, e^{-2\pi ink/N} \qquad n=0,1,\ldots,N-1 \ , \qquad \text{A2.1}$$

$$x_k = \frac{1}{N} \sum_{n=0}^{N-1} X_n \, e^{2\pi ink/N} \qquad k=0,1,\ldots,N-1 \ . \qquad \text{A2.2}$$

The X_n's are called the Fourier coefficients at frequency

$$f_n = \frac{n}{\Delta N} \ . \qquad \text{A2.3}$$

Observe that

$$X_0 = \sum_{k=0}^{N-1} x_k = N\bar{x} \ , \qquad \text{A2.4}$$

where the overbar indicates a sample average.

Let us establish an orthogonality relation for Fourier analysis. We require that A2.1 substituted into A2.2 yield an identity. That is,

$$x_k = \frac{1}{N} \sum_{n=0}^{N-1} e^{2\pi ink/N} \sum_{k'=0}^{N-1} x_{k'} \, e^{-2\pi ink'/N}$$

$$= \frac{1}{N} \sum_{k'=0}^{N-1} x_{k'} \sum_{n=0}^{N-1} e^{2\pi in(k-k')/N} \ . \qquad \text{A2.5}$$

Look closely at $\sum_{n=0}^{N-1} e^{2\pi in(k-k')/N}$. If we define

$$W \equiv e^{2\pi i(k-k')/N} ,$$

then

$$\sum_{n=0}^{N-1} W^n = 1 + W + W^2 + \ldots + W^{N-1} . \qquad \text{A2.6}$$

But recall

$$\frac{1}{1-W} = 1 + W + W^2 + \ldots + W^{N-1} + W^N + \ldots .$$

So A2.6 can be simplified to

$$\sum_{n=0}^{N-1} W^n = \frac{1}{1-W} - W^N \left(\frac{1}{1-W}\right) = \frac{1-W^N}{1-W} . \qquad \text{A2.7}$$

Consider the properties of A2.7. k-k' is always an integer less than N; therefore, W^N is always one. And since W is less than one except for k=k', A2.7 is zero whenever $k \neq k'$. At k=k' we invoke L'Hospital's Rule,

$$\lim_{m\to 0} \sum_{n=0}^{N-1} W^n = \lim_{m\to 0} \frac{1-e^{2\pi imn}}{1-e^{2\pi imn/N}}$$

$$= \lim_{m\to 0} \frac{-2\pi in\ e^{2\pi imn}}{-\frac{2\pi in}{N}\ e^{2\pi imn/N}}$$

$$= N .$$

In summary,

$$\frac{1}{N}\sum_{n=0}^{N-1} e^{2\pi i n(k-k')/N} = \delta_{kk'} \,, \qquad \text{A2.8}$$

a relation which will be useful throughout our ensuing discussion.

Now returning to A2.5,

$$x_k = \sum_{k'=0}^{N-1} x_{k'}\, \delta_{kk'} = x_k \,,$$

which is the identity we sought; hence, our transform pair is valid.

Notice finally a symmetry in the Fourier coefficients when $\{x_k\}$ is a real time series:

$$X_{N-n} = \sum_{k=0}^{N-1} x_k\, e^{-2\pi i(N-n)k/N}$$

$$= \sum_{k=0}^{N-1} x_k\, e^{-2\pi ik}\, e^{2\pi ink/N}$$

$$X_{N-n} = X_n^* \,, \qquad \text{A2.9}$$

where * indicates complex conjugation.

A3. THE POWER SPECTRUM

The power spectrum of a time series $\{x_k\}$ is simply the complex product of its Fourier coefficients,

$$P_{xn} = X_n X_n^* \qquad n=0,1,\ldots,N-1 \ . \tag{A3.1}$$

Because of A2.9, P_{xn} also has a symmetry if the time series is real:

$$P_{x,N-N} = P_{xn} \qquad n=1,2,\ldots,N-1 \ . \tag{A3.2}$$

That is, P_{xn} is symmetric about N/2 excluding n=0.

Let us investigate just what the power spectrum means. Suppose we sum P_{xn} over n:

$$\sum_{n=0}^{N-1} P_{xn} = \sum_{n=0}^{N-1} X_n X_n^*$$

$$= \sum_{n=0}^{N-1} \sum_{k=0}^{N-1} x_k \, e^{-2\pi ink/N} \sum_{k'=0}^{N-1} x_{k'} \, e^{2\pi ink'/N}$$

$$= N \sum_{k=0}^{N-1} x_k^2 \ . \tag{A3.3}$$

But remember $X_0 = N\bar{x}$, so A3.3 yields

$$\sum_{n=1}^{N-1} P_{xn} + N^2\bar{x}^2 = N \sum_{k=0}^{N-1} x_k^2 \ .$$

Or

$$\frac{1}{N^2} \sum_{n=1}^{N-1} P_{xn} = \frac{1}{N} \sum_{k=0}^{N-1} (x_k - \bar{x})^2 \ , \tag{A3.4}$$

where now the right side of A3.4 is the sample variance (see Brunk, 1965). Consequently, we interpret P_{xn} to be a measure of what motions of frequency $n/\Delta N$ contribute to the variance of our observable.

We can also define a power spectrum of two distinct series $\{x_k\}$ and $\{y_k\}$. This is the cross spectrum:

$$P_{xyn} = X_n Y_n^* \ . \qquad \text{A3.5}$$

Notice here again a symmetry about N/2,

$$\begin{aligned} P_{xy,N-n} &= X_{N-n} Y_{N-n}^* \\ &= X_n^* Y_n \\ &= P_{xyn}^* \qquad n=1,2,\ldots,N-1. \end{aligned} \qquad \text{A3.6}$$

As before, sum P_{xyn} to see what interpretation we can offer:

$$\sum_{n=0}^{N-1} P_{xyn} = \sum_{n=0}^{N-1} \sum_{k=0}^{N-1} x_k \, e^{-2\pi i n k/N} \sum_{k'=0}^{N-1} y_k \, e^{2\pi i n k'/N} \ .$$

Proceeding as above, we find

$$\sum_{n=1}^{N-1} P_{xyn} + N^2 \bar{x}\,\bar{y} = N \sum_{k=0}^{N-1} x_k y_k \ , \qquad \text{A3.7}$$

and

$$\frac{1}{N^2} \sum_{n=1}^{N-1} P_{xyn} = \frac{1}{N} \sum_{k=0}^{N-1} (x_k - \bar{x})(y_k - \bar{y}) , \qquad \text{A3.8}$$

the covariance between $\{x_k\}$ and $\{y_k\}$. Or in the perhaps more familiar correlation notation

$$\overline{x'y'} = \frac{1}{N^2} \sum_{n=0}^{N-1} P_{xyn} \quad , \qquad \text{A3.9}$$

the primes denoting fluctuations from the mean. Thus, the cross power spectrum is a measure of what the frequencies $n/\Delta N$ contribute to the correlation between $\{x_k\}$ and $\{y_k\}$.

Observe what A3.6 implies about A3.8. We could write

$$\sum_{n=1}^{N-1} P_{xyn} = \sum_{n=0}^{N/2-1} (P_{xyn} + P_{xy,N-n}) + P_{xy,N/2}$$

$$= \sum_{n=1}^{N/2-1} (P_{xyn} + P^*_{xyn}) + P_{xy,N/2} \quad .$$

But $P_{xyn} + P^*_{xyn}$ is real as is $P_{xy,N/2}$ (see equation A2.1). Hence, though the P_{xyn} are, in general, complex, $\overline{x'y'}$ is real since P_{xyn} is antisymmetric about N/2 in its imaginary part. We, thus, could simplify things by writing

$$\overline{x'y'} = \frac{2}{N} \sum_{n=1}^{N/2-1} R[\, P_{xyn} \,] + \frac{1}{N^2} P_{xy,N/2} \quad , \qquad \text{A3.10}$$

where $R[\ ]$ indicates the real part.

A4. THE SPECTRAL DENSITY

Equations A3.2, A3.4, A3.6, and A3.8 and our anticipation of some method of smoothing the raw spectral estimates

lead us to the consideration of spectral density estimates. In the smoothing process we will in some way combine spectral estimates over a frequency band to produce a single estimate. Therefore, to preserve the variance and covariance relations of A3.4 and A3.8 we need an altered definition of the spectrum to account for the length of the frequency band: this is the spectral density -- the contribution to the total variance or covariance per unit of frequency.

To get the feeling of spectral densities, we will first neglect the complications of smoothing. In A3.4 each P_{xn} is appropriate to a frequency band of length

$$df_n = \frac{1}{\Delta N} . \qquad \text{A4.1}$$

We also know that for a real time series P_{xn} is symmetric about N/2. So A3.4 rewritten in terms of the spectral density Φ_{xn} and the frequency interval df_n would be

$$\overline{x'x'} = \sum_{n=1}^{N/2-1} \Phi_{xn} df_n + \Phi_{x,N/2} df_{N/2} . \qquad \text{A4.2}$$

Clearly, the spectral density in this case is related to the power spectrum by

$$\Phi_{xn} = \frac{2\Delta}{N} P_{xn} \qquad n=1,2,\ldots,N/2-1 \qquad \text{A4.3}$$

$$\Phi_{x,N/2} = \frac{\Delta}{N} P_{x,N/2} .$$

We can likewise rewrite A3.8 in terms of a cross spectral density,

$$\overline{x'y'} = \sum_{n=1}^{N-1} \Phi_{xyn} df_n \ , \qquad \text{A4.4}$$

where

$$\Phi_{xyn} = \frac{\Delta}{N} P_{xyn} \qquad n=1,2,\ldots,N-1 \ . \qquad \text{A4.5}$$

However, the interpretation of this cross spectral density, Φ_{xyn}, is obscure because P_{xyn} is complex. So we choose to write Φ_{xyn} as the sum of its real and imaginary parts -- the cospectral and quadrature spectral densities --

$$\Phi_{xyn} = Co_{xyn} - i\, Qd_{xyn} \qquad n=1,2,\ldots N/2 \ . \qquad \text{A4.6}$$

To understand the origin of these look at

$$R[\Phi_{xyn}] = \tfrac{1}{2}[\Phi_{xyn} + \Phi^*_{xyn}] \qquad n=1,2,\ldots,N-1$$

$$= \frac{\Delta}{2N} [P_{xyn} + P_{xy,N-n}] \ ,$$

where $R[\ ]$ again indicates the real part. Now rather than summing everything twice, we recognize the symmetry about N/2 and define the cospectral density

$$Co_{xyn} = \frac{\Delta}{N} [P_{xyn} + P_{xy,N-n}] \qquad n=1,2,\ldots,N/2-1$$

$$Co_{xy,N/2} = \frac{\Delta}{N} P_{xy,N/2} \ . \qquad \text{A4.7}$$

Similarly,

$$-i\, I[\Phi_{xyn}] = \tfrac{1}{2}[\Phi_{xyn} - \Phi^*_{xyn}] \qquad n=1,2,\ldots,N-1$$

$$= \frac{\Delta}{2N}\,[P_{xyn} - P_{xy,N-n}]\ ,$$

where $I[\ ]$ indicates the imaginary part. Again because of the symmetry the quadrature spectral density is

$$Qd_{xyn} = \frac{i\Delta}{N}\,[P_{xyn} - P_{xy,N-n}] \qquad n=1,2,\ldots,N/2-1$$

$$Qd_{xy,N/2} = 0\ . \qquad \text{A4.8}$$

Henceforth, when we write 'spectrum' we will mean the spectral density or these cross spectral densities.

As we've explained in Section A3, the imaginary part of the cross spectrum cannot contribute to the covariance of x and y; thus, a summation from one to N/2 of Qd_{xyn} does not have a ready interpretation (a summation from one to N-1 of $I[P_{xyn}]$ is zero). The summation of Co_{xyn} is, on the other hand, the covariance:

$$\sum_{n=1}^{N/2} Co_{xyn}df_n = \frac{\Delta}{N}\sum_{n=1}^{N/2-1}(P_{xyn}+P_{xy,N-n})\,\frac{1}{N\Delta} + \frac{\Delta}{N}\,P_{xy,N/2}\,\frac{1}{N\Delta}$$

$$= \frac{1}{N^2}\sum_{n=1}^{N-1} P_{xyn}$$

$$\sum_{n=1}^{N/2} Co_{xyn}df_n = \overline{x'y'}\ . \qquad \text{A4.9}$$

We could choose an alternative formulation to A4.6, representing Φ_{xyn} as a length and an angle in a complex polar plane. That is,

$$\Phi_{xyn} = |G_{xyn}| e^{-i\Theta_{xyn}} \qquad n=1,2,\ldots,N/2 \ , \qquad \text{A4.10}$$

where the vertical bars indicate magnitude. Here G_{xyn} is related to the coherence spectrum and Θ_{xyn} is the phase spectrum. Obviously,

$$\begin{aligned} Co_{xyn} &= |G_{xyn}| \cos \Theta_{xyn} \ , \\ Qd_{xyn} &= |G_{xyn}| \sin \Theta_{xyn} \ . \end{aligned} \qquad \text{A4.11}$$

Therefore, the phase spectrum is

$$\Theta_{xyn} = \arctan \frac{Qd_{xyn}}{Co_{xyn}} \ , \qquad \text{A4.12}$$

and the length $|G_{xyn}|$ is

$$|G_{xyn}| = (Co^2_{xyn} + Qd^2_{xyn})^{\frac{1}{2}} . \qquad \text{A4.13}$$

By squaring A4.13 and normalizing with the spectral densities of x and y we define the coherence spectrum,

$$Ch_{xyn} = \frac{G^2_{xyn}}{\Phi_{xn}\Phi_{yn}} = \frac{Co^2_{xyn} + Qd^2_{xyn}}{\Phi_{xn}\Phi_{yn}} \ . \qquad \text{A4.14}$$

'Coherence' is an appropriate term because on looking back at A4.6 we realize Ch_{xyn} is also

$$Ch_{xyn} = \frac{\Phi^2_{xyn}}{\Phi_{xn}\Phi_{yn}} \quad , \qquad \text{A4.15}$$

which may be interpreted as the square of the spectral correlation coefficient.

Notice if Co_{xyn}, Qd_{xyn}, Φ_{xn}, and Φ_{yn} are simple multiples of the power and cross power spectra (i.e., if no smoothing has been done), then

$$Ch_{xyn} = \frac{(1-\frac{1}{2}\delta_{n,N/2})^2[(P_{xyn}+P_{xy,N-n})^2+(P_{xyn}-P_{xy,N-n})^2]}{(2-\delta_{n,N/2})^2 P_{xn}P_{yn}}$$

$$= \frac{4\ P_{xyn}P^*_{xyn}}{4\ P_{xn}P_{yn}}$$

$$= \frac{(X_nY^*_n)(X^*_nY_n)}{(X_nX^*_n)(Y_nY^*_n)}$$

$$Ch_{xyn} = 1 \ . \qquad \text{A4.16}$$

Thus, the coherence of raw spectral densities is always one regardless of the physical process.

Just for fun let's try to give equations A4.10 to A4.13 a more solid geometric interpretation. Consider two vectors in a complex plane; their decomposition is

$$\vec{X} = X^R + iX^I$$

$$\vec{Y} = Y^R + iY^I \quad , \qquad \text{A4.17}$$

where the superscripts indicate real and imaginary parts. Figure A4.1 defines our notation. Suppose we seek the angle between the vectors, α. That's easy to find if we rotate to a new coordinate system X', Y' in which X' coincides with $\vec{X}$. The matrix of this transformation is

$$\begin{pmatrix} \cos\gamma & \sin\gamma \\ -\sin\gamma & \cos\gamma \end{pmatrix} \qquad \text{A4.18}$$

and

$$\cos\gamma = \frac{X^R}{(X^{R2} + X^{I2})^{\frac{1}{2}}}$$

$$\sin\gamma = \frac{X^I}{(X^{R2} + X^{I2})^{\frac{1}{2}}} \quad . \qquad \text{A4.19}$$

Hence,

$$\alpha = \arctan\frac{s}{r} = \arctan\left[\frac{X^R Y^I - X^I Y^R}{X^R Y^R + X^I Y^I}\right] \quad . \qquad \text{A4.20}$$

Now can we draw an analogy between A4.20 and A4.12? Using A3.5, A3.6, A4.7, and A4.8 write

$$\frac{Qd_{xyn}}{Co_{xyn}} = \frac{i(X_n Y^*_n - X^*_n Y_n)}{X_n Y^*_n + X^*_n Y_n} \quad . \qquad \text{A4.21}$$

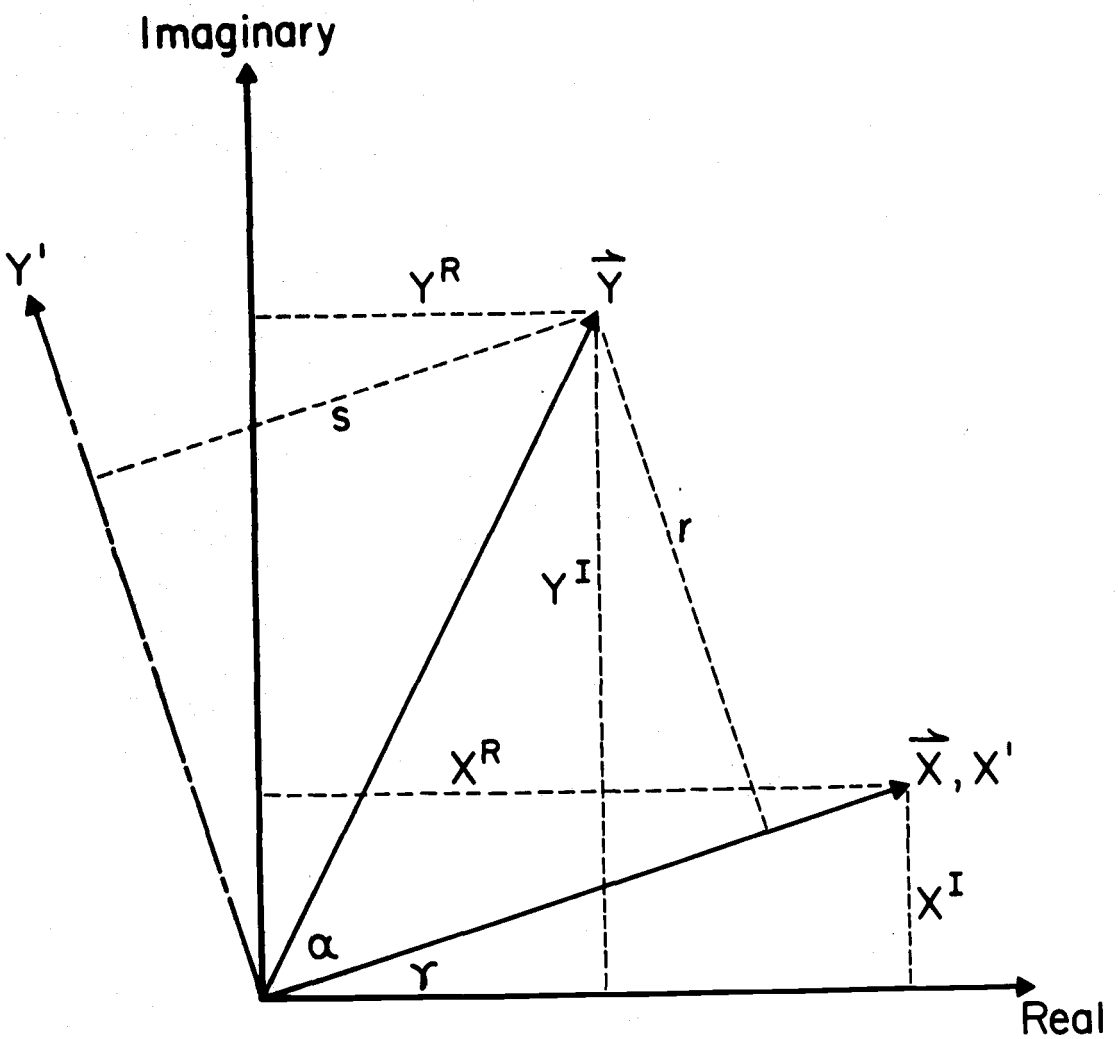

Figure A4.1. The decomposition of two vectors in a complex plane.

Recognizing X_n and Y_n are complex we expand to

$$\frac{Qd_{xyn}}{Co_{xyn}} = \frac{i(X_n^R + iX_n^I)(Y_n^R - iY_n^I) - i(X_n^R - iX_n^I)(Y_n^R + iY_n^I)}{(X_n^R + iX_n^I)(Y_n^R - iY_n^I) + (X_n^R - iX_n^I)(Y_n^R + iY_n^I)}$$

$$= \frac{X_n^R Y_n^I - X_n^I Y_n^R}{X_n^R Y_n^R + X_n^I Y_n^I} \quad . \qquad \text{A4.22}$$

So

$$\Theta_{xyn} = \arctan\left[\frac{X_n^R Y_n^I - X_n^I Y_n^R}{X_n^R Y_n^R + X_n^I Y_n^I}\right] , \qquad \text{A4.23}$$

which has exactly the same form as A4.20. The lesson is that if we interpret the Fourier coefficients X_n and Y_n as complex vectors, Θ_{xyn} is the angle between these in the complex plane.

Next look at equation A4.13. We can again substitute A4.7 and A4.8 to get

$$|G_{xyn}| = (1-\tfrac{1}{2}\delta_{n,N/2})[(P_{xyn}+P^*_{xyn})(P^*_{xyn}+P_{xyn}) + (P_{xyn}-P^*_{xyn})(P^*_{xyn}-P_{xyn})]^{\frac{1}{2}}$$

$$= \frac{\Delta}{N}(2-\delta_{n,N/2})[X_n Y^*_n X^*_n Y_n]^{\frac{1}{2}} ,$$

or

$$|G_{xyn}| = \frac{\Delta}{N}(2-\delta_{n,N/2})|X_n||Y_n| \quad . \qquad \text{A4.24}$$

Excellent! This result gives the cospectrum and quadrature spectrum as defined by A4.11 ready geometric significance. We rewrite,

$$Co_{xyn} = \frac{\Delta}{N} (2 - \delta_{n,N/2}) |X_n||Y_n| \cos \Theta_{xyn}$$

$$Qd_{xyn} = \frac{\Delta}{N} (2 - \delta_{n,N/2}) |X_n||Y_n| \sin \Theta_{xyn} \; . \qquad \text{A4.25}$$

Now Co_{xyn} looks much like a scalar product -- the product of the lengths of two vectors multiplied by the cosine of the angle between them. In turn, Qd_{xyn} evokes memories of the cross product between the two vectors. And these two vectors are the Fourier coefficients of the two time series of interest.

A5. BAND AND BLOCK AVERAGING

In the last section a one point estimate defined the raw spectral density. But band and block averaging reduce computer storage requirements and improve confidence in the estimates. Therefore, we combine the N/2 raw spectral density estimates per block into b band-averaged estimates and further average together the estimates for each of the B blocks.

The band averaging is really a smoothing process; however, because of the nature of turbulence spectra we need not consider the more sophisticated smoothing windows.

Rather our window will be (in the vernacular) non-overlapping boxcars of unit height. Generally, the high frequency limit of each boxcar is an exponential function of the band index; thus, on a logarithm of frequency plot the smoothed spectral densities will be evenly spaced. Table A5.1 is an example of exponentially spaced frequency bands for N = 4096.

If we let BE_n be the upper bandedge of the nth frequency band (the high frequency limit of the nth boxcar) and define

$$BE_0 = 0 \ ,$$

our smoothed spectral density is

$$\tilde{\Phi}_n = \frac{1}{B(BE_n - BE_{n-1})} \sum_{j=1}^{B} \sum_{k=BE_{n-1}+1}^{BE_n} \Phi_{kj} \qquad n=1,2,\ldots,b \ , \qquad \text{A5.1}$$

where Φ_{kj} is the raw spectral density, A4.3, or the raw cross spectral density, A4.6, at frequency

$$f_k = \frac{k}{\Delta N} \qquad \text{A5.2}$$

in the jth block. We associate this smoothed estimate with the center frequency of the band

$$\tilde{f}_n = \frac{BE_n + BE_{n-1} + 1}{2\Delta N} \ . \qquad \text{A5.3}$$

Table A5.1. Example of exponentially spaced spectral bands for a block length of 4096.

Band Index (n)	Upper Frequency Index (BE_n)	Count ($BE_n - BE_{n-1}$)	Center Frequency $\left(\frac{BE_n + BE_{n-1} + 1}{2\Delta N}\right)$
			($x\Delta$)
1	1	1	2.44×10^{-4}
2	2	1	4.88×10^{-4}
3	3	1	7.32×10^{-4}
4	4	1	9.77×10^{-4}
5	6	2	1.34×10^{-3}
6	9	3	1.95×10^{-3}
7	12	3	2.69×10^{-3}
8	17	5	3.66×10^{-3}
9	23	6	5.00×10^{-3}
10	32	9	6.84×10^{-3}
11	45	13	9.52×10^{-3}
12	62	17	1.32×10^{-2}
13	85	23	1.81×10^{-2}
14	117	32	2.48×10^{-2}
15	161	44	3.41×10^{-2}
16	221	60	4.68×10^{-2}
17	304	83	6.42×10^{-2}
18	418	114	8.83×10^{-2}
19	574	156	1.21×10^{-1}
20	789	215	1.67×10^{-1}
21	1084	295	2.29×10^{-1}
22	1490	406	3.14×10^{-1}
23 = b	2043	558	4.32×10^{-1}

As mentioned earlier, one motive for choosing the simple smoothing procedure of A5.1 is to preserve the variance and covariance. In analogy with A4.2 and A4.4 we can compute the variance or covariance from the smoothed spectral densities thusly,

$$\overline{x'x'} = \sum_{n=1}^{b} \tilde{\Phi}_{xn} \tilde{df}_n \ , \qquad \text{A5.4}$$

where

$$\tilde{df}_n = \frac{BE_n - BE_{n-1}}{\Delta N} \qquad \text{A5.5}$$

is the frequency interval over which $\tilde{\Phi}_{xn}$ is defined. If, to continue, we substitute A5.1 in for $\tilde{\Phi}_{xn}$ in A5.4,

$$\overline{x'x'} = \sum_{n=1}^{b} \frac{BE_n - BE_{n-1}}{\Delta N} \left[\frac{1}{B(BE_n - BE_{n-1})}\right] \sum_{j=1}^{B} \sum_{k=BE_{n-1}+1}^{BE_n} \Phi_{xkj}$$

$$= \frac{1}{B} \sum_{j=1}^{B} \sum_{n=1}^{b} df_n \sum_{k=BE_{n-1}+1}^{BE_n} \Phi_{xkj} \ . \qquad \text{A5.6}$$

But the sum at each frequency within band n and then over the b bands is equivalent to summing over the N/2 raw estimates. That is,

$$\sum_{n=1}^{b} \sum_{k=BE_{n-1}+1}^{BE_n} \neq \sum_{n=1}^{N/2} \ .$$

Equation A5.6 obviously includes a summation over the B blocks which we were not yet considering in A4.2 or A4.4; otherwise, in all respects A5.6 is mathematically equivalent to A4.2. In other words, the smoothing operation, A5.1, does not alter the sample variance or covariance if we pair the smoothed estimate with its appropriate frequency interval, A5.5.

A6. EXTENDING THE SPECTRUM

The zeroth Fourier coefficient, A2.4, cannot contain any information pertaining to frequencies of $1/\Delta N$ or higher, and the higher order coefficients contain no information about frequencies lower than $1/\Delta N$. However, the series of averages $\{\bar{x}_j\}$ we generate when Fourier transforming B consecutive blocks most likely contains information at frequencies lower than $1/\Delta N$. In essence, applying the Fourier transform to B blocks each of length N is a low pass filter with the time series $\{\bar{x}_j\}$ the output of the filter. Since we derive one $\bar{x}_j$ for each time step of ΔN, the sampling frequency of this new series is $1/\Delta N$. Hence, we see the possibility of extending the spectrum to lower frequencies by working our Fourier magic on this series of averages.

This concept of extending the spectrum is easier to see mathematically if we return to A3.7

$$\frac{1}{N}\sum_{k=0}^{N-1} x_k y_k = \bar{x}\,\bar{y} + \frac{1}{N^2}\sum_{n=1}^{N-1} P_{xyn} \quad . \qquad \text{A6.1}$$

Or changing to the more familiar notation of the spectral density

$$\frac{1}{N}\sum_{k=0}^{N-1} x_k y_k = \bar{x}\,\bar{y} + \sum_{n=1}^{N-1} \Phi_{xyn}\, df_n \quad . \qquad \text{A6.2}$$

Now consider what happens when we sum over B consecutive blocks. We get from A6.2

$$\frac{1}{BN}\sum_{j=1}^{B}\sum_{k=0}^{N-1} x_{kj} y_{kj} = \frac{1}{B}\sum_{j=1}^{B} \bar{x}_j \bar{y}_j + \frac{1}{B}\sum_{j=1}^{B}\sum_{n=1}^{N-1} \Phi_{xynj} df_n . \qquad \text{A6.3}$$

As promised we'll transform the series of the averages. But first suppose B isn't a power of two -- we transform only series with lengths a power of two. For such a series, somehow choose N^e consecutive values from the B averages, where N^e is the largest power of two less than B, and work with these N^e samples. That is, in A6.3 we make the approximation

$$\frac{1}{B}\sum_{j=1}^{B} \bar{x}_j \bar{y}_j \approx \frac{1}{N^e}\sum_{m=0}^{N^e-1} \bar{x}_m \bar{y}_m \quad . \qquad \text{A6.4}$$

As usual, the transform pairs of $\{\bar{x}_j\}$ and $\{\bar{y}_j\}$ are

$$\hat{X}_n = \sum_{j=0}^{N^e-1} \bar{x}_j\, e^{-2\pi i n j / N^e} \qquad \text{A6.5}$$

$$\hat{Y}_n = \sum_{j=0}^{N^e-1} \bar{y}_j \, e^{-2\pi inj/N^e}$$

and

$$\bar{x}_j = \frac{1}{N^e} \sum_{n=0}^{N^e-1} \hat{X}_n \, e^{2\pi inj/N^e}$$

A6.6

$$\bar{y}_j = \frac{1}{N^e} \sum_{n=0}^{N^e-1} \hat{Y}_n \, e^{2\pi inj/N^e} ,$$

where

$$\hat{X}_0 = N^e \, \bar{x}$$

A6.7

$$\hat{Y}_0 = N^e \, \bar{y}$$

(new averages, not to be confused with the $\bar{x}$ and $\bar{y}$ of A6.1).

Substituting A6.6 into A6.4 and using the ubiquitous A2.8 we continue,

$$\frac{1}{N^e} \sum_{m=0}^{N^e-1} \bar{x}_m \bar{y}_m = \frac{1}{N^{e3}} \sum_{m=0}^{N^e-1} \sum_{n=0}^{N^e-1} \hat{X}_n \, e^{2\pi inm/N^e} \sum_{n'=0}^{N^e-1} \hat{Y}_{n'} e^{-2\pi in'm/N^e}$$

$$= \frac{1}{N^{e2}} \sum_{n=0}^{N^e-1} \hat{X}_n \hat{Y}_n \, . \qquad \text{A6.8}$$

This result in A6.3 yields

A6.9

$$\frac{1}{BN} \sum_{j=1}^{B} \sum_{k=0}^{N-1} x_{kj} \, y_{kj} = \bar{x} \, \bar{y} + \frac{1}{N^{e2}} \sum_{n=1}^{N^e-1} \hat{X}_n \hat{Y}_n + \frac{1}{B} \sum_{j=1}^{B} \sum_{n=1}^{N-1} \Phi_{xynj} df_n .$$

Not surprisingly, we again find the covariance:

$$\overline{x'y'} = \frac{1}{BN} \sum_{j=1}^{B} \sum_{k=0}^{N-1} x_{kj} y_{kj} - \bar{x}\,\bar{y}$$

$$= \frac{1}{N^{e2}} \sum_{n=1}^{N^e-1} \hat{X}_n \hat{Y}_n + \frac{1}{B} \sum_{j=1}^{B} \sum_{n=1}^{N-1} \Phi_{xynj} df_n \quad . \qquad \text{A6.10}$$

Clearly, we can get the variance through the same routine by substituting x for y.

We've seen how to band average the spectra -- we do likewise with the extended spectra. In fact, to preserve the same logarithmic spacing the b^e extended spectral averaging bands can be those of the regular spectra -- only the frequencies and perhaps the highest bandedge are altered. Table A6.1 is an example of extended spectral bands for $N^e = 128$ and $N = 4096$.

In analogy with the band-averaged spectral density estimates, A5.1, we define the smoothed extended spectral density. This is

$$\tilde{\Phi}^e_n = \frac{1}{BE_n - BE_{n-1}} \sum_{k=BE_{n-1}+1}^{BE_n} \Phi^e_k \quad , \qquad \text{A6.11}$$

where

$$\Phi^e_k = \frac{\Delta N}{N^e} (2 - \delta_{k,N^e/2}) \hat{X}_k \hat{X}^*_k \qquad \text{A6.12}$$

for spectral density estimates, and

Table A6.1. Example of averaging bands of an extended spectrum for N^e = 128 blocks, each of length N = 4096.

Band Index (n)	Upper Frequency Index (BE_n)	Count ($BE_n - BE_{n-1}$)	Center Frequency $\left(\frac{BE_n + BE_{n-1} + 1}{2\Delta N \; N^e}\right)$
			(xΔ)
1	1	1	1.91×10^{-6}
2	2	1	3.81×10^{-6}
3	3	1	5.72×10^{-6}
4	4	1	7.63×10^{-6}
5	6	2	1.05×10^{-5}
6	9	3	1.53×10^{-5}
7	12	3	2.10×10^{-5}
8	17	5	2.86×10^{-5}
9	23	6	3.91×10^{-5}
10	32	9	5.34×10^{-5}
11	45	13	7.44×10^{-5}
$12 = b^e$	64	19	1.05×10^{-4}

$$\Phi_k^e = Co_{xyk}^e - iQd_{xyk}^e \qquad \text{A6.13}$$

for cross spectral density estimates. Obviously, in the second case

$$\tilde{\Phi}_n^e = \tilde{Co}_{xyn}^e - iQ\tilde{d}_{xyn}^e \; . \qquad \text{A6.14}$$

We associate these $\tilde{\Phi}_n^e$ with the frequency

$$\tilde{f}_n^e = \frac{BE_n + BE_{n-1} + 1}{2\ \Delta N\ N^e} \qquad \text{A6.15}$$

and the frequency interval

$$\tilde{df}_n^e = \frac{BE_n - BE_{n-1}}{\Delta N\ N^e} \; . \qquad \text{A6.16}$$

Hence, A6.10 finally becomes

$$\overline{x'x'} = \sum_{n=1}^{b^e} \tilde{\Phi}_{xn}^e \tilde{df}_n^e + \frac{1}{B} \sum_{j=1}^{B} \sum_{n=1}^{b} \tilde{\Phi}_{xnj} \tilde{df}_n \qquad \text{A6.17}$$

and

$$\overline{x'y'} = \sum_{n=1}^{b^e} \tilde{Co}_{xyn}^e \tilde{df}_n^e + \frac{1}{B} \sum_{j=1}^{B} \sum_{n=1}^{b} \tilde{Co}_{xynj} \tilde{df}_n \; . \qquad \text{A6.18}$$

A7. CONFIDENCE INTERVAL FOR Γ_n

Because assigning confidence limits to the results of a process requires knowing or assuming the probability

distribution of that process, we should spend a few moments reviewing the notation of probability and statistics before moving on to a discussion of confidence intervals.

We will denote a 'random variable' by $\underline{x}$: $\underline{x}_i$ and $\underline{x}_j$ are observations of the random variable at times i and j, respectively, with x_i and x_j the results of these observations. Assume $\underline{x}$ is normally distributed with mean zero and variance one: that is, $\underline{x}$ is normal(0,1). If a random variable $\underline{y}$ is instead normal with mean μ and variance σ^2, we can make it normal(0,1) with the transformation

$$\underline{x} = \frac{\underline{y} - \mu}{\sigma} .$$

Let us generate a series of observations of $\underline{x}$, $\{\underline{x}_k\}$, containing N samples. The 'sample average' of this series is

$$\bar{\underline{x}} = \frac{1}{N} \sum_{i=0}^{N-1} \underline{x}_i ,$$

and the 'sample variance' is

$$\underline{s}^2 = \frac{1}{N} \sum_{i=0}^{N-1} (\underline{x}_i - \bar{\underline{x}})^2$$

$$= \frac{1}{N} \sum_{i=0}^{N-1} \underline{x}_i^2 - \bar{\underline{x}}^2 .$$

The true distribution mean of a quantity of interest is the 'ensemble average' (Lumley and Panofsky, 1964) or the

'expected value' (Brunk, 1965) and is denoted by E[ ]. For the expected value of the variance of the distribution we write V[ ]. Hence,

$$E[\underline{x}] = 0$$

$$E[\bar{\underline{x}}] = E[\frac{1}{N} \sum_{i=0}^{N-1} \underline{x}_i]$$

$$= \frac{1}{N} \sum_{i=0}^{N-1} E[\underline{x}_i] = 0$$

$$V[\underline{x}] = E[\underline{x} - E[\underline{x}]]^2$$

$$= E[\underline{x}^2] - E[\underline{x}]^2 = 1$$

$$E[\underline{y}] = \mu$$

$$V[\underline{y}] = E[\underline{y}^2] - \mu^2 = \sigma^2 .$$

Finally, we define the correlation coefficient,

$$\rho_{i-j} = \frac{E[(\underline{y}_i - \mu)(\underline{y}_j - \mu)]}{\sigma^2} . \qquad \text{A7.1}$$

Clearly, this is an even function,

$$\rho_{i-j} = \rho_{j-i} .$$

And

$$|\rho| \leq 1$$

since for i=j the numerator of A7.1 is σ^2,

The crux of defining the probability distribution of Φ_n and thereby establishing a mathematical basis for assigning a confidence interval to Γ_n, the true spectrum, is proving the independence of any two members $\underline{x}_i$ and $\underline{x}_j$ of the time series $\{\underline{x}_k\}$. The masterworks in the field of spectral analysis either beg the question or do not treat confidence intervals at all. For example, Jenkins and Watts (1968) assume their time series is white noise and so by definition uncorrelated. However, most time series are not as trivial as this. In turbulence research we might study a time series of the horizontal wind speed, $\{\underline{u}_k\}$. Everyone knows this series is correlated: the correlation coefficient

$$\rho_{i-j} = \frac{E[(\underline{u}_i - \mu)(\underline{u}_j - \mu)]}{\sigma^2}$$

is not always zero but rather depends on the time separation, k = i-j, between observations. The smaller k is, the better the correlation. For large k the correlation coefficient becomes zero -- the series eventually 'forgets' what has happened before. After such reflection there seems little hope of showing any two $\underline{x}_i$ and $\underline{x}_j$ of a geophysical time series are uncorrelated. We can, however, design our experiment to approximate this condition as closely as we like.

Consider the sample correlation between $\underline{x}_i$ and $\underline{x}_j$. That is

$$\overline{\underline{x}_i \underline{x}_j} = \frac{1}{N^2} \sum_{i=0}^{N-1} \sum_{j=0}^{N-1} \underline{x}_i \underline{x}_j \ .$$

The expected value of this is

$$E[\overline{\underline{x}_i \underline{x}_j}] = \frac{1}{N^2} \sum_{i=0}^{N-1} \sum_{j=0}^{N-1} \rho_{i-j} \qquad \text{A7.2}$$

since the standard deviation of $\underline{x}$ is 1. To strictly establish the independence of any two observations in the time series, A7.2 must be zero. As we've explained, this is obviously not true for most geophysical time series. However, let us continue on to investigate just how close to zero A7.2 is.

Write A7.2 as

$$E[\overline{\underline{x}_i \underline{x}_j}] = \frac{1}{N^2} \sum_{i=0}^{N-1} \left[\sum_{j=0}^{i} \rho_{i-j} + \sum_{j=i}^{N-1} \rho_{i-j} \right] - \frac{1}{N} \ . \qquad \text{A7.3}$$

In the second summation on the right make the substitutions

$$n = N - 1 - i$$

$$m = N - 1 - j \ .$$

Then

$$\sum_{i=0}^{N-1} \sum_{j=i}^{N-1} \rho_{i-j} = \sum_{n=0}^{N-1} \sum_{j=N-1-n}^{N-1} \rho_{N-1-n-j}$$

$$= \sum_{n=0}^{N-1} \sum_{m=0}^{n} \rho_{m-n} \ .$$

Thus, because ρ_{i-j} is even,

$$E[\overline{\underline{x}_i \underline{x}_j}] = \frac{2}{N^2} \sum_{i=0}^{N-1} \sum_{j=0}^{i} \rho_{j-i} - \frac{1}{N} \quad . \qquad \text{A7.4}$$

Next let k = j-i. We get from A7.4

$$E[\overline{\underline{x}_i \underline{x}_{i+k}}] \approx \frac{2}{N^2} \sum_{i=0}^{N-1} \sum_{k=0}^{i} \rho_k \quad . \qquad \text{A7.5}$$

Suppose now for illustrative purposes that ρ_k is a correlation coefficient linearly decreasing with time separation:

$$\begin{aligned} \rho_k &= 1 - \frac{k}{r} \qquad \text{for } 0 \leq |k| < r \ , \\ &= 0 \qquad\qquad\ \ \text{for } |k| \geq r \ . \end{aligned} \qquad \text{A7.6}$$

Tennekes and Lumley (1972, p. 210) explain that the integral scale

$$T = \Delta \sum_{k=0}^{\infty} \rho_k \qquad \text{A7.7}$$

is a measure of the time over which $\underline{x}$ remains correlated with itself. For the correlation coefficient modeled by A7.6 the integral scale is about $\Delta r/2$. Keep this in mind. On substituting A7.6 into A7.5 we can at last approximate

$$E[\overline{\underline{x}_i \underline{x}_{i+k}}] = \frac{2}{N^2} \sum_{i=0}^{r} \sum_{k=0}^{i} (1 - \frac{k}{r})$$

$$= \frac{2}{N^2} \sum_{i=0}^{r} [i - \frac{i(i+1)}{2r}]$$

$$= \frac{1}{N^2}[r(r+1) - \frac{1}{r}[\frac{r(r+1)(2r+1)}{6} + \frac{r(r+1)}{2}]]$$

$$= \frac{2(r+1)(r-1)}{3N^2} \quad . \qquad \text{A7.8}$$

The result A7.8 demonstrates what is important in determining the correlation of a process: the longer the sampling time or the poorer the 'memory' of the signal, the smaller the expected value of the correlation. For example, if Δr is of order ten seconds and our sampling time ΔN is five minutes, then

$$E[\overline{\underline{x}_i \underline{x}_{i+k}}] \sim (\frac{10}{300})^2 \sim 0.001 :$$

that is, the expected value of the correlation is 0.1% of the sample variance. Our conclusion is that given a finite integral scale, we can choose a sampling time for any process which forces the expected value of the correlation to be approximately zero. In other words, the assumption that any two observations in our sample are independent is well justified.

Now we can go on to establish the probability distribution of the spectral density estimates. We'll assume our observable is the $\underline{y}$ defined earlier which was normal(μ,σ^2). As always

$$\underline{Y}_n = \sum_{k=0}^{N-1} \underline{y}_k \, e^{-2\pi ink/N} \; .$$

And since by proper sampling we can force the $\underline{y}_k$'s to be approximately independent,

$$E[\underline{y}_i \underline{y}_j] = \sigma^2 \delta_{ij} - \mu^2 \; . \qquad \text{A7.9}$$

Our first step is to determine the mean and variance of $\underline{Y}_n$:

$$E[\underline{Y}_n] = \sum_{k=0}^{N-1} E[\underline{y}_k] \, e^{-2\pi ink/N}$$

$$= N\mu\delta_{n0} \qquad \text{A7.10}$$

from A2.8. The correlation between any two $\underline{Y}_n$'s is

$$E[\underline{Y}_n \underline{Y}_m^*] = \sum_{k=0}^{N-1} e^{-2\pi ink/N} \sum_{k'=0}^{N-1} e^{2\pi imk'/N} E[\underline{y}_k \underline{y}_{k'}]$$

$$= N \, \sigma^2 \, \delta_{mn} - N^2 \, \mu^2 \, \delta_{n0} \, \delta_{m0} \qquad \text{A7.11}$$

on the basis of A7.9 and A2.8. That is,

$$E[\underline{Y}_0 \underline{Y}_0^*] = N \, \sigma^2 - N^2 \mu^2$$

$$E[\underline{Y}_n \underline{Y}_n^*] = N \, \sigma^2 \qquad n \neq 0 \qquad \text{A7.12}$$

$$E[\underline{Y}_n \underline{Y}_m^*] = 0 \qquad n \neq m \ .$$

Consequently,

$$V[\underline{Y}_n] = N\,\sigma^2 \qquad n=0,1,\ldots,N-1 \ . \quad \text{A7.13}$$

Therefore, since the $\underline{y}_k$'s are normally distributed, the $\underline{Y}_n$'s are also normally distributed such that

$$\underline{Y}_0 \rightarrow \text{normal}(N\mu, N\sigma^2)$$

$$\underline{Y}_n \rightarrow \text{normal}(0, N\sigma^2) \ .$$

Our development will continue along smoothly if we write $\underline{Y}_n$ as

$$\underline{Y}_n = \sum_{k=0}^{N-1} [\underline{y}_k \cos \frac{2\pi nk}{N} + i \sin \frac{2\pi nk}{N}]$$

$$= \underline{Y}_n^R + i\,\underline{Y}_n^I \ . \quad \text{A7.14}$$

With little trouble we can show that $\underline{Y}_n^R$ and $\underline{Y}_n^I$ are uncorrelated for all n and m and that each is uncorrelated with itself unless n = m. For example, look at

$$E[\underline{Y}_n^R \underline{Y}_m^R] = \tfrac{1}{4} \sum_{k=0}^{N-1} (e^{2\pi ink/N} + e^{-2\pi ink/N}) \sum_{k'=0}^{N-1} (e^{-2\pi imk'/N}$$

$$+ e^{2\pi imk'/N}) E[\underline{y}_k \underline{y}_{k'}] \ .$$

Substituting A7.9 and summing, this is

$$E[\underline{Y}^R_{-n}\underline{Y}^R_{-m}] = \frac{N\sigma^2}{4}\sum_{k=0}^{N-1}(e^{2\pi i(n-m)k/N} + e^{2\pi i(n+m)k/N} + e^{-2\pi i(n+m)k/N} + e^{-2\pi i(n-m)k/N}) - N^2\mu^2\delta_{n0}\delta_{m0}\,, \qquad \text{A7.15}$$

which reduces to

$$E[\underline{Y}^R_{-n}\underline{Y}^R_{-m}] = \frac{N\sigma^2}{2}[\delta_{nm} + \delta_{n,-m}] - N^2\mu^2\delta_{n0}\delta_{m0}\,. \qquad \text{A7.16}$$

But notice

$$e^{2\pi i(n+m)k/N} = e^{2\pi i(n+m-N)k/N}\,.$$

Hence, A7.15 is also

$$E[\underline{Y}^R_{-n}\underline{Y}^R_{-m}] = \frac{N\sigma^2}{2}[\delta_{nm} + \delta_{n,N-m}] - N^2\mu^2\delta_{n0}\delta_{m0}\,. \qquad \text{A7.17}$$

Therefore, if we insist on our frequency index ranging between zero and N-1, $\delta_{n,-m}$ is non-zero only at n = m = 0, and $\delta_{n,N-m}$ is non-zero only when n = m = N/2. Thus, A7.16 and A7.17 are in summary

$$E[\underline{Y}^R_{-0}\underline{Y}^R_{-0}] = N\sigma^2 - N^2\mu^2$$

$$E[\underline{Y}^R_{-n}\underline{Y}^R_{-m}] = \frac{N\sigma^2}{2}\delta_{nm} \qquad n \neq 0, N/2$$

$$E[\underline{Y}^R_{-N/2}\underline{Y}^R_{-N/2}] = N\sigma^2\,.$$

The remaining statistical properties of $\underline{Y}^R_n$ and $\underline{Y}^R_n$ follow similarly. These are

$$\underline{Y}_0^R \rightarrow \text{normal}(N\mu, N\sigma^2)$$

$$\underline{Y}_n^R \rightarrow \text{normal}(0, \frac{N\sigma^2}{2}) \qquad n\neq 0, N/2$$

$$\underline{Y}_{N/2}^R \rightarrow \text{normal}(0, N\sigma^2) \qquad \text{A7.18}$$

$$\underline{Y}_n^I \rightarrow \text{normal}(0, \frac{N\sigma^2}{2}) \qquad n\neq 0, N/2$$

$$\underline{Y}_0^I \text{ and } \underline{Y}_{N/2}^I \rightarrow \text{identically zero}$$

Recall that

$$\underline{P}_{yn} = \underline{Y}_n \underline{Y}_n^* = \underline{Y}_n^R \underline{Y}_n^R + \underline{Y}_n^I \underline{Y}_n^I \ . \qquad \text{A7.19}$$

Since, $\underline{P}_{yn}$ is, thus, a random variable found by summing the squares of two independent, normally distributed random variables, $2\ \underline{P}_{yn}/N\sigma^2$ for $n\neq 0, N/2$ is a chi-square random variable with two degrees of freedom (see Brunk, 1965, p. 230). That is,

$$\frac{2\ \underline{P}_{yn}}{N\sigma^2} \rightarrow \underline{\chi}_2^2 \qquad n\neq 0, N/2$$

$$\text{A7.20}$$

$$\frac{\underline{P}_{y,N/2}}{N\sigma^2} \rightarrow \underline{\chi}_1^2 \ .$$

And we've arrived! Having established the probability distribution of $\underline{P}_{yn}$, we at last reach the firm footing of probability theory and should find the going easier. But before trekking on let us review the fundamentals of a chi-

square distribution. Remember, if a chi-square random variable has ν degrees of freedom, then

$$E[\underline{\chi}_\nu^2] = \nu$$
$$V[\underline{\chi}_\nu^2] = 2\nu \; ; \qquad \text{A7.21}$$

consequently,

$$\nu = \frac{2E[\underline{\chi}_\nu^2]^2}{V[\underline{\chi}_\nu^2]} \; . \qquad \text{A7.22}$$

Rather than working with the power spectrum in A7.20, we prefer to use the spectral density

$$\underline{\Phi}_{yn} = \frac{\Delta}{N}(2 - \delta_{n,N/2})\underline{P}_{yn} \qquad n=1,2,\ldots,N/2. \quad \text{A7.23}$$

By substituting A7.23 into A7.20, we show that

$$\frac{\underline{\Phi}_{yn}}{\Delta\sigma^2} \rightarrow \underline{\chi}_2^2 \qquad n=1,2,\ldots N/2-1$$
$$\frac{\underline{\Phi}_{y,N/2}}{\Delta\sigma^2} \rightarrow \underline{\chi}_1^2 \; . \qquad \text{A7.24}$$

However, Sections A4 and A5 explained that we are seldom concerned with the raw spectral density, $\underline{\Phi}_{yn}$, but instead will average c_n raw densities (note: $c_n = BE_n - BE_{n-1}$) to get the nth band average and further average each band over B blocks (refer to equation A5.1). Hence, the smoothed spectral density estimate, $\underline{\tilde{\Phi}}_{yn}$, is the result of adding the squares of $2c_nB$ independent, normally distributed random

variables. It will, thus, have approximately $2c_nB$ degrees of freedom.

Therefore, we wish to form a random variable from $\underline{\tilde{\Phi}}_{yn}$ such that

$$\frac{a\,\underline{\tilde{\Phi}}_{yn}}{\Delta\sigma^2} \rightarrow \chi^2_{2c_nB} \quad . \qquad \text{A7.25}$$

From A7.21 we can find a. That requires

$$2c_nB = \frac{a}{\Delta\sigma^2}\left[\frac{1}{c_nB}\sum_{j=1}^{B}\sum_{k=BE_{n-1}+1}^{BEn} E[\underline{\Phi}_{kj}]\right] .$$

Using A7.23 and A7.19 we get

$$2c_nB = \frac{a}{\Delta\sigma^2}\frac{1}{c_nB}\frac{\Delta}{N}(2 - \delta_{n,N/2})\sum_{j=1}^{B}\sum_{k} E[\underline{Y}^R_{jk}Y^R_{jk} + \underline{Y}^I_{jk}\underline{Y}^I_{jk}] ,$$

which from A7.18 reduces to

$$2c_nB = \frac{a}{\sigma^2 N}(2 - \delta_{n,N/2})\left[\frac{N\sigma^2}{(2-\delta_{n,N/2})} + \frac{N\sigma^2}{2}\delta_{n,N/2}\right] ,$$

or

$$a = c_nB \quad .$$

With more algebra than we care to mess with here it can be shown that $\underline{\tilde{\Phi}}_{yn}$ is an unbiased estimator of Γ_{yn}, the true spectral density: that is,

$$E[\underline{\tilde{\Phi}}_{yn}] = \Gamma_{yn} \quad .$$

Hence, recalling A5.1 and using A7.23 and A7.19,

$$E[\tilde{\underline{\Phi}}_{yn}] = \Gamma_{yn} = 2\Delta\sigma^2 \ . \qquad \text{A7.27}$$

Substituting A7.26 and A7.27 into A7.25, we finally demonstrate that

$$\frac{2c_nB\ \tilde{\underline{\Phi}}_{yn}}{\Gamma_{yn}} \rightarrow \chi^2_{2c_nB} \ . \qquad \text{A7.28}$$

Because of the fact that the Fourier coefficients are only approximately independent for a non-trival time series, we prefer to estimate the degrees of freedom rather than assume ν is simply $2c_nB$. To do that we appeal to A7.22 using the sample mean and the variance of the sample mean. So note that if for a series of observables $\{x_k\}$ we calculate

$$\bar{x} = \frac{1}{N} \sum_{k=1}^{N} x_k \ ,$$

then

$$V[\bar{x}] = \frac{1}{N^2} \sum_{k=1}^{N} V[x_k] = \frac{1}{N} V[x_k] \ .$$

Likewise we relate the sample standard deviation, s, to the sample standard deviation of the mean, S:

$$S^2 = \frac{1}{N} s^2 \ . \qquad \text{A7.29}$$

In our problem $\tilde{\Phi}_{yn}$ is the sample mean. The sample standard deviation, s_{yn}, is consequently

$$s_{yn}^2 = \frac{1}{c_n B} \sum_{j=1}^{B} \sum_{k=BE_{n-1}+1}^{BE_n} \Phi_{ykj}^2 - \tilde{\Phi}_{yn}^2 \quad . \qquad \text{A7.30}$$

Hence, from A7.29 the sample variance of the mean, S_{yn}^2, is

$$S_{yn}^2 = \frac{1}{c_n B} s_{yn}^2 \quad . \qquad \text{A7.31}$$

Then finally

$$\nu_n = \frac{2 \tilde{\Phi}_{yn}^2}{S_{yn}^2} \qquad \text{A7.32}$$

and we, consequently, modify A7.28 to read

$$\frac{\nu_n \tilde{\Phi}_{yn}}{\Gamma_{yn}} \rightarrow \chi_{\nu_n}^2 \quad . \qquad \text{A7.33}$$

In general, considering A7.31, we expect ν_n will be roughly $2c_n B$.

Everything is now ready for our placing confidence limits of Γ_{yn}. Because of A7.33 we can make the probability statements

$$\Pr\{\frac{\nu \tilde{\Phi}_{yn}}{\Gamma_{yn}} < \chi_{\nu,\alpha}^2\} = \alpha$$

$$\Pr\{\frac{\nu \tilde{\Phi}_{yn}}{\Gamma_{yn}} \leq \chi_{\nu,1-\alpha}^2\} = 1 - \alpha \ , \qquad \text{A7.34}$$

where α is an arbitrary, small number and $\chi^2_{\nu,\alpha}$ is the 100α percentage point of a chi-square distribution with ν degrees of freedom. Rearranging A7.34 we have expressions for the confidence limits of Γ_{yn}.

$$\Pr\{b = \frac{\nu\ \tilde{\Phi}_{yn}}{\chi^2_{\nu,\alpha}} < \Gamma_{yn}\} = \alpha$$

$$\Pr\{a = \frac{\nu\ \tilde{\Phi}_{yn}}{\chi^2_{\nu,1-\alpha}} \leq \Gamma_{yn}\} = 1 - \alpha\ . \qquad \text{A7.35}$$

[a,b] is, thus, a $100(1 - 2\alpha)\%$ confidence interval for Γ_{yn}.

An an exercise, suppose we find $\nu = 30$ and desire a 95% confidence interval on Γ_{yn}: in other words, $\alpha = 0.025$. From readily available tables

$$\chi^2_{30,0.025} = 16.79$$

$$\chi^2_{30,0.975} = 46.98\ ,$$

so

$$a = \frac{30\ \tilde{\Phi}_{yn}}{46.98}$$

$$b = \frac{30\ \tilde{\Phi}_{yn}}{16.79}\ .$$

That was pretty easy. But many time series will contain so many blocks and/or such long records that a smoothed spectral density estimate could have anywhere from 100 to

20,000 degrees of freedom. Few tables tabulate the chi-square distribution beyond 100 degrees of freedom. However, for large degrees of freedom a normal approximation is well-founded: the C.R.C. handbook of probability and statistics (Beyer, 1966) gives the following approximation for the 100α percentage point of a chi-square distribution with more than thirty degrees of freedom:

$$\chi^2_{\nu,\alpha} = \tfrac{1}{2}[z_\alpha + (2\nu - 1)^{\frac{1}{2}}]^2 \ , \qquad \text{A7.36}$$

where z_α is the 100α percentage point of a cumulative normal distribution.

A8. CONFIDENCE INTERVAL FOR Γ_{xyn}

We have yet to find a proof which establishes the probability distribution of $\underline{\tilde{\Phi}}_{xyn}$, the cross spectral density estimate; therefore, we appeal to the Central Limit Theorem as a basis for assigning confidence limits to Γ_{xyn}. That theorem states that the distribution of the sample mean approaches a normal distribution as the size of the sample gets large. Because our block and band averages may be comprised of from 50 to 10,000 raw spectral estimates, assuming $\underline{\tilde{\Phi}}_{xyn}$ is normal seems reasonable. Hence, drawing on the volumes written about the normal distribution we can easily place rough confidence limits on Γ_{xyn}.

If we again define the sample variance $\underline{S}^2_{xyn}$, of the sample mean, $\underline{\tilde{\Phi}}_{xyn}$, as in A7.30 and A7.31, we can form an

approximately normal(0,1) random variable, thusly,

$$\underline{z} = \frac{\tilde{\underline{\Phi}}_{xyn} - \Gamma_{xyn}}{\underline{S}_{xyn}} \quad . \qquad \text{A8.1}$$

The reader might argue that because we must use the sample variance, a t-statistic would be more appropriate. But recall, the t-distribution approaches a normal distribution as the sample size grows.

Probability statements about A8.1 follow immediately.

$$\Pr\{\frac{\tilde{\underline{\Phi}}_{xyn} - \Gamma_{xyn}}{\underline{S}_{xyn}} < -z_{\alpha}\} = \alpha \ ,$$

$$\Pr\{\frac{\tilde{\underline{\Phi}}_{xyn} - \Gamma_{xyn}}{\underline{S}_{xyn}} \leq z_{\alpha}\} = 1 - \alpha, \qquad \text{A8.2}$$

where z_{α} is the 100α percentage point of the normal distribution. A few manipulations of A8.2 yield

$$\Pr\{b = \tilde{\underline{\Phi}}_{xyn} + z_{\alpha}\underline{S}_{xyn} < \Gamma_{xyn}\} = \alpha$$

$$\Pr\{a = \tilde{\underline{\Phi}}_{xyn} - z_{\alpha}\underline{S}_{xyn} \leq \Gamma_{xyn}\} = 1 - \alpha. \qquad \text{A8.3}$$

Obviously, [a,b] is a $100(1 - 2\alpha)\%$ confidence interval for Γ_{xyn}. If, for example, we desire a 95% confidence interval for Γ_{xyn}, then $z_{\alpha} = 1.960$. So

$$a = \tilde{\Phi}_{xyn} - 1.960\ S_{xyn}$$
$$b = \tilde{\Phi}_{xyn} + 1.960\ S_{xyn} \ .$$

A9. THE FAST FOURIER TRANSFORM

Most of the spectral analysis we do is economically possible (with respect to both money and time) only because of the fast Fourier transform (FFT). That algorithm is roughly N times faster than the direct transform of equation A2.1. Therefore, since, we've spent most of our energy describing the mathematics of spectral analysis given the Fourier coefficients, it might be worthwhile to at last add a few words about the mechanics of generating those coefficients.

Let us look again at the series used in A2.1. Write the Fourier transform as

$$X_n^N = \sum_{k=0}^{N-1} x_k \, e^{-2\pi i n k/N} , \qquad \text{A9.1}$$

where we introduce the superscript N to indicate the number of samples in the data series. Suppose we divide the series $\{x_k\}$ into two unique series $\{y_k\}$ and $\{z_k\}$ each of length N/2, thusly,

$$y_k = x_{2k}$$
$$z_k = x_{2k+1} \cdot \qquad k=0,1,\ldots,N/2-1$$

Then the Fourier coefficients of these new series are

$$Y_n^{N/2} = \sum_{k=0}^{N/2-1} y_k \, e^{-4\pi ink/N}$$

$$n=0,1,\ldots,N-1 \qquad \text{A9.2}$$

$$Z_n^{N/2} = \sum_{k=0}^{N/2-1} z_k \, e^{-4\pi ink/N} \, .$$

Or we could write X_n^N in terms of the new series

$$X_n^N = \sum_{k=0}^{N/2-1} [y_k \, e^{-2\pi in(2k)/N} + z_k \, e^{-2\pi in(2k+1)/N}] \, ,$$

which yields

$$X_n^N = Y_n^{N/2} + e^{-2\pi in/N} \, Z_n^{N/2} \, . \qquad \text{A9.3}$$

Now let's go another step farther -- divide each of our new series in two again. Set

$$y'_k = y_{2k}$$

$$z'_k = y_{2k+1}$$

$$k=0,1,\ldots,N/4-1$$

$$y''_k = z_{2k}$$

$$z''_k = z_{2k+1} \, .$$

As before

$$Y'^{N/4}_n = \sum_{k=0}^{N/4-1} y'_k \, e^{-8\pi ink/N}$$

$$n=0,1,\ldots,N/2-1 \qquad \text{A9.4}$$

$$Z'^{N/4}_n = \sum_{k=0}^{N/4-1} z'_k \, e^{-8\pi ink/N}$$

and so forth. In terms of the new series

$$Y_n^{N/2} = \sum_{k=0}^{N/4-1} [y'_k \, e^{-4\pi in(2k)/N} + z'_k \, e^{-4\pi in(2k+1)/N}] \; .$$

Or

$$Y_n^{N/2} = Y'^{N/4}_n + e^{-4\pi in/N} \, Z'^{N/4}_n$$

$$n=0,1,\ldots,N/2-1 \qquad \text{A9.5}$$

$$Z_n^{N/2} = Y''^{N/4}_n + e^{-4\pi in/N} \, Z''^{N/4}_n \; .$$

It's now possible to generalize from A9.3 and A9.5. If we've divided our original N samples into N/m series of m samples each, then

$$X_n^{2m} = Y_n^m + W^n \, Z_n^m \qquad \text{A9.6}$$

where

$$W \equiv e^{-\pi i/m} \; . \qquad \text{A9.7}$$

But from A9.2 and A9.4 we can show that

$$Y_{n+m}^m = Y_n^m$$

$$Z_{n+m}^m = Z_n^m \; . \qquad \text{A9.8}$$

And from A9.7

$$W^{n+m} = -W^n \; . \qquad \text{A9.9}$$

Thus, the computation of X_n^{2m} is further simplified because

$$X_{n+m}^{2m} = Y_n^m - W^n \, Z_n^m \; . \qquad \text{A9.10}$$

Equations A9.6 and A9.10, thus, constitute the fast Fourier transform algorithm:

$$X_n^{2m} = Y_n^m + W^n Z_n^m$$

$$X_{n+m}^{2m} = Y_n^m - W^n Z_n^m \qquad \text{A9.11}$$

$$n=0,1,\ldots,m-1.$$

By now the scheme for use of the FFT should be glimmering, at least faintly. If the number of samples, N, in our original series is a power of two, we can continually divide it in two until we have formed N new series of one sample each. But the direct Fourier transforms of these one-sample series are the sample values themselves. We then climb back up the ladder generating progressively higher order Fourier coefficients using the algorithm of A9.11 until we reach the ultimate coefficient, X_n^N. If N is not a power of two, we divide it by two until reaching an odd number, p, split our N samples into N/p series of p samples each, compute the direct Fourier transform of these N/p series, and again apply the FFT algorithm, A9.11, to compute higher order Fourier coefficients.

It might facilitate our understanding the FFT to look at an example. Take a time series $\{x_k\}$ for which N=8. Figure A9.1 is a signal flow graph (after Cochran, et al., 1967) which demonstrates the workings of the FFT in this case. On a signal flow graph the dots (or nodes) represent

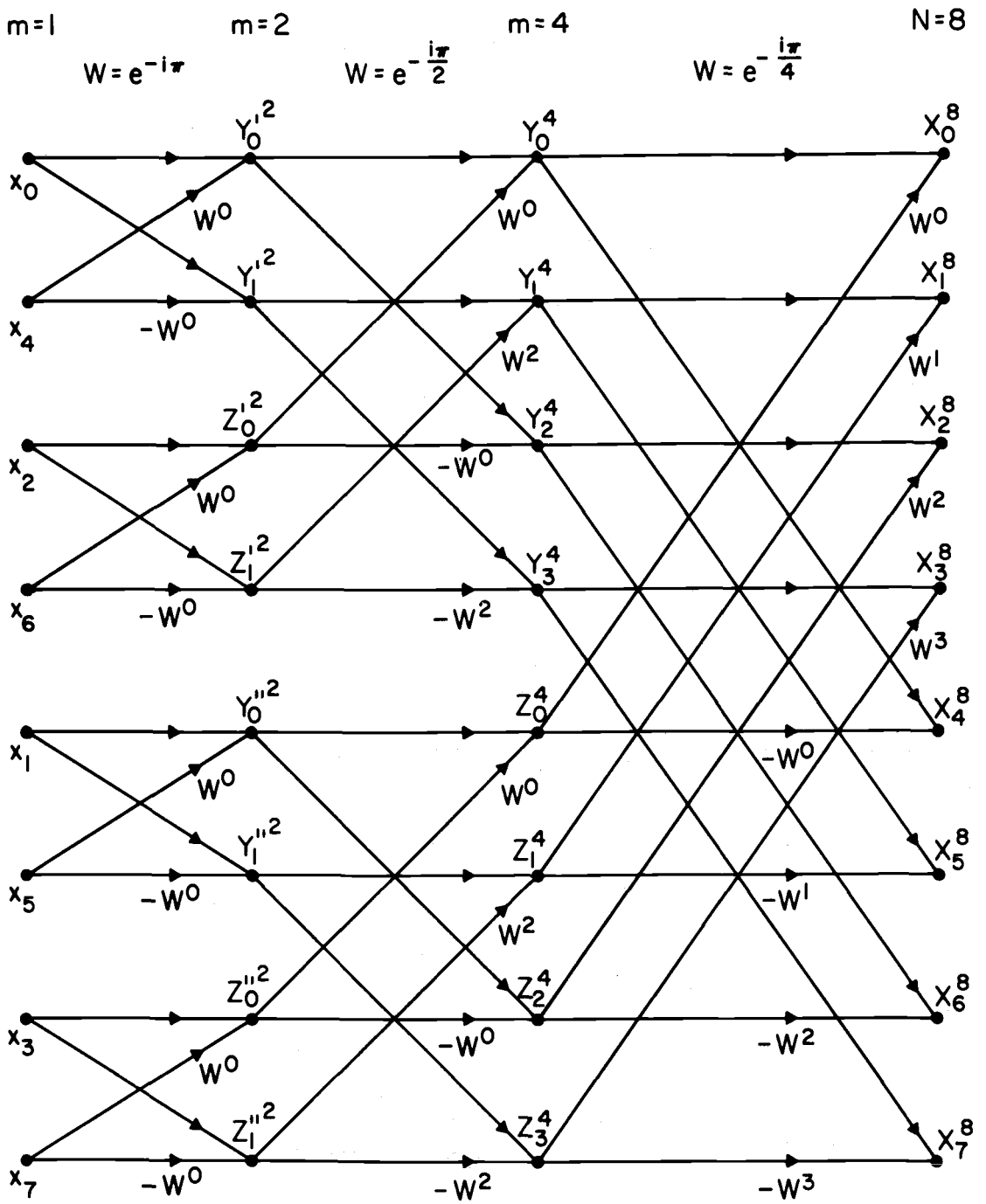

Figure A9.1. A signal flow graph demonstrating the fast Fourier transform for N = 8.

variables and the arrow heads specify transmissions. Each node is the sum of the nodes pointing into it with weight factors noted near the arrow heads. So, for example in Figure A9.1, X_0^8 in the upper right is

$$X_0^8 = Y_0^4 + W^0 \, Z_0^4 \ .$$

In this FFT signal flow graph the variables down the left side are the original eight one-sample time series and are themselves the Fourier coefficients contributing to the next level of nodes. On the right are the final Fourier coefficients. The arrows lead from the time series to its Fourier transform specifying the summations and multiplications required by A9.11.

A10. FFT PECULIARITIES

Because the time series $\{x_k\}$ used in A2.1 need not be real, it's economical for any FFT computer software to always process a complex time series. Hence, most FFT packages yield the transform of the complex series $\{x_k\}$, where

$$x_k = y_k + i \, z_k \ , \qquad \text{A10.1}$$

$\{y_k\}$ and $\{z_k\}$ being real series. Consequently, if we have only real data, it's feasible and, in fact, prudent to transform two time series simultaneously by entering them in the form of A10.1.

We may, for example, have a horizontal and a vertical velocity series, $\{u_k\}$ and $\{w_k\}$, respectively, and so could call for the Fourier transform of $\{x_k\}$, where

$$x_k = u_k + i\, w_k \ . \qquad \text{A10.2}$$

This is simply

$$X_n = \sum_{k=0}^{N-1} x_k\, e^{-2\pi ink/N} \ . \qquad \text{A10.3}$$

On substituting A10.2 into A10.3 we get the individual transforms of the u and w series,

$$X_n = \sum_{k=0}^{N-1} [u_k\, e^{-2\pi ink/N} + i\, w_k\, e^{-2\pi ink/N}]$$

$$= U_n + i\, W_n \ . \qquad \text{A10.4}$$

As usual

$$U_n = \sum_{k=0}^{N-1} u_k\, e^{-2\pi ink/N}$$

$$\text{A10.5}$$

$$W_n = \sum_{k=0}^{N-1} w_k\, e^{-2\pi ink/N} \ .$$

Because U_n and W_n are, in general, complex -- that is,

$$U_n = U_n^R + i\, U_n^I$$

$$\text{A10.6}$$

$$W_n = W_n^R + i\, W_n^I$$

-- they will not be as easy to retrieve as A10.4 might imply. To enter the data in the form A10.2 we stored $\{u_k\}$ in a real array and $\{w_k\}$ in an imaginary array. The transform coefficients are likewise returned with the real part in the real array and the imaginary part in the imaginary array. So it would be more appropriate to write A10.4 as

$$X_n = X_n^R + i\, X_n^I \quad , \qquad \text{A10.7}$$

where now X_n^R and X_n^I are the real and imaginary parts, respectively, and so both real numbers. Clearly,

$$\begin{aligned} X_n^R &= U_n^R - W_n^I \\ X_n^I &= U_n^I + W_n^R \ . \end{aligned} \qquad \text{A10.8}$$

To deduce the four quantities U_n^R, U_n^I, W_n^R, and W_n^I from the two stored terms X_n^R and X_n^I will require some algebra. From A10.5 we show that since u_k and w_k are real

$$\begin{aligned} U_n^* &= U_{N-n} \\ W_n^* &= W_{N-n} \ . \end{aligned} \qquad \text{A10.9}$$

Thus, if

$$X_n = U_n + i\, W_n \ ,$$

then

$$X^*_{N-n} = U_n - i\, W_n \ .$$

Hence,

$$U_n = \tfrac{1}{2}[X_n + X^*_{N-n}]$$

$$W_n = -i/2[X_n - X^*_{N-n}] \ . \qquad \text{A10.10}$$

Or using A10.7 and rearranging, we finally get expressions for the real and imaginary parts of the Fourier coefficients U_n and W_n:

$$U_n = \tfrac{1}{2}[(X^R_n + X^R_{N-n}) + i(X^I_n - X^I_{N-n})]$$

$$W_n = \tfrac{1}{2}[(X^I_n + X^I_{N-n}) + i(X^R_n - X^R_{N-n})] \qquad \text{A10.11}$$

$$n=0,1,\ldots,N-1.$$

Usually the software sets

$$X_N = X_0 \ ,$$

so for n=0 and n=N/2 both U_n and W_n are real as expected.

In performing the FFT a computer must sometimes scale the results to keep the numbers in a range it can accommodate. This scaling is simply multiple divisions by two of every coefficient. When the FFT is completed, the computer notes the scale factor, c, which is the number of such divisions. The true Fourier coefficients are, thus, related to the stored coefficients by

$$U_n^{true} = 2^c U_n$$

$$W_n^{true} = 2^c W_n \quad . \qquad \text{A10.12}$$

A.11 CALIBRATION COMPLICATIONS

Our introduction explained that we record turbulence data -- transducer voltage signals -- in analog form on magnetic tape, digitize this analog data, and store the digital results as integers on a computer-compatible magnetic tape. All the spectral analysis is done using this digitized data. Thus, there are several processing steps between the physical observable and its spectral density: a calibration equation for each of these will likely be necessary.

Suppose we are fortunate -- suppose every step in our data handling involves only a linear calibration. If x is the observable, t the corresponding transducer voltage, v the analog tape voltage, and m the digital tape integer, a typical set of calibration equations might include the following:

1. Calibration of the transducer--

$$x = a_1 t + b_1 \qquad \text{A11.1}$$

2. Signal processing and analog tape conversion--

$$t = a_2 v + b_2 \qquad \text{A11.2}$$

3. Analog to digital conversion--

$$v = a_3 m + b_3 \ . \qquad \text{A11.3}$$

Obviously, with these happy circumstances the observable is a linear function of the mag tape integer,

$$x = a_1 a_2 a_3 m + a_1 a_2 b_3 + a_1 b_2 + b_1 \ , \qquad \text{A11.4}$$

$$x = a_x m + b_x \ . \qquad \text{A11.5}$$

Next look at what A2.1 says about the Fourier coefficients of the integers,

$$X_n = \sum_{k=0}^{N-1} (a_x m_k + b_x)\ e^{-2\pi i n k/N}$$

$$X_n = a_x M_n + b_x\ \delta_{n0} \ , \qquad \text{A11.6}$$

where as usual

$$M_n = \sum_{k=0}^{N-1} m_k\ e^{-2\pi i n k/N} \ . \qquad \text{A11.7}$$

The result A11.6 is extraordinarily convenient. It suggests the possibility of doing the FFT on the integer series rather than converting the integers back to

observables before the FFT. Because integer variables require half the computer memory that floating point variables do, such a routine has a lot to recommend it. If, for example, as in Section A10 we have time series of horizontal and vertical velocities which obey A11.5, we would write

$$u_k = a_u m_k + b_u \qquad w_k = a_u q_k + b_w \qquad \text{A11.8}$$

and

$$U_n = a_u M_n + b_u \delta_{n0} \qquad W_n = a_w Q_n + b_w \delta_{n0} \ . \qquad \text{A11.9}$$

The averages of u and w are by A11.9 simply

$$N\,\bar{u} = U_0 = a_u M_0 + b_u \qquad N\,\bar{w} = W_0 = a_w Q_0 + b_w \ . \qquad \text{A11.10}$$

From A3.1 and A4.3 the raw spectral density estimates are

$$\Phi_{un} = \frac{\Delta}{N} (2 - \delta_{n,N/2})\ a_u^2\ M_n M_n^* \qquad \Phi_{wn} = \frac{\Delta}{N} (2 - \delta_{n,N/2})\ a_w^2\ Q_n Q_n^* \qquad \text{A11.11}$$

$$n=1,2,\ldots,N/2 \ .$$

The import here is that since the multiplicative constants can be factored out of each of these spectral estimates and

because our smoothing operation, A5.1, is such a simple process, we save a lot of computing time by doing the FFT on the series of the integers, block and band averaging the raw spectral densities formed from the integer transforms, and then applying the calibration as the very last step instead of converting each individual integer to an observable by A11.8.

A12. DIGITIZING CONSIDERATIONS

In the introduction we simply assumed we had a time series sampled at $1/\Delta$ and containing B blocks, each of block length N. Now the reader has the background to understand how to select these three parameters, Δ, B, and N.

Δ is the most fundamental of the three because as A5.2 implies, the spectral analysis cannot provide information about frequencies higher than $1/2\Delta = f_{Ny}$, the Nyquist frequency of the sampling process. If disturbances with frequencies above the Nyquist frequency occur in the original signal, their contributions to the variance or covariance will be 'folded back' or 'aliased' in the spectral estimates at frequencies lower than $1/2\Delta$ and so must alter the true shape and variance of the spectrum.

To demonstrate this let us suppose $\{x_k\}$ contains frequencies higher than $1/2\Delta$; represent these by

$$f = \frac{m}{2\Delta} + \frac{r}{\Delta N} = m\, f_{Ny} + f_r \ , \qquad \text{A12.1}$$

where m is an integer greater than zero and r is an integer such that $0 < r < N/2$. Then $\{x_k\}$ will have components of the form

$$x_k = a\, e^{2\pi i f \Delta k} = a\, e^{2\pi i (m/2 + r/N) k} \ . \qquad \text{A12.2}$$

If m is an even number

$$X_n = a \sum_{k=0}^{N-1} e^{2\pi i (m/2+r/N) k}\ e^{-2\pi i n k/N}$$

$$= a\, N\, \delta_{nr} \ . \qquad \text{A12.3}$$

That is, frequencies of

$$f = 2f_{Ny} + f_r \ , \ 4f_{Ny} + f_r \ , \ 6f_{Ny} + f_r, \ldots$$

all contribute to the Fourier coefficient X_r.

If m is odd

$$X_n = a \sum_{k=0}^{N-1} e^{2\pi i (m/2+1/2-1/2+r/N) k}\ e^{-2\pi i n k/N}$$

$$= a \sum_{k=0}^{N-1} e^{\pi i (m+1)}\ e^{-2\pi i (n-N/2+r) k/N}$$

$$= a\, N\, \delta_{n,N/2-r} \ . \qquad \text{A12.4}$$

So each of the frequencies

$$f = f_{Ny} + f_r,\ 3f_{Ny} + f_r,\ 5f_{Ny} + f_r,\ \ldots$$

are aliased in the Fourier coefficient $X_{N/2-r}$. Figure A12.1 tries to show why we call this aliasing process 'folding': the frequency axis is apparently folded accordian fashion at multiples of f_{Ny}.

The moral of this exhibition is to choose Δ so that the Nyquist frequency is higher than any frequency in the signal. Or if we're unsure a priori just how high frequencies in the signal can be, filtering the data to remove all frequencies above the Nyquist would be a plausible alternative.

The selection of N is fairly straightforward. We wrote in the introduction that N was a power of two: Section A9, where we described the mechanics of the FFT, emphasized the reasons for this choice. Though some larger computers may have software to accommodate an arbitrary N, don't be surprised if most FFT packages categorically refuse to handle any N not a power of two. In general, N should be as large as computer storage limitations allow: the FFT is more economical and more accurate for large N.

The choice of the number of blocks, B, may, in the end, be a matter of convenience since ΔNB is the elapsed time of the experimental run. However, equation A6.15 indicates that B does play a crucial role in the shape of the spectrum. Because N^e is less than or equal to B, the lowest frequency the extended spectral estimates can

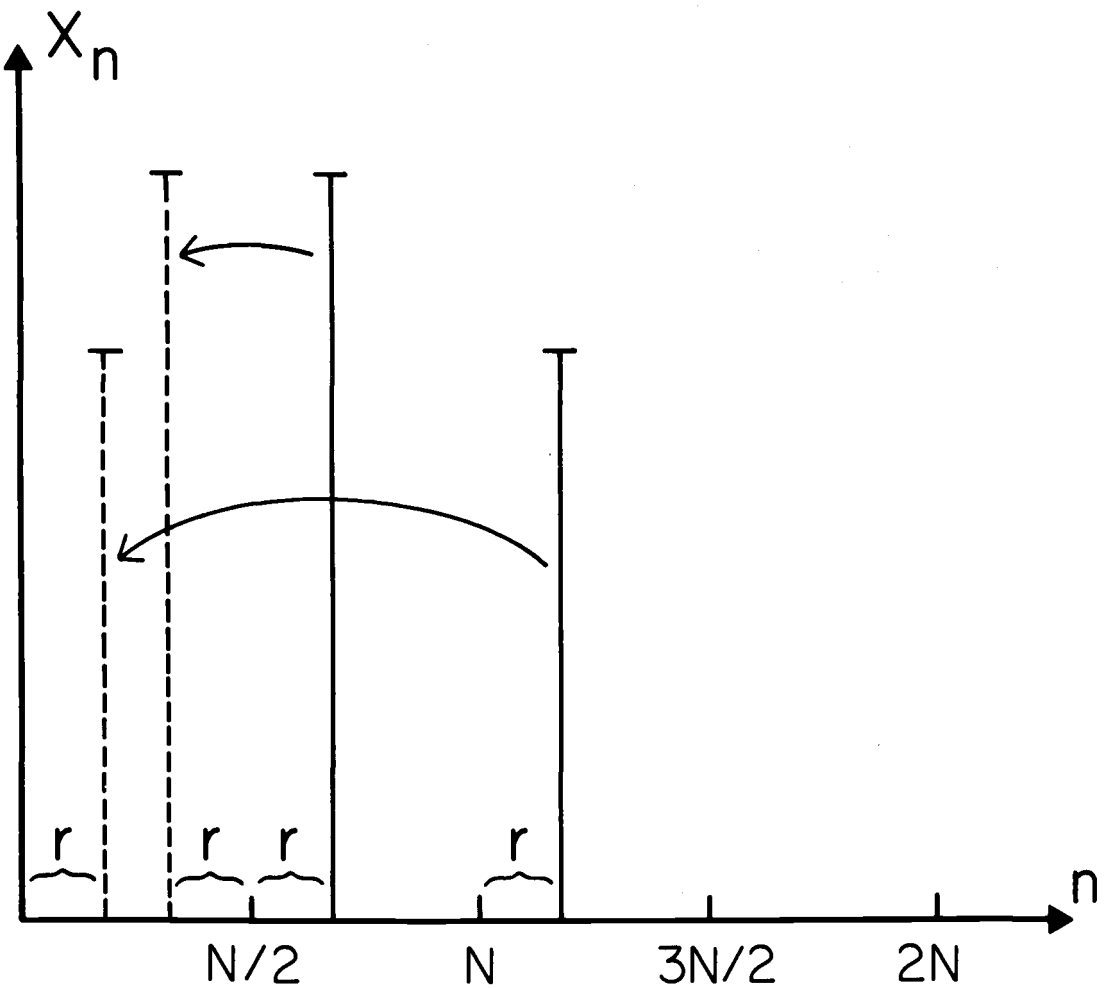

Figure A12.1. Aliasing of frequencies at $f_{Ny} + r/\Delta N$ and $2f_{Ny} + r/\Delta N$. The scale on the frequency axis is the frequency index. Notice the 'folding' about N/2 and N.

resolve is

$$f^{e}_{low} = \frac{1}{\Delta NB} \, . \qquad \text{A12.5}$$

Thus, our first thought might be to make ΔNB longer than the longest period oscillation we expect to encounter in our observable. But if that period is too long, synoptic changes may affect our signal and so ruin assumptions about stationarity. Consequently, to compromise let ΔNB be some small fraction of the synoptic period (say 1/10 or less) yet long enough to adequately sample the more energetic frequencies at the low frequency end of the spectrum. This isn't double talk because if we extend the spectrum to low enough frequencies we'll likely find $\tilde{\Phi}^{e}_{n} d\tilde{f}^{e}_{n}$ approaches zero and so no longer contributes to the variance or covariance in A6.17 and A6.18.

REFERENCES

BENDAT, J. S., and PIERSOL, A. G. 1971. Random Data: Analysis and Measurement Procedures. Wiley-Interscience, 407p.

BEYER, W. H., ed. 1966. Handbook of Tables for Probability and Statistics. The Chemical Rubber Co., 362p.

BRUNK, H. D. 1965. An Introduction to Mathematical Statistics, 2nd ed. Blaisdell Publishing Co., 429p.

COCHRAN, W. T., COOLEY, J. W., FAVIN, D. L., HELMS, H. D., KAENEL, R. A., LANG, W. W., MAILING, G. C., JR., NELSON, D. E., RADER, C. M., and WELCH, P. D. 1967. What is the fast Fourier transform? IEEE Trans. Audio Electroacoust. AU-15: 45-55.

JENKINS, G. M., and WATTS, D. G. 1968. Spectral Analysis and Its Applications. Holden-Day, 525p.

KANASEWICH, E. R. 1975. Time Sequence Analysis in Geophysics, 2nd ed. University of Alberta Press, 364p.

LUMLEY, J. L., and PANOFSKY, H. A. 1964. The Structure of Atmospheric Turbulence. Interscience, 239p.

OTNES, R. K., and ENOCHSON, L. 1972. Digital Time Series Analysis. Wiley-Interscience, 467p.

TENNEKES, H., and LUMLEY, J. L. 1972. A First Course in Turbulence. MIT Press, 300p.

APPENDIX B

THE ALEX PROFILE DATA

> Data! data! data! I can't make bricks without clay.
>
> Arthur Conan Doyle
> "The Adventure of the Copper Beeches"

On the following pages we list what we consider the highest quality downwind velocity and temperature profile data from the AIDJEX Lead Experiment. Lindsay (1976) makes a similar listing of the corresponding upwind profiles.

Our run number is referenced to the sequence number of the analog tape on which the raw data was recorded. The hundreds and tens digits of the run number give that analog tape number. The units digit specifies a section of selected data on an individual analog tape. And a number after the decimal point indicates that such a section was broken down into shorter intervals which are, thus, consecutive. For example, Run 121.1 and Run 121.2 are consecutive 21 minute runs from the first section of good data on analog tape 12.

The bulk Richardson number characterizes the flow over the lead. It is

$$Ri_B = \frac{g}{T_w} \frac{(T_{0.5} - T_w)(50\ \text{cm})}{U_{0.5}^2}, \qquad \text{B1}$$

where $T_{0.5}$ and $U_{0.5}$ are the temperature and velocity,

respectively, each at a height of 50 cm; T_w is the water temperature; and g is the appropriate acceleration of gravity, 982.7 cm/sec^2.

There are six profile levels. The velocity at the highest level was measured with a cup anemometer and averaged over the entire run. The velocities at the lower five levels are from the straight hot-film sensor, which spent one-fifth of the run at each of the five levels.

The lowest five temperature points were generated by the profiling thermocouple, which was also at each height for one-fifth of the run. The sixth point of the temperature profile comes from the differencing thermocouples. All are potential temperatures.

The occasional zeroes which appear in the profiles show where bad data points have been removed.

RUN: 11.0
****
DATE: MARCH 11, 1974
TIME: 1633 AST
DURATION: 14.93 MINUTES

FETCH (M)	T-WATER (C)	T-ICE (C)	BAROMETER (MM-HG)	RI-BULK
8.5	-2.0	-21.0	774.0	-0.0160

ZU (CM)	U (CM/SEC)	ZT (CM)	T (C)
10.	393.	10.	-19.65
26.	436.	26.	-20.46
56.	466.	56.	-20.82
94.	514.	94.	-20.94
140.	541.	140.	-21.04
235.	626.	190.	-21.08

RUN: 12.0
****
DATE: MARCH 11, 1974
TIME: 1657 AST
DURATION: 14.00 MINUTES

FETCH (M)	T-WATER (C)	T-ICE (C)	BAROMETER (MM-HG)	RI-BULK
8.5	-2.0	-20.8	774.0	-0.0153

ZU (CM)	U (CM/SEC)	ZT (CM)	T (C)
10.	372.	10.	-19.55
26.	427.	26.	-20.31
56.	477.	56.	-20.66
92.	502.	92.	-20.76
139.	524.	139.	-20.84
233.	622.	189.	-20.88

RUN: 31.0
****
DATE: MARCH 11, 1974
TIME: 2200 AST
DURATION: 15.36 MINUTES

FETCH (M)	T-WATER (C)	T-ICE (C)	BAROMETER (MM-HG)	RI-BULK
8.5	-2.1	-21.5	771.0	-0.0265

ZU (CM)	U (CM/SEC)	ZT (CM)	T (C)
10.	308.	10.	-19.93
26.	333.	26.	-20.95
56.	368.	56.	-21.41
93.	394.	93.	-21.62
140.	419.	140.	-21.68
232.	469.	190.	-21.71

RUN: 32.1
****
DATE: MARCH 11, 1974
TIME: 2222 AST
DURATION: 15.36 MINUTES

FETCH (M)	T-WATER (C)	T-ICE (C)	BAROMETER (MM-HG)	RI-BULK
8.5	-2.1	-21.6	771.0	-0.0226

ZU (CM)	U (CM/SEC)	ZT (CM)	T (C)
10.	318.	10.	-19.82
26.	359.	26.	-20.91
56.	398.	56.	-21.36
93.	419.	93.	-21.53
140.	443.	140.	-21.62
232.	497.	190.	-21.68

RUN: 32.2
****

DATE: MARCH 11, 1974
TIME: 2237 AST
DURATION: 15.36 MINUTES

FETCH (M)	T-WATER (C)	T-ICE (C)	BAROMETER (MM-HG)	RI-BULK
8.5	-2.1	-21.7	771.0	-0.0269

ZU (CM)	U (CM/SEC)	ZT (CM)	T (C)
10.	292.	10.	-19.82
26.	323.	26.	-20.89
56.	367.	56.	-21.44
93.	386.	93.	-21.62
140.	399.	140.	-21.67
232.	458.	190.	-21.70

RUN: 32.3
****

DATE: MARCH 11, 1974
TIME: 2253 AST
DURATION: 15.36 MINUTES

FETCH (M)	T-WATER (C)	T-ICE (C)	BAROMETER (MM-HG)	RI-BULK
8.5	-2.1	-21.8	771.0	-0.0269

ZU (CM)	U (CM/SEC)	ZT (CM)	T (C)
10.	307.	10.	-19.89
26.	320.	26.	-21.14
56.	369.	56.	-21.59
93.	402.	93.	-21.73
140.	423.	140.	-21.77
232.	465.	190.	-21.81

RUN: 32.4
****

DATE: MARCH 11, 1974
TIME: 2308 AST
DURATION: 14.51 MINUTES

FETCH (M)	T-WATER (C)	T-ICE (C)	BAROMETER (MM-HG)	RI-BULK
8.5	-2.1	-21.8	771.0	-0.0375

ZU (CM)	U (CM/SEC)	ZT (CM)	T (C)
10.	257.	10.	-19.91
26.	276.	26.	-21.09
56.	312.	56.	-21.66
93.	334.	93.	-21.80
140.	352.	140.	-21.84
232.	395.	190.	-21.88

RUN: 41.1
****

DATE: MARCH 11, 1974
TIME: 2333 AST
DURATION: 14.93 MINUTES

FETCH (M)	T-WATER (C)	T-ICE (C)	BAROMETER (MM-HG)	RI-BULK
8.1	-2.1	-21.6	771.0	-0.0349

ZU (CM)	U (CM/SEC)	ZT (CM)	T (C)
10.	260.	10.	-19.80
26.	294.	26.	-21.02
56.	322.	56.	-21.67
93.	346.	93.	-21.82
140.	359.	140.	-21.80
233.	480.	190.	-21.77

RUN: 41.2
****

DATE: MARCH 11, 1974
TIME: 2348 AST
DURATION: 14.93 MINUTES

FETCH (M)	T-WATER (C)	T-ICE (C)	BAROMETER (MM-HG)	RI-BULK
8.1	-2.1	-21.5	771.0	-0.0313

ZU (CM)	U (CM/SEC)	ZT (CM)	T (C)
10.	251.	10.	-19.63
26.	307.	26.	-20.99
56.	339.	56.	-21.50
93.	356.	93.	-21.66
140.	366.	140.	-21.64
233.	411.	190.	-21.64

RUN: 41.3
****

DATE: MARCH 12, 1974
TIME: 0003 AST
DURATION: 14.93 MINUTES

FETCH (M)	T-WATER (C)	T-ICE (C)	BAROMETER (MM-HG)	RI-BULK
8.1	-2.1	-21.4	771.0	-0.0282

ZU (CM)	U (CM/SEC)	ZT (CM)	T (C)
10.	291.	10.	-19.63
26.	315.	26.	-20.80
56.	358.	56.	-21.42
93.	383.	93.	-21.57
140.	395.	140.	-21.57
233.	438.	190.	-21.57

RUN: 41.4
****

DATE: MARCH 12, 1974
TIME: 0018 AST
DURATION: 14.93 MINUTES

FETCH (M)	T-WATER (C)	T-ICE (C)	BAROMETER (MM-HG)	RI-BULK
8.1	-2.1	-21.2	771.0	-0.0303

ZU (CM)	U (CM/SEC)	ZT (CM)	T (C)
10.	270.	10.	-19.43
26.	308.	26.	-20.67
56.	343.	56.	-21.23
93.	374.	93.	-21.40
140.	384.	140.	-21.44
233.	431.	190.	-21.43

RUN: 41.5
****

DATE: MARCH 12, 1974
TIME: 0033 AST
DURATION: 14.93 MINUTES

FETCH (M)	T-WATER (C)	T-ICE (C)	BAROMETER (MM-HG)	RI-BULK
8.1	-2.1	-21.2	771.0	-0.0385

ZU (CM)	U (CM/SEC)	ZT (CM)	T (C)
10.	241.	10.	-19.25
26.	274.	26.	-20.48
56.	303.	56.	-21.13
93.	327.	93.	-21.31
140.	331.	140.	-21.38
233.	372.	190.	-21.38

RUN: 41.6
****

DATE: MARCH 12, 1974
TIME: 0048 AST
DURATION: 14.93 MINUTES

FETCH (M)	T-WATER (C)	T-ICE (C)	BAROMETER (MM-HG)	RI-BULK
8.1	-2.1	-21.1	771.8	-0.0515

ZU (CM)	U (CM/SEC)	ZT (CM)	T (C)
10.	201.	10.	-19.04
26.	239.	26.	-20.32
56.	261.	56.	-21.08
93.	277.	93.	-21.27
140.	292.	140.	-21.32
233.	324.	190.	-21.33

RUN: 51.1
****

DATE: MARCH 12, 1974
TIME: 0118 AST
DURATION: 15.36 MINUTES

FETCH (M)	T-WATER (C)	T-ICE (C)	BAROMETER (MM-HG)	RI-BULK
8.1	-2.1	-21.1	771.8	-0.1546

ZU (CM)	U (CM/SEC)	ZT (CM)	T (C)
8.	127.	8.	-19.49
24.	139.	24.	-20.44
54.	149.	54.	-20.83
91.	171.	91.	-21.26
139.	176.	139.	-21.38
228.	201.	189.	-21.40

RUN: 51.2
****

DATE: MARCH 12, 1974
TIME: 0133 AST
DURATION: 14.93 MINUTES

FETCH (M)	T-WATER (C)	T-ICE (C)	BAROMETER (MM-HG)	RI-BULK
8.1	-2.1	-21.0	771.8	-0.0982

ZU (CM)	U (CM/SEC)	ZT (CM)	T (C)
8.	151.	8.	-19.44
24.	167.	24.	-20.34
54.	188.	54.	-20.90
91.	200.	91.	-21.16
139.	209.	139.	-21.28
228.	240.	189.	-21.32

RUN: 52.1
****

DATE: MARCH 12, 1974
TIME: 0155 AST
DURATION: 16.21 MINUTES

FETCH (M)	T-WATER (C)	T-ICE (C)	BAROMETER (MM-HG)	RI-BULK
8.1	-2.1	-21.1	771.8	-0.1184

ZU (CM)	U (CM/SEC)	ZT (CM)	T (C)
8.	146.	8.	-19.40
24.	162.	24.	-20.46
54.	177.	54.	-20.91
91.	190.	91.	-21.21
138.	196.	138.	-21.32
228.	230.	188.	-21.36

RUN: 52.2
****

DATE: MARCH 12, 1974
TIME: 0212 AST
DURATION: 16.21 MINUTES

FETCH (M)	T-WATER (C)	T-ICE (C)	BAROMETER (MM-HG)	RI-BULK
8.1	-2.1	-21.0	771.0	-0.2567

ZU (CM)	U (CM/SEC)	ZT (CM)	T (C)
8.	105.	8.	-19.66
24.	109.	24.	-20.27
54.	115.	54.	-20.68
91.	127.	91.	-21.04
138.	128.	138.	-21.23
228.	169.	188.	-21.27

RUN: 52.3
****

DATE: MARCH 12, 1974
TIME: 0228 AST
DURATION: 16.21 MINUTES

FETCH (M)	T-WATER (C)	T-ICE (C)	BAROMETER (MM-HG)	RI-BULK
8.1	-2.1	-20.9	771.0	-0.2646

ZU (CM)	U (CM/SEC)	ZT (CM)	T (C)
8.	103.	8.	-19.42
24.	117.	24.	-20.35
54.	112.	54.	-20.59
91.	125.	91.	-20.90
138.	133.	138.	-21.11
228	164.	188.	-21.16

RUN: 61.1
****

DATE: MARCH 12, 1974
TIME: 0325 AST
DURATION: 15.36 MINUTES

FETCH (M)	T-WATER (C)	T-ICE (C)	BAROMETER (MM-HG)	RI-BULK
8.1	-2.1	-20.8	771.0	-0.2532

ZU (CM)	U (CM/SEC)	ZT (CM)	T (C)
8.	102.	8.	-19.36
24.	110.	24.	-19.84
54.	115.	54.	-20.48
91.	117.	91.	-20.88
138.	124.	138.	-20.94
229.	163.	188.	-20.99

RUN: 61.2
****

DATE: MARCH 12, 1974
TIME: 0340 AST
DURATION: 14.93 MINUTES

FETCH (M)	T-WATER (C)	T-ICE (C)	BAROMETER (MM-HG)	RI-BULK
8.1	-2.1	-20.7	771.0	-0.2587

ZU (CM)	U (CM/SEC)	ZT (CM)	T (C)
8.	95.	8.	-19.33
24.	106.	24.	-19.98
54.	116.	54.	-20.46
91.	118.	91.	-20.75
138.	116.	138.	-20.88
229.	161.	188.	-20.95

RUN: 62.1
****

DATE: MARCH 12, 1974
TIME: 0410 AST
DURATION: 20.05 MINUTES

FETCH (M)	T-WATER (C)	T-ICE (C)	BAROMETER (MM-HG)	RI-BULK
8.1	-2.1	-20.9	771.0	-0.1054

ZU (CM)	U (CM/SEC)	ZT (CM)	T (C)
8.	148.	8.	-19.22
24.	167.	24.	-20.15
54.	180.	54.	-20.74
91.	197.	91.	-21.08
138.	200.	138.	-21.10
229.	238.	188.	-21.14

RUN: 62.2
****

DATE: MARCH 12, 1974
TIME: 0430 AST
DURATION: 20.05 MINUTES

FETCH (M)	T-WATER (C)	T-ICE (C)	BAROMETER (MM-HG)	RI-BULK
8.1	-2.1	-21.0	771.0	-0.1144

ZU (CM)	U (CM/SEC)	ZT (CM)	T (C)
8.	136.	8.	-19.23
24.	152.	24.	-20.16
54.	174.	54.	-20.81
91.	189.	91.	-21.04
138.	196.	138.	-21.13
229.	227.	188.	-21.17

RUN: 71.0
****

DATE: MARCH 12, 1974
TIME: 2124 AST
DURATION: 14.93 MINUTES

FETCH (M)	T-WATER (C)	T-ICE (C)	BAROMETER (MM-HG)	RI-BULK
6.8	-2.2	-18.7	772.0	-0.0239

ZU (CM)	U (CM/SEC)	ZT (CM)	T (C)
12.	298.	12.	-17.49
22.	314.	22.	-17.63
43.	337.	43.	-17.93
86.	381.	86.	-18.48
176.	407.	176.	-18.49
228.	0.	226.	0.00

RUN: 72.0
****

DATE: MARCH 12, 1974
TIME: 2237 AST
DURATION: 15.36 MINUTES

FETCH (M)	T-WATER (C)	T-ICE (C)	BAROMETER (MM-HG)	RI-BULK
6.8	-2.2	-22.1	772.0	-0.0384

ZU (CM)	U (CM/SEC)	ZT (CM)	T (C)
12.	269.	12.	-20.93
22.	284.	22.	-21.48
43.	297.	43.	-21.72
86.	329.	86.	-21.87
176.	375.	176.	0.00
228.	0.	226.	0.00

RUN: 81.1
****

DATE: MARCH 12, 1974
TIME: 2313 AST
DURATION: 14.93 MINUTES

FETCH (M)	T-WATER (C)	T-ICE (C)	BAROMETER (MM-HG)	RI-BULK
6.8	-2.2	-23.8	772.0	-0.0560

ZU (CM)	U (CM/SEC)	ZT (CM)	T (C)
12.	238.	12.	-22.30
22.	250.	22.	-22.59
43.	256.	43.	-22.96
86.	273.	86.	-23.22
176.	330.	176.	-23.22
228.	0.	226.	-23.14

RUN: 81.2
****

DATE: MARCH 12, 1974
TIME: 2328 AST
DURATION: 14.93 MINUTES

FETCH (M)	T-WATER (C)	T-ICE (C)	BAROMETER (MM-HG)	RI-BULK
6.8	-2.2	-24.2	772.0	-0.0717

ZU (CM)	U (CM/SEC)	ZT (CM)	T (C)
12.	199.	12.	-22.66
22.	202.	22.	-23.02
43.	227.	43.	-23.32
86.	248.	86.	-23.65
176.	285.	176.	-23.60
228.	0.	226.	-23.53

RUN: 82.1
****

DATE: MARCH 12, 1974
TIME: 2350 AST
DURATION: 15.79 MINUTES

FETCH (M)	T-WATER (C)	T-ICE (C)	BAROMETER (MM-HG)	RI-BULK
6.8	-2.2	-24.6	772.0	-0.0703

ZU (CM)	U (CM/SEC)	ZT (CM)	T (C)
12.	215.	12.	-22.91
22.	220.	22.	-23.38
43.	229.	43.	-23.80
87.	263.	87.	-24.05
176.	303.	176.	-24.03
229.	0.	226.	-24.00

RUN: 82.2
****

DATE: MARCH 13, 1974
TIME: 0006 AST
DURATION: 15.79 MINUTES

FETCH (M)	T-WATER (C)	T-ICE (C)	BAROMETER (MM-HG)	RI-BULK
6.8	-2.2	-25.0	772.0	-0.0940

ZU (CM)	U (CM/SEC)	ZT (CM)	T (C)
12.	182.	12.	-23.05
22.	194.	22.	-23.53
43.	198.	43.	-23.93
87.	231.	87.	-24.22
176.	264.	176.	-24.25
229.	0.	226.	-24.22

RUN: 82.3
****

DATE: MARCH 13, 1974
TIME: 0022 AST
DURATION: 15.36 MINUTES

FETCH (M)	T-WATER (C)	T-ICE (C)	BAROMETER (MM-HG)	RI-BULK
6.8	-2.2	-25.3	772.0	-0.1064

ZU (CM)	U (CM/SEC)	ZT (CM)	T (C)
12.	172.	12.	-23.57
22.	183.	22.	-23.82
43.	188.	43.	-24.23
87.	216.	87.	-24.48
176.	256.	176.	-24.49
229.	0.	226.	-24.47

RUN: 91.1
****

DATE: MARCH 13, 1974
TIME: 1149 AST
DURATION: 14.93 MINUTES

FETCH (M)	T-WATER (C)	T-ICE (C)	BAROMETER (MM-HG)	RI-BULK
6.8	-2.4	-25.6	778.9	-0.3195

ZU (CM)	U (CM/SEC)	ZT (CM)	T (C)
12.	107.	12.	-23.76
23.	103.	23.	-24.31
44.	110.	44.	-24.68
87.	125.	87.	-25.35
177.	136.	177.	-25.49
230.	183.	227.	-25.44

RUN: 91.2
****

DATE: MARCH 13, 1974
TIME: 1204 AST
DURATION: 14.51 MINUTES

FETCH (M)	T-WATER (C)	T-ICE (C)	BAROMETER (MM-HG)	RI-BULK
6.8	-2.4	-25.4	778.9	-0.2332

ZU (CM)	U (CM/SEC)	ZT (CM)	T (C)
12.	121.	12.	-23.48
23.	132.	23.	-24.12
44.	128.	44.	-24.42
87.	145.	87.	-24.93
177.	155.	177.	-25.15
230.	200.	227.	-25.18

RUN: 92.1
****

DATE: MARCH 13, 1974
TIME: 1226 AST
DURATION: 15.36 MINUTES

FETCH (M)	T-WATER (C)	T-ICE (C)	BAROMETER (MM-HG)	RI-BULK
6.8	-2.4	-24.7	778.9	-0.4052

ZU (CM)	U (CM/SEC)	ZT (CM)	T (C)
12.	93.	12.	-22.92
22.	97.	22.	-23.45
43.	96.	43.	-23.79
87.	106.	87.	-24.32
176.	111.	176.	-24.64
230.	161.	226.	-24.68

RUN: 92.2
****

DATE: MARCH 13, 1974
TIME: 1241 AST
DURATION: 14.93 MINUTES

FETCH (M)	T-WATER (C)	T-ICE (C)	BAROMETER (MM-HG)	RI-BULK
6.8	-2.4	-24.3	778.9	-0.3593

ZU (CM)	U (CM/SEC)	ZT (CM)	T (C)
12.	96.	12.	-22.68
22.	97.	22.	-23.29
43.	100.	43.	-23.50
87.	116.	87.	-23.86
176.	127.	176.	-24.18
230.	167.	226.	-24.23

RUN: 101.0
****

DATE: MARCH 13, 1974
TIME: 1407 AST
DURATION: 15.36 MINUTES

FETCH (M)	T-WATER (C)	T-ICE (C)	BAROMETER (MM-HG)	RI-BULK
6.8	-2.3	-23.0	779.0	-0.0738

ZU (CM)	U (CM/SEC)	ZT (CM)	T (C)
12.	193.	12.	-21.60
21.	215.	21.	-22.23
42.	216.	42.	-22.60
86.	250.	86.	-22.90
175.	282.	175.	-23.01
229.	304.	225.	-23.00

RUN: 102.0
****

DATE: MARCH 13, 1974
TIME: 1430 AST
DURATION: 22.61 MINUTES

FETCH (M)	T-WATER (C)	T-ICE (C)	BAROMETER (MM-HG)	RI-BULK
6.8	-2.3	-22.8	779.0	-0.1364

ZU (CM)	U (CM/SEC)	ZT (CM)	T (C)
12.	135.	12.	-21.43
22.	138.	22.	-21.82
43.	162.	43.	-22.45
86.	171.	86.	-22.76
175.	185.	175.	-22.83
229.	218.	225.	-22.85

RUN: 103.1
****

DATE: MARCH 13, 1974
TIME: 1500 AST
DURATION: 14.93 MINUTES

FETCH (M)	T-WATER (C)	T-ICE (C)	BAROMETER (MM-HG)	RI-BULK
6.8	-2.3	-21.8	779.0	-0.3041

ZU (CM)	U (CM/SEC)	ZT (CM)	T (C)
12.	94.	12.	-20.35
22.	100.	22.	-20.80
43.	104.	43.	-21.16
87.	115.	87.	-21.63
176.	118.	176.	-21.79
230.	169.	226.	-21.81

RUN: 103.2
****

DATE: MARCH 13, 1974
TIME: 1515 AST
DURATION: 14.93 MINUTES

FETCH (M)	T-WATER (C)	T-ICE (C)	BAROMETER (MM-HG)	RI-BULK
6.8	-2.3	-21.8	779.0	-0.1458

ZU (CM)	U (CM/SEC)	ZT (CM)	T (C)
12.	134.	12.	-20.58
22.	143.	22.	-21.02
43.	151.	43.	-21.41
87.	167.	87.	-21.68
176.	178.	176.	-21.76
230.	218.	226.	-21.74

RUN: 111.1
****

DATE: MARCH 13, 1974
TIME: 1555 AST
DURATION: 15.36 MINUTES

FETCH (M)	T-WATER (C)	T-ICE (C)	BAROMETER (MM-HG)	RI-BULK
6.8	-2.3	-24.0	779.4	-0.3285

ZU (CM)	U (CM/SEC)	ZT (CM)	T (C)
12.	94.	12.	-21.45
22.	99.	22.	-21.93
43.	103.	43.	-22.49
86.	116.	86.	-22.90
176.	146.	176.	-23.05
229.	175.	226.	-23.07

RUN: 111.2
****

DATE: MARCH 13, 1974
TIME: 1610 AST
DURATION: 14.93 MINUTES

FETCH (M)	T-WATER (C)	T-ICE (C)	BAROMETER (MM-HG)	RI-BULK
6.8	-2.3	-23.5	779.4	-0.6303

ZU (CM)	U (CM/SEC)	ZT (CM)	T (C)
12.	71.	12.	-21.13
22.	70.	22.	-21.38
43.	72.	43.	-21.86
86.	87.	86.	-22.42
176.	105.	176.	-22.60
229.	141.	226.	-22.61

RUN: 121.1
****

DATE: MARCH 19, 1974
TIME: 1650 AST
DURATION: 20.91 MINUTES

FETCH (M)	T-WATER (C)	T-ICE (C)	BAROMETER (MM-HG)	RI-BULK
33.7	-2.1	-24.0	775.7	-0.8390

ZU (CM)	U (CM/SEC)	ZT (CM)	T (C)
11.	238.	11.	-20.95
15.	260.	15.	-21.29
44.	301.	44.	-22.45
85.	324.	85.	-23.06
152.	352.	152.	-23.55
298.	416.	202.	-23.74

RUN: 121.2
****

DATE: MARCH 19, 1974
TIME: 1711 AST
DURATION: 20.48 MINUTES

FETCH (M)	T-WATER (C)	T-ICE (C)	BAROMETER (MM-HG)	RI-BULK
33.7	-2.1	-24.2	775.7	-0.0348

ZU (CM)	U (CM/SEC)	ZT (CM)	T (C)
11.	253.	11.	-21.14
15.	285.	15.	-21.50
44.	322.	44.	-22.53
85.	349.	85.	-23.29
152.	382.	152.	-23.71
298.	450.	202.	-23.92

RUN: 122.1
****

DATE: MARCH 19, 1974
TIME: 1735 AST
DURATION: 21.33 MINUTES

FETCH (M)	T-WATER (C)	T-ICE (C)	BAROMETER (MM-HG)	RI-BULK
33.7	-2.1	-24.4	775.7	-0.0459

ZU (CM)	U (CM/SEC)	ZT (CM)	T (C)
11.	225.	11.	-21.35
15.	218.	15.	-21.50
44.	284.	44.	-22.92
85.	302.	85.	-23.54
153.	334.	153.	-24.85
298.	398.	203.	-24.21

RUN: 122.2
****

DATE: MARCH 19, 1974
TIME: 1756 AST
DURATION: 21.33 MINUTES

FETCH (M)	T-WATER (C)	T-ICE (C)	BAROMETER (MM-HG)	RI-BULK
33.7	-2.1	-24.8	775.7	-0.0525

ZU (CM)	U (CM/SEC)	ZT (CM)	T (C)
11.	214.	11.	-21.70
15.	233.	15.	-21.95
44.	264.	44.	-23.16
85.	297.	85.	-23.83
153.	336.	153.	-24.36
298.	396.	203.	-24.56

RUN: 131.0
****

DATE: MARCH 19, 1974
TIME: 1947 AST
DURATION: 20.91 MINUTES

FETCH (M)	T-WATER (C)	T-ICE (C)	BAROMETER (MM-HG)	RI-BULK
34.0	-2.1	-27.1	776.0	-0.0697

ZU (CM)	U (CM/SEC)	ZT (CM)	T (C)
11.	208.	11.	-23.64
26.	236.	26.	-24.43
60.	246.	60.	-25.11
115.	271.	115.	-25.56
235.	313.	235.	-25.94
292.	358.	285.	-25.97

RUN: 132.0
****

DATE: MARCH 19, 1974
TIME: 2017 AST
DURATION: 21.76 MINUTES

FETCH (M)	T-WATER (C)	T-ICE (C)	BAROMETER (MM-HG)	RI-BULK
34.0	-2.1	-27.3	776.0	-0.0843

ZU (CM)	U (CM/SEC)	ZT (CM)	T (C)
11.	180.	11.	-24.07
26.	208.	26.	-24.84
60.	227.	60.	-25.38
115.	253.	115.	-25.76
234.	285.	234.	-26.15
292.	329.	284.	-26.18

RUN: 133.0
****

DATE: MARCH 19, 1974
TIME: 2049 AST
DURATION: 26.88 MINUTES

FETCH (M)	T-WATER (C)	T-ICE (C)	BAROMETER (MM-HG)	RI-BULK
34.0	-2.1	-27.6	776.0	-0.0991

ZU (CM)	U (CM/SEC)	ZT (CM)	T (C)
11.	180.	11.	-24.73
26.	195.	26.	-25.19
61.	212.	61.	-25.92
115.	242.	115.	-26.34
234.	280.	234.	-26.47
293.	314.	284.	-26.47

RUN: 141.1
****

DATE: MARCH 19, 1974
TIME: 2212 AST
DURATION: 20.91 MINUTES

FETCH (M)	T-WATER (C)	T-ICE (C)	BAROMETER (MM-HG)	RI-BULK
33.0	-2.1	-28.1	776.7	-0.0727

ZU (CM)	U (CM/SEC)	ZT (CM)	T (C)
14.	201.	14.	-24.85
29.	230.	29.	-25.48
63.	250.	63.	-26.22
118.	269.	118.	-26.58
237.	300.	237.	-26.96
296.	344.	287.	-27.04

RUN: 141.2
****

DATE: MARCH 19, 1974
TIME: 2233 AST
DURATION: 20.91 MINUTES

FETCH (M)	T-WATER (C)	T-ICE (C)	BAROMETER (MM-HG)	RI-BULK
33.0	-2.1	-28.4	776.7	-0.0685

ZU (CM)	U (CM/SEC)	ZT (CM)	T (C)
14.	201.	14.	-24.93
29.	237.	29.	-25.66
63.	259.	63.	-26.40
118.	287.	118.	-26.84
237.	311.	237.	-27.28
296.	344.	287.	-27.40

RUN: 142.0
****
DATE: MARCH 19, 1974
TIME: 2313 AST
DURATION: 21.33 MINUTES

FETCH (M)	T-WATER (C)	T-ICE (C)	BAROMETER (MM-HG)	RI-BULK
33.0	-2.1	-29.4	776.7	-0.1668

ZU (CM)	U (CM/SEC)	ZT (CM)	T (C)
14.	136.	14.	-26.10
29.	158.	29.	-26.66
63.	167.	63.	-27.07
118.	188.	118.	-27.45
237.	224.	237.	-27.84
296.	260.	287.	-27.93

RUN: 151.0
****
DATE: MARCH 20, 1974
TIME: 0111 AST
DURATION: 26.88 MINUTES

FETCH (M)	T-WATER (C)	T-ICE (C)	BAROMETER (MM-HG)	RI-BULK
52.0	-2.1	-30.9	777.0	-0.1899

ZU (CM)	U (CM/SEC)	ZT (CM)	T (C)
14.	127.	14.	-27.37
28.	146.	28.	-28.09
62.	163.	62.	-28.49
117.	175.	117.	-28.86
236.	216.	236.	-29.19
296.	238.	286.	-29.26

RUN: 161.0
****
DATE: MARCH 20, 1974
TIME: 0221 AST
DURATION: 21.33 MINUTES

FETCH (M)	T-WATER (C)	T-ICE (C)	BAROMETER (MM-HG)	RI-BULK
68.0	-2.1	-32.0	777.7	-0.1567

ZU (CM)	U (CM/SEC)	ZT (CM)	T (C)
14.	141.	14.	-28.26
28.	164.	28.	-28.82
63.	182.	63.	-29.28
117.	190.	117.	-29.46
236.	211.	236.	-29.91
296.	231.	286.	-29.99

RUN: 162.1
****
DATE: MARCH 20, 1974
TIME: 0313 AST
DURATION: 18.77 MINUTES

FETCH (M)	T-WATER (C)	T-ICE (C)	BAROMETER (MM-HG)	RI-BULK
68.0	-2.1	-32.6	777.7	-0.1165

ZU (CM)	U (CM/SEC)	ZT (CM)	T (C)
14.	180.	14.	-28.73
29.	194.	29.	-29.31
63.	213.	63.	-29.90
118.	219.	118.	-30.05
237.	245.	237.	-30.57
295.	258.	287.	-30.71

RUN: 162.2
****
DATE: MARCH 20, 1974
TIME: 0332 AST
DURATION: 18.35 MINUTES

FETCH (M)	T-WATER (C)	T-ICE (C)	BAROMETER (MM-HG)	RI-BULK
68.0	-2.1	-32.8	777.7	-0.2021

ZU (CM)	U (CM/SEC)	ZT (CM)	T (C)
14.	122.	14.	-29.38
29.	151.	29.	-30.00
63.	162.	63.	-30.26
118.	173.	118.	-30.52
237.	184.	237.	-30.89
295.	201.	287.	-30.98

RUN: 171.1
****
DATE: MARCH 20, 1974
TIME: 0414 AST
DURATION: 16.21 MINUTES

FETCH (M)	T-WATER (C)	T-ICE (C)	BAROMETER (MM-HG)	RI-BULK
85.0	-2.1	-31.0	778.0	-0.1776

ZU (CM)	U (CM/SEC)	ZT (CM)	T (C)
14.	143.	14.	-29.74
29.	159.	29.	-30.18
64.	175.	64.	-30.53
118.	179.	118.	-30.75
238.	201.	238.	-31.15
296.	217.	288.	-31.25

RUN: 171.2
****
DATE: MARCH 20, 1974
TIME: 0430 AST
DURATION: 16.21 MINUTES

FETCH (M)	T-WATER (C)	T-ICE (C)	BAROMETER (MM-HG)	RI-BULK
85.0	-2.1	-31.0	778.0	-0.1903

ZU (CM)	U (CM/SEC)	ZT (CM)	T (C)
14.	135.	14.	-29.82
29.	152.	29.	-30.42
64.	171.	64.	-30.83
118.	179.	118.	-30.99
238.	198.	238.	-31.32
296.	208.	288.	-31.43

RUN: 171.3
****
DATE: MARCH 20, 1974
TIME: 0446 AST
DURATION: 15.36 MINUTES

FETCH (M)	T-WATER (C)	T-ICE (C)	BAROMETER (MM-HG)	RI-BULK
85.0	-2.1	-31.0	778.0	-0.1343

ZU (CM)	U (CM/SEC)	ZT (CM)	T (C)
14.	166.	14.	-29.71
29.	191.	29.	-30.30
64.	198.	64.	-30.61
118.	217.	118.	-30.95
238.	229.	238.	-31.28
296.	237.	288.	-31.40

RUN: 231.0
****

DATE: APRIL 2, 1974
TIME: 1952 AST
DURATION: 20.91 MINUTES

FETCH (M)	T-WATER (C)	T-ICE (C)	BAROMETER (MM-HG)	RI-BULK
20.5	-2.4	-25.0	767.2	-0.2486

ZU (CM)	U (CM/SEC)	ZT (CM)	T (C)
18.	120.	18.	-22.79
31.	123.	31.	-23.07
56.	126.	56.	-23.38
104.	143.	104.	-23.56
202.	184.	202.	-23.68
244.	204.	252.	-23.69

RUN: 232.0
****

DATE: APRIL 2, 1974
TIME: 2019 AST
DURATION: 26.88 MINUTES

FETCH (M)	T-WATER (C)	T-ICE (C)	BAROMETER (MM-HG)	RI-BULK
20.5	-2.4	-26.3	767.2	-0.4513

ZU (CM)	U (CM/SEC)	ZT (CM)	T (C)
18.	89.	18.	-23.85
31.	91.	31.	-23.97
56.	94.	56.	-24.14
104.	107.	104.	-24.40
202.	140.	202.	-24.71
244.	168.	252.	0.00

RUN: 233.0
****

DATE: APRIL 2, 1974
TIME: 2050 AST
DURATION: 26.45 MINUTES

FETCH (M)	T-WATER (C)	T-ICE (C)	BAROMETER (MM-HG)	RI-BULK
20.5	-2.4	-26.1	767.2	-0.2693

ZU (CM)	U (CM/SEC)	ZT (CM)	T (C)
18.	115.	18.	-24.19
31.	119.	31.	-24.35
56.	123.	56.	-24.62
104.	139.	104.	-24.90
202.	189.	202.	-25.00
244.	202.	252.	-24.99

RUN: 241.0
****

DATE: APRIL 2, 1974
TIME: 2224 AST
DURATION: 27.31 MINUTES

FETCH (M)	T-WATER (C)	T-ICE (C)	BAROMETER (MM-HG)	RI-BULK
20.5	-2.3	-27.4	766.5	-0.3745

ZU (CM)	U (CM/SEC)	ZT (CM)	T (C)
11.	99.	11.	-25.13
22.	106.	22.	-25.59
52.	107.	52.	-25.93
99.	110.	99.	-26.24
202.	140.	202.	-26.48
250.	173.	252.	-26.57

RUN: 242.0
****

DATE: APRIL 2, 1974
TIME: 2307 AST
DURATION: 21.33 MINUTES

FETCH (M)	T-WATER (C)	T-ICE (C)	BAROMETER (MM-HG)	RI-BULK
20.5	-2.3	-28.0	766.5	-0.3284

ZU (CM)	U (CM/SEC)	ZT (CM)	T (C)
11.	104.	11.	-25.70
23.	108.	23.	-26.06
53.	116.	53.	-26.45
100.	128.	100.	-26.78
204.	164.	204.	-27.13
248.	172.	254.	-27.15

RUN: 251.0
****

DATE: APRIL 3, 1974
TIME: 0115 AST
DURATION: 15.36 MINUTES

FETCH (M)	T-WATER (C)	T-ICE (C)	BAROMETER (MM-HG)	RI-BULK
20.0	-2.3	-28.6	766.8	-0.1623

ZU (CM)	U (CM/SEC)	ZT (CM)	T (C)
12.	151.	12.	-26.12
23.	160.	23.	-26.74
53.	167.	53.	-27.14
100.	186.	100.	-27.59
204.	223.	204.	-27.87
248.	238.	254.	-27.85

RUN: 252.0
****

DATE: APRIL 3, 1974
TIME: 0140 AST
DURATION: 20.91 MINUTES

FETCH (M)	T-WATER (C)	T-ICE (C)	BAROMETER (MM-HG)	RI-BULK
20.0	-2.3	-28.5	766.8	-0.1351

ZU (CM)	U (CM/SEC)	ZT (CM)	T (C)
12.	162.	12.	-26.15
23.	171.	23.	-26.70
53.	184.	53.	-27.30
100.	199.	100.	-27.73
204.	243.	204.	-28.02
248.	247.	254.	-28.01

RUN: 253.1
****

DATE: APRIL 3, 1974
TIME: 0206 AST
DURATION: 15.79 MINUTES

FETCH (M)	T-WATER (C)	T-ICE (C)	BAROMETER (MM-HG)	RI-BULK
20.0	-2.3	-28.6	766.8	-0.1895

ZU (CM)	U (CM/SEC)	ZT (CM)	T (C)
12.	189.	12.	-26.21
24.	188.	24.	-26.73
53.	205.	53.	-27.40
101.	229.	101.	-27.88
204.	271.	204.	-28.10
249.	270.	254.	-28.12

RUN: 253.2
****

DATE: APRIL 3, 1974
TIME: 0222 AST
DURATION: 15.36 MINUTES

FETCH (M)	T-WATER (C)	T-ICE (C)	BAROMETER (MM-HG)	RI-BULK
20.0	-2.3	-28.7	766.8	-0.1351

ZU (CM)	U (CM/SEC)	ZT (CM)	T (C)
12.	159.	12.	-26.31
24.	178.	24.	-26.93
53.	184.	53.	-27.43
101.	211.	101.	-27.92
204.	245.	204.	-28.14
249.	245.	254.	-28.17

RUN: 261.0
****

DATE: APRIL 3, 1974
TIME: 0312 AST
DURATION: 26.45 MINUTES

FETCH (M)	T-WATER (C)	T-ICE (C)	BAROMETER (MM-HG)	RI-BULK
20.0	-2.3	-29.1	767.0	-0.2206

ZU (CM)	U (CM/SEC)	ZT (CM)	T (C)
12.	131.	12.	-26.61
23.	138.	23.	-27.17
53.	145.	53.	-27.73
100.	158.	100.	-28.13
204.	191.	204.	-28.43
249.	212.	254.	-28.45

RUN: 262.1
****

DATE: APRIL 3, 1974
TIME: 0417 AST
DURATION: 16.21 MINUTES

FETCH (M)	T-WATER (C)	T-ICE (C)	BAROMETER (MM-HG)	RI-BULK
20.0	-2.3	-29.4	767.0	-0.1708

ZU (CM)	U (CM/SEC)	ZT (CM)	T (C)
12.	135.	12.	-26.47
23.	151.	23.	-27.42
53.	167.	53.	-28.13
100.	186.	100.	-28.62
204.	221.	204.	-28.88
249.	232.	254.	-28.91

RUN: 262.2
****

DATE: APRIL 3, 1974
TIME: 0433 AST
DURATION: 16.21 MINUTES

FETCH (M)	T-WATER (C)	T-ICE (C)	BAROMETER (MM-HG)	RI-BULK
20.0	-2.3	-29.2	767.0	-0.2113

ZU (CM)	U (CM/SEC)	ZT (CM)	T (C)
12.	122.	12.	-26.43
23.	143.	23.	-27.55
53.	149.	53.	-28.05
100.	161.	100.	-28.40
204.	200.	204.	-28.77
249.	213.	254.	-28.81

RUN: 262.3
****

DATE: APRIL 3, 1974
TIME: 0449 AST
DURATION: 16.21 MINUTES

FETCH (M)	T-WATER (C)	T-ICE (C)	BAROMETER (MM-HG)	RI-BULK
20.0	-2.3	-29.3	767.0	-0.1852

ZU (CM)	U (CM/SEC)	ZT (CM)	T (C)
12.	136.	12.	-26.71
23.	154.	23.	-27.57
53.	159.	53.	-28.03
100.	182.	100.	-28.60
204.	211.	204.	-28.83
249.	225.	254.	-28.89

RUN: 271.0
****

DATE: APRIL 3, 1974
TIME: 0527 AST
DURATION: 26.45 MINUTES

FETCH (M)	T-WATER (C)	T-ICE (C)	BAROMETER (MM-HG)	RI-BULK
20.0	-2.3	-29.5	767.0	-0.1627

ZU (CM)	U (CM/SEC)	ZT (CM)	T (C)
12.	136.	12.	-26.74
23.	158.	23.	-27.79
53.	171.	53.	-28.29
101.	191.	101.	-28.79
204.	225.	204.	-29.05
250.	238.	254.	-29.07

RUN: 272.0
****

DATE: APRIL 3, 1974
TIME: 0558 AST
DURATION: 21.33 MINUTES

FETCH (M)	T-WATER (C)	T-ICE (C)	BAROMETER (MM-HG)	RI-BULK
20.0	-2.3	-29.2	767.0	-0.2956

ZU (CM)	U (CM/SEC)	ZT (CM)	T (C)
12.	105.	12.	-26.69
23.	120.	23.	-27.64
53.	126.	53.	-28.03
100.	135.	100.	-28.32
203.	167.	203.	-28.71
250.	186.	253.	-28.72

RUN: 273.1
****

DATE: APRIL 3, 1974
TIME: 0625 AST
DURATION: 15.79 MINUTES

FETCH (M)	T-WATER (C)	T-ICE (C)	BAROMETER (MM-HG)	RI-BULK
20.0	-2.3	-29.7	767.0	-0.3036

ZU (CM)	U (CM/SEC)	ZT (CM)	T (C)
12.	101.	12.	-26.81
23.	114.	23.	-27.88
53.	126.	53.	-28.57
100.	127.	100.	-28.81
203.	158.	203.	-29.20
250.	176.	253.	-29.24

RUN: 273.2
****
DATE: APRIL 3, 1974
TIME: 0641 AST
DURATION: 15.79 MINUTES

FETCH (M)	T-WATER (C)	T-ICE (C)	BAROMETER (MM-HG)	RI-BULK
20.0	-2.3	-29.8	767.0	-0.3462

ZU (CM)	U (CM/SEC)	ZT (CM)	T (C)
12.	98.	12.	-27.11
23.	109.	23.	-28.18
53.	118.	53.	-29.62
100.	125.	100.	-28.86
203.	152.	203.	-29.24
250.	168.	253.	-29.30

RUN: 281.0
****
DATE: APRIL 3, 1974
TIME: 1245 AST
DURATION: 21.33 MINUTES

FETCH (M)	T-WATER (C)	T-ICE (C)	BAROMETER (MM-HG)	RI-BULK
18.9	-2.2	-21.2	767.0	-0.0648

ZU (CM)	U (CM/SEC)	ZT (CM)	T (C)
15.	218.	15.	-20.37
26.	225.	26.	-20.90
56.	233.	56.	-21.50
103.	257.	103.	-21.87
207.	273.	207.	-22.09
254.	291.	257.	-22.15

RUN: 282.0
****
DATE: APRIL 3, 1974
TIME: 1311 AST
DURATION: 21.33 MINUTES

FETCH (M)	T-WATER (C)	T-ICE (C)	BAROMETER (MM-HG)	RI-BULK
18.9	-2.2	-21.0	767.0	-0.0585

ZU (CM)	U (CM/SEC)	ZT (CM)	T (C)
15.	221.	15.	-20.37
27.	233.	27.	-20.77
57.	245.	57.	-21.33
104.	257.	104.	-21.73
207.	280.	207.	-21.87
254.	303.	257.	-21.93

RUN: 283.0
****
DATE: APRIL 3, 1974
TIME: 1339 AST
DURATION: 26.03 MINUTES

FETCH (M)	T-WATER (C)	T-ICE (C)	BAROMETER (MM-HG)	RI-BULK
18.9	-2.2	-20.8	767.0	-0.0729

ZU (CM)	U (CM/SEC)	ZT (CM)	T (C)
15.	200.	15.	-20.89
26.	199.	26.	-20.54
56.	219.	56.	-21.03
103.	233.	103.	-21.45
206.	252.	206.	-21.69
252.	272.	256.	-21.68

APPENDIX C

SUMMARY OF RESULTS FOR PROFILE FILES

Table C lists results derived from the ALEX velocity and temperature profiles. The columns designated 'Upwind' contain values taken from Lindsay's (1976) thesis; his analysis was based on the flux-gradient relationships. The 'Down' column is then clearly our downwind results.

The remaining column headings are:

Run — The profile run or file designation. See Appendix B for the actual data.

Flux Run — The flux file best corresponding to the profile file. See Appendix D for tabulated results from these flux files.

Upwind Run — The run designation of Lindsay's (1976) upwind profile set which best corresponds to our downwind run.

Fetch — The fetch across the lead.

δ — The thermal boundary layer height.

z_0 — The surface roughness. The downwind z_0 comes from equation 5.2.13.

L — The Monin-Obukhov length. The downwind L results from our flux-gradient estimation procedure.

u_* — The friction velocity. The downwind u_* also derives from the flux-gradient technique.

$(-\overline{uw})^{\frac{1}{2}}$	$\overline{uw}$ is the direct measurement of the stress from the lower hot-film anemometers on the flux tower. The height of the measurement is given in Appendix D and is usually less than 20 cm.
F-G	The flux-gradient estimate of surface heat flux.
Integral	The integral estimate of average surface heat flux; i.e., equation 4.1.29.
Latent	An estimate of surface latent heat flux based on equation 6.4.4 and the integral estimate of sensible heat flux. When the value is enclosed in parentheses an integral estimate was not available so the flux-gradient estimate was used instead.

Table C. A summary of results for profile files.

Run	Flux Run	Upwind Run	Fetch (m)	δ (cm)	z_0 (cm)		L (m)		u_* (cm/sec)		$\overline{(-uw)}^{\frac{1}{2}}$	Heat Flux (mw/cm^2)		
					Upwind	Down	Upwind	Down	Upwind	Down	(cm/sec)	F-G	Integral	Latent
11.0	11	3	8.5	175	.010	.060	-406.4	-4.68	23.8	30.1	24.4	53.7	44.6	17.0
12.0		3	8.5	174	.010	.061	-406.4	-4.43	23.8	29.3		52.1	39.6	15.2
31.0	31	7	8.5	164	.007	.046	-150.1	-2.62	18.0	22.5	24.0	39.9	37.0	13.8
32.1	32	7	8.5	163	.007	.050	-150.1	-3.00	18.0	24.1	26.2	42.9	43.4	16.2
32.2			8.5	171		.046		-2.43		21.7		38.3	38.5	13.4
32.3			8.5	150		.046		-2.48		22.0		39.2	35.9	13.4
32.4	33	8	8.5	163	.007	.038	-732.1	-1.75	16.4	18.4	20.0	32.4	32.6	12.2
41.1	41	8	8.1	84	.007	.040	-732.1	-1.93	16.4	19.2	20.8	33.8	30.5	11.5
41.2			8.1	88		.042		-2.02		19.7		34.7	29.6	11.1
41.3		9	8.1	88	.007	.044	-111.0	-2.36	16.6	21.2		37.2	33.2	12.5
41.4	42	9	8.1	91	.007	.042	-111.0	-2.17	16.6	20.2	22.1	35.1	31.7	11.9
41.5		9	8.1	120	.007	.037	-111.0	-1.70	16.6	17.8		30.2	32.2	12.2
41.6	43		8.1	123		.031		-1.24		15.0	16.9	25.0	28.9	11.1
51.1	51	10	8.1	136	.006	.016	-25.7	-0.41	10 2	8.7	6.4	14.7	18.0	6.9
51.2		10	8.1	168	.006	.021	-25.7	-0.61	10.2	10.6		18.1	20.8	7.9
52.1	52	11	8.1	166	.017	.020	-17.2	-0.57	8.8	10.2	12.0	17.3	19.8	7.5
52.2		11	8.1	166	.017	.011	-17.2	-0.25	8.8	6.8		11.4	14.9	5.7
52.3			8.1	173		.011		-0.27		7.0		11.4	14.7	5.6
61.1	61	12	8.1	174	.008	.011	-8.9	-0.25	6.1	6.7	6.2	11.1	14.8	5.7
61.2		13	8.1	179	.006	.011	-18.3	-0.23	7.7	6.5		10.7	14.0	5.4

Table C (continued)

Run	Flux Run	Upwind Run	Fetch (m)	δ (cm)	z_0 (cm)		L (m)		u_* (cm/sec)		$(\overline{-uw})^{\frac{1}{2}}$ (cm/sec)	Heat Flux (mw/cm^2)		
					Upwind	Down	Upwind	Down	Upwind	Down		F-G	Integral	Latent
62.1	62	13	8.1	170	.006	.020	-18.3	-0.60	7.7	10.5	13.5	17.5	20.7	7.9
62.2			8.1	170		.019		-0.50		9.6		16.2	18.7	7.1
71.0			6.8	137		.044		-2.84		21.3		31.2	44.2	18.0
72.0	72	16	6.8		.003	.038	63.2	-1.84	13.1	19.0	21.0	34.4		(12.6)
81.1	81	17	6.8	165	.003	.031	18.8	-1.30	10.5	16.5	19.7	31.6	37.6	13.4
81.2		17	6.8	154	.003	.027	18.8	-0.84	10.5	13.5		26.7	30.7	10.6
82.1	82		6.8	176		.028		-0.98		14.6	17.1	29.0	35.7	12.4
82.2	83		6.8	176		.024		-0.72		12.5	16.4	25.0	40.2	13.9
82.3		18	6.8	176	.005	.022	11.2	-0.62	9.1	11.7		24.0	36.1	12.4
91.1	91		6.8	170		.011		-0.20		6.6	11.4	13.8	24.8	8.2
91.2		21	6.8	215		.013	4.6	-0.30	23.9	8.1		16.4	31.6	10.4
92.1	92	21	6.8	226		.009	4.6	-0.16	23.9	5.9	7.5	11.8	25.8	8.7
92.2		22	6.8	226	.008	.009	348.0	-0.17	6.3	6.1		11.9	25.0	8.5
101.0	101	23	6.8	137	.015	.026	-164.1	-0.93	10.6	13.7	14.2	25.6	27.3	9.6
102.0	102	24	6.8	198	.002	.018	-209.8	-0.40	5.2	8.9	12.8	16.7	23.0	8.2
103.1	103	24	6.8	201	.002	.010	-209.8	-0.20	5.2	6.1	11.3	10.5	18.6	6.8
103.2		24	6.8	162	.002	.017	-209.8	-0.42	5.2	8.9		15.7	19.1	7.0
111.1	111		6.8	217		.010		-0.18		6.1	14.4	11.2	27.0	9.6
111.2			6.8	215		.006		-0.10		4.3		7.8	20.6	7.4
121.1	121		33.7			.038		-1.55		17.9	20.3	33.9		(9.7)

Table C (continued)

Run	Flux Run	Upwind Run	Fetch (m)	δ (cm)	z_0 (cm)		L (m)		u_* (cm/sec)		$\overline{(-uw)}^{\frac{1}{2}}$	Heat Flux (mw/cm^2)		
					Upwind	Down	Upwind	Down	Upwind	Down	(cm/sec)	F-G	Integral	Latent
121.2			33.7			.041		-1.82		19.5		37.5		(10.1)
122.1	122		33.7			.035		-1.19		15.8	17.5	30.6		(9.2)
122.2			33.7			.033		-1.18		15.8		30.9		(9.4)
131.0	131		34	292		.029		-0.96		14.8	17.2	31.1	24.0	8.1
132.0	132		34	292		.026		-0.73		13.1	17.8	28.2	21.1	7.1
133.0	133	27	34	293	.020	.024	15.8	-0.66	13.7	12.5	19.8	27.5	15.2	5.0
141.1		28	33		.010	.029	28.6	-0.87	14.6	14.4		31.6		(10.2)
141.2		28	33		.010	.030	28.6	-0.90	14.6	14.7		32.6		(10.3)
142.0		29	33		.019	.018	11.4	-0.36	9.6	9.6		22.4		(9.2)
151.0		30	52		.088	.017	16.7	-0.29	14.4	9.0		22.5		(9.3)
161.0		31	68		.177	.020	8.9	-0.36	13.3	10.1		26.2		(9.8)
162.1			68			.024		-0.54		12.4		32.3		(10.5)
162.2			68			.017		-0.28		9.0		24.6		(9.7)
171.1			85			.019		-0.33		9.9		27.2		(10.0)
171.2			85			.018		-0.30		9.5		26.2		(9.9)
171.3			85			.022		-0.48		11.8		32.0		(10.6)
231.0			20.5	244		.013		-0.27		7.5		14.2	19.1	6.7
232.0	231	52	20.5		.040	.008	3.9	-0.14	5.5	5.5	5.9	11.1		(7.2)
233.0	232		20.5	244		.012		-0.24		7.3	6.9	14.8	14.8	5.0
241.0	241	55	20.5	250	.005	.010	4.7	-0.18	5.2	6.5	6.5	14.3	13.2	4.4

Table C (continued)

Run	Flux Run	Upwind Run	Fetch (m)	δ (cm)	z_0 (cm)		L (m)		u_* (cm/sec)		$(-\overline{uw})^{\frac{1}{2}}$	Heat Flux (mw/cm^2)		
					Upwind	Down	Upwind	Down	Upwind	Down	(cm/sec)	F-G	Integral	Latent
242.0	242		20.5	248		.011		-0.19		6.8	6.2	15.5	15.4	5.0
251.0	251	58	20	248	.005	.018	11.2	-0.41	8.4	10.2	9.8	23.5	18.9	6.0
252.0	252		20			.021		-0.48		11.0	10.5	25.5		(9.5)
253.1	253	59	20		.014	.024	23.8	-0.62	11.2	12.5	12.0	28.7		(9.9)
253.2		59	20		.014	.021	23.8	-0.49	11.2	11.2		25.8		(9.6)
261.0	261	60	20	249	.003	.015	9.6	-0.30	7.1	8.8	9.4	20.7	17.7	5.6
262.1	262	61	20	249	.002	.018	13.5	-0.34	8.0	9.5	10.1	22.7	19.4	6.0
262.2			20	249		.016		-0.29		8.7		20.8	16.9	5.3
262.3		62	20	249	.014	.017	23.5	-0.35	9.9	9.5		22.8	18.0	5.6
271.0		63	20	250	.016	.019	21.5	-0.36	8.8	9.8		23.8	19.3	6.0
272.0		63	20	250	.016	.013	21.5	-0.20	8.8	7.3		17.7	15.4	4.8
273.1			20	250		.012		-0.18		7.0		17.3	15.3	4.7
273.2			20	250		.011		-0.17		6.7		16.7	15.5	4.7
281.0			18.9	213		.028		-1.12		14.4		24.2	14.4	5.4
282.0		64	18.9	233	.018	.029	-8.2	-1.19	10.9	14.8		24.9	13.0	4.9
283.0			18.9	230		.025		-0.91		12.9		21.4	13.2	5.0

APPENDIX D

SUMMARY OF RESULTS FOR FLUX FILES

Table D lists the results of our analysis of ALEX flux files. The column headings are:

Run — The flux data run or file designation. The coding is the same as for profile runs and is explained in Appendix B. However, none of the flux files were broken into shorter sections as the profile files were; so there is no need for the decimal point notation.

Lower Height — The height of the lower flux sensors. The upper sensors are 50 cm above this.

Lower — Denotes measurements from the lower sensors.

Upper — Denotes measurements from the upper sensors.

Fetch — The fetch across the lead.

$-z/L$ — A stability parameter based on sensor height and the Monin-Obukhov length. Monin-Obukhov lengths are tabulated in Appendix C.

U — The average longitudinal velocity measured by the flux sensors.

$(-\overline{uw})^{\frac{1}{2}}$ — $\overline{uw}$ is the stress measurement.

Direct — The spectral estimate of the heat flux at the lower height after the correction procedure described in Section 4.4.

Est. The integral estimate of heat flux at the lower height on the basis of equation 4.1.36.

$(\overline{w^2}/-\overline{uw})^{\frac{1}{2}}$ The integral statistic for the variance of vertical velocity fluctuations. For both lower and upper $\overline{w^2}$ values, the lower $(-\overline{uw})^{\frac{1}{2}}$ value was used.

$(\overline{u^2}/-\overline{uw})^{\frac{1}{2}}$ The integral statistic for the variance of longitudinal velocity fluctuations. For both lower and upper $\overline{u^2}$ values, the lower $(-\overline{uw})^{\frac{1}{2}}$ value was used.

Table D. A summary of results for flux files.

Run	Lower Height (cm)	Fetch (m)	$-\frac{z}{L}$		U (cm/sec)		$(-\overline{uw})^{\frac{1}{2}}$ (cm/sec)		Heat Flux (mw/cm^2)		$(\frac{\overline{w^2}}{-\overline{uw}})^{\frac{1}{2}}$		$(\frac{\overline{u^2}}{-\overline{uw}})^{\frac{1}{2}}$	
			Lower	Upper	Lower	Upper	Lower	Upper	Direct	Est.	Lower	Upper	Lower	Upper
11	10	7.5	.02	.13	367	462	24.4	25.2	5.2	26.2	1.10	1.23	2.63	2.87
12	10	7.5			271	435	30.1	21.7			.81	.97	1.77	2.29
23	10	7.5			241	388	25.2	20.4			.82	.92	1.75	2.18
31	12.8	7.5	.05	.24	303	360	24.0	19.2	12.3	18.9	.95	.87	2.18	2.24
32	12.8	7.5	.04	.21	321	381	26.2	18.8	16.3	23.8	.91	.89	2.18	2.17
33	12.8	7.5	.07	.36	259	312	20.0	12.0	16.1	16.2	.94	.88	2.09	2.08
41	12	7.2	.06	.32	258	311	20.8	12.1	7.8	13.9	.91	.83	2.20	2.09
42	12	7.2	.06	.29	284	340	22.1	15.4	13.3	14.9	.90	.86	2.16	2.08
43	12	7.2	.10	.50	215	261	16.9	13.0	17.8	15.3	.92	.90	2.19	2.34
51	11	7.2	.27	1.49	132	152	6.4		9.6	11.3	1.96	2.09	5.45	5.75
52	11	7.2	.20	1.08	122	139	12.0		11.9	12.0	.84	.87	2.52	3.79
61	9.3	7.2	.37	2.33	101	105	6.2		7.6	10.2	1.29	1.34	3.39	4.16
62	9.3	7.2	.15	.98	157	177	13.5		11.6	13.4	.79	.74	2.25	3.06
72	17	8.5	.09	.36	277	318	21.0	20.9	12.3		1.08	1.12	1.96	2.27
81	17	8.0	.13	.51	238	266	19.7	18.8	11.1	16.7	.99	1.08	2.02	2.46
82	17	8.0	.17	.68	222	246	17.1	17.8	14.3	15.3	.99	1.24	1.97	2.10
83	17	8.0	.24	.94	207	256	16.4	54.5	8.9	21.3	1.02	3.96	2.02	3.45
91	12	8.2	.61	3.16	90	102	11.4	3.4	11.1	14.8	1.08	1.10	2.35	2.68
92	12	8.2	.73	3.76	98	98	7.5	7.4	8.9	17.3	1.09	1.18	1.91	1.90
101	14	8.2	.15	.69	185	207	14.2	15.0	10.8	11.3	1.01	1.08	2.21	2.60

Table D (continued)

Run	Lower Height (cm)	Fetch (m)	$-\frac{z}{L}$		U (cm/sec)		$(-\overline{uw})^{\frac{1}{2}}$ (cm/sec)		Heat Flux (mw/cm^2)		$(\frac{\overline{w^2}}{-\overline{uw}})^{\frac{1}{2}}$		$(\frac{\overline{u^2}}{-\overline{uw}})^{\frac{1}{2}}$	
			Lower	Upper	Lower	Upper	Lower	Upper	Direct	Est.	Lower	Upper	Lower	Upper
102	14	8.2	.35	1.62	162	181	12.8	10.9	8.7	11.6	.95	.96	2.84	3.21
103	14	8.2	.71	3.23	74	99	11.3	4.8	11.6	10.8	1.15	.83	2.33	2.16
111	14.5	8.4	.78	3.49	100	125	14.4	6.8	10.3	17.0	.93	.68	2.49	2.85
112	16.5	8.4			86	85	8.4	10.4	6.7	13.1	1.11	1.21	2.09	2.94
121	50	33.7	.32	.64	308	391	20.3	31.7	12.7		1.16	1.55	2.50	2.96
122	42	33.7	.35	.78	292	362	17.5	27.9	15.2		1.38	1.67	2.54	2.93
131	50	34	.52	1.04	263	297	17.2	21.4	10.8	12.5	1.31	1.45	2.28	2.48
132	50	34	.68	1.37	250	287	17.8	21.5	14.0	11.4	1.19	1.33	2.10	2.33
133	50	34	.76	1.52	226	266	19.8	22.1	13.9	6.6	1.06	1.11	2.08	2.24
231	23	19.8	1.68	5.34	88	106	5.9	7.8			1.49	1.90	2.30	2.62
232	23	19.8	.98	3.09	110	135	6.9	8.6	2.8	9.2	1.40	1.68	2.10	3.30
241	19	19.8	1.08	3.90	93	116	6.5	8.6	7.3	9.2	1.27	1.90	2.08	2.40
242	19	19.8	1.02	3.96	96		6.2		7.4	11.1	1.28		2.24	
243	19	19.8			109		7.8		8.3		1.10		2.02	
251	15	19	.36	1.57	142	158	9.8	11.5	4.1	12.7	1.18	1.47	2.04	2.16
252	15	19	.31	1.35	151	168	10.5	12.2	9.7		1.17	1.40	1.99	2.11
253	15	19	.24	1.05	166	189	12.0	13.3	9.3		1.02	1.30	2.18	2.18
261	15	19	.50	2.19	117	145	9.4	15.2	5.4	12.2	1.07	1.62	2.15	3.82
262	15	19	.44	1.89	137	167	10.1	12.7	6.2	13.2	1.23	1.52	2.07	2.27

APPENDIX E

ENERGY AND MASS BUDGET APPROACH

Equation 4.1.27 can be derived by considering the energy and mass budgets in a control volume over the lead. Let one end of this volume be at the upwind edge of the lead, x = 0; its other end is over the lead at x = F. The height of the volume, h, is greater than $\delta(x)$ for all x between zero and F. $U_i(z)$ and $T_i(z)$ are upwind velocity and temperature profiles. $U(F,z)$ and $T(F,z)$ are the velocity and temperature profiles at the downwind end of the control volume. W is the vertical velocity; $\overline{wt}_i$ the upwind vertical temperature flux; and $\overline{wt}_o$ the flux at the surface of the lead.

If conditions are steady-state, the energy content of the volume will not change. Its energy budget is thus

$$\rho c_p \int_o^h U_i(z)T_i(z)dz - \rho c_p \int_o^F [W(x,h)T_i(h) + \overline{wt}_i]dx$$

$$- \rho c_p \int_o^h U(F,z)T(F,z)dz + \rho c_p \int_o^F \overline{wt}_o \, dx = 0 , \quad E1$$

or

$$\int_o^F (H_o - H_i)dx = \rho c_p \int_o^h U(F,z)T(F,z)dz$$

$$- \rho c_p \int_o^h U_i(z)T_i(z)dz + \rho c_p \int_o^F W(x,h)T_i(h)dx . \quad E2$$

The third integral on the right above can be rewritten using the continuity equation,

$$\int_o^h \partial_x U \, dz = -\int_o^h \partial_z W \, dz = -W(x,h) \ . \qquad \text{E3}$$

Therefore,

$$\int_o^F W(x,h)T_i(h)dx = -\int_o^F T_i(h)dx \int_o^h \partial_x U \, dz$$

$$= -\int_o^h T_i(h)dz \int_o^F \partial_x U \, dx$$

$$= -\int_o^h [U(F,z) - U_i(z)]T_i(h)dz \ . \qquad \text{E4}$$

Equation E2 now becomes

$$\int_o^F (H_o - H_i)dx = \rho \, c_p \int_o^h U(F,z) \, [T(F,z) - T_i(z)] \, dz$$

$$+ \rho \, c_p \int_o^h [U(F,z) - U_i(z)][T_i(z) - T_i(h)] \, dz \ . \qquad \text{E5}$$

Because the two integrals on the right have the same limits of integration, let us compare them by estimating the magnitudes of their integrands:

$$U[T - T_i] \sim (100)(5) = 500 \ , \qquad \text{E6}$$

$$[U - U_i][T_i - T_i(h)] \sim (10)(0.2) = 2 \ . \qquad \text{E7}$$

Hence, on the right side of E5, the second integral is negligible in comparison to the first. We are left with

$$\int_o^F (H_o - H_i)dx = \rho \, c_p \int_o^{\delta(F)} U(F,z)[T(F,z) - T_i(z)]dz \ , \qquad \text{E8}$$

since $[T(F,z) - T_i(z)]$ is zero above $\delta(F)$ by definition. E8 is exactly 4.1.27: the budget approach leads to the same result that the differential equations do. Apparently condition 4.1.18, the smallness of the product of the vertical velocity and the upwind temperature gradient, is equivalent to E7.